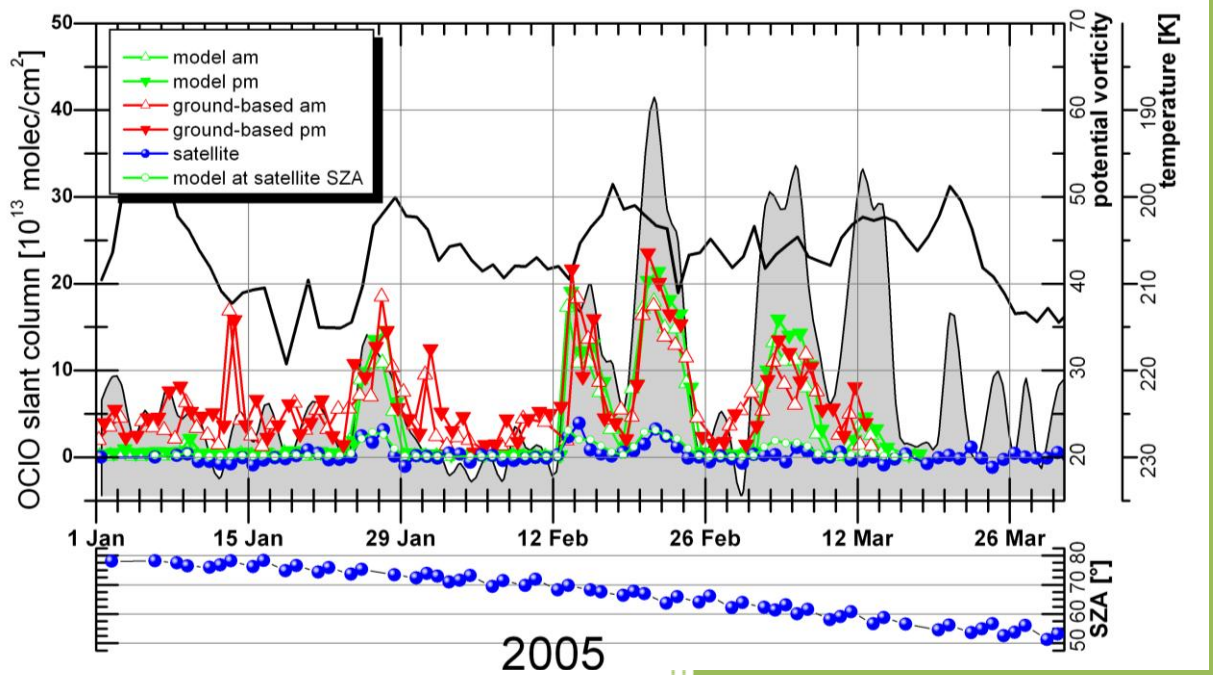


# Measurements of halogen oxides by scattered sunlight differential optical absorption spectroscopy



Measurements of halogen oxides  
by scattered sunlight differential optical  
absorption spectroscopy

Fachbereich für Physik und Elektrotechnik  
der Universität Bremen

zur Erlangung des akademischen Grades eines  
Doktor der Naturwissenschaften (Dr. rer. nat.)

von

Hilke Oetjen  
aus Rotenburg (Wümme)

Gutachter

1. Prof. John P. Burrows
2. Prof. Otto Schrems

Eingereicht am: 27. Januar 2009

Mündliche Prüfung am: 1. Dezember 2009

## Abstract

This work describes measurements of the tropospheric halogen species iodine monoxide (IO) and bromine monoxide (BrO) with multi-axis differential optical absorption spectroscopy (MAX-DOAS) at various locations: Svalbard (79°N), Andøya (69°N), List (55°N), Crete (35°N), and Maldives (5°N). Furthermore, the radiative transfer model SCIATRAN was used to investigate the sensitivity of the MAX-DOAS technique towards tropospheric absorbers as well as to estimate concentrations of IO and upper limits only for BrO. IO was detected at Svalbard, List, and Maldives with concentrations of 0.4 ppt, 2.2 ppt, and 2.8 ppt, respectively, but was below the average detection limits of 0.6 ppt and 1.3 ppt for Andøya and Crete, respectively. Uncertainties are estimated to be in the range of 2-3 ppt. These concentrations are averaged horizontally as well as vertically assuming a well-mixed surface layer of 500 m thickness or in the case of Svalbard and List 200 m. On a local scale, higher concentrations can occur. Tropospheric BrO could not be measured at any location outside the polar spring. Minimum detection limits for BrO were 2.2 ppt.

Ground-based zenith-sky DOAS measurements of stratospheric chlorine dioxide have been performed at the Arctic sites Svalbard and Summit (73°N) as well as at the mid-latitudinal site Bremen (53°N) and used to validate SCIAMACHY OCIO data for the exceptionally cold stratospheric spring 2005. OCIO was also derived with a chemical stacked box model. The agreement of all three data sets is excellent for the time of overpass of the satellite instrument, i.e. 10 AM. However, the ground-based measurements could not be reproduced with the model simulations for large solar zenith angles as well as for large concentrations. Sensitivity studies have been performed with the chemistry model and this exercise demonstrated that the measured OCIO columns cannot be explained within the known uncertainties of the model parameters including the involved photochemical data.



# TABLE OF CONTENTS

<b>1 OBJECTIVES.....</b>	<b>7</b>
<b>2 RELEVANT ASPECTS OF ATMOSPHERIC PHYSICS AND CHEMISTRY.....</b>	<b>9</b>
<b>2.1 Introduction to the atmosphere .....</b>	<b>10</b>
2.1.1 Composition of the atmosphere	10
2.1.2 Structure of the atmosphere	12
2.1.3 Polar stratosphere	14
<b>2.2 Radiation in the atmosphere .....</b>	<b>16</b>
2.2.1 Introduction to solar and terrestrial radiation	16
2.2.2 Interaction of light with matter	18
2.2.3 Radiative transfer for solar radiation	21
<b>2.3 Ozone and reactive halogens in the troposphere .....</b>	<b>22</b>
2.3.1 Oxidising Capacity of the Troposphere	23
2.3.2 Tropospheric halogens	26
2.3.3 Halogens in the marine boundary layer	28
2.3.4 BrO events at polar sunrise and further sources of reactive halogen species in the troposphere	31
<b>2.4 Stratospheric ozone chemistry .....</b>	<b>32</b>
2.4.1 The ozone hole	40
<b>3 THE MAX-DOAS TECHNIQUE .....</b>	<b>43</b>
<b>3.1 The viewing geometry.....</b>	<b>44</b>
<b>3.2 DOAS theory .....</b>	<b>46</b>
<b>3.3 Instrumentation .....</b>	<b>48</b>
3.3.1 Telescope including calibration unit	49
3.3.2 Automatic measurement mode	51
<b>3.4 Retrieval of the slant column density and error sources .....</b>	<b>52</b>
<b>4 INTERPRETATION OF MAX-DOAS MEASUREMENTS .....</b>	<b>55</b>
<b>4.1 The radiative transfer model SCIATRAN and calculation of air mass factors .....</b>	<b>57</b>

<b>4.2</b>	<b>Case studies for block air mass factors: Results for a radiative transfer modelling workshop in 2005.....</b>	<b>59</b>
<b>4.3</b>	<b>Profiles, total column densities and tropospheric column densities ..</b>	<b>77</b>
<b>5</b>	<b>MEASUREMENTS OF TROPOSPHERIC HALOGEN OXIDES .....</b>	<b>87</b>
<b>5.1</b>	<b>Sylt: Mudflats at the German North Sea coast.....</b>	<b>94</b>
<b>5.2</b>	<b>Svalbard: Fjord in the Arctic at Ny-Ålesund .....</b>	<b>111</b>
<b>5.3</b>	<b>Maldives: Open ocean site in the Indian Ocean .....</b>	<b>116</b>
<b>5.4</b>	<b>Andøya: Coastal zone at the Norwegian Sea.....</b>	<b>119</b>
<b>5.5</b>	<b>Crete: Island in the Mediterranean.....</b>	<b>120</b>
<b>5.6</b>	<b>Summary and discussion.....</b>	<b>121</b>
<b>6</b>	<b>STRATOSPHERIC OCLO IN THE 2005 NORTH POLAR SPRING .....</b>	<b>129</b>
<b>6.1</b>	<b>Data sets .....</b>	<b>133</b>
6.1.1	SCIAMACHY	134
6.1.2	Ground-based measurement sites	136
6.1.3	Modelling	136
<b>6.2</b>	<b>Validation .....</b>	<b>137</b>
<b>6.3</b>	<b>OCIO over Bremen .....</b>	<b>139</b>
<b>6.4</b>	<b>SZA dependence of OCIO.....</b>	<b>140</b>
<b>6.5</b>	<b>Model studies .....</b>	<b>142</b>
6.5.1	CIO-dimer cycle chemistry	142
6.5.2	BrO-CIO cycle chemistry	147
6.5.3	Further sensitivity tests	150
<b>6.6</b>	<b>Discussion and summary.....</b>	<b>152</b>
<b>7</b>	<b>SUMMARY .....</b>	<b>155</b>
	<b>Danksagung / Acknowledgements .....</b>	<b>157</b>
	<b>List of acronyms.....</b>	<b>159</b>
	<b>Bibliography.....</b>	<b>163</b>

# 1 Objectives

In this study, aspects of halogen chemistry in the atmosphere are examined. The method of the multi-axis differential optical absorption spectroscopy (MAX-DOAS) has been applied to measure the halogen oxides iodine monoxide IO and bromine monoxide BrO in the troposphere and the possibilities and limitations of this technique have been assessed. Furthermore, zenith-sky DOAS measurements have been performed for retrieving chlorine dioxide OCIO in the stratosphere. The results are presented in the following sections of this work:

- Sensitivity studies for the multi-axis observation geometry have been performed with the radiative transfer model SCIATRAN in order to investigate the information content of the measurements towards absorbers in the lower atmosphere. In addition, radiative transfer calculations have been applied to retrieve vertical column densities and profiles from the DOAS data and the results are validated with independent data: sections 4.2 and 4.3, pages 59-85.
- Measurements of tropospheric IO and BrO have been carried out, analysed and interpreted at five island sites ranging from polar regions to the tropics: chapter 5, pages 87-128.
- Stratospheric OCIO densities have been quantified and interpreted with a chemical stacked box model for the 2005 north polar spring: chapter 6, pages 129-154.

But first, the context of the results is given in an overview over the relevant aspects of atmospheric physics and chemistry (chapter 2), followed by a review of the multi-axis DOAS measurement technique (chapters 3 to 4.1).



## 2 Relevant aspects of atmospheric physics and chemistry

The mixture of gases surrounding a planet or star is called atmosphere and it is attached by gravitational attraction. In the case of our planet Earth, the atmosphere has developed into its current oxygen-rich composition in a slow evolutionary process initiated right after the birth of the planet some 4.5 billion years ago. The atmosphere is crucial for life by providing oxygen to breathe and carbon dioxide for photosynthesis via an equilibrium of biogenic activities. In addition, owing to the ozone layer higher up in the atmosphere, the atmosphere also acts as a protective shield against harmful solar ultra-violet radiation which would otherwise destroy all life forms at the surface. Through anthropogenic emissions starting with the onset of the industrial revolution, the atmospheric composition, resulting from a balance of natural emissions of species at the surface and their subsequent removal, has been substantially disturbed. E.g. in cities, the emissions of nitrogen oxides through combustion processes can lead to the build-up of large quantities of ozone and in the worst case to so-called photochemical smog situations threatening human health. Also some man-made halocarbons having a life-time of up to 100 years can be mixed higher up into the atmosphere and destroy the vital ozone layer. But also species occurring naturally through biological processes can locally alter the background composition of the atmosphere. E.g. halogenated compounds emitted from the sea can destroy the ozone in the lowest layers of the atmosphere.

This chapter will provide an overview on the fundamentals of the atmosphere and the chemistry relevant to this study. More details can be found in the textbooks by (Finlayson-Pitts and Pitts, 1986; Brasseur et al., 1999; Wayne, 2000). In addition to a general introduction to the atmosphere and its constituents, its structure and specifically the meteorology of the polar stratosphere will be presented in section 2.1. The basis of spectroscopy applied in this work for the remote sensing technique DOAS (see chapter 3) is the interaction of light with atmospheric gases as well as particles and this is reviewed in section 2.2. This chapter then continues with an overview of tropospheric background chemistry and how this chemistry can be perturbed through natural emissions of halogen species (sections 2.3). The basic chemistry of strato-

spheric ozone together with the anthropogenic interference leading to the development of the so-called ozone hole is reviewed in section 2.4.

## 2.1 Introduction to the atmosphere

The air pressure  $p$  in the atmosphere is a function of the height  $z$ . Due to the Earth's gravitational acceleration  $g$ , the pressure  $p(z)$  shows an exponential decline:

$$p(z) = p_0 \exp\left(-\frac{z}{H_s}\right) \quad (2.1)$$

with  $p_0$  being the atmospheric pressure at the surface and the atmospheric scale height  $H_s$  is usually in the order of 7 km:

$$H_s = \frac{RT}{g} \quad (2.2)$$

with  $T$  being the mean planetary surface temperature, and  $R = 287 \text{ J/K/kg}$  the universal constant for an ideal gas.

Consequently an upper limit of the atmosphere cannot be easily determined, but 100 km is commonly assumed as the boundary to outer space in atmospheric research. According to equation (2.1), 50% of the atmospheric mass is below 5.6 km and 99.9% within the lowest 50 km.

The general atmospheric composition will be summarised in section 2.1.1. Section 2.1.2 details the structure of and terminology for the atmosphere including the planetary boundary layer. Section 2.1.3 will introduce the reader to the polar stratosphere, a region of special interest for interpreting the results presented in this work.

### 2.1.1 Composition of the atmosphere

The dominant constituents in the atmosphere are nitrogen and oxygen which together make up 99% of dry air. They are long-lived species, i.e. they remain long enough in the atmosphere to become well-mixed up to a height of about 80 km. Other long-lived species are noble gases like argon, neon, and helium.

On the other hand, many trace gases are rather short-lived. Their temporal and spatial distribution is controlled by a complex balance of sources and sinks, i.e. emission and deposition, chemical and photochemical conversions, as well as dynamical transport. Emissions can be natural (volcanic eruptions, biological activity in the oceans and on the continents, forest fires, marshlands) as well as anthropogenic (biomass burning, industry, agriculture, e.g. cattle, rice paddies). Sources also include chemical and photochemical transformations which in turn of course also can act as sinks. Loss can also take place through wet and dry deposition. The conversion in so-called reservoir species is important for the transport and storage of pollutants.

The most important trace gas in the atmosphere is ozone which concentrations can be significantly perturbed through human, but also natural activities as already mentioned in the introduction to this chapter. The photochemical processes responsible for the formation and destruction of ozone will be discussed in detail in the sections 2.3 and 2.4. Other key compounds are the three major greenhouse gases water vapour, carbon dioxide, and methane, but also other organics like non-methane hydrocarbons, carbon monoxide, nitric oxide, nitric acid, the hydrogen compounds OH and HO<sub>2</sub>, and sulphur compounds.

Also, solids or liquids can be suspended in the atmosphere. These aerosols contain particles with diameters ranging from about 0.002 to 100 μm. Larger particles would sediment to the ground. Aerosols are important for the condensation of water vapour as so-called cloud condensation nuclei (CCN). They also provide a surface for heterogeneous reactions in the atmosphere and can act as sink for reactive species. As can be observed in smog situations, particles can influence the optical properties of the atmosphere. But aerosols can also have severe health impacts.

Anthropogenic sources of particles include combustion, man-made biomass burning and wind blown dust from open land areas with no vegetation like harvested fields or construction sites. Biogenic particles originate from volcanoes, dust storms, forest fires, vegetation (e.g. pollen), meteoric debris, and sea spray. So-called secondary particles are formed in the atmosphere by nucleation and subsequent growth.

## 2.1.2 Structure of the atmosphere

The temperature profile in the atmosphere displays a specific behaviour which provides a basis for separating the atmosphere into four horizontal regimes. These are characterised by alternating positive and negative temperature gradients (Figure 2-1). These four layers show very different behaviour in their thermodynamics, chemistry and dynamics.

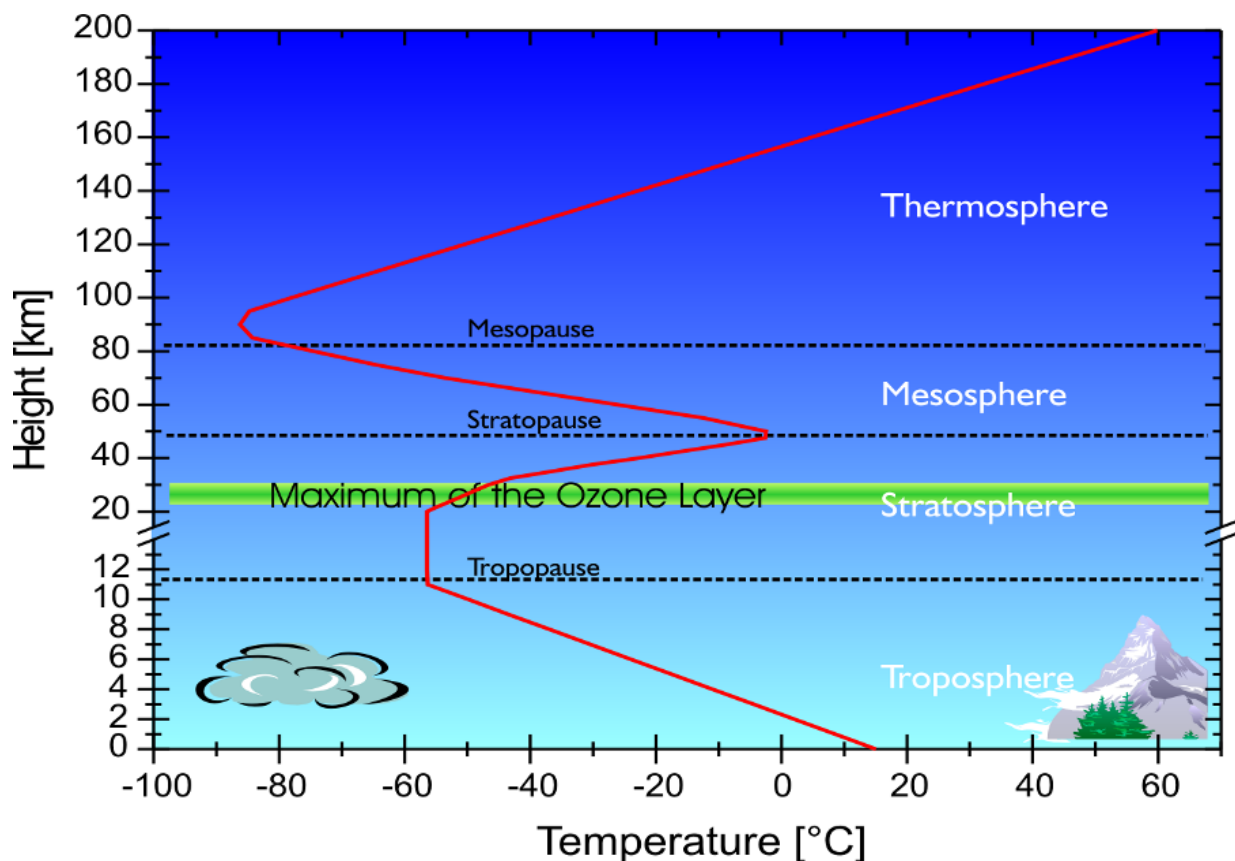


Figure 2-1 Vertical profile of the temperature between the surface and 100 km altitude according to the U.S. Standard Atmosphere ([http://modelweb.gsfc.nasa.gov/atmos/us\\_standard.html](http://modelweb.gsfc.nasa.gov/atmos/us_standard.html)). Note that the tropopause level represents mid-latitude conditions. Two different vertical scales are used

The troposphere, the lowermost atmospheric layer, contains about 80% of the atmosphere's mass as well as almost all water vapour and aerosols. The troposphere is mostly radiatively heated from the ground: The Earth absorbs solar radiation and releases this energy in the form of thermal infrared radiation (see next section 2.2). Consequently in a first approximation, the temperature decreases linearly from the

ground to the upper boundary of the troposphere, termed the tropopause. This decrease of temperature is caused by the pressure gradient in the atmosphere. The lapse rate of about 6.5 K per kilometre can be calculated from the first law of thermodynamics. However, this number presents rather an average. Locally, the lapse rate can vary or be reversed. The height of the tropopause ranges from 6 to 8 km in polar regions, about 12 km in midlatitudes to approximately 18 km at the equator.

The troposphere is often highly unstable and vertical mixing occurs. However, the tropopause acts as a barrier for mixing into the stratosphere due to the temperature inversion. As a consequence of the positive temperature gradient above the troposphere, air parcels can rise adiabatically up to the tropopause but cannot go any further. Also, water vapour and polar, i.e. water soluble substances cannot pass this barrier due to condensation or freezing. Transport through the tropopause mainly occurs locally in the vicinity of the jet streams in so-called tropopause foldings or in the tropics, through overshooting of cumulonimbus clouds (Andrews et al., 1987; Holton et al., 1995).

Above the tropopause, the stratosphere begins and extends up to a height of about 50 km to the stratopause. The temperature inversion of the stratosphere provides a stable stratification and residence times are substantially longer here than in the troposphere. This layer is extremely dry and contains approximately 90% of the atmospheric ozone. In the ozone layer, ozone as well as molecular oxygen absorbs the ultraviolet radiation from the sun resulting in a heating stronger than the cooling caused by the emission of infrared radiation. The first explanation for the presence of the ozone layer was given by Chapman (1930). Details about the involved chemistry are presented in section 2.4. The fundamental dynamics and cloud microphysics of the polar stratosphere, that lead to the development of the ozone hole, will be reviewed in the next section (2.1.3).

In the mesosphere, the temperature profile decreases again with increasing altitude. The mesosphere is capped by the mesopause in a height of about 85 km. The stratosphere and mesosphere are collectively termed the middle atmosphere.

The last of the four layers is the thermosphere. In this layer, atomic oxygen and nitrogen absorb very short-waved solar radiation causing photo-dissociation and photo-ionisation. The very fast movement of these atoms results in extremely high temperatures.

The troposphere can be further sub-divided into the planetary boundary layer and the above free troposphere. The planetary boundary layer (PBL) is the lowermost region in the atmosphere where surface effects play a significant role, having a height of a few hundred metres up to 2 km. It responds to surface forcings like exchange of gases and aerosols with terrestrial, biospheric, oceanic, or ice surfaces as well as dynamical interactions, and heat exchange. Over the land, this layer is highly turbulent due to heating from the ground during the day. Because of the well-mixed nature of the boundary layer, the temperature is homogenised and there is a jump towards the temperature of the overlaying free troposphere. This capping inversion in turn traps the turbulence of the boundary layer and is still present when at night, the surface cools much faster than the air above. Consequently, the mixing ceases. In polar regions during sunlit periods, the inversion is usually about 500 m high.

In the marine boundary layer (MBL), the ocean surface cools down slower than the atmosphere at night maintaining the turbulent mixing. Hence the diurnal variation of the planetary boundary layer is less pronounced in marine environments. There the height usually extends to about 1km. More details can be found in the textbook by Wallace and Hobbs (2006).

### **2.1.3 Polar stratosphere**

In the previous section (2.1.2) the link between the temperature of the stratosphere and the ozone layer has been indicated. However in the high-latitude winter, as a result of the absence of direct solar radiation, the absorption of light by ozone ceases and hence the temperature decreases in the winter-time stratosphere due to radiative cooling. This causes the air masses to sink which creates steep temperature and pressure gradients between the polar regions and the midlatitudes. A cyclonic vortex develops whose wind speed is peaking in the stratospheric polar night jet exceeding 100 m/sec (Schoeberl and Hartmann, 1991). Mixing of polar air masses with the warmer mid-latitudinal air is inhibited by this barrier. The so-called polar vortex is governed by persistent low temperatures often less than 195 K. This is the threshold temperature for the formation of polar stratospheric clouds (PSC) at a height of about 20 km.

From the tropopause up to 30 km height, the Earth is surrounded by a layer of liquid particles. This layer is referred to as Junge layer (Junge et al., 1961). The aerosols

are primarily composed of water and sulphuric acid  $\text{H}_2\text{SO}_4$  originating from sulphur dioxide  $\text{SO}_2$  emitted by volcanoes. During periods without volcanic activities the Junge layer is replenished from the oceans with carbonyl sulphide  $\text{OCS}$  which is oxidised and subsequently photolysed in the stratosphere (Crutzen, 1976). In this layer, polar stratospheric clouds can form under the cold vortex conditions (Carslaw et al., 1997). These clouds but also the aerosols themselves provide surfaces for heterogeneous reactions (see section 2.4.1).

Although the formation processes of PSCs are not fully understood, three types of PSCs may be defined depending on their chemical composition and optical properties: Type 1a PSCs consist of crystalline nitric acid trihydrate and sulphuric acid tetrahydrate, type 1b PSCs are composed of a supercooled ternary solution of water, nitric acid  $\text{HNO}_3$ , and sulphuric acid. Both types of clouds are optically thin and start forming at a temperature of 195 K. At 188 K water freezes onto the cloud droplets of type 1 PSCs. These clouds are then referred to as type 2 PSCs which are optically thick and brilliant in colour (Koop et al., 1997). Gravitational sedimentation of large PSC particles can occur with subsequent re-evaporation in lower atmospheric layers or permanent removal from the stratosphere.

In the northern hemisphere, the polar vortex is regularly disturbed by planetary waves. These originate in the troposphere, caused by the temperature contrast due to the alternating land-sea distribution, and can reach the stratosphere within one to four days, when westerly winds prevail (Holton, 1992). The dissipation of the waves causes a so-called stratospheric warming: Since the air density decreases with height, the amplitude of the Rossby waves grows. This effect reduces the speed of the polar night jet and the polar vortex can get distorted and displaced. The area of the vortex decreases through erosion. Afterwards, the shrunken and weakened vortex moves back to the centre of the pole and gains in strength. Often to the end of the winter, right before sunrise, the vortex is destroyed completely in a last stratospheric warming. The polar vortex over Antarctica is more stable since the landmass is symmetrically surrounded by water usually preventing the development of planetary waves. Hence, the Antarctic stratosphere is on average about 10 K colder than its northern counterpart and the ozone hole is more pronounced there. On the other hand, a more local phenomenon can occur in the Arctic: In the lee of mountains, waves may be generated that lead to the formation of PSCs due to the adiabatic cooling of rising air parcels.

## 2.2 Radiation in the atmosphere

The importance of radiation in the atmosphere has already been hinted at in the previous section (2.1): For instance, it influences the temperature of the atmosphere directly via the emission of terrestrial thermal infrared radiation but also through photochemical processes such as ozone formation in the stratosphere. Radiation also drives the chemistry occurring in the troposphere which will be shown in the next section 2.3.

In section 2.2.1, the basics of the solar and terrestrial radiation will be introduced. For remote sensing techniques, radiative transfer is crucial as photons transport the necessary information to the instrument. The interactions of light with the gases and particles in the atmosphere will be reviewed in the following section (2.2.2). As in this work, the measurements are confined to the light in the visible and the ultraviolet wavelength region, the theory of the radiative transfer only for the solar radiation is described in section 2.2.3.

### 2.2.1 Introduction to solar and terrestrial radiation

According to Planck's law of a blackbody, any object emits electromagnetic radiation depending on its temperature. The greater the temperature the larger is the emissive power. Also, as temperature increases, the maximum spectral irradiance is shifted to shorter wavelengths (Planck, 1902).

The sun can be approximated as a blackbody with a temperature of about 5800 K. The solar spectrum covers wavelengths from the long radio waves ( $\sim 10^8$ - $10^{13}$  nm) to gamma radiation ( $\leq 0.1$  nm). The maximum of the solar flux is in the visible wavelength region, more precisely between about 460 to 480 nm (Figure 2-2). Around 43% of the total radiation is emitted at visible, 49% at near-infrared and 7% at ultraviolet wavelengths.

Figure 2-2 shows the extraterrestrial solar irradiance as well as the blackbody radiation for an emitter at 5800 K. The third curve in Figure 2-2 describes the solar radiation measured at the Earth's surface after passing through the atmosphere showing significant attenuation of the radiation at some wavelengths. Also, the extraterrestrial spectrum displays some characteristic absorption lines. These are called Fraunhofer

lines according to their discoverer Joseph von Fraunhofer and are caused by the absorption of light by atoms and ions in the sun's photosphere and chromosphere.

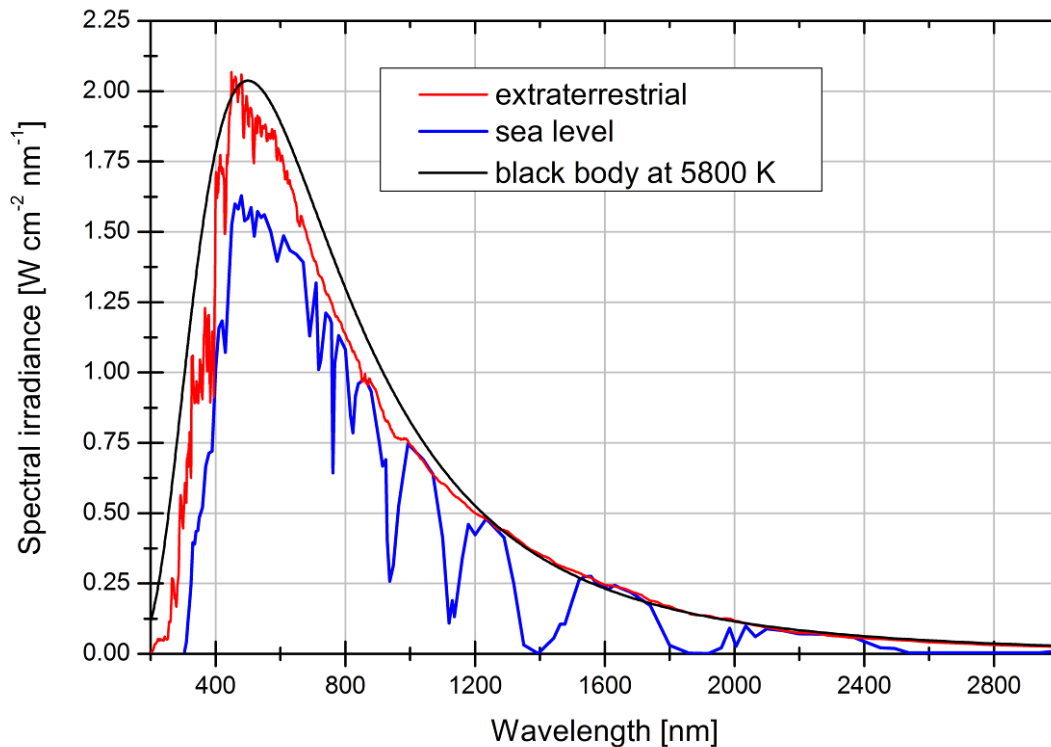


**Figure 2-2 Comparison of the solar radiation at the top and the bottom of the atmosphere to the black body radiation at 5800 K according to Planck's law. The absorption of some of the solar radiance observed at sea level is mainly caused by atomic and molecular oxygen, ozone, water and carbon dioxide. Absorption lines in the extraterrestrial solar spectrum are so-called Fraunhofer structures caused by the absorption in the solar atmosphere itself mainly by calcium, hydrogen, sodium, iron and magnesium.**

Absorption and scattering of radiation will be discussed in more detail in the next section 2.2.2. Here, only the global picture is given: Total radiation from the sun is attenuated by approximately 50% by passing the Earth's atmosphere: About 30% of the incoming solar energy is reflected back into space by clouds, by the Earth's surface and also by the atmosphere itself. This is the so-called planetary albedo of 0.31. Another roughly 20% is absorbed in the atmosphere mainly by ozone, oxygen and water vapour. The remaining 50% of the solar energy reaches the surface where it is absorbed and warms the Earth.

The Earth emits thermal infrared radiation. The equivalent blackbody temperature calculated from the amount of solar radiation received by the Earth is 256 K. But the average surface temperature is actually more than 30 K higher, i.e. 289 K. This discrepancy can be attributed to the natural greenhouse effect. The sun mainly emits in the visible and the atmosphere is almost transparent for visible electromagnetic waves. However, infrared-active molecules and cloud droplets can trap the terrestrial radiation in the atmosphere. The most important so-called greenhouse gases are water vapour, carbon dioxide and methane, but ozone, N<sub>2</sub>O, CO and chlorofluorocarbons (CFCs) also contribute to the greenhouse effect. These gases absorb infrared radiation and warm up, but subsequently radiate the energy away again in spaceward as well as earthward direction. This trapping leads to a delay of the loss of energy. The relationship between solar and terrestrial radiation is very delicate. However, among others, the anthropogenic emission of greenhouse gases and also aerosols alter the radiation budget of the Earth system leading to the man-made greenhouse effect.

### 2.2.2 Interaction of light with matter

Light that interacts with a gaseous medium like the atmosphere can undergo the following modifications relevant to this work: absorption by molecules and aerosols as well as scattering on molecules and aerosols. Both are considered as extinction processes. In the following section the different processes are discussed in more detail:

**Absorption** denotes the interaction of light with an object where the total energy of the photon is transferred to the molecule and thus the photon is destroyed. The probability for absorption of a photon depends on the specific wavelength  $\lambda$  and is described by the absorption cross section  $\sigma_{abs}(\lambda)$  that is expressed in units of cm<sup>2</sup>/molecule.

Whereas solid and liquid bodies can absorb light at continuous wavelengths, gases show a continuous as well as a discrete spectrum with sharp spectral lines. The energy of the consumed photon is used to change into another electronic, vibrational or rotational state. The latter two processes only exist for certain molecules depending on their structure. Transitions between different electronic states require the high energy of visible or ultraviolet photons. In molecules, for every electronic state, several

vibrational energy levels exist with energy transitions corresponding to light of infrared wavelengths. These vibrational states occur due to the flexibility of the bonds between individual atoms in the molecule. In addition, the whole molecule can be excited to rotate around one of its axes. This causes the vibrational levels, in turn, to split into a number of finer rotational energy levels equivalent to the microwave and far-infrared spectrum. The absorbed energy can be lost by radiation (emission of a new photon), transferred to kinetic energy or be used in chemical reactions.

Every molecule features a unique absorption cross section. The strength of the absorption lines can be temperature dependent because the probability for the occupation of a specific energy level depends on the temperature. The position of the absorption lines observed in the light from a continuous light source after passing through a gas can be used to identify absorbers and the depth of the lines to quantify the amount present in the probe (see section 3.2). Cross sections have to be measured in laboratory experiments since theoretical calculations are usually not accurate enough.

Also particles can absorb light. Black carbon or soot which originates from the combustion of fossil fuels is a strong absorber of visible light. This absorption, which is a broad-band absorption (e.g. absorption cross section for an ensemble of diesel soot particles  $\sigma_{aer-abs}(\lambda) \sim \lambda^{-1.9}$  (Schnaiter et al., 2003)) can lead to decreased visibility.

**Scattering** is the redirection of a photon by a particle or gas molecule. It produces diffused light in the atmosphere which is responsible for the brightness of the sky when the sun is hidden behind clouds. The probability of a photon for being scattered is described by the scattering cross section  $\sigma_{scat}(\lambda)$  also measured in units of  $\text{cm}^2/\text{molecule}$  and the probability for the angular distribution of the direction the photon is scattered in, by the phase function  $P(\gamma)$  where  $\gamma$  is the angle between the incident and the scattered radiation.

**Elastic scattering** can be described by theories related to the relative size of the scatterer in comparison to the incident wavelength:

**Mie scattering** is an approximation for scattering on particles with average diameters in the same size range as the wavelength of the incident light. Examples for visible radiation are aerosols (diameter:  $\sim 1 \mu\text{m}$ ) and cloud droplets ( $\sim 10 \mu\text{m}$ ). As the size and form of particles is highly variable, normally an approximation of spherical particles is applied for the scattering cross section:  $\sigma_{Mie} \sim \lambda^{-k}$  with  $k$  between 0 and 2.

This weak dependence on the wavelength is reflected in the whiteness of clouds. The phase function of Mie scattering exhibits a strong forward peak.

**Rayleigh scattering** is the theory that describes scattering on very small particles, primarily gas molecules (mainly O<sub>2</sub> and N<sub>2</sub> since these are the major atmospheric components) with a diameter ( $\sim 10^{-4}$  μm), small compared to the incident wavelength. Rayleigh scattering depends on the wavelength by  $\sigma_{Ray} \sim \lambda^{-4}$ : Blue and violet light is therefore scattered more than the light of the longer wavelengths causing the sky to be red and orange at sunset and sunrise as well as the blueness of the sky for overhead sun conditions. It can be concluded that the bluer the sky, the cleaner with respect to particles, is the air since Mie scatterers would result in a more white sky. Maximum intensities occur symmetrically in the forward and in the backward direction resulting in a peanut shape of the phase function.

**Raman scattering (inelastic component of Rayleigh scattering)** plays only a minor role in radiative transfer. However, it is important for DOAS measurements since it alters the spectral structures measured with the instrument (see section 3.2). Initially, this effect was recognised by Grainger and Ring (1962) in the atmosphere and was subsequently termed the Ring effect. Grainger and Ring had observed changes in the depth of the Fraunhofer lines when comparing direct and scattered radiation. Modifications in the atmospheric absorption structures are termed molecular Ring effect.

The energy taken up or released during the inelastic scattering process corresponds to the differences in rotational or vibrational energy levels. One differentiates between Stokes scattering where the molecule absorbs energy and anti-Stokes scattering where energy is lost.

A scattering cross section  $\sigma_{Ring}$  for the Ring effect consistent with the cross sections defined above can be calculated with a radiative transfer model (Vountas et al., 1998). It simulates the redistribution of the solar radiance due to the Raman scattering on O<sub>2</sub> and N<sub>2</sub> molecules for a specific light path through the medium, here, the atmosphere.

### 2.2.3 Radiative transfer for solar radiation

Mathematically, the light intensity  $I(\lambda)$  after passing through a medium decreases exponentially with the path length  $s$ , the extinction cross section  $\sigma_{ext}(\lambda)$ , and the number density  $\rho$  of the absorbers or scatterers and can be expressed by the Beer-Lambert-Bouguer-law:

$$I(\lambda) = I_0(\lambda) \exp[-s\rho\sigma_{ext}(\lambda)] \quad (2.3)$$

where  $I_0(\lambda)$  is the incident intensity. The contributions to the extinction are additive:

$$\sigma_{ext}(\lambda) = \sum_i \sigma_{abs,i}(\lambda) + \sigma_{Mie}(\lambda) + \sigma_{Ray}(\lambda) + \sigma_{Ring}(\lambda) + \sigma_{aero-abs}(\lambda) \quad (2.4)$$

with the summation over every gaseous species  $i$  present in the sampled medium. The optical depth  $\tau$  can be defined as:

$$\tau(\lambda) = -\ln \left[ \frac{I(\lambda)}{I_0(\lambda)} \right] \quad (2.5)$$

In the atmosphere, the change in intensity of the radiation field at any given point  $\mathbf{r}$  and in the direction  $\mathbf{e}_s$  can be described by the radiative transfer equation:

$$\frac{dI(\mathbf{r}, \mathbf{e}_s)}{ds} = -\alpha(\mathbf{r})I(\mathbf{r}, \mathbf{e}_s) + \alpha(\mathbf{r})B(\mathbf{r}, \mathbf{e}_s) \quad (2.6)$$

here given in its coordinate independent form and without indicating the wavelength dependence of the intensity. Equation (2.6) is a partial differential equation of first order. The term on the left side describes the change of intensity along a path  $s$ . The right hand side of equation (2.6) assigns this change to a loss due to extinction and a gain of intensity through scattering of radiation into the line of sight, i.e. into the direction  $\mathbf{e}_s$ . In analogy to the extinction cross section, the extinction coefficient  $\alpha$  includes absorption and scattering with

$$\alpha(\lambda) = \rho\sigma_{ext}(\lambda) \quad (2.7)$$

$B$  is the source function which is the sum of the single scattering source function  $B_{SS}$  and the multiple scattering source function  $B_{MS}$ :

$$B_{SS}(\mathbf{r}, \mathbf{e}_s) = \frac{\varpi(\mathbf{r})}{4} F_0 P(\mathbf{r}, \gamma_0) \exp \left( -\int_0^s ds \alpha(s) \right) \quad (2.8)$$

and

$$B_{MS}(\mathbf{r}, \mathbf{e}_s) = \frac{\varpi(\mathbf{r})}{4\pi} \int d\tilde{\omega} P(\mathbf{r}, \gamma) I_{dif}(\mathbf{r}, \mathbf{e}_s) \quad (2.9)$$

The source function  $B_{SS}$  represents the gain of radiation through light scattered only once and into the direction of  $\gamma_0$  which is the angle between the direct solar beam and the scattered radiation. The single scattering source function depends on the incident solar flux  $\pi F_0$  on the top of the atmosphere. The single scattering albedo  $\varpi$  gives the probability for a photon for being scattered rather than being absorbed. The exponent in the exponential function is the optical depth with the integration performed along the direct solar beam. In general, the optical depth  $\tau$  is defined as:

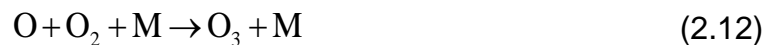
$$\tau = \int ds \alpha(s) \quad (2.10)$$

Combining equations (2.3) and (2.7) and assuming the extinction coefficient does not vary along the light path  $s$ , yields again equation (2.5) from the general definition of the optical depth. The multiple scattering source function  $B_{MS}$  is influenced by the diffuse radiation field  $I_{dif}$ , which describes the radiation that has been scattered in the atmosphere or reflected from the Earth's surface at least once before. The integral in equation (2.9) accounts for all possible scattering events within a solid angle  $d\tilde{\omega}$ . More details can be found in the textbook by Liou (1992).

## 2.3 Ozone and reactive halogens in the troposphere

Central to the chemistry of the troposphere is the formation and removal of ozone. Unlike the protective shield, that is provided by the stratospheric ozone, tropospheric ozone is a major constituent of photochemical smog and is harmful to human health causing among others respiratory problems.

Only the reaction of atomic with molecular oxygen yields ozone. In the troposphere, the atomic oxygen is provided by the photolysis of nitrogen dioxide  $\text{NO}_2$ :



with M being a background molecule necessary to balance energy and momentum in the reaction. Consequently, the formation of ozone depends critically on the availabil-

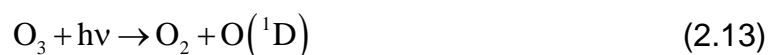
ity of this molecule. Nitrogen oxides  $\text{NO}_x$  ( $= \text{NO}_2 + \text{NO}$ ) are mainly released in the form of nitric oxide  $\text{NO}$ , but are rapidly converted into each other. They are produced through the combustion of fossil fuels and in forest fires. A small fraction is also generated by lightning (e.g. Huntrieser et al., 1998). Also, soils are an important source of  $\text{NO}_x$ . An introduction to the major oxidation chains in the troposphere, leading to formation or destruction of ozone, will be presented in the next section 2.3.1.

Halogens are very reactive species in the troposphere but also in the stratosphere (see section 2.4). Locally, they can be emitted in significant quantities e.g. in so-called bromine explosions or from biota in the oceans, and subsequently destroy ozone. Halogen species of importance to atmospheric chemistry are chlorine, bromine, and iodine. In this study, the tropospheric species  $\text{IO}$  and  $\text{BrO}$  have been quantified (see chapter 5). Sources and sinks of these trace gases will be discussed in the sections 2.3.3 and 2.3.4 and their effects on tropospheric chemistry in the following section 2.3.2.

### 2.3.1 Oxidising Capacity of the Troposphere

Into the troposphere, numerous species of natural or anthropogenic origin are directly emitted from the Earth's surface. These include as natural sources emissions from volcanoes, oceans, forest fires and biological activity as well as man-made emissions from industrial activities, fossil fuel burning and also emissions from livestock and agriculture. The ability of the atmosphere to remove, i.e. oxidise such substances is termed oxidising capacity: Photochemically driven oxidation chains are initiated by certain oxidative radicals that can react with a variety of species. At the end of such an oxidation chain, a species is formed that is either no longer reactive like e.g.  $\text{H}_2\text{O}$  or  $\text{O}_2$  or the products can be removed from the atmosphere by wet or dry deposition. The hydroxyl radical  $\text{OH}$ , as the most effective oxidant for almost every pollutant, dominates the daytime atmosphere having a lifetime of about 1 sec.

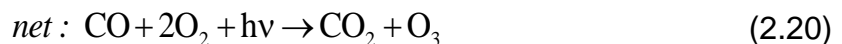
In the background atmosphere, the photolysis of ozone, which may originate from the stratosphere, with light of wavelengths shorter than 320 nm leads to the formation of  $\text{OH}$ :



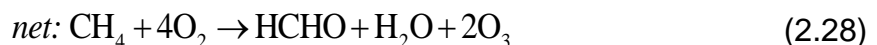
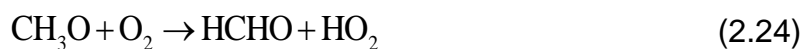


Note that only a small fraction (~1-10% depending on humidity) of the excited oxygen  $\text{O}({}^1\text{D})$  reacts with water vapour to generate hydroxyl radicals. The remaining part is quenched to its ground state ( ${}^3\text{P}$ ) which quickly recombines with molecular oxygen to form ozone. Thus there is no net effect on ozone.

Most importantly, OH initiates the oxidation chains of carbon monoxide CO:



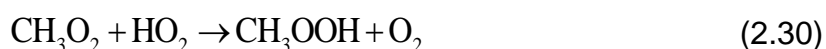
and methane  $\text{CH}_4$ :



both resulting in a production of ozone in a polluted atmosphere with  $\text{NO}_x$  available. The hydroxyl radical as well as NO are reformed in this reaction scheme.

Methane is an important greenhouse gas and is produced in wetlands like swamps, marshes or rice paddies, but is also emitted from decaying organic matter in soils, oceans, as well as landfills. Cattle, termites, and natural gas are also major sources of CH<sub>4</sub>. Typical northern hemisphere concentrations range approximately from 1700 to 1760 ppb (Schneising et al., 2008). The oxidation of methane leads to the formation of formaldehyde HCHO (reaction (2.24)). Oxidation as well as photolysis of HCHO in turn produces CO. Also, other hydrocarbons can be oxidised to form carbon monoxide. CO is released from the surface through incomplete combustion of fossil fuels and in biomass burning. Observations obtained mixing ratios of about 60 ppb in the remote troposphere, but CO mixing ratios were shown to exceed 500 ppb during pollution events (Tanimoto et al., 2008).

The oxidation chains are terminated, when there is little or no nitric oxide NO available. Then the products of reactions (2.16) and (2.22) react with the hydroperoxy radical HO<sub>2</sub>:



producing hydrogen peroxide H<sub>2</sub>O<sub>2</sub> and methyl hydroperoxide CH<sub>3</sub>OOH, which both can be removed by wet deposition. The oxidation chain can also be interrupted by:



These three reactions lead to net ozone destruction. But, reactions (2.29)-(2.31) can compete with (2.17) and (2.23) only when the NO concentrations are in the range of 10 to 50 ppt. However, on a global level, ozone is increasing significantly since the increasing usage of fossil fuels (Finlayson-Pitts and Pitts, 1986).

The night-time chemistry is dominated by the nitrate radical NO<sub>3</sub> which is formed through the reaction of ozone with NO<sub>2</sub>:



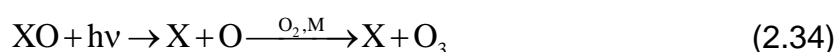
Although the reactions of NO<sub>3</sub> with organic compounds are relatively slow, it initiates nevertheless the dominant oxidation processes at night when OH concentrations are low. NO<sub>3</sub> is rapidly photolysed and hence cannot survive daylight.

### 2.3.2 Tropospheric halogens

Halogen species alter the oxidation capacity of the troposphere by destroying ozone (Chameides and Davis, 1980) and they can change the  $[\text{OH}]/[\text{HO}_2]$ -ratio. Halogen oxides react with dimethyl sulphide DMS inhibiting the production of  $\text{SO}_2$  and hence the source of new sulphate particles in the marine boundary layer (Toumi, 1994; Nakano et al., 2003). On the other hand, iodine oxides can play an important role in the formation of aerosols (O'Dowd et al., 1998) leading to a possible climate feedback. Of significance in the stratosphere are mainly chlorine and bromine radicals (see chapter 2.4) and in the troposphere, bromine and iodine radicals. Fluorine is quite stably bound as hydrogen fluoride HF and does not act as important radical. For some recent comprehensive overviews on tropospheric halogen chemistry see Simpson et al (2007b) and von Glasow and Crutzen (2007).

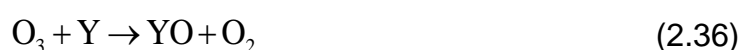
The tropospheric sources of halogen are discussed in more detail in the next sections (2.3.3 and 2.3.4). Here, the main reaction pathways in the troposphere are presented. In the following, the letter X stands for chlorine Cl, bromine Br, or iodine I, although, about half of the chlorine is bound in the form of HCl and chlorine nitrate  $\text{ClONO}_2$  and does hardly participate in the following reaction schemes (Simpson et al., 2007b).

A halogen radical X can react with ozone. If the formed halogen oxide subsequently photolyses, a steady-state is established during daytime:



For a net ozone destruction the halogen oxides have to react with each other or with  $\text{HO}_2$ . There are two main reactions initialising the ozone destruction cycles. In the case of high halogen mixing ratios, the XO can react with a second halogen oxide (the second halogen in this reaction scheme is represented by Y):

#### cycle 1





The cross reactions BrO+ClO and BrO+IO are faster than the BrO+BrO reaction (Le-Bras and Platt, 1995; Solomon et al., 1994), however, under conditions of high bromine concentrations, the BrO self-reaction is the main ozone destroying mechanism (see section 2.3.4).

Iodine behaves somewhat differently to the sequence of reactions (2.35) to (2.37) though: The main products of the IO-self-reaction are OIO and IOIO (Gomez Martin et al., 2007) although the latter molecule is unstable and dissociates to OIO and I (Saunders and Plane, 2005). Recent laboratory studies have shown that OIO can be efficiently photolysed to yield I atoms (J. C. Gomez Martin, University of Leeds, personal communication, 2008) establishing another powerful ozone destruction cycle:

### cycle 2



In the troposphere, only OIO is of importance, OBrO and OCIO are produced with a lower efficiency and are readily photolysed.

Another ozone destruction cycle involves the reaction of the halogen oxide with HO<sub>2</sub>:

### cycle 3



This sequence can alter the [OH]/[HO<sub>2</sub>]-ratio which has so far been only observed in the unpolluted atmosphere (Bloss et al., 2005).

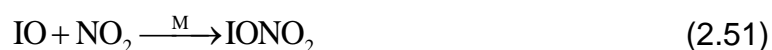
Observations of IO during night-time (see introduction to chapter 5) can be explained through the reaction of I<sub>2</sub> with the nitrate radical and subsequent reaction with ozone:



followed by reaction of IO with NO<sub>3</sub> to form OIO:



Until recently, it was assumed that in a polluted atmosphere iodine can be quite stably bound as iodine nitrate formed by the reactions (2.48) and (2.51) inhibiting the ozone loss:



However, Kaltsoyannis and Plane (2008) showed through quantum chemical calculations that IONO<sub>2</sub> can be effectively recycled back to active iodine species through the inverse of reaction (2.48):



After the photolysis of the produced molecular iodine, ozone destruction can start again (reaction (2.39)).

Particle formation in the marine boundary layer establishes a loss of gas-phase iodine. This has been observed in the atmosphere (McFiggans et al., 2004) and in the laboratory (O'Dowd et al., 2002; Jimenez et al., 2003), but the exact pathways are still under investigation. However, the particles seem to be made up of I<sub>2</sub>O<sub>5</sub> (Saunders and Plane, 2005). Further removal processes occur through the reaction of halogens with HO<sub>2</sub> to form HX which is highly soluble as well as the uptake of the halogen nitrates XONO<sub>2</sub> into the aerosol phase.

### 2.3.3 Halogens in the marine boundary layer

Reactive halogen species originate from the degradation of halocarbons released from macroalgae and phytoplankton or from the sea salt halides. The main source of iodine appears to be di-iodimethane CH<sub>2</sub>I<sub>2</sub> (Carpenter, 2003) and locally also I<sub>2</sub> (Saiz-

Lopez and Plane, 2004b) whereas bromine is suggested to be produced by acid-catalysed multi-phase reactions on sea salt.

Halogens are present in the sea water and the organisms living in the ocean are accumulating it for their metabolism. The oxygen, essential for aerobic processes in cells, results in the appearance of toxic reactive oxygen species. If those reactive oxygen species build up to high concentrations, damage can occur to the cell and finally leads to its death. This oxidative stress can be induced by environmental stress factors, e.g. UV-radiation, temperature changes, high temperature, or nutrient deficiency. For macroalgae or so-called seaweed also desiccation during low tide stresses the organism since algae are missing the vascular tissues of higher plants. The defence mechanisms against those reactive oxygen species involve enzymes and antioxidants. Among others, hydrogen peroxide  $H_2O_2$  is a very reactive oxygen species. Enzymes can transfer one of the oxygen atoms to a suitable substrate. The enzyme families that are responsible for the release of halocarbons are halide ion methyltransferases and haloperoxidases (Theiler et al., 1978; Carpenter, 2003). The substrate incorporates in this case a halide and it results in the production of the electrophilic compounds  $XO^-$  (X being chlorine, bromine or iodine). These, in turn, react with organic material in the cell walls generating halocarbons. Subsequently, they are released as waste products and since they exhibit a low solubility, can easily become supersaturated in the sea causing a flux to the atmosphere (Singh et al., 1983).

It has also been suggested that the macroalgae along the shores in the intertidal zone of the oceans are emitting molecular iodine in addition to the halocarbons when being exposed to the atmosphere at low tide (Saiz-Lopez and Plane, 2004b). The involved mechanisms for that are not fully understood yet. However it was observed that seaweed releases iodide directly under stress and it was suggested that this  $I^-$  would react with ozone on the surface of the plant to produce  $I_2$  (Küpper et al., 2008; but see also discussion in Verhaeghe et al., 2008). Whereas the direct emission of molecular iodine seems to be mainly associated with certain *laminaria* species (*laminaria digitata* (Küpper et al., 2008)), i.e. brown algae which are also known as kelp and being restricted to coastal sites, methyl iodide  $CH_3I$  is the dominant iodine species in the troposphere (Yokouchi et al., 2008).  $CH_3I$  as well as methyl bromide  $CH_3Br$  are known to be produced by some phytoplankton species (e.g. Itoh et al., 1997; Manley and de la Cuesta, 1997), but are only a negligible sources of iodine

and bromine atoms in the marine boundary layer due to their relatively long lifetime of 3-5 days (Rattigan et al., 1997) and about 1 year (Yokouchi et al., 2000), respectively. A direct link to the emission of higher halogenated compounds has been established so far for macroalgae (e.g. Schall et al., 1994; Giese et al., 1999; Yokouchi et al., 2005; Carpenter et al., 2000), for some polar microalgae, i.e. diatoms (Moore et al., 1996), for two species of marine bacteria (Fuse et al., 2003) and only recently for cyano-bacteria (classified as phytoplankton) in the Baltic Sea (Karlsson et al., 2008). The di-halogenated species bromiodomethane  $\text{CH}_2\text{BrI}$  and chloriodomethane  $\text{CH}_2\text{ClI}$  can exist in the atmosphere for about 1 hour and diiodomethane  $\text{CH}_2\text{I}_2$  about 5 min (Rattigan et al., 1997; Mössinger et al., 1998). The latter being the main source of atomic iodine in the marine boundary layer. Alkyl iodides are more photolabile than their brominated or chlorinated counterpart: e.g. the photolytic lifetime of di-bromomethane  $\text{CH}_2\text{Br}_2$  is in the order of years (Mössinger et al., 1998), but see also the lifetimes of methyl iodide and methyl bromide. Bromocarbons and chlorocarbons can be transported to the stratosphere and can contribute to ozone depletion there (see also section 2.4), although recently, it was suggested that bromocarbons might be responsible for the observed concentrations of BrO in the free troposphere (Yang et al., 2005; Salawitch, 2006).

Recently, Martino et al. (Martino et al., 2009) observed the direct release of  $\text{CH}_2\text{I}_2$ ,  $\text{CHClI}_2$  as well as  $\text{CHI}_3$  from sea water when being exposed to ambient concentrations of ozone. They suggest formation of hypoiodous acid HOI and molecular iodine  $\text{I}_2$  when dissolved iodide  $\text{I}^-$  reacts with ozone on the sea surface followed by reactions with dissolved organic matter. This leads in turn to the formation of the iodocarbons.

Bromine and chlorine is readily available in the marine boundary layer in the form of sea salt particles. Sea salt contains 55.7% of chlorine, 0.19% of bromine, and only  $2 \times 10^{-5}\%$  of iodine by weight (Wayne, 2000). Sea salt aerosols are generated by bubble bursting at the ocean's surface. The bubbles are mainly formed by the breaking of waves.

The bromine and chlorine can be released in acid-catalysed autocatalytic multiphase reaction cycles as proposed by Fan and Jacob (1992). Those cycles are initiated by:



The HOBr is produced in the gas-phase by reaction (2.44) and then taken up by the aerosol where it reacts with the halide  $\text{X}^-$  (either  $\text{Br}^-$  or  $\text{Cl}^-$ ) in the presence of  $\text{H}^+$ . The

Br<sub>2</sub> or the inter-halogen species BrCl is then released into the gas-phase again where it is readily photolysed. The preferred mechanism is the release of Br<sub>2</sub> as has been shown in laboratory studies. Only at low bromine concentrations in the particles, BrCl is the preferred product (Fickert et al., 1999). Models predict BrO concentrations of 1 to 4 ppt from acid-catalysed activation of bromine from sea-salt aerosol (von Glasow et al., 2002; Vogt et al., 1996).

Also, the reactions of N<sub>2</sub>O<sub>5</sub> with NaCl and NaBr have been studied and lead to the release of halogen nitrates ClNO<sub>2</sub> or BrNO<sub>2</sub> from the aerosol which can be photolysed (e.g. Finlayson-Pitts et al., 1989; Schweitzer et al., 1998). The uptake of BrONO<sub>2</sub> onto the particle leads to the degassing of Br<sub>2</sub> and BrCl (more details can be found in von Glasow and Crutzen, 2007).

It has been observed that supermicrometer sea salt aerosol can be depleted in bromine on average by 50% (Sander et al., 2003a). Iodine on the other hand is enriched in particles (Duce et al., 1963) indicating that aerosols are rather a sink than a source for gaseous iodine compounds.

#### **2.3.4 BrO events at polar sunrise and further sources of reactive halogen species in the troposphere**

For the first time in the 80s of the last century, sudden ozone depletion events were observed in the Arctic after polar sunrise (Bottenheim et al., 1986; Oltmans and Komhyr, 1986). These coincided with enhanced filterable bromine (Barrie et al., 1988) and subsequently, also the BrO radical was identified during these events (Hausmann and Platt, 1994). BrO events have also been reported from Antarctica (e.g. Kreher et al., 1997; Saiz-Lopez et al., 2007b) and can be observed from space indicating its widespread nature (Wagner and Platt, 1998; Richter et al., 1998).

The sources of the observed reactive bromine species are the sea salt ions (see also the previous section 2.3.3). When a salt solution, here the sea ice freezes, the halides get concentrated in a highly saline brine at the surface (Koop et al., 2000). Several possible sources are under discussion: frost flowers which are highly saline ice crystals that grow on fresh sea ice (Kaleschke et al., 2004), young sea ice itself, less than one year old (Wagner et al., 2001b; Simpson et al., 2007a), and blowing snow that was in contact with sea ice (Yang et al., 2008). In general, the bromine is re-

leased in the acid-catalysed autocatalytic multiphase reaction triggering an exponential growth of the gas-phase bromine as described above with X and Y both being Br (see reaction (2.53)). In this reaction one active bromine species, i.e. HOBr is consumed while two bromine atoms are released through the conversion of inactive bromide Br<sup>-</sup> in the brine. Obviously, some active halogens must be present in the atmosphere to trigger the bromine explosion. These might originate from biogenic emissions.

Other sources of halogens include industrial use of chlorinated hydrocarbons for paper manufacturing and water treatment to prevent bacterial growth in swimming pools and cooling towers. Also, fossil fuel burning can release chlorine compounds in the case of coal and chlorine as well as bromine from leaded fuel. Biomass burning also produces methyl chloride and methyl bromide. Methyl bromide is also used as fumigation agent although methyl halides are mainly of importance for stratospheric chemistry due to their long photolytic lifetime (see section 2.3.3). The acid hydrogen chloride HCl is released into the atmosphere through incineration of waste as well as through steel making. Hydrochloric acid is also used for the production of polyvinyl chloride (PVC).

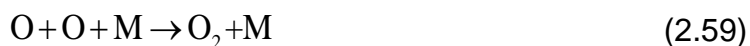
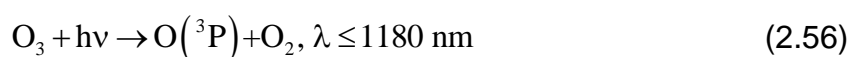
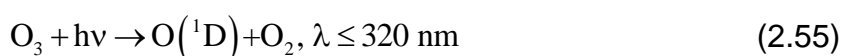
Further, halogens are also emitted from volcanoes through degassing mainly in the form of HCl (Oppenheimer et al., 2006). But also reactive halogens in the form of BrO, ClO and OCIO have been observed in volcanic plumes (Bobrowski et al., 2007; Lee et al., 2005). Active forms of bromine, iodine and chlorine have been reported from the Dead Sea and other salt pans, e.g. the Great Salt Lake (U.S.A.) (Hebestreit et al., 1999; Zingler and Platt, 2005; Stutz et al., 2002). Other natural sources involve emissions from rice paddies, peatlands, and coastal marshes.

## 2.4 Stratospheric ozone chemistry

Also the stratospheric chemistry is dominated by the production and loss mechanisms of ozone. However, unlike in the troposphere, stratospheric ozone is vital for life on Earth through the molecule's ability to absorb ultraviolet light. UV-B (290 to 320 nm) and UV-C (100 to 290 nm) radiation can also be absorbed by the deoxyribonucleic acid (DNA) in living organisms. The resulting excited electronic states can

then lead to a mutation of the DNA in a way that conditions such as skin cancer can occur in humans (Crespo-Hernández et al., 2005). The ozone layer, that surrounds the Earth, hinders this harmful radiation to reach the surface.

Absorption of light causes ozone to dissociate and produce atomic oxygen. This can in turn react with molecular oxygen to form ozone again. The first theory for the presence of the ozone layer was hypothesised by Sir Sydney Chapman (Chapman, 1930). An updated Chapman cycle involving oxygen species only is:



Reaction (2.59) is too slow to be of importance in the atmosphere. Reaction (2.54) describes the only production of odd oxygen. The term odd oxygen is commonly applied for ozone and atomic oxygen together since they are rapidly converted into each other by the reactions (2.55) to (2.57). The only real loss of ozone is given by reaction (2.58). A mechanism involving only odd and molecular oxygen does not explain the ozone distribution in the atmosphere. Other loss mechanisms also contribute, predominantly, in the form of catalytic cycles, as suggested by Bates and Nicolet (1950):



with the radical X being NO, OH, or the halogen radicals Cl, Br, and I. These species are reproduced in the process and are able to destroy ozone until they are converted into stable reservoirs that can be transported into the troposphere where they are washed out.

All radicals involved in reactions (2.60) and (2.61) have natural precursors. However, human activities have increased the stratospheric halogen content via the release of chlorofluorocarbons (CFC) and other halogenated hydrocarbons like halons. These molecules have almost unlimited lifetimes in the troposphere and are only dissociated by higher energy UV light above the ozone layer, setting free the bromine, fluorine and chlorine radicals. Under normal stratospheric conditions, these radicals are for the most part stably bound in reservoirs. However, this situation changes in the winter polar stratosphere under the cold vortex conditions which leads to the development of the ozone hole (see section 2.1.3 and 2.4.1). But also at midlatitudes, an ozone decrease of about 3-6% was observed when comparing averaged concentrations from 2002-2005 to the averaged concentrations of the period 1964-1980 (WMO, 2007).

In addition to the standard cycle in reactions (2.60) to (2.62), several variations and combinations of cycles involving species from two different primary groups are possible. The most important ones for stratospheric background conditions, i.e. non-vortex air masses, are reviewed in the following.

### ***HO<sub>x</sub> cycles***

(Bates and Nicolet, 1950) suggested OH and H as possible catalysts for ozone destruction. The hydroxyl radical OH has the same production mechanisms in the stratosphere as in the troposphere. In the mesosphere, photolysis of water vapour yields OH.

Overall, there are four major cycles involving odd hydrogen HO<sub>x</sub> (= OH + HO<sub>2</sub>):

#### cycle 1



#### cycle 2





### cycle 3



### cycle 4



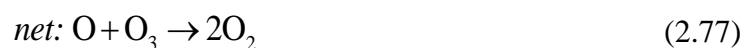
Cycle 1 and 2 primarily influence the ozone budget above 40 km and cycle 3 below 40 km. The fourth cycle does not require atomic oxygen and thus is the main HO<sub>x</sub> mechanism below 30 km. Furthermore, this is the fastest of the four cycles. The HO<sub>x</sub> cycles dominate ozone destruction in the lower stratosphere. Reservoirs of HO<sub>x</sub> are hydrogen peroxide H<sub>2</sub>O<sub>2</sub> and nitric acid HNO<sub>3</sub>.

### **NO<sub>x</sub> cycles**

Nitric oxide NO is formed from nitrous oxide N<sub>2</sub>O which is in turn produced by bacteria in the soil. N<sub>2</sub>O has a long life time and hence can reach the stratosphere where it reacts with atomic oxygen to form two NO molecules. Furthermore, fertilisers release N<sub>2</sub>O, and high-altitude supersonic aircrafts emit NO directly into the stratosphere. There are two important cycles involving NO (Crutzen, 1970; Johnston, 1971):

### cycle 5





### cycle 6



The fifth cycle is responsible for about 70% of the ozone loss in the middle stratosphere, i.e. between 20 and 40 km.

Via the formation of the relatively stable reservoirs  $\text{HNO}_3$  and chlorine nitrate  $\text{ClONO}_2$ , nitrogen dioxide  $\text{NO}_2$  also limits the catalytic cycles of the  $\text{HO}_x$  and the  $\text{ClO}_x$  families. Another important reservoir for  $\text{NO}_x$  is nitric pentoxide  $\text{N}_2\text{O}_5$ .

### ***ClO<sub>x</sub> cycles***

The most important natural source for stratospheric chlorine with an overall lifetime of 1.3 years is methyl chloride  $\text{CH}_3\text{Cl}$  emitted from the oceans (see also section 2.3.3) but it is also produced in biomass burning. The chlorine radical is generated through photolysis of methyl chloride or through its reaction with OH. Chlorine species are also emitted through out-gassing from volcanoes (see section 2.3.4). In addition, the anthropogenically released halogenated halocarbons, i.e. CFCs contribute to the stratospheric chlorine loading (Molina and Rowland, 1974; Crutzen, 1974). CFCs were initially synthesised in 1928 (Midgley and Henne, 1930). Substantial production of these non-toxic and non-flammable gases started in the late 1950s. The CFCs, also known under their trade name Freon, were used as propellants, as foaming agents, in refrigerators, as solvents and in air-conditioning systems. The CFCs with the largest potential to destroy ozone are CFC-11 ( $\text{CCl}_3\text{F}$ ), CFC-12 ( $\text{CF}_2\text{Cl}_2$ ), and CFC-113 ( $\text{CF}_2\text{ClCFCl}_2$ ). These species have been limited or phased out under the Montreal Protocol (signed in 1987) and its amendments. Although the atmospheric load of many of these CFCs is decreasing or levelling off (e.g. Elkins et al., 1993), a full recovery of the stratospheric chlorine content is delayed, as some of the CFCs have very long lifetime of up to 100 years. Only photolysis of the CFCs in the strato-

sphere breaks them down and releases fluorine and chlorine atoms. The fluorine radical does not participate in ozone depletion since it is immediately and permanently converted to hydrofluoric acid HF.

About 70% of  $Cl_y$ , i.e. the sum of all inorganic chlorine species, is bound up as hydrogen chloride HCl. Other reservoirs are the above mentioned  $ClONO_2$  and hypochlorous acid HOCl.

Following Molina and Rowland (1974) and Stolarski and Cicerone (1974), the catalytic cycles of the  $ClO_x$  family are:

cycle 7



cycle 8



cycle 9



cycle 10





Cycle 7 is mainly active in heights above 45 km. The cycles 8 to 10 establish important coupling mechanisms of families. Also, the BrO-ClO-cycle has to be mentioned here but will be presented in the following paragraph.

### **BrO<sub>x</sub> cycles**

The oceans are believed to be the main natural source of methyl bromide CH<sub>3</sub>Br also termed bromomethane (see section 2.3.3). Mainly in agriculture, soils are treated with CH<sub>3</sub>Br as a fumigator and it is also applied as rodent and termite control in food storage depots. In addition, food for the international trade is disinfected with methyl bromide before being shipped. A small fraction of methyl bromide is also emitted in motor car exhausts using leaded fuel (Harsch and Rasmussen, 1977). In a meeting of the parties of the Montreal Protocol in 2001, the phase-out of the production of methyl bromide was decided as well.

Halons are chemicals which have been used as fire extinguishing agents since World War II. As they are gaseous, they were preferred in situations where water or foam may have caused additional hazards or damage e.g. in museums. They consist of a combination of bromine, fluorine, as well as carbon and sometimes chlorine. Halons can only be photo-dissociated in the stratosphere. The potential of bromine for ozone depletion is much higher than that of chlorine as its reservoirs hydrogen bromide HBr and bromine nitrate BrONO<sub>2</sub> are less stable than their chlorine counterparts. However, bromine is not as abundant as chlorine in the atmosphere. Halons were also banned under an amendment of the Montreal Protocol.

The cycles involving bromine species are (Wofsy et al., 1975):

#### cycle 11



and the above-mentioned synergistic cycle with the chlorine family which is mainly active below 20 km (Yung et al., 1980) :

### cycle 12



### ***IO<sub>x</sub> cycles***

Solomon et al. (1994) proposed iodine-related ozone loss mechanisms for the stratosphere. Sources are believed to be methyl iodine of natural origin (see section 2.3.3). Observations of IO in the stratosphere are sparse and controversial (Wittrock et al., 2000; Bösch et al., 2003; Pundt et al., 1998; Wennberg et al., 1997) indicating that iodine does not contribute considerably to stratospheric ozone depletion.

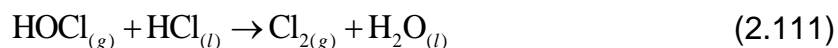
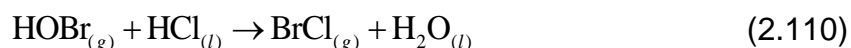
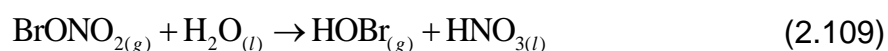
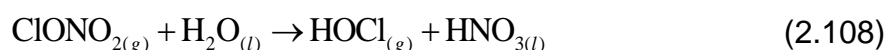
### ***Summary***

In general, high up in the stratosphere, the odd oxygen is mainly partitioned in atomic oxygen hence cycles with a net reaction converting two oxygen atoms into molecular oxygen ( $2\text{O} \rightarrow \text{O}_2$ ) are dominating the ozone loss there. Because of a decreased availability of UV radiation, ozone exceeds atomic oxygen in the lower stratosphere resulting in a preferred net reaction of  $2\text{O}_3 \rightarrow 3\text{O}_2$ . The middle stratosphere is governed by a combination of these:  $\text{O} + \text{O}_3 \rightarrow 2\text{O}_2$  (Lary, 1997). Also several null and holding cycles take place in the stratosphere.

### 2.4.1 The ozone hole

The picture described in the previous section changes in the cold polar stratosphere: In the presence of PSCs, heterogeneous reactions take place. These reactions are faster than gas-phase reactions since energy barriers are reduced. These mechanisms mainly release chlorine from its reservoirs, but also traps  $\text{NO}_x$  in the PSCs as nitric acid  $\text{HNO}_3$  hindering the restoration of reservoir species. This process is referred to as denoxification and sedimentation of particles leads to permanent denitri-fication in a given layer. But it also could possibly cause a re-supply with  $\text{NO}_x$  in a lower, warmer layer.

The two-phase reactions include:



where the subscripts  $g$  and  $l$  denote the gaseous or liquid/solid state of the molecule, respectively. Bromine species are less abundant than chlorine compounds. Consequently, in the polar stratosphere, chlorine plays the foremost role in ozone destruction. After sunrise the preconditioned halogen species are photolysed and start the ozone depletion that causes the dramatic decrease of ozone over the springtime pole. This effect is known as ozone hole and was discovered initially in the 1980s over Antarctica (e.g. Chubachi, 1984; Farman et al., 1985). The Antarctic ozone hole develops every austral spring. However, the formation of the Arctic vortex is highly variable in time and shape which is a consequence of the large temperature differences between northern and southern hemisphere (see section 2.1.3 and Figure 2-3).

In the polar vortex, there are mainly two catalytic cycles involved in the large ozone depletion. In addition to the above-mentioned BrO-ClO-cycle (cycle 12, reactions (2.103) to (2.106)), this is the ClO-dimer cycle:

cycle 13



In a side channel of the BrO+ClO reaction (2.105) and to some extent as well in the ClO+ClO reaction, chlorine dioxide OClO is produced. This is a molecule which can be observed by the technique of the differential optical absorption spectroscopy and measurements of this species are presented in chapter 6. Concentrations of OClO are an indicator for the degree of chlorine activation in the polar vortex.

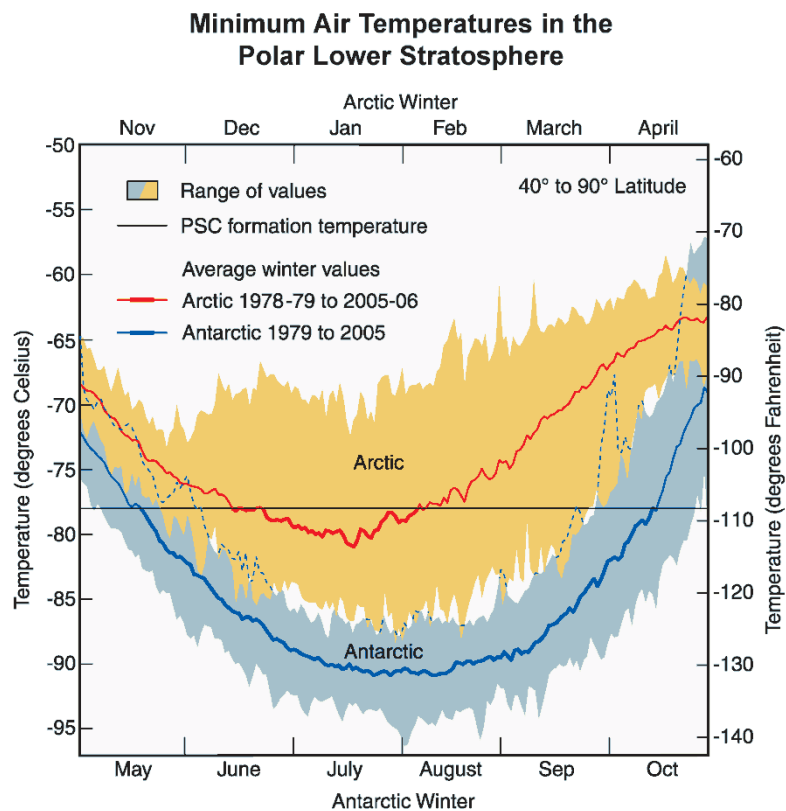


**Figure 2-3 Arctic and Antarctic temperatures for the lower stratosphere (figure from WMO, 2007). On average, the minimum temperatures in wintertime are about 10 K warmer in the northern hemisphere in comparison to the southern hemisphere.**

After the break-up of the polar vortex, the stratosphere warms up. The nitric acid  $\text{HNO}_3$  evaporates from the PSCs and is converted into  $\text{NO}_x$  by photolysis. Subsequently,  $\text{ClO}$  can react with nitrogen dioxide to form the stable reservoir species chlorine nitrate  $\text{ClONO}_2$  causing an abrupt deactivation of chlorine. In the absence of ozone and under denitrified conditions, the formation of the reservoir species hydrogen chloride  $\text{HCl}$  is favoured. However, the conversion of active chlorine to chlorine nitrate is about four times faster than the conversion to  $\text{HCl}$  (Prather and Jaffe, 1990; Douglass et al., 1995; Drdla and Schoeberl, 2002).

### 3 The MAX-DOAS technique

A first spectroscopic remote sensing technique for studying the composition of the atmosphere was developed in the 1920s by Gordon Dobson in order to study stratospheric ozone (Dobson and Harrison, 1926). Noxon (1975) was the first to measure spectra of scattered sun-light over a larger wavelength region. These measurements were analysed with the differential optical absorption spectroscopy (DOAS) technique although this name was given to this method only later by Platt et al. (1979). Due to the numerous processes a photon can undergo on its travel from the sun to the telescope (see section 2.2.2), the absolute light intensity of the recorded spectrum cannot easily be simulated. This lack of information is overcome by investigating only the narrowband absorption features of some trace species. This is expressed by the term *differential* in DOAS. In general, this technique can be applied to a variety of target species, light sources and platforms as well as observation geometries: Occultation measurements of the sun (e.g. Brewer et al., 1973), moon (e.g. Schlieter, 2001; Wagner et al., 2000) and stars (e.g. Roscoe et al., 1994). But also artificial light sources can be used in the field in the so-called long-path DOAS technique (e.g. Perner and Platt, 1979) or for cavity-enhanced measurements where the light path is folded several times with the help of a set of highly reflective mirrors. This technique can as well be applied in laboratory studies (see review by Ball and Jones, 2003). Scattered sun-light can be observed from the ground (e.g. Solomon et al., 1987b), from aircrafts (e.g. Pfeilsticker and Platt, 1994; Wang et al., 2005), and from satellite platforms (e.g. Burrows and Chance, 1992). With balloon-borne instruments, usually occultation measurements are performed (e.g. Pommereau and Piquard, 1994). Target species include OH, HO<sub>2</sub>, HONO, HCHO, CHOCHO, O<sub>3</sub>, NO<sub>2</sub>, NO<sub>3</sub>, ClO, OCIO, IO, OIO, I<sub>2</sub>, and BrO.

In the study presented here, the scattered sunlight is recorded under a multi-axis (MAX) observation geometry. Only the absorption along the light path can be determined with DOAS. Simplifying the analysis with the help of a two-step approach by separating the quantification of the absorption from the radiative transfer is possible for an optically thin atmosphere. The next chapter 4 explains the simulation of the light-path with radiative transfer calculations. Here, the principles of the DOAS method are described. In the first part, the advantages of the multi-axis viewing ge-

ometry of the telescope are compared to the traditional exclusive zenith-sky technique (3.1). After this, a mathematical description of the DOAS method is given (3.2). In section 3.3, the general instrumental set-up that was used for this study will be described. The retrieval algorithm and associated error sources are presented in section 3.4.

### 3.1 The viewing geometry

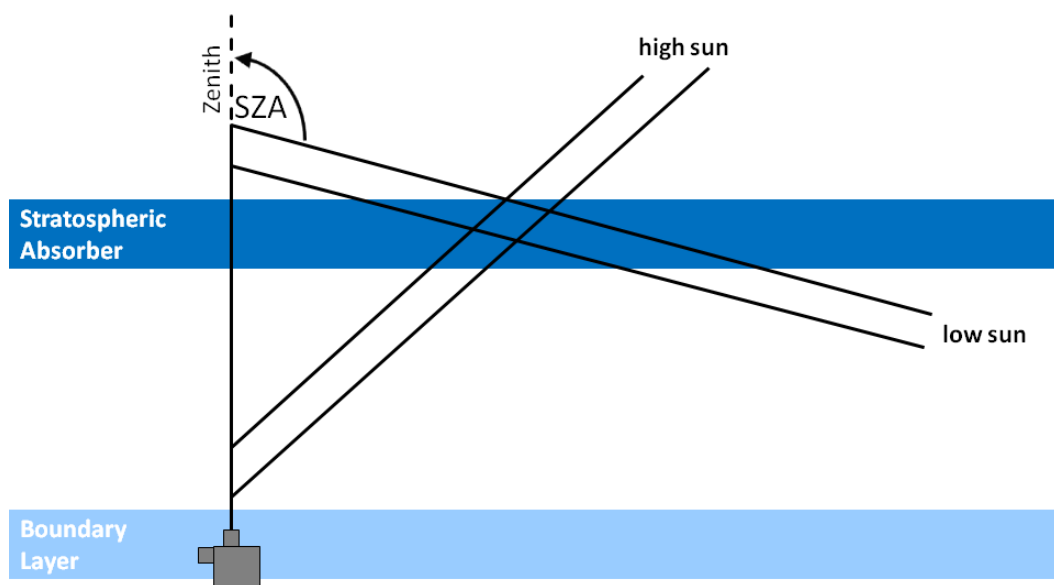


**Figure 3-1** Illustration for the zenith-sky viewing geometry. The path of only one photon is shown which is also scattered only once. With the sun sinking, the light path in the stratosphere is enhanced in comparison to observations at high sun. This makes the zenith measurements particularly sensitive towards stratospheric absorbers at twilight whereas the tropospheric light path does not change during the course of a day.

Figure 3-1 and Figure 3-2 illustrate the light path of the photons from the sun to the telescope. Here, only the path of a single photon is shown. However, in reality the signal recorded at the instrument is produced by an ensemble of photons none having taken exactly the same path from the sun to the telescope. Three angles are needed to describe the viewing geometry, namely the solar zenith angle (SZA), the elevation angle of the telescope relative to the horizon as well as the relative solar azimuth angle (SAA) which is the angle between the viewing direction of the tele-

scope and the position of the sun, both projected to the plane of the surface level (compare Figure 4-1).

For zenith measurements (see Figure 3-1), the viewing geometry can often be approximated by considering only single scattering: Photons are scattered only once above the instrument into the line of sight. Before that, they have passed a large distance through the stratosphere. The height of the scattering process depends on the scattering probability which is proportional to the product of the light intensity times the density of scatterers. The density of the scatterers, which is in a first approximation simply the air density, decreases exponentially with height. Consequently, the light intensity decreases when getting closer to the ground due to attenuation by scattering in lower layers of the atmosphere. This yields a most probable height for scattering which changes with the SZA: When the sun is setting, the light intensity decreases close to the ground even further and the most likely scattering height is shifted upwards. Independent of the solar zenith angle, the light path through the troposphere stays almost unchanged. As a result, the zenith measurements are especially sensitive to absorbers in the stratosphere.

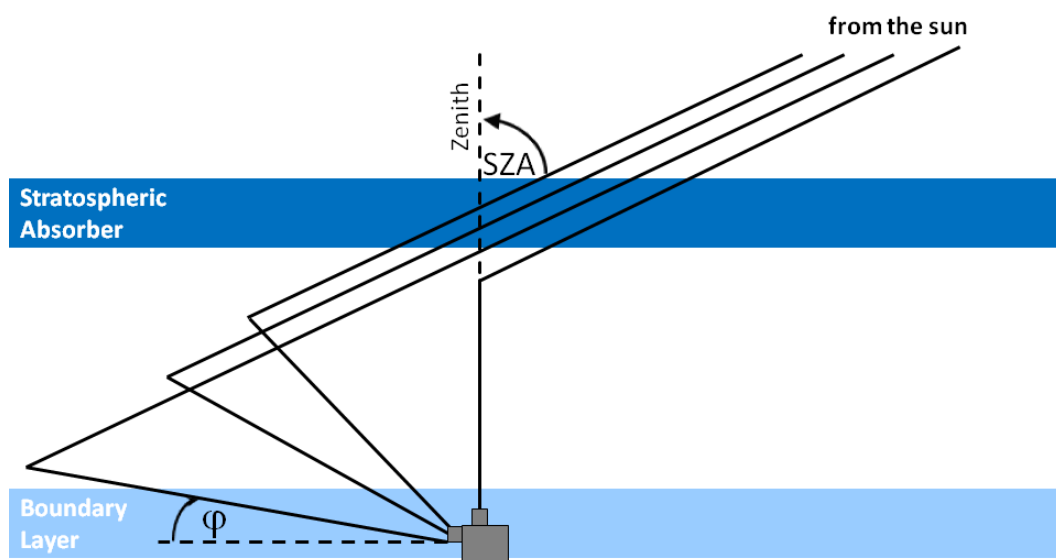


Figure 3-2 Illustration for the multi-axis viewing geometry. With decreasing elevation angle  $\phi$ , the light path through the boundary layer is enhanced whereas the stratospheric light path stays unchanged. Compare also Figure 3-1.

In order to obtain a better sensitivity to absorbers in lower layers of the atmosphere, the light path in the troposphere has to be enhanced. This can be achieved by pointing the telescope under an angle closer towards the horizon. By combining several measurements of different elevation angles together with a zenith measurement, some profile information of a trace gas can be retrieved (see section 4.3). The stratospheric light path is approximately the same for all elevation angles. Figure 3-2 demonstrates this viewing geometry for the single scattering scenario. However, the sensitivity of an off-axis measurement strongly depends on the visibility and hence on the aerosol load of the atmosphere. Consequently, the accurate interpretation of the light path for these measurements requires the consideration of multiple scattering of photons making it necessary to employ a radiative transfer model to fully understand the possible photon paths (see chapter 4).

## 3.2 DOAS theory

For applying the Beer-Lambert-Bouguer-Law to the atmosphere, it has to be considered that the density of an absorber or scatterer is different in different heights as well as that the cross sections depend on the temperature. Thus, equation (2.3) has to be rewritten in integral form with the integration performed along the photon path  $s$  through the atmosphere:

$$I(\lambda) = \alpha I_0(\lambda) \exp \left[ - \int ds \left\{ \begin{array}{l} \sum_i \rho_{abs,i}(s) \sigma_{abs,i}(\lambda, s) \\ + \rho_{Ray}(s) \sigma_{Ray}(\lambda, s) \\ + \rho_{Mie}(s) \sigma_{Mie}(\lambda, s) \\ + \rho_{Ring}(s) \sigma_{Ring}(\lambda, s) \\ + \rho_{aero-abs}(s) \sigma_{aero-abs}(\lambda, s) \end{array} \right\} \right] \quad (3.1)$$

with  $\rho_{abs,i}$ ;  $\rho_{Ray}$ ;  $\rho_{Mie}$ ;  $\rho_{Ring}$ ;  $\rho_{aero-abs}$  as the number densities to the corresponding cross sections  $\sigma_{abs,i}$ ;  $\sigma_{Ray}$ ;  $\sigma_{Mie}$ ;  $\sigma_{Ring}$ ;  $\sigma_{aero-abs}$  of the absorbers and scatterers (see section 2.2.2). The factor  $\alpha$  determines the intensity of the scattered light and depends on the density of scatterers and their phase function. It is a smooth function of wavelength.

Several approximations have to be made since equation (3.1) cannot be solved in this form due to too many unknown variables:

- The height dependence of the absorption cross section  $\sigma_{abs,i}$  can be neglected when cross sections are used that are valid for the temperature in the specific layer height of the given absorber (e.g. 220 K for a stratospheric absorber and 270 K for a the tropospheric absorber). This approximation allows exchanging the integral and the summation and the so-called slant column density  $SC$  can be defined as the absorption along the light path:

$$SC \equiv \int \rho_{abs}(s) ds \quad (3.2)$$

- At this point, the DOAS method is introduced: The absorption cross sections are separated into two components:

$$\sigma_{abs,i} = \sigma_i' + \sigma_i^0 \quad (3.3)$$

whereas  $\sigma_i^0$  represents the broadband spectral structures and  $\sigma_i'$  the differential structures of the absorption cross section.

- All broadband structures such as the aerosol absorption, Rayleigh and Mie scattering features (see section 2.2.2 for the relatively weak wavelength dependence of their cross sections) as well as the factor  $\alpha$  and the absorption due to the cross section  $\sigma_i^0$  are approximated by a polynomial:

$$P = \sum_p a_p \lambda^p \quad (3.4)$$

- For reasons of abbreviation, the Ring effect with the scattering cross section  $\sigma_{Ring}$  will be mathematically treated like an additional absorber.

Applying those four steps and afterwards, taking the natural logarithm of equation (3.1) yields an equation that can be readily applied to the measurement:

$$\ln \left[ \frac{I(\lambda)}{I_0(\lambda)} \right] = - \sum_i \sigma_i'(\lambda) SC_i - \sum_p a_p \lambda^p \quad (3.5)$$

once a reference spectrum  $I_0$  is specified.

An ideal reference spectrum would be an extraterrestrial solar spectrum recorded with the same instrument as used for the measurements. Since this is obviously not possible for ground-based instruments and a solar spectrum measured with a satellite instrument would only introduce uncertainties due to the unknown instrumental specifics, a reference is chosen that includes as little absorption as possible from the Earth's atmosphere. This can be achieved with a noon zenith spectrum  $I_0^{NZ}(\lambda)$ . Usually, the daily noontime spectrum is used because this compensates not only general instrumental characteristics, but also long-term temporal changes of these. The disadvantage of this is of course the lack of information about the atmospheric absorption already present in this spectrum. Consequently, only the differential slant column density (dSCD), i.e. the difference between the actual slant column density  $SC$  and the noontime zenith slant column density  $SC^{NZ}$  can be determined yielding the DOAS equation in the final form:

$$\ln \left[ \frac{I(\lambda)}{I_0^{NZ}(\lambda)} \right] = - \sum_i \sigma_i'(\lambda) (SC_i - SC_i^{NZ}) - \sum_p a_p \lambda^p \quad (3.6)$$

### 3.3 Instrumentation

In this section, the general instrumental set-up is described (see Figure 3-3): The scattered light collected by the telescope (section 3.3.1) is transmitted via a quartz fibre bundle to a grating spectrograph that is equipped with a cooled CCD (charge-coupled device) detector. A software package running on a standard computer collects the data and also configures the automatic measurements including calibrations (section 3.3.2). The bundle of quartz fibres not only efficiently depolarises the light, which is important because Rayleigh scattering is polarised and the light through-put of a spectrometer depends on the polarisation, but also facilitates a flexible installation of the spectrograph away from the telescope. Also, it provides the possibility to use one telescope for two spectrographs by simply splitting the fibres coming from the telescope and distributing them to the two spectrometers. This allows covering a larger wavelength interval. At the spectrograph aperture, the fibres are arranged in a vertical line forming the entrance slit with a width of 150  $\mu\text{m}$ . The spectrometers are temperature-stabilised to avoid any drifts in the wavelength axis with ambient air

temperature. In general, the spectral resolution represented by the full width half maximum (FWHM) of a typical mercury line measured with the given instrumental set-up, is between 0.4 and 0.9 nm. The resolution can be chosen by the grating and this on the other hand is selected according to the wavelength region where the target species of interest absorb, usually 1200 grooves/mm in the UV and 600 grooves/mm in the visible wavelength range. Further specifications of the different instrumental set-ups, like wavelength regions or viewing geometry, are described in the according sections 5.1 to 5.5 as well as 6.1.2. The instruments are NDSC (Network for Detection of Stratospheric Change) or NDACC (Network for the Detection of Atmospheric Composition and Change) approved (Aliwell et al., 2002; Vandaele et al., 2005).

### 3.3.1 Telescope including calibration unit

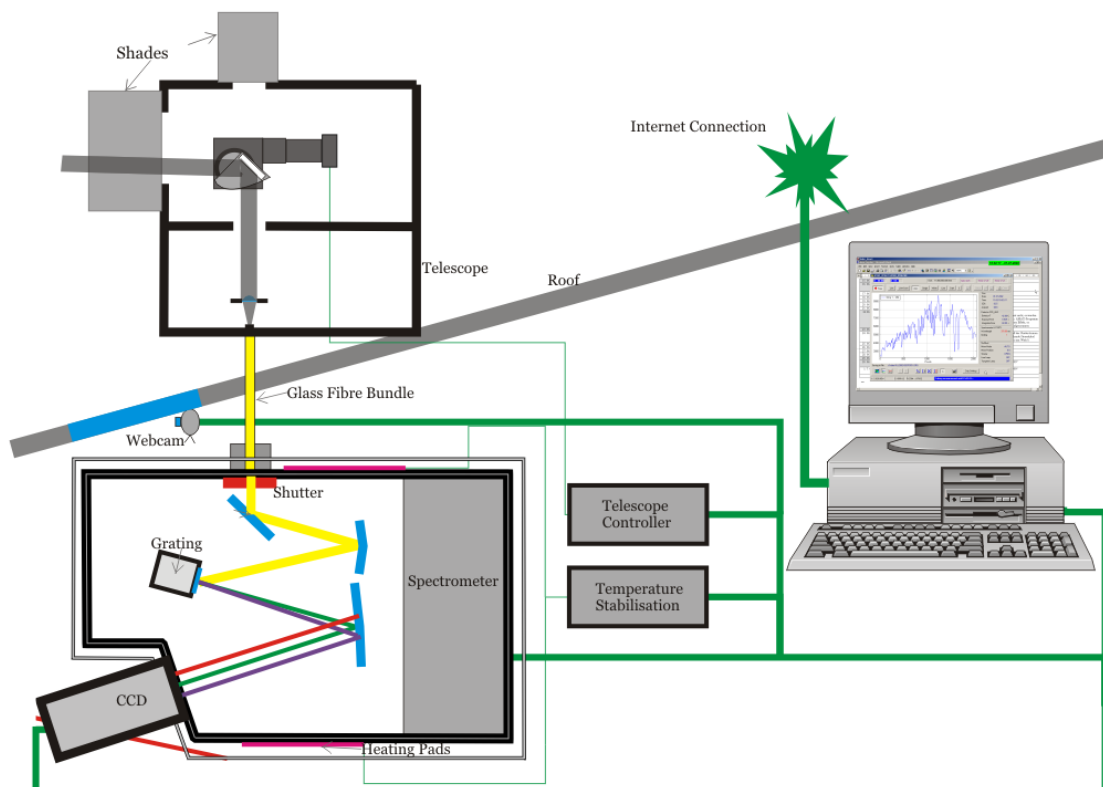


**Figure 3-3** Illustration of the overall instrumental set-up: The light is collected by the telescope (see also Figure 3-4) and transferred into the spectrometer by a glass fibre bundle. A CCD detector records the spectra and a PC is used as the data acquisition device.

The telescope unit is illustrated in Figure 3-4. The housing is made from a commercial stainless steel box of 40 x 40 x 18 cm<sup>3</sup> with a door over the entire front. Two openings are inserted, the zenith window in the top and an elongated window on the left hand side for the off-axis observations.

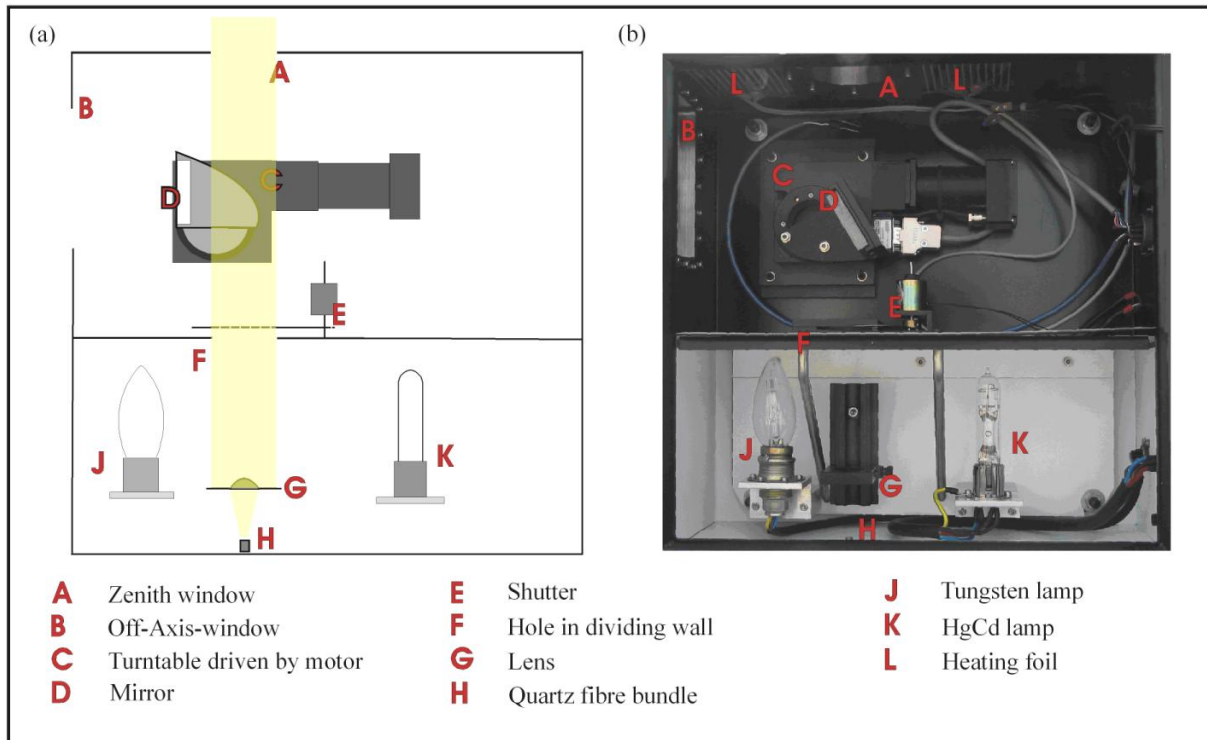


**Figure 3-4** Illustration and photo of the multi-axis telescope including the calibration unit (J and k) in the lower part of the box. a) The mirror (D) blocks the light from the off-axis window (B) and the light from the zenith is permitted to enter the glass fibre (H). b) Here, the mirror is positioned to block the zenith window and to reflect light from 2° elevation towards the glass fibre.

The off-axis viewing directions can be set with the help of a mirror that is mounted onto a rotating table connected to a stepper motor. The right hand panel of Figure 3-4 shows the mirror in an off-axis position of 2°. The size of the window limits the possible angles to be between -5° and 30° elevation. For zenith measurements, the mirror is turned into an upright position to the left in order to block the light from the off-axis port (see left panel of Figure 3-4). The lens in front of the glass fibre bundle reduces the field of view to a cone with an opening angle of about 1°. Not shown in Figure 3-4 are the shades around the sides of the windows to prevent direct light from entering the telescope.

The lower part of the telescope holds the calibration unit containing a white-light lamp and a spectral mercury-cadmium (HgCd) lamp. These are used for possible etalon corrections and for the wavelength mapping, respectively. The calibration unit can be separated from the multi-axis unit by a shutter to shut out stray light.

The system is heated by several heating pads to ensure the operating temperature of the stepper motor and to keep the windows ice-free in cold environments.

### **3.3.2 Automatic measurement mode**

A software package has been developed (Richter, 1997) that coordinates measurements and saves the recorded spectra. In this way, the systems can operate in a stand-alone mode for long-term measurements at remote sites. Access to the computer, the measurement programme as well as the data is possible via an internet connection.

The measurements automatically begin for solar zenith angles smaller than  $96^\circ$ . The exposure time, that is optimal for the CCD camera, is determined via a short test measurement prior to the actual measurement. Spectra are then averaged over at least one minute, but depending on the location. There are two options for using the off-axis mode: The older set-ups have only five directions including the zenith (only two for Kaashidhoo, see section 5.3). Newer measurements are performed with scanning the horizon in  $1^\circ$ - or  $2^\circ$ -steps, followed by a measurement at  $30^\circ$  elevation angle and the zenith. One telescope can be used for two spectrograph-computer-systems. The two computers then communicate in a master-and-slave mode with each other to ensure the synchronisation of the measurements with the telescope settings.

During night, calibration measurements are recorded: lamp spectra with the white-light lamp and the HgCd lamp. Furthermore, the dark signal of the CCD detector is determined for the exposure times according to the daytime scattered light measurements.

### 3.4 Retrieval of the slant column density and error sources

Before the actual DOAS retrieval, first, the dark counts have to be subtracted from the measured spectra. Also, a wavelength calibration has to be performed: The CCD pixel position of the measured HgCd lines is mapped onto the wavelength position of the HgCd lines from the literature in a linear fit. The retrieved wavelength axis is added to every spectrum recorded during that one day. A similar procedure is repeated for every individual spectrum during the DOAS fit for the Fraunhofer lines (see 2.2.1) to account for small wavelength drifts during the course of the day. Also an instrumental line shape is retrieved from the recorded HgCd spectrum. This is then subsequently used to convolve the high-resolution absorption cross sections to mimic the resolution of the instrument.

A suitable polynomial has to be subtracted from the measured optical density i.e. the left hand side of equation (3.6). This is selected according to the size of the wavelength window and also according to the target species. Then the differential cross sections of all relevant absorbers, in a chosen wavelength interval, are fitted to the measured optical density in a least-squares fit, i.e. the residual is minimised. These residual structures can for example originate from unknown absorbers or from detector noise. This spectral fitting procedure is achieved by the programme NLin (Richter, 1997).

The smallest detectable concentration of an absorber can be retrieved from the residual: Only absorber structures exceeding the magnitude of the residual in the wavelength interval can be interpreted as positive detection. Mathematically, this can be estimated by comparing the so-called root-mean-square RMS of the absorption cross section to the RMS of the residual in the given wavelength region.

The RMS is a statistical measure for the quality of the fit assessing the variability of the residual within the wavelength interval made up of a discrete number of elements  $n$ . It is given by:

$$\text{RMS} = \sqrt{\frac{1}{n} \sum_n (\text{residual})^2} \quad (3.7)$$

This definition assumes that the individual data points of the residual are independent from each other. However, this is not the case and the division should be performed

with the divisor  $n$  reduced to the number of the actual degrees of freedom. Consequently, the RMS calculated by equation (3.7) gives the lower limit of the actual RMS. For calculating the limit of detection for an absorber, this effect cancels out as long as the calculations are performed on a common wavelength grid for absorber cross section and residual, i.e. the number  $n$  is the same for both spectra.

The random error of the measured intensities is mainly made up of the signal shot noise and is inversely proportional to the signal strength of the measurement. Temporal averaging reduces this error by the square-root of the number of measurements. This error dominates under bright conditions. When observing low intensities, the dark signal shot noise, the detector noise as well as the read-out noise becomes more important. But also systematic errors can occur like off-set problems. The conversion of the intensity error to the error associated with a slant column density is not trivial. Here, the ratio of the residual to the strength of the differential absorption is given as an approximation to the random error. However, this error only represents the lower limit of the actual error of the slant column densities. The main uncertainty in the DOAS method is caused by systematic errors. These include the uncertainties in the absolute reference absorption cross sections, uncertainties in the wavelength calibration, errors due to correlations of cross sections from different absorbers, uncertainties in the calculation of the Ring effect and unknown absorbers not accounted for in the retrieval. Multiplicative errors from the instrument are cancelled out through the division of the reference spectrum recorded with the same instrument.



## 4 Interpretation of MAX-DOAS measurements

The DOAS technique, described in chapter 3, only yields the column density of an absorber integrated along the light path in the atmosphere. The more useful quantities, however, are the total column density or profile. Consequently, in a next step, the quantified slant column density, which depends among many other parameters on the viewing geometry of the telescope and the position of the sun, has to be distributed over a certain height in the atmosphere. For this, the air mass factor (AMF) concept is introduced (Noxon, 1975; Solomon et al., 1987b; Perliski and Solomon, 1993): The AMF is the ratio between the slant column density and the total or vertical column density  $VC$  and represents the enhancement of the light path relative to the vertical:

$$AMF = \frac{SC}{VC} \quad (4.1)$$

In a single-scattering atmosphere tracing one photon only, the AMF can be obtained in a first approximation by a geometrical approach. For a tropospheric absorber, assuming that the scattering takes place above the trace gas layer, the air mass factor is  $AMF = 1/\sin\varphi$  and for an absorber positioned above the scattering height  $AMF = 1/\cos\theta$  with  $\varphi$  being the elevation angle of the telescope and  $\theta$  the SZA (see Figure 4-1).

However for the real atmosphere, several parameters e.g. the wavelength and optical properties have to be considered while determining the appropriate AMF for a given viewing geometry. This can be achieved by a radiative transfer model that calculates the intensity at a given point in the atmosphere by solving the radiative transfer equation (equation (2.6)). In this study, the validated model SCIATRAN developed in Bremen is applied. Section 4.1 gives an introduction to the basic theory and how air mass factors are calculated from the simulated intensities.

The AMF is not only a conversion factor but can also be used to investigate the sensitivity of the multi-axis observation geometry under different atmospheric conditions. Here, sensitivity tests have been performed (see section 4.2). This study was part of a larger intercomparison exercise of different radiative transfer codes and the results are published in Wagner et al. (2007). The aims of this exercise included:

- The comparison of current RTMs from different research groups and quantification of these differences.
- The identification of shortcomings and the assessment of the uncertainties of the model results
- The investigation of the sensitivity of MAX-DOAS observations for different viewing geometries with particular focus on the influence of aerosols.

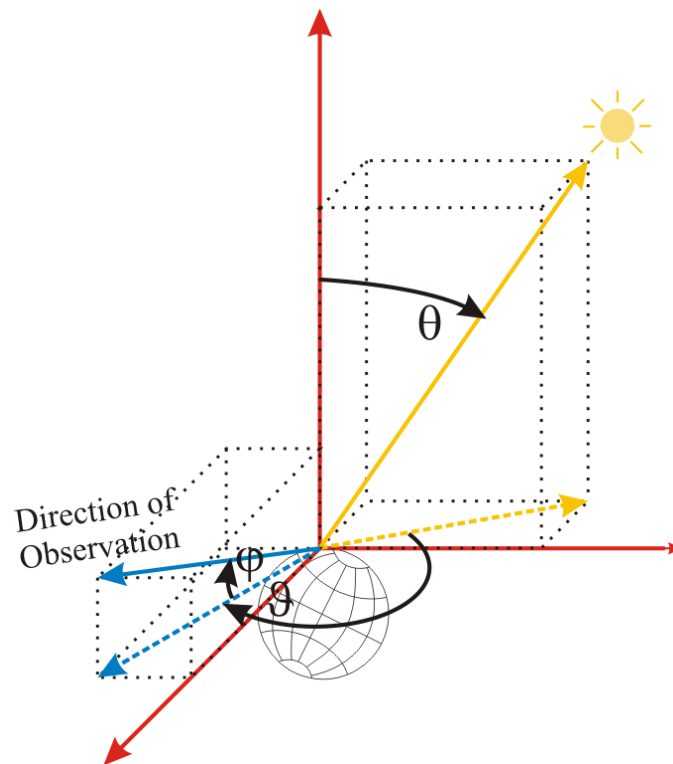


**Figure 4-1 Illustration of the multi-axis observation geometry:  $\theta$  is the solar zenith angle,  $\varphi$  the elevation angle of the telescope and  $\vartheta$  the relative azimuth angle between the telescope and the sun.**

Section 4.3 presents different techniques for the conversion from the slant column density to more physical quantities, like the total column density, a tropospheric column density, or a profile of the absorber. The technique for the retrieval of profiles has been validated with independent data sets at the DANDELIONS campaign.

## 4.1 The radiative transfer model SCIATRAN and calculation of air mass factors

In the atmosphere, various parameters are of importance when assessing the actual path of a photon: The position of the sun as well as the presence of clouds, the vertical profiles of aerosols and absorbers as well as temperature and pressure profiles, the surface albedo, but also the refraction of light depending on the density of the air. All these effects can be simulated with a radiative transfer model (RTM).

For all application described in this study, version 2.2 of the SCIATRAN software family was used (<http://www.iup.uni-bremen.de/sciatran>, Rozanov, 2001; Rozanov et al., 2001; Rozanov et al., 2005; Rozanov and Rozanov, 2007b). The radiative transfer equation in its differential form (equation (2.6)) is transformed into an integral form applying the characteristics method where an integration is performed along the line of sight. The single-scattering source function (equation (2.8)) is calculated in a truly spherical atmosphere whereas the multiple-scattering source function (equation (2.9)) is initialised with the pseudo-spherical radiative field. This is calculated by employing the discrete ordinates method to the integro-differential (ID) RTE. For solving both the ID-RTE for the multiple-scattering diffuse radiation as well as for the overall calculation of the RTE, a Fourier series expansion is performed and each Fourier term of the radiative transfer equation is calculated independently. In summary, the single-scattering radiation field, the direct solar beam as well as the integration along the line of sight are calculated in a fully spherical atmosphere whereas for the multiple-scattering radiation, a pseudo-spherical approximation is applied.

The air mass factor is obtained by performing two model runs calculating the intensity field with the respective absorber  $I_{+i}$  and without  $I_{-i}$ :

$$\text{AMF}_i(\theta, \varphi, \vartheta, \lambda) = \frac{1}{\tau_i} \ln \left( \frac{I_{-i}(\theta, \varphi, \vartheta, \lambda)}{I_{+i}(\theta, \varphi, \vartheta, \lambda)} \right) \quad (4.2)$$

with the angles  $\theta, \varphi, \vartheta$  being the solar zenith angle, the elevation angle, and the relative azimuth angle, respectively, as defined in Figure 4-1. The vertical optical depth  $\tau_i$  with respect to the extinction due to a specific absorber  $i$  is:

$$\tau_i(\lambda) \equiv \int_0^{\text{TOA}} dh \cdot \rho_i(h) \cdot \sigma_i(\lambda, h) \quad (4.3)$$

The integration is performed from the ground to the top of the atmosphere (TOA). Compare also equation (2.10). Equation (4.2) is only valid for an optically thin atmosphere. This means that the effective light path has to be the same for an atmosphere with as well as without the absorber. In addition, it should be noted that for the calculation of the AMF the relative concentration profile must be known. This is especially problematic for absorbers in the planetary boundary layer since not only its height is not exactly known, but it can also change during the course of a day (see section 2.1.2). However, this already assumes that the absorber is well-mixed within the PBL which is not the case for short-lived species.

Block air mass factors are AMFs corresponding to a specific layer  $j$  of thickness  $\Delta z$  in the atmosphere. They characterise the sensitivity of a measurement towards an arbitrary trace gas in a specific altitude layer. This implies that the radiative transfer within this layer is independent from the absorber density in this but also in the neighbouring ones. Then the SCD can be also expressed as:

$$SC(\lambda) = \sum_{j=0}^{\text{TOA}} B\text{AMF}_j(\lambda) \cdot VC_j \quad (4.4)$$

where  $B\text{AMF}_j$  is the block AMF and  $VC_j$  is the individual vertical column density for each layer  $j$ . Block AMFs are independent of the trace gas and can be used to calculate the total AMF of any trace gas with a respective profile combining equation (4.4) and (4.1):

$$\text{AMF} = \sum_{j=0}^{\text{TOA}} B\text{AMF}_j \frac{VC_j}{VC} \quad (4.5)$$

Block AMFs are calculated from the weighting function in SCIATRAN. Weighting functions are normally used to solve inverse problems in atmospheric remote sensing (Rodgers, 2000). These weighting functions give the absolute change in intensity for a relative change of a certain parameter. In SCIATRAN, these functions are calculated by the adjoint method. For this, Rozanov and Rozanov (2007b) formulate a generalised radiative transfer equation (RTE) in the operator form and retrieve the adjoint operator as well as the adjoint RTE. The response function of the radiation field to any changes in the atmospheric parameters can then be calculated with the

linear perturbation technique (Rozanov and Rozanov, 2007a). For an optically thin atmosphere, the intensity weighting functions  $WF^l$  can be directly converted into block AMFs for each individual layer:

$$BAMF_j(\lambda, z) = -\frac{WF_j^l(\lambda, z)}{I^{TOA}(\lambda) \cdot \sigma_j(\lambda) \cdot \rho^{air}(z) \Delta z} \quad (4.6)$$

where  $I^{TOA}$  is the absolute intensity at the top of the atmosphere,  $\sigma_j$  is the absorption cross-section of the absorber of interest, and  $\rho^{air}$  is the number density of air. Within the layer  $j$ , the number density of the absorber is assumed to be constant.

SCIATRAN can also be used to simulate the slant column density of an absorber. For this, the calculated AMF is multiplied by the vertical column density, i.e. the integrated profile of the absorber.

In the following the results for a sensitivity study of the block AMFs for the MAX-DOAS measurement geometries are presented. This study was published in Wagner et al. (2007).

## 4.2 Case studies for block air mass factors: Results for a radiative transfer modelling workshop in 2005

Eight international research groups with nine different models participated in an inter-comparison exercise for radiative transfer codes held in Heidelberg in summer 2005. In the frame of this work, the different scenarios, as described below, have been simulated and are utilised to discuss the information content of the MAX-DOAS measurements.

As basic settings for the radiative transfer calculations, the data for pressure, temperature and the ozone profile were approximated by the U.S. standard atmosphere ([http://modelweb.gsfc.nasa.gov/atmos/us\\_standard.html](http://modelweb.gsfc.nasa.gov/atmos/us_standard.html)). The only absorber included is ozone using an absorption cross section measured at 273 K (Bogumil et al., 2003). The number of boxes for the AMF simulations is 17 and the lower boundaries and the extension of these layers are listed in Table 1. The vertical discretisation, on which the calculations are performed, has to be significantly finer than the step size of the

AMF grid. After several tests, an optimum was found where the spacing between the grid points increase exponentially from the ground to 100 km altitude in overall 248 layers.

**Table 1 Lower boundaries and vertical extensions of the layers for which the block AMF have been calculated.**

atmospheric layer	lower boundary	vertical extension
1	ground	100 m
2	100 m	100 m
3	200 m	100 m
4	300 m	100 m
5	400 m	100 m
6	500 m	100 m
7	600 m	100 m
8	700 m	100 m
9	800 m	100 m
10	900 m	100 m
11	1000 m	100 m
12	1500 m	100 m
13	2000 m	100 m
14	3000 m	100 m
15	5000 m	100 m
16	10000 m	1000 m
17	20000 m	1000 m

Three basic aerosol scenarios are examined: First of all, an atmosphere without aerosols is simulated; i.e. only Rayleigh scattering takes place (see section 2.2.2). The other two scenarios include extinction due to scattering on aerosols. In scenario 2, the extinction coefficient is set to  $0.5 \text{ km}^{-1}$  in the lowermost two kilometres of the atmosphere and in scenario 3, to  $0.1 \text{ km}^{-1}$  within the first kilometre (see Table 2). The wavelength dependence of the Mie scattering is neglected. In the visible wavelength

region, an extinction coefficient of  $0.5 \text{ km}^{-1}$  approximately corresponds to a visibility of 6 km and  $0.1 \text{ km}^{-1}$  to about 30 km. this can be calculated with the Koschmieder's law (Finlayson-Pitts and Pitts, 1986):

$$\text{visibility} = \frac{3.9}{\text{extinction}} \quad (4.7)$$

Besides the seventeen block AMFs, also the vertical optical depth (VOD) considering extinction only with respect to scattering and the radiances at the detector normalised with respect to the solar radiance are compared. Three main exercises have been performed.

**Table 2 Settings for the extinction coefficient in the three different aerosol scenarios.**

aerosol scenario	aerosol extinction [ $\text{km}^{-1}$ ]	altitude range
1	0	-
2	0.5	0 – 2 km
3	0.1	0 – 1 km

### **Exercise 0**

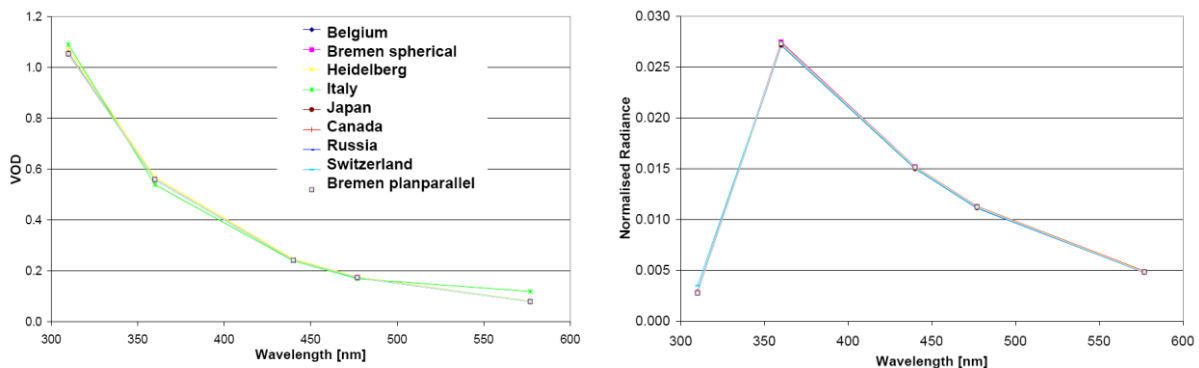
The first set of calculations was used to test the basic model properties and to track down elementary mistakes. As a simple observation geometry, the zenith viewing direction in combination with  $70^\circ$  SZA is chosen. The aerosol load of the atmosphere is set to zero and the albedo to 0.03. The basic settings are summarised in Table 3. The output wavelengths were chosen to be representative for specific absorbers: 310 nm for  $\text{SO}_2$ , 360 nm for BrO, formaldehyde, and the oxygen dimer  $\text{O}_4$ , 440 nm for  $\text{NO}_2$ , IO, and glyoxal, 477 nm and 577 nm again for  $\text{O}_4$ .

Figure 4-2 and Figure 4-3 are taken from the publication by Wagner et al. (2007). The decrease in the VOD (Figure 4-2, left) reflects the  $\lambda^{-4}$  wavelength dependence of Rayleigh scattering (see section 2.2.2). The normalised radiances (Figure 4-2, right) are calculated including the ozone absorption and consequently, display a combined effect for the shape of the curve: The decrease with increasing wavelength due the Rayleigh scattering is superimposed by the strong decrease of radiation due to the ozone absorption in the UV in the stratosphere (see section 2.4).

**Table 3 Settings for exercise 0.**

input parameters	output parameters
<ul style="list-style-type: none"> <li>- Rayleigh atmosphere</li> <li>- wavelengths 310, 360, 440, 477, and 577 nm</li> <li>- albedo 0.03</li> <li>- zenith viewing geometry</li> <li>- SZA: 70°</li> </ul>	<ul style="list-style-type: none"> <li>- radiances</li> <li>- vertical optical depths</li> <li>- all block air mass factors</li> </ul>

In Figure 4-3, the block AMFs are presented for the five different wavelengths. The geometric AMFs for the given viewing geometry are unity for a tropospheric absorber and about 3 for a stratospheric absorber (see introduction to this chapter 4). Close to the surface, the block AMFs follow the geometric approximation showing that the observed photons have travelled on a vertical path through the lowest layer of the atmosphere. Almost entirely, the direct solar beam determines the path of the photons through the highest layer although one exclusion applies: Several block AMFs have higher values which are caused by an enhancement with respect to the geometric light path due to multiple scattering. Also, at 310 nm, the limit of the geometric AMF is not reached at all indicating that a substantial fraction of the photons are already scattered above the last layer, i.e. above 20 km. Between the surface layer and the top one, combinations for the light path occur with some photons being scattered above, others below the layer of interest.



**Figure 4-2 Exercise 0: Modelled vertical optical depth with respect to Rayleigh-scattering showing the  $\lambda^{-4}$  wavelength dependence of Rayleigh scattering (left panel) and radiances as a function of wavelength normalised with respect to the solar irradiance and taking into account ozone absorption hence a decrease of the radiance can be observed towards the UV (right).**

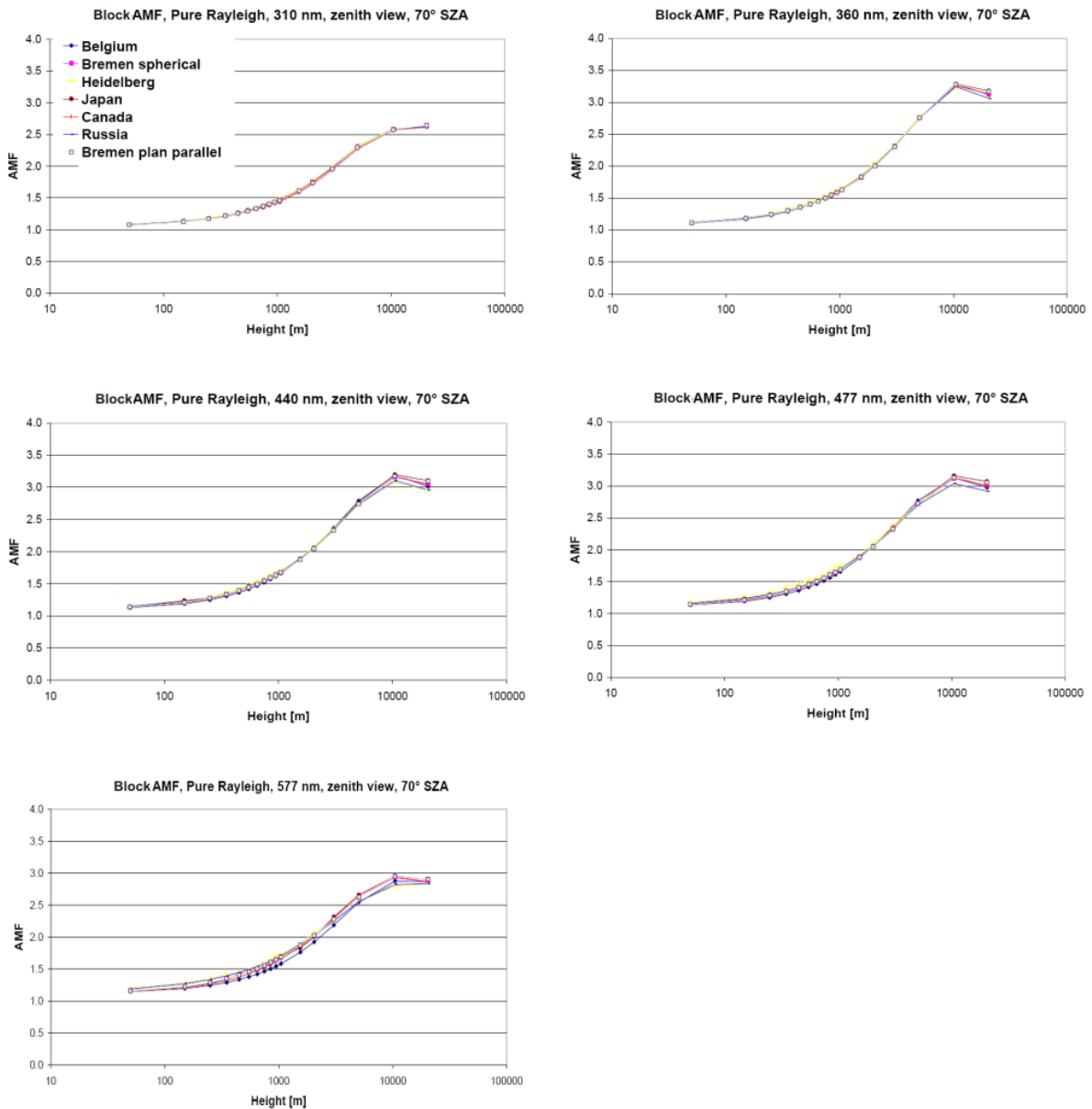


**Figure 4-3 Exercise 0: Block AMFs for zenith viewing geometry at 70° SZA as a function of the height in the atmosphere for five different wavelengths. The geometric approach yields AMFs of 1 and 3 for a tropospheric and a stratospheric absorber, respectively. Higher values can be found due to multiple scattering.**

Here, also the data from the plane-parallel version of SCIATRAN is presented (Bremen plane-parallel). However, for a SZA as large as 70° in combination with the zenith viewing geometry, the differences between a spherical and a plane-parallel model are, as expected, negligibly small. The performance of all models is excellent

and the results also for the following two exercises agreed within 5% for most of the simulated test cases.

Although for an intercomparison the format of the graphs in the form of Figure 4-3 is most descriptive, to interpret the sensitivity of a given viewing geometry, in the following, a slightly different format has been used and data only from SCIATRAN are presented.

### **Exercise 1**

In the second exercise, the focus was on the information that can be retrieved using different elevation angles, here 1°, 2°, 3°, 6°, 10°, 20°, and the zenith. The SZA and the relative azimuth angle were fixed to 20° and 0°, respectively. In addition to the pure Rayleigh atmosphere, also the aerosol scenario 2 is examined. This exercise is performed for two wavelengths only: 360 nm and 577 nm. Table 4 summarises the settings for exercise 1 and Table 5 lists the vertical optical depth for the different aerosol scenarios and the two selected wavelengths. As before, the VOD decreases towards longer wavelengths.

**Table 4 Settings for exercise 1: Variations of the viewing angle.**

input parameters	output parameters
<ul style="list-style-type: none"> <li>- Rayleigh atmosphere and aerosol scenario 2</li> <li>- wavelengths 360 nm and 577 nm</li> <li>- albedo 0.03</li> <li>- elevation angles: 1°, 2°, 3°, 6°, 10°, 20°, and 90°</li> <li>- SZA: 20°</li> <li>- azimuth angle: 0° (looking towards the sun)</li> <li>- asymmetry factor of aerosol phase function: 0.68</li> </ul>	<ul style="list-style-type: none"> <li>- radiances</li> <li>- vertical optical depths</li> <li>- all block air mass factors</li> </ul>

For a Rayleigh atmosphere, the length of the geometrical path determines the number of photons scattered into the telescope hence the intensity decreases towards larger elevation angles. For a large optical depth due to scattering on aerosols, the intensity increases towards larger elevation angles because the angle between the

viewing direction and the direct sunbeam decreases and especially for a relative azimuth of  $0^\circ$ , the strong forward peak of the Mie-scattering phase function causes the observed increase in radiance (Figure 4-4).

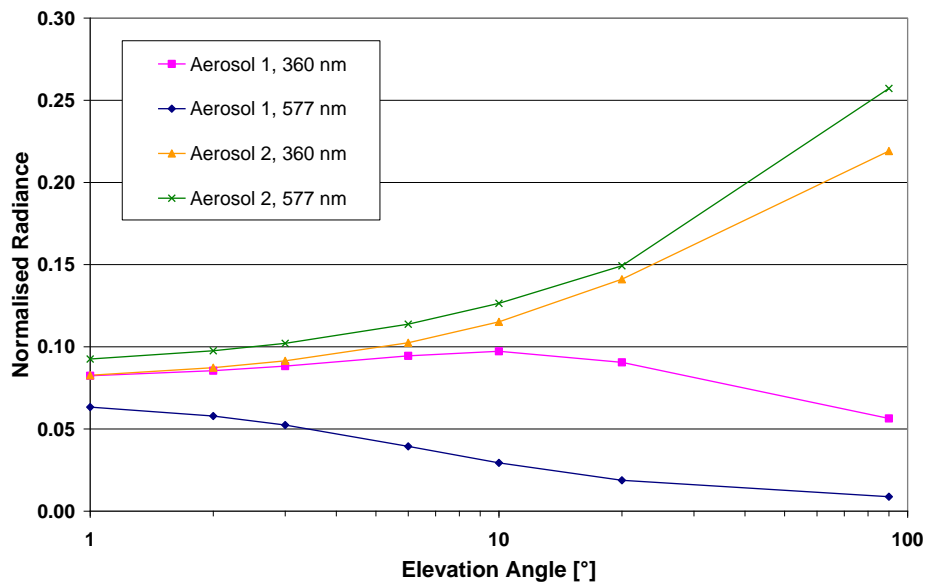


**Figure 4-4 Exercise 1: Radiances normalised with respect to the incident solar irradiance as a function of the elevation angle for  $20^\circ$  SZA and  $0^\circ$  relative azimuth angle for an aerosol-free atmosphere (scenario 1) as well as for a large aerosol load (scenario 2). Since the telescope points towards the direction of the direct sunlight, the radiances increase with increasing elevation angle when aerosols are included, due to the strong forward maximum of the Mie scattering phase function.**

The block AMFs for this exercise are presented in Figure 4-5 to Figure 4-8. In general, the largest block AMFs can be found for the lowest lines of sight and layers and they decrease with altitude indicating that also the sensitivity of the MAX-DOAS measurements decreases towards higher altitudes making profile retrieval for that part of the atmosphere difficult or even impossible. In addition, the block AMFs decrease significantly when aerosols are present. The geometric AMFs for the lowest viewing directions are only valid within the lowest 100 m in the aerosol-free atmosphere and only when observing light in the visible (see Table 6).

The interesting features in these graphs are the crossing points of the curves of the block AMFs for the different lines of sight: At these points, another viewing direction takes over being the most sensitive one for the given altitude. This can be observed e.g. in Figure 4-7: For the lowest level, the  $1^\circ$  elevation direction is most sensitive,

but in the layer above, between 100 and 200 m, observations under 3° hold the most information. These different sensitivities can then be used to obtain some layer information of the concentration in the lower atmosphere. The number of these layers depends on the aerosol load and of course on the wavelength (see section 4.3).

**Table 5 Calculated vertical optical depth with respect to scattering, see also Figure 4-2, left panel.**

	VOD at 360 nm	VOD at 577 nm
aerosol scenario 1 (Rayleigh atmosphere)	0.56	0.08
aerosol scenario 2	1.58	1.10
aerosol scenario 3	0.67	0.19

**Table 6 Exercise 1: Comparison of geometric AMFs with the block AMFs for the lowest layer at 50 m. Only in the aerosol-free atmosphere and when observing light in the visible, the geometric approach yields a reasonable approximation for the lowest viewing angles of the telescope. Data is also presented in the figures as indicated in the table.**

elevation angle	1°	2°	3°	6°	10°	20°	90°
geometric AMF	57	29	19	10	6	3	1
block AMF at 50m: Rayleigh atmosphere, 360nm (see Figure 4-5)	48	27	19	10	6	3	1
block AMF at 50m: Rayleigh atmosphere, 577nm (see Figure 4-6)	55	28	19	10	6	3	1
block AMF at 50m: Aerosol scenario 2, 360nm (see Figure 4-7)	19	17	14	9	6	3	1
block AMF at 50m: Aerosol scenario 2, 577nm (see Figure 4-8)	21	18	15	9	6	3	1

In the Rayleigh atmosphere, the block AMFs for the different viewing directions converge only above 10 km indicating that in this case, photons from rather high up in the atmosphere can be scattered into the lines of sight of the lowest elevation angles. In the more realistic scenario including aerosols, though scenario 2 has a rather high aerosol-load, height-resolved information of a trace gas can only be obtained within

the lowest kilometres of the atmosphere. The thickness of this layer increases with a decrease in aerosol extinction. The results for these two extreme aerosol scenarios demonstrate that the profile information content is mainly determined by the aerosol content of the atmosphere. The observed differences between the block AMFs for different wavelengths can be used when retrieving profile information of a given trace gas such as NO<sub>2</sub> that absorbs light over a wide range of wavelengths (Bruns et al., 2004).

However, although this exercise demonstrates quite nicely the possible information content of MAX-DOAS measurements, in practice, it is fairly redundant since at 0° relative azimuth the instrument is normally not taking horizon measurements to avoid detecting direct sunlight. In addition, this relative azimuth rather constitutes an exceptional situation due to the shape of the phase functions having forward peaks for both Mie and Rayleigh scattering (Figure 4-13). This will be demonstrated in the next exercise 2.

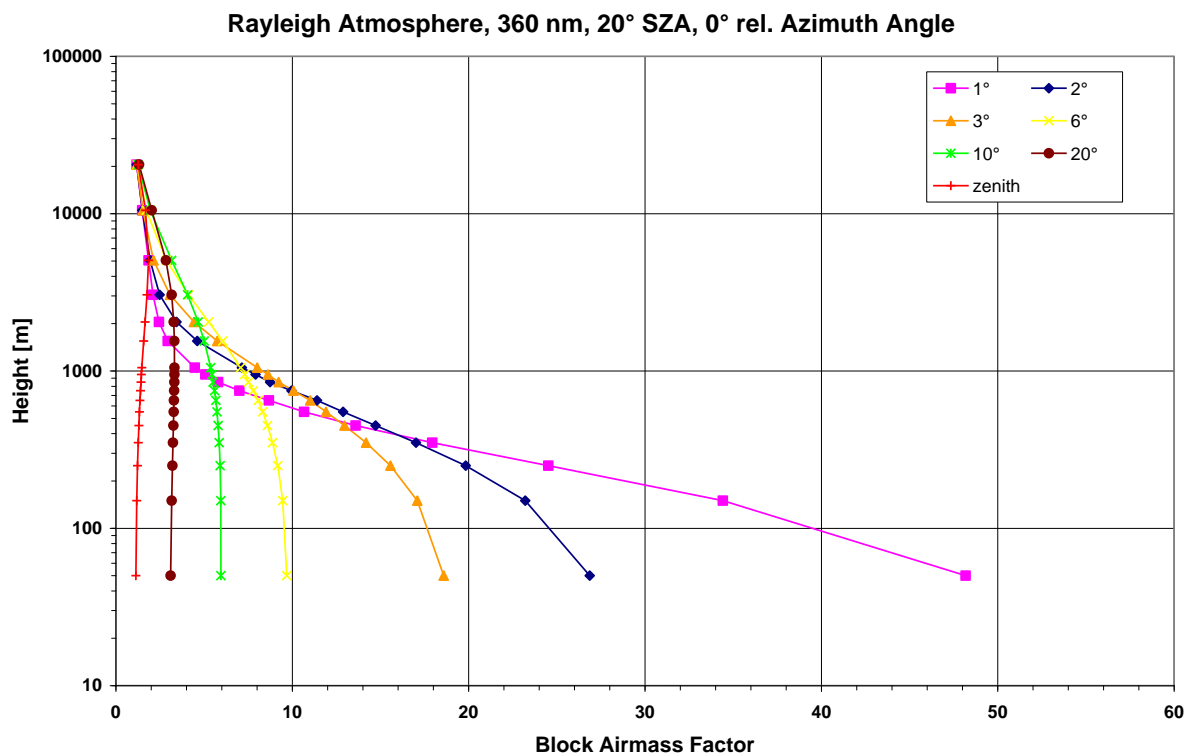


**Figure 4-5 Exercise 1: Block air mass factors as a function of height for different elevation angles, here, for 360 nm and an aerosol-free atmosphere.**

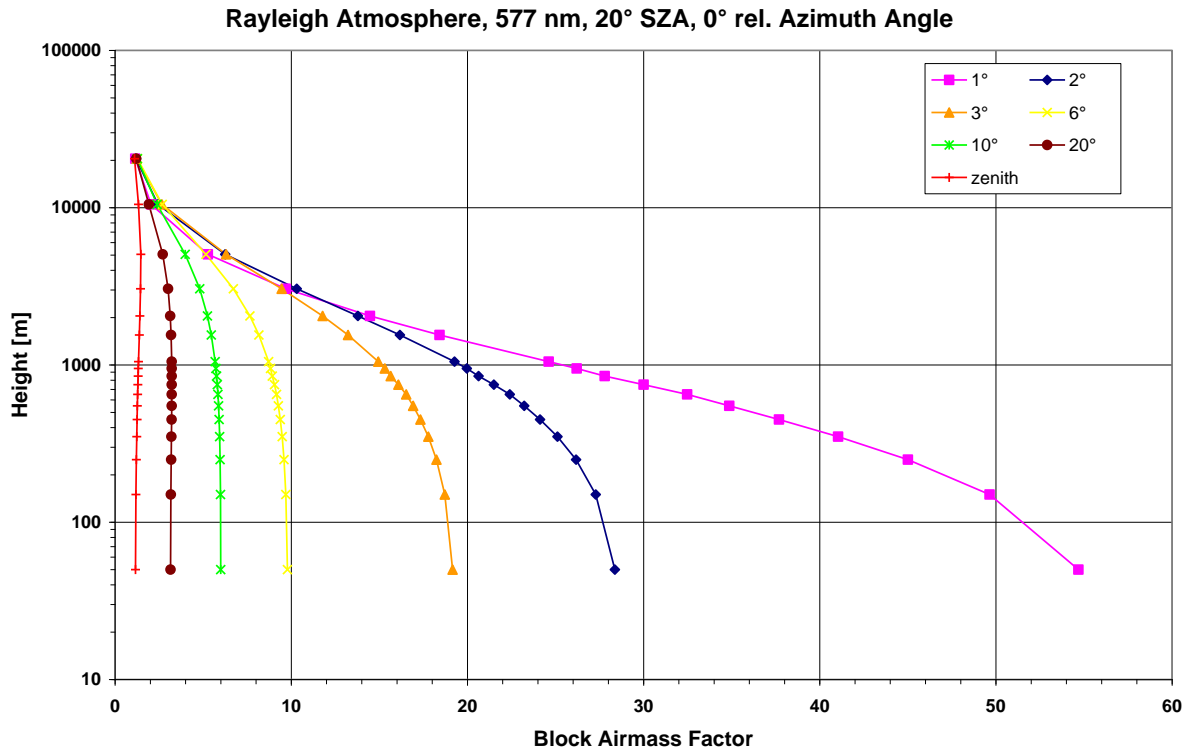


Figure 4-6 Exercise 1: Same as Figure 4-5, but for 577 nm.

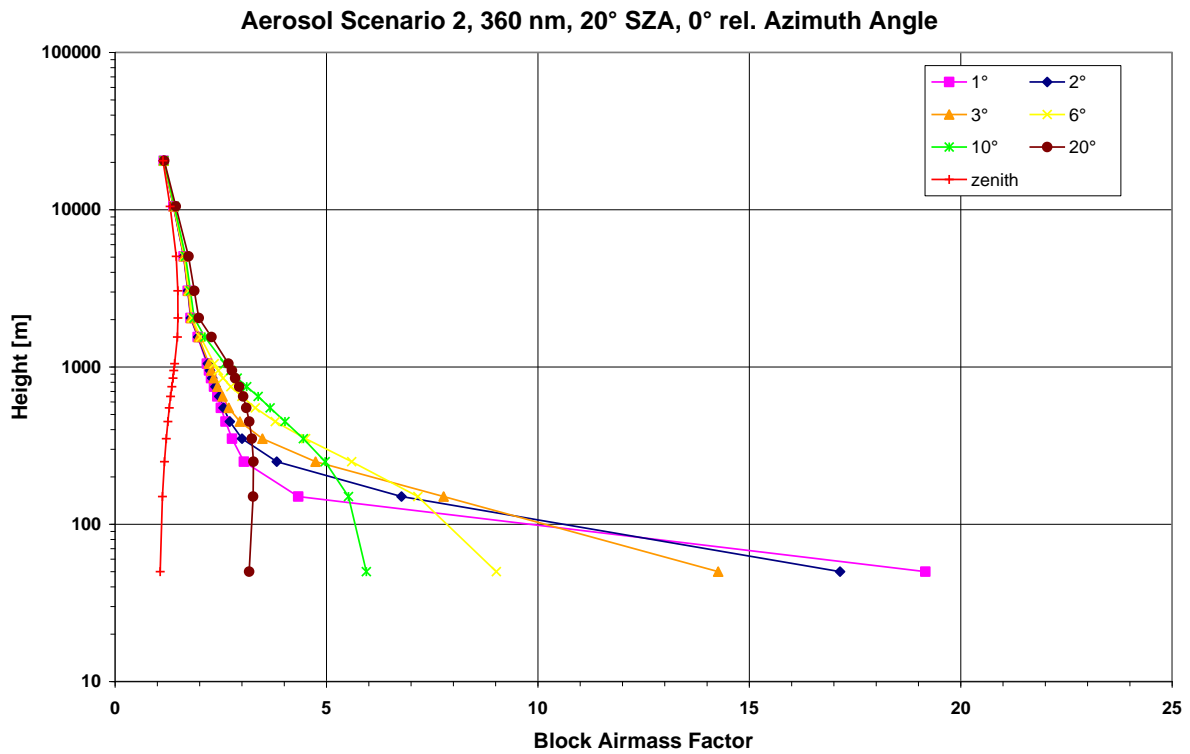
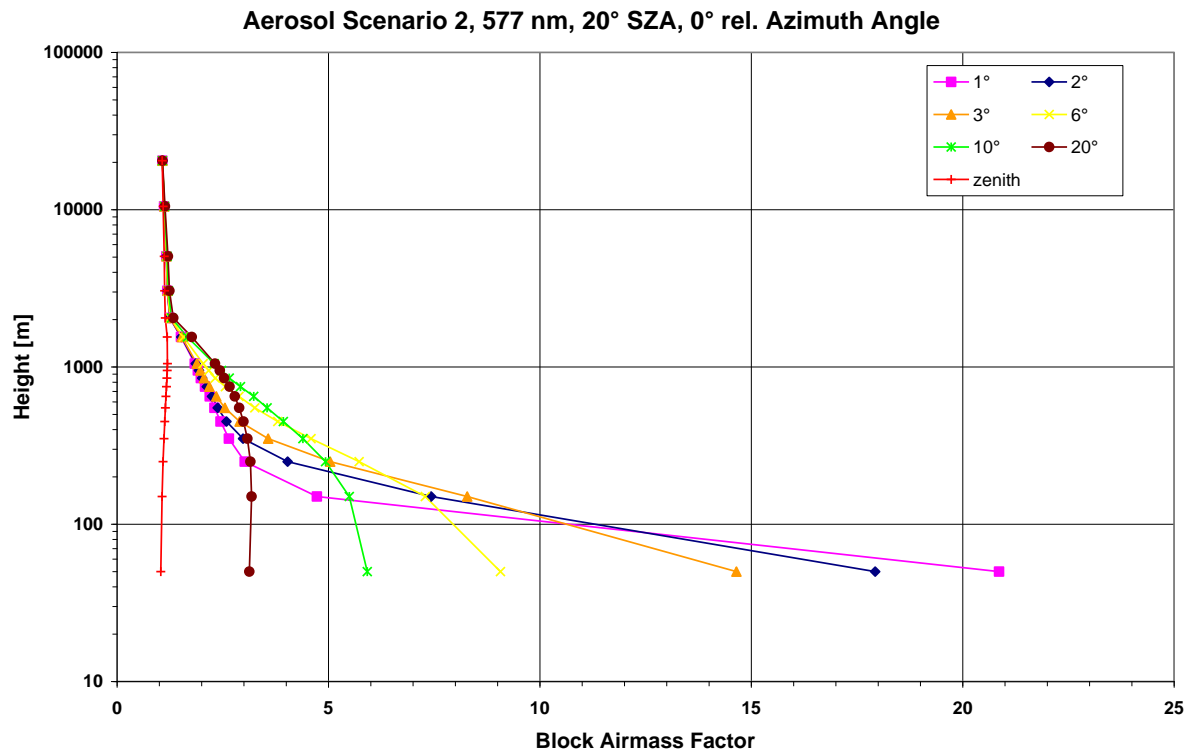


Figure 4-7 Exercise 1: Block air mass factors as a function of height for different elevation angles, here, for 360 nm and  $0.5 \text{ km}^{-1}$  aerosol extinction in the lowest 2 km.



**Figure 4-8 Exercise 1: Same as Figure 4-7, but for 577 nm.**

### Exercise 2

In the last of the three main exercises, the dependency on the azimuth angle is tested. The settings and the calculated output parameters are summarised in Table 7.

**Table 7 Settings for exercise 2: Variations of the azimuth angle.**

input parameters	output parameters
- aerosol scenarios1 (no aerosols), 2, and 3	- radiances
- wavelengths 360 nm and 577 nm	- vertical optical densities
- albedo 0.03	- all block air mass factors
- elevation angle: 2°	
- SZA: 80°	
- azimuth angles: 0°, 30°, 60°, 90°, 120°, 150°, and 180°	
- asymmetry factor of aerosol phase function: 0.68	

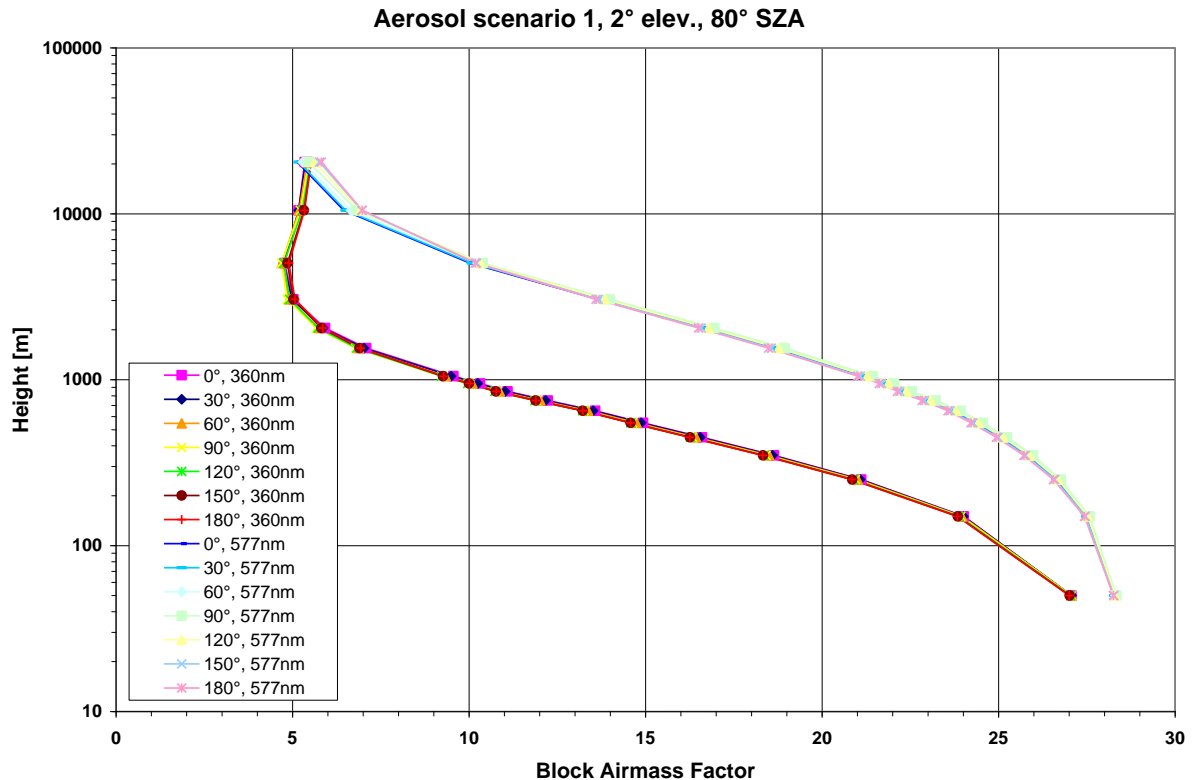


**Figure 4-9 Exercise 2: Test on the azimuth dependence of the block AMF in the Rayleigh atmosphere (aerosol scenario 1). The Rayleigh phase function does not strongly depend on the incident direction of the photon and the differences in the block AMFs are negligible.**

The azimuth dependence of the radiances and of the block AMF is determined by the angular distribution of the scattering phase function. Scattering on particles is approximated by the Mie theory (see also section 2.2.2). The phase function describes the probability of a photon to be scattered into a certain direction. The Mie phase function has a very strong forward peak. This is illustrated in Figure 4-13. On the other hand, scattering on molecules is described by the Rayleigh theory. The Rayleigh phase function has two symmetric maxima in the forward and in the backward direction and can be described as peanut-shaped (Figure 4-13). Consequently the differences in the block AMFs are negligible for this test case (see Figure 4-9).

Almost no effect of the azimuth dependence can be observed for the block AMFs in the aerosol scenario 2. In this case the signal is made up of photons that have often been scattered more than once (Figure 4-10). Consequently, the angular distribution of the scattering phase function becomes less important in a multiple-scattering atmosphere. The largest differences can be observed in the block AMFs for the moderate aerosol load (Figure 4-11). At about 1 km height, the block AMFs for 180° and

0° azimuth angle differ by almost a factor 2. Here, the signal is made up mainly of photons that have travelled on a slant path to this point in the atmosphere and then being single-scattered into the telescope. It is also interesting to look at the difference between block AMFs for 360 nm and 577 nm in Figure 4-11: The azimuthal effect is much smaller for shorter wavelengths. That can be explained by the large optical depth of 0.56 due to Rayleigh scattering in the UV. Rayleigh scattering has a strong wavelength dependency of  $\lambda^{-4}$ . The overall vertical depth for aerosol scenario 3 is 0.67 and only slightly larger than for the aerosol-free scenario (compare also Table 5). At 577 nm, the VOD increases from 0.08 to 0.19 when particles are added to the atmosphere. The contribution of the Mie scattering to the optical depth is 0.11 independent of the wavelength.

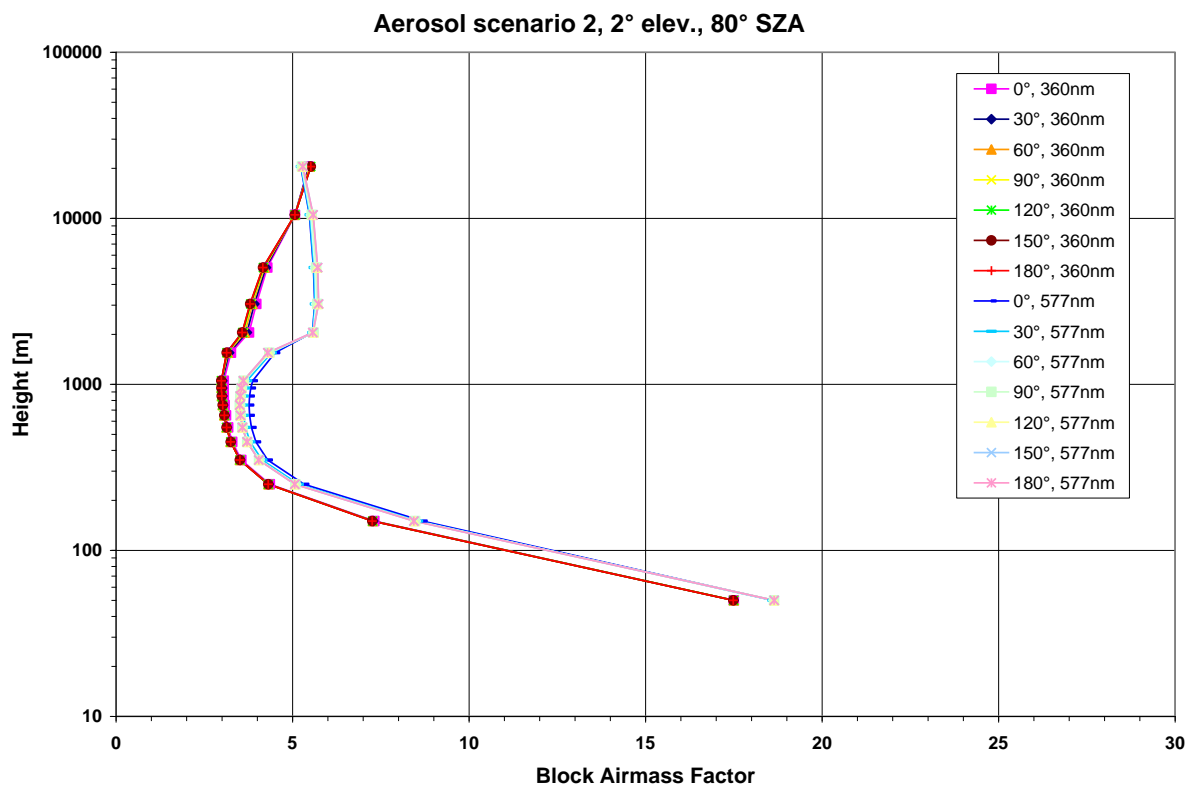
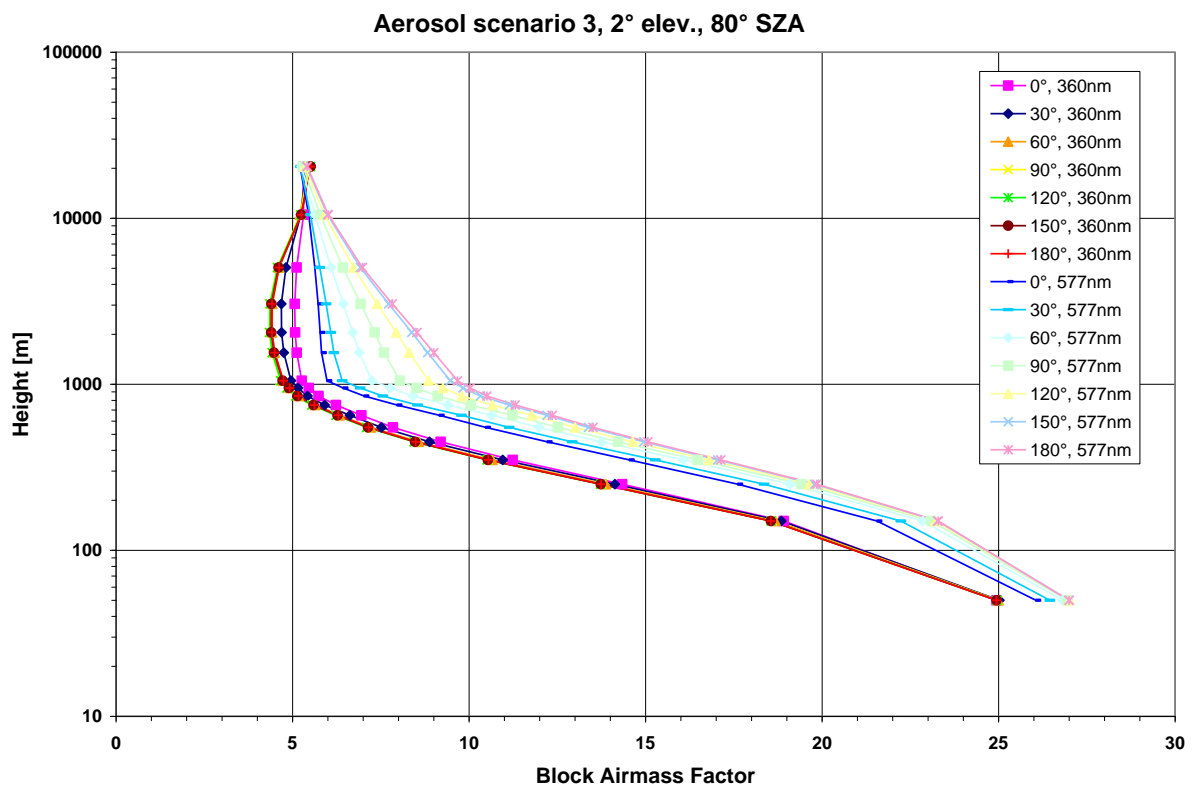


Figure 4-10 Exercise 2: Test on the azimuth dependence of the block AMF for a large aerosol load (aerosol scenario 2). Here, the signal is mainly made up of photons that have been scattered more than once hence the angular distribution of the Mie phase function loses its importance (compare also Figure 4-11).

Figure 4-12 shows the dependence of the dSCDs of the tropospheric species  $O_4$  on the azimuth but also on the elevation angle. The oxygen dimer  $O_4$  is explained in

more detail in the following section 4.3. These measurements under cloud-free conditions show that the largest azimuthal effect can be observed for SZAs smaller than  $80^\circ$  which was the selected angle for exercise 2. In the case of the eastward-facing instrument (Figure 4-12a), the dSCDs increase by about 75% when the sun is positioned in the back compared to  $0^\circ$  relative azimuth at  $70^\circ$  SZA and  $2^\circ$  elevation angle. Furthermore, these figures show the increase of the dSCDs towards a decrease in elevation angle.



**Figure 4-11 Exercise 2: Test on the azimuth dependence of the block AMF for a moderate aerosol load (aerosol scenario 3). Only here, an effect of the azimuth on the block AMF can be observed due to the strong forward peak of the Mie scattering phase function (compare also Figure 4-9 and Figure 4-10) since the signal is dominated by photons being scattered only once.**

Besides the three main exercises as described above, additional tests include simulating the effects on the block AMFs towards changes in the surface albedo and in the asymmetry factor of the aerosol phase function, and testing the effects of the spherical version of the RTE versus a plane-parallel approach, which is basically a test on the influence of refraction.

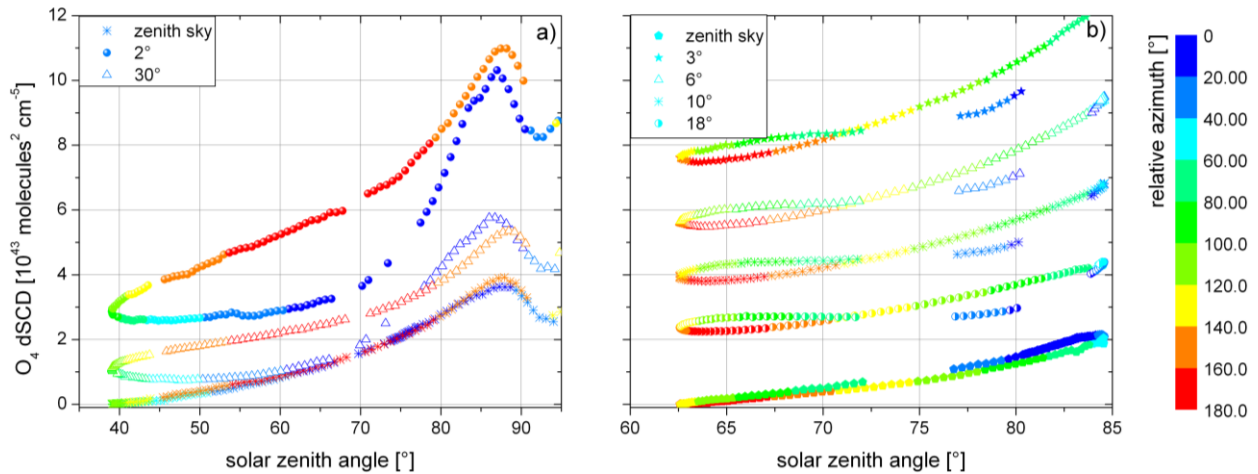


**Figure 4-12** Observed azimuth and elevation angle effect on dSCDs of the tropospheric absorber  $O_4$  (see section 4.3 for an explanation of the oxygen dimer  $O_4$ ) at a wavelength of 455 nm: a) Measurements from List (see section 5.1) with an eastward facing telescope. b) Measurements from Ny-Ålesund (see section 5.2) with a telescope pointing towards the northwest.

### ***Asymmetry factor***

A change in the asymmetry parameter in the aerosol phase function is examined: 0.68 for an urban environment and 0.75 for marine aerosol. The stronger forward peak for the marine particles is caused by their smaller sizes in comparison to particles of a polluted atmosphere (see Figure 4-13a). The block AMFs are shown in Figure 4-14. As can be seen, the differences are negligible for both aerosol scenarios 2 and 3 as well as for both wavelength regions in the UV and in the visible.

### ***Albedo***

Here, the influence of the ground albedo is tested. The albedo of 0.03 is representative for many land surfaces with the exception of deserts. For comparison, an albedo of 0.8 is chosen. Such a high albedo can occur over fresh snow.

Photons that hit a ground with an albedo of 0.03 are mostly absorbed. But for 0.8, a large fraction of the photons are reflected back into the atmosphere and can increase the radiance especially for low observation angles (not shown). Due to this, also the sensitivity towards the lowest layers in the atmosphere is enhanced: Photons having travelled a long path close to the surface are less likely to be absorbed before they can reach the detector (see Figure 4-15).

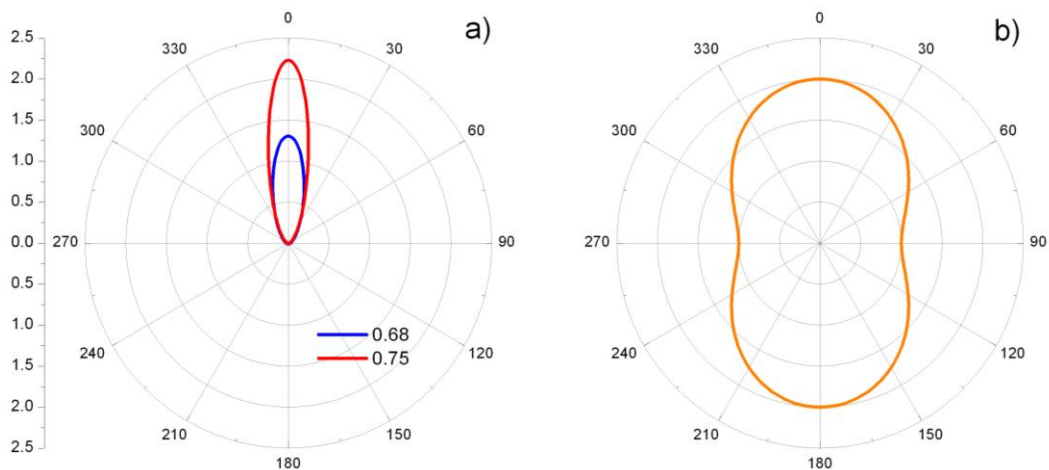


Figure 4-13 Phase functions in arbitrary units with the photon incident angle  $\gamma = 180^\circ$ : a) Mie phase function for two different asymmetry factors 0.68 and 0.75 representing an urban environment and for marine aerosol, respectively. Note that the backward peak is so small that it cannot be observed on the scale of this graph. The larger forward peak for the asymmetry factor of 0.75 is associated with smaller particles. The phase function is calculated after Henyey and Greenstein (1941). b) Rayleigh phase function calculated with  $1+\cos^2 \gamma$ .

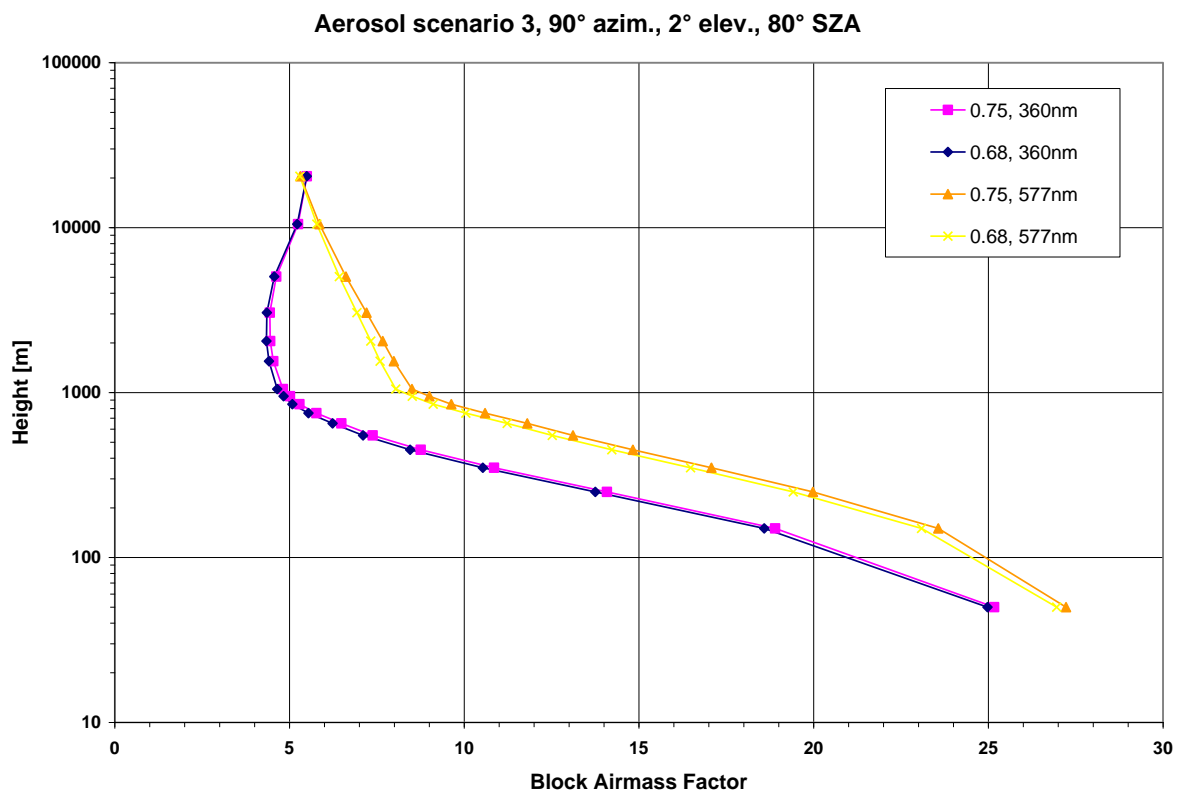
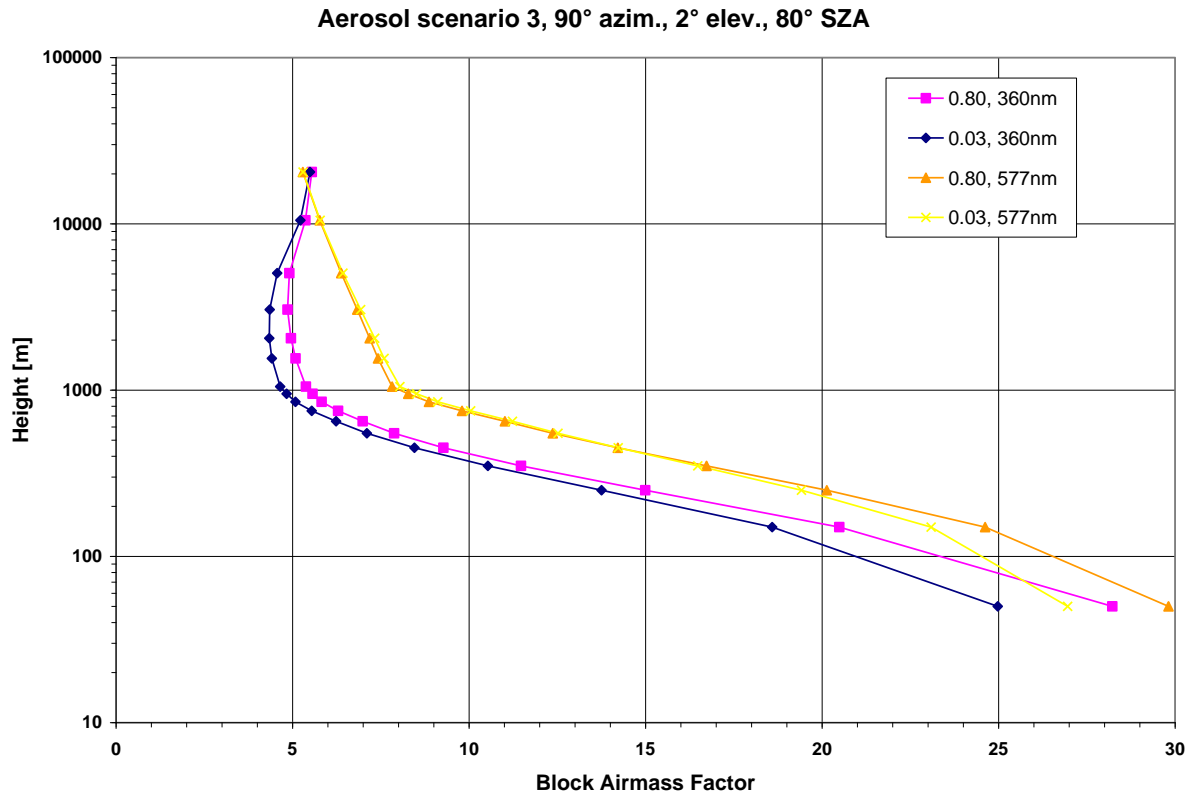


Figure 4-14 The influence of the asymmetry factor of the Mie phase function on the block AMFs is negligible for aerosol scenario 3. The asymmetry factors of 0.68 and 0.75 represent urban and marine aerosol, respectively. Compare also Figure 4-13 for shape the two phase functions.



**Figure 4-15 Influence of the surface albedo on the block AMFs for aerosol scenario 3: A high albedo of 0.8, as can occur over fresh snow, enhances the sensitivity towards the lowest layers in the atmosphere.**

### ***Refraction***

The light coming from the sun experiences changes in the density of the air. This causes the light beam to refract according to Snell's law. Especially for SZAs larger than 90°, this results in the fact that the sun can still be observed above the horizon although it is physically below. The effect of refraction on the block AMF is tested by comparing the block AMFs from the full-spherical version of SCIATRAN including refraction to the one that treats the atmosphere as plane-parallel. Interestingly, refraction seems to be only important in higher altitudes where the light path is mainly the direct sun beam. The photons will be deflected towards the denser medium, i.e. the distance travelled will be shorter and hence the block AMF smaller (Figure 4-16).

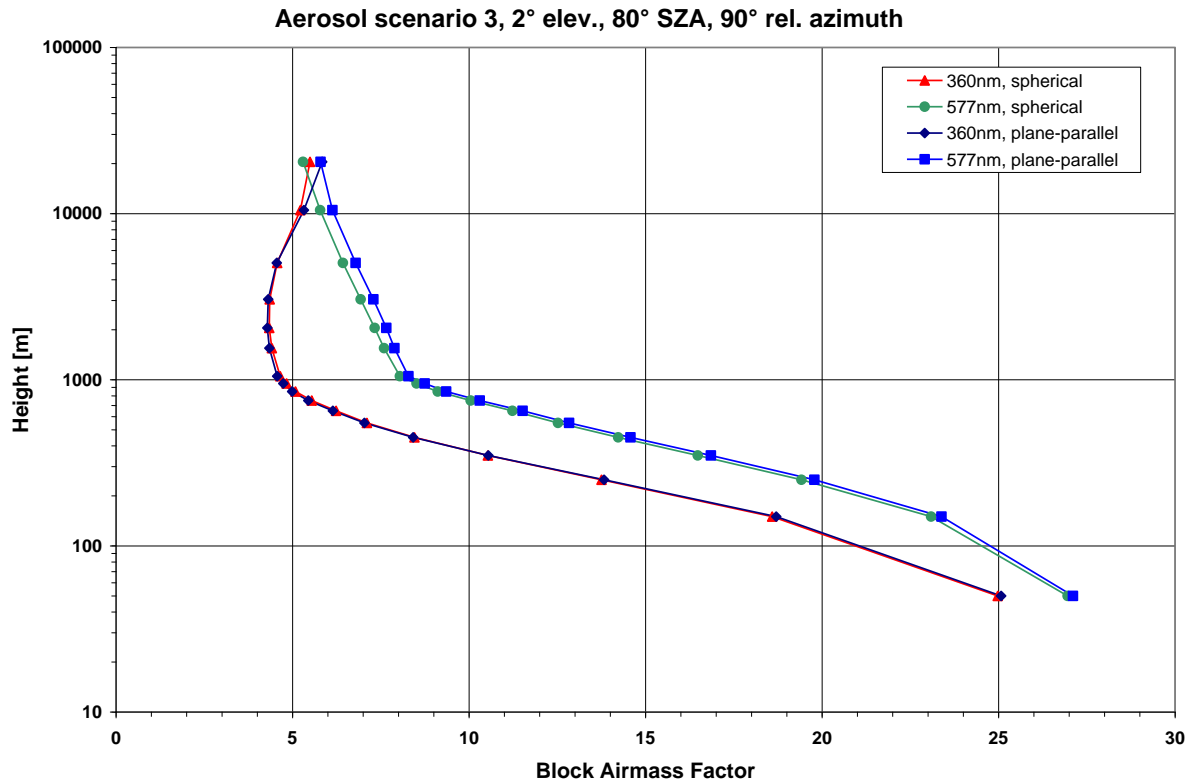


Figure 4-16 Testing the influence of the refraction of the solar beam in the atmosphere on the block AMF: The full-spherical version of SCIATRAN includes refraction whereas the plane-parallel approximation does not. Refraction only seems to be important in higher altitudes where the light path is mainly the direct sun beam.

### Summary

Previous studies for the interpretation of scattered sunlight measurements only looked at AMFs but not block AMFs (Wittrock et al., 2004; Wagner et al., 2004; Hendrick et al., 2006). However, block AMFs are useful to test the sensitivity of MAX-DOAS measurements towards a certain altitude in the atmosphere. Two main exercises were performed here: The sensitivity towards the elevation angle and the sensitivity towards the azimuth angle. For this, different aerosol scenarios from the aerosol-free atmosphere over a moderate aerosol load to a boundary layer with strong extinction were compared. It was shown that off-axis measurements are particularly sensitive to the lowest layers in the atmosphere. But this sensitivity is strongly dependent on wavelength and aerosol load. The second exercise showed that especially particles alter the radiative transfer in a way resulting in an azimuthal dependency owing to the Mie phase function. This effect has also been illustrated by the measurements. However, the asymmetry parameter of the aerosol phase function

has a rather small effect. Further tests showed that snow-covered environments increase the intensity but also the sensitivity towards the lowest layers and that refraction is not very important in the studied case scenarios.

### 4.3 Profiles, total column densities and tropospheric column densities

It was shown in the previous section, that the geometrical approach is only a very crude approximation for the actual AMF at least for  $\text{LOS} < 10^\circ$ . In this section, several approaches will be described to convert SCDs into more meaningful quantities like profiles. This theory has been applied to data from the DANDELIONS campaign and the MAX-DOAS  $\text{NO}_2$  results have been compared to independent data sets.

#### **Total column densities**

The zenith-sky DOAS was developed to retrieve total column densities of stratospheric absorbers. For this, look-up tables for the zenith AMF can be easily created with a radiative transfer model like SCIATRAN for different SZAs and stratospheric absorbers with a known profile like ozone. These AMFs are usually simulated for a wavelength  $\lambda$  that refers to the centre of the DOAS fitting interval. The total vertical column density VC can then be calculated for the differential slant column densities SC retrieved in the DOAS fitting by:

$$\text{VC} = \frac{\text{SC}(\theta, \lambda) - \text{SC}^{\text{noon}}(\theta^{\text{noon}}, \lambda)}{\text{AMF}(\theta, \lambda) - \text{AMF}^{\text{noon}}(\theta^{\text{noon}}, \lambda)} \quad (4.8)$$

with  $\theta$  being the solar zenith angle of the measurements and  $\theta^{\text{noon}}$  the SZA of the background spectrum with the corresponding slant column density  $\text{SC}^{\text{noon}}$  and the corresponding AMF for the noon geometry  $\text{AMF}^{\text{noon}}$ .

However, for example for absorbers with an unknown stratospheric profile like BrO or for photolabile absorbers like chlorine dioxide OClO where not only the absolute column but also the profile changes during the day (see chapter 6), accurate AMFs are impossible to simulate and usually only SCDs are reported.

### ***Tropospheric column densities***

The tropospheric column density of an absorber can be derived using the geometric approach for the AMF. For this, the measurements at a high off-axis elevation angle are used. It is assumed that the last scattering event of a photon, before it reaches the telescope, happens above the absorber layer. In this case, the AMF is determined by the elevation angle only. This is illustrated in Figure 4-17.

A differential tropospheric SCD can be obtained from the difference between the off-axis slant column density  $SC^{\text{off-axis}}$  for the elevation angle  $\varphi$  and the zenith slant column density  $SC^{\text{zenith}}$  interpolated to the time of measurement. In analogy to equation (4.8), the tropospheric column density  $VC_{\text{trop}}$  can be calculated by:

$$VC_{\text{trop}} = \frac{SC^{\text{off-axis}}(\theta, \varphi, \lambda) - SC^{\text{zenith}}(\theta, \lambda)}{\frac{1}{\sin(\varphi)} - 1} \quad (4.9)$$

If the last scattering occurs within the layer of the absorber, the path length will be overestimated and hence the tropospheric column density underestimated (see red and dashed lines in Figure 4-17). The conditions, under which this geometric approach can succeed, are a thin absorber layer, using high elevation angles only, as well as clear weather or high clouds. In practice, this method can be tested for consistency by comparing the retrieved tropospheric column densities of two different elevation angles, e.g. 15° and 30°, and discarding the measurements if these do not agree within a set limit. This approach can be used for strong tropospheric absorbers like NO<sub>2</sub> and is particularly useful for satellite validation.

An example is given in Figure 4-18a. These measurements were performed during the first campaign of the Dutch Aerosol and Nitrogen Dioxide Experiments for Validation of OMI and SCIAMACHY (DANDELIONS) at Cabauw (The Netherlands) in summer 2005 (Brinksma et al., 2008, <http://www.knmi.nl/omi/research/validation/dandelions>). The horizon was scanned by the MAX-telescope in 1°-steps from 1° to 15° elevation, followed by a measurement at 30° elevation angle and the zenith. The measured spectra were then analysed for NO<sub>2</sub> and the tropospheric column density was determined according to equation (4.9) for the 15° and 30° dSCDs. Only measurements that agreed within 15% were included. This data was compared to

SCIAMACHY tropospheric column densities (data provided by A. Richter, University of Bremen, see section 6.1.1 for a description of the SCIAMACHY instrument). Figure 4-18a shows that the satellite rather yields lower values than the ground-based measurements. This is expected as very local emission plumes might be missed due to the ground pixel size for observations from space. However looking at Figure 4-19a for the correlation of this comparison, the slope is inverted, i.e.  $0.87 \pm 0.20$ , although this is not significant within the errors and the scatter is rather large due to the fact that only 20 data points for SCIAMACHY could be included after all cloudy pixels have been removed. The offset is  $(0.18 \pm 0.18) \times 10^{16}$  molecules/cm<sup>2</sup> and a correlation of 0.72 could be achieved (see also Table 8).

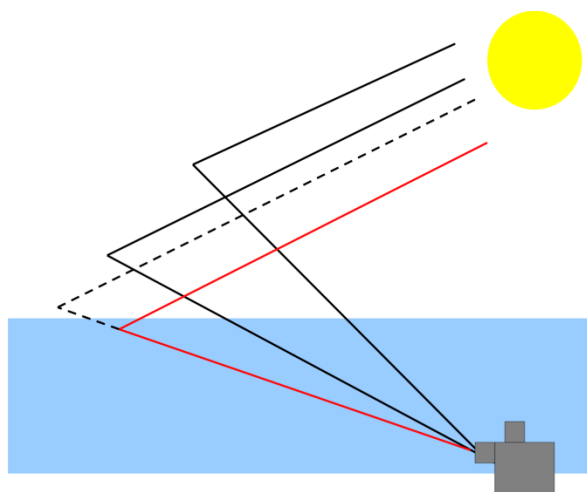


**Figure 4-17** Illustration of the observational geometry in relation to the absorber layer depth (blue shaded area) applicable for retrieving tropospheric column densities with the geometric AMF (equation (4.9)). Measurements only from large elevation angles ( $>10^\circ$ ) are utilised and it is assumed that the last scattering event of the photons takes place above the absorber layer.

### ***Mixing ratios in the lowest layer***

Several older measurements analysed in this study were performed with only a limited number of off-axis directions, sometimes only one. Hence also only limited information about the vertical distribution of a tropospheric trace gas can be obtained. To find a rough estimate of the concentration in the bottom layer in the atmosphere, an off-axis AMF can be calculated with SCIATRAN with an assumed profile for the aerosol extinction as well as an assumed block profile for the absorber. Again, the

corresponding zenith slant column densities  $SC^{\text{zenith}}$  have to be subtracted from the off-axis ones  $SC^{\text{off-axis}}$  and the tropospheric column density  $VC_{\text{trop}}$  is given by:

$$VC_{\text{trop}} = \frac{SC^{\text{off-axis}}(\theta, \varphi, \vartheta, \lambda) - SC^{\text{zenith}}(\theta, \lambda)}{AMF^{\text{off-axis}}(\theta, \varphi, \vartheta, \lambda) - AMF^{\text{zenith}}(\theta, \lambda)} \quad (4.10)$$

with  $\vartheta$  being the relative azimuth angle. The resulting vertical column densities can then be homogeneously distributed over the assumed layer height to retrieve a rough estimation of the concentration of an absorber. A possible strong gradient of the trace gas will not be recognised though and the maximum mixing ratios in that layer underestimated. This approach is also problematic since the lowest elevation angles are particularly sensitive to the aerosol and assumptions about the actual height of the mixed layer of an absorber have to be made. The knowledge of these parameters is essential to retrieve the correct amount of the chosen absorber.

Recent studies (Wagner et al., 2004; Wittrock et al., 2004; Heckel et al., 2005; Frieß et al., 2006; Irie et al., 2008) have shown that the measured slant column densities of the oxygen dimer  $O_4$  can be used to derive aerosol information, i.e. the extinction profile and to some extent also the particle type in the atmosphere. Consequently, the method described here can be extended by first simulating  $O_4$  slant column densities with SCIATRAN and adjusting the extinction profile until the measured and modelled column densities agree. This aerosol information can then be applied to retrieve the AMFs used in equation (4.10).

The oxygen dimer  $O_4$  is a collision complex of two oxygen molecules and its concentrations can be quantified by DOAS (Perner and Platt, 1980). The  $O_4$  profile depends on the pressure and temperature profiles  $p(z)$  and  $T(z)$ , respectively. The vertical column density  $VC^{O_4}$  can be calculated from the volume mixing ratio of oxygen  $VMR^{O_2}$  integrated from the ground to the top of the atmosphere TOA:

$$VC^{O_4} = \int_{z=0}^{\text{TOA}} \left( \frac{VMR^{O_2} \cdot p(z)}{T(z) \cdot k_B} \right)^2 dz \quad (4.11)$$

with  $k_B$  being the Boltzmann constant. The unit of the vertical column density is given in  $[\text{molecules}^2 \text{cm}^{-5}]$ . This is consistent with the unit of the *absorption spectrum* of  $O_4$  of  $[\text{cm}^5 \text{molecules}^{-2}]$  (Greenblatt et al., 1990) which is the absorption cross section multiplied by the equilibrium constant  $k$  for the reactions:



The oxygen dimer has several strong absorption features in the UV and visible and hence can be retrieved by DOAS in several wavelength region (compare also section 4.2, exercise 0).

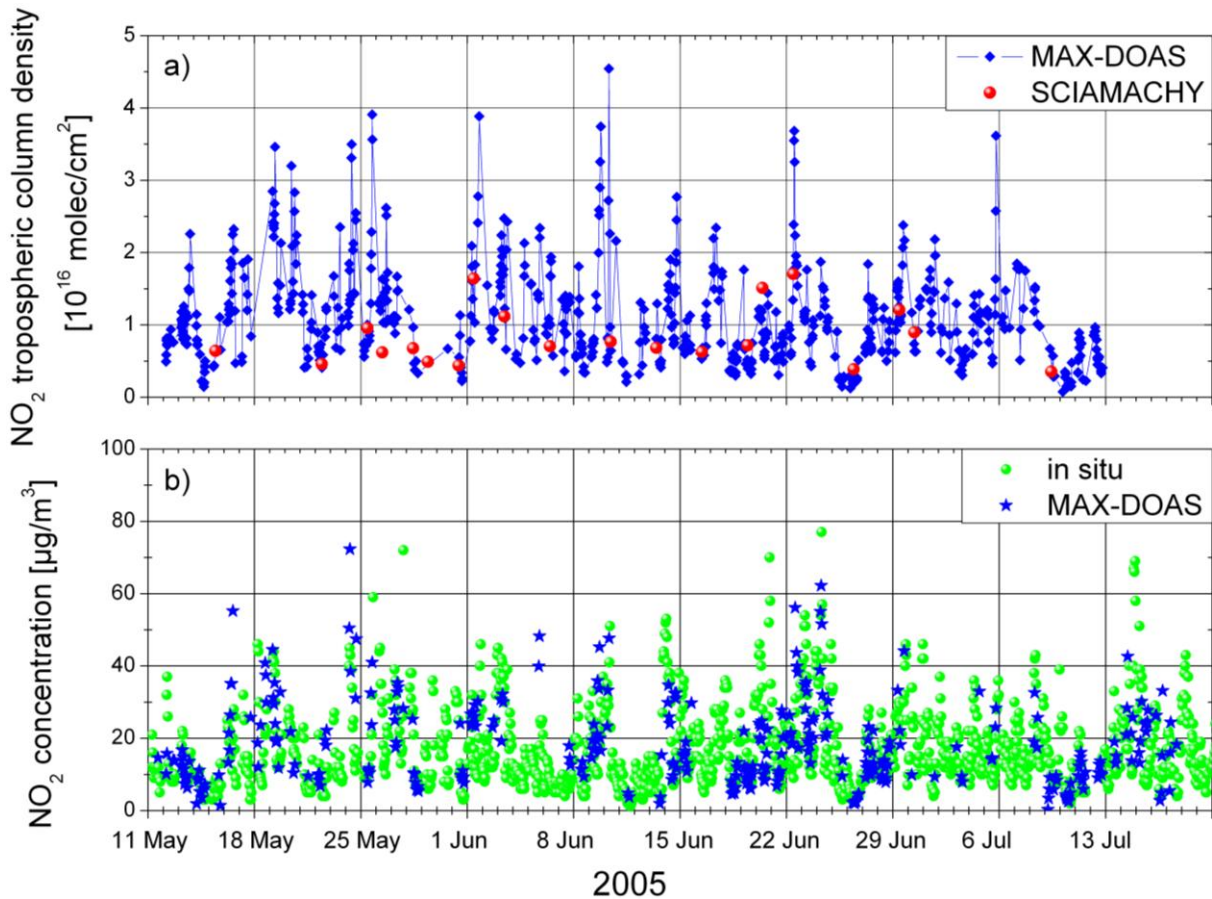


**Figure 4-18** Intercomparison of MAX-DOAS data with SCIAMACHY (see section 6.1.1 for a description of the satellite instrument) tropospheric column densities (a) and with *in-situ* measurements on the ground (b) for the first of the two DANDELIONS campaigns in Cabauw (The Netherlands) in 2005. The correlation of this data is shown in Figure 4-19 and in Table 8.

### Profiles

The technique described above is a compromise to be able to interpret some of the older MAX-DOAS spectra recorded by instruments from the Institute of Environmental Physics (University of Bremen) since 1999. However, it was shown that ideally the measurements are performed scanning the horizon in 1° step sizes (Wittrock, 2006). To interpret these multi-axis measurements, BREAM, an automated profile

retrieval, has been developed at the Institute of Environmental Physics, University of Bremen (Wittrock, 2006).

The first step in BREAM is similar to the one described above: An a priori extinction profile is scaled in an iterative process and the modelled  $O_4$  dSCDs for all viewing directions are compared to the measured ones in order to reduce uncertainties due to particles in the atmosphere. The optimum extinction profile is determined by optimising the following two parameters:

- The height of the boundary layer determines the correlation between the retrieved and the modelled column densities.
- The extinction determines the mean deviation between measured and modelled column densities.

In a second step, block air mass factors for the exact angles of the measurements using the obtained aerosol information are calculated with SCIATRAN. These can be converted into elements of a weighting function matrix. The weighting function matrix  $\mathbf{K}$  has the dimensions number of measurement, i.e. number of viewing directions, times the number of height layers, i.e.  $I \times J$ . The elements  $K_{ji}$  of the weighting function matrix give the change in the  $i$ -th SCD caused by a change in the concentration of an absorber at a certain layer  $j$ :

$$K_{ij} = \frac{dBAMF_{ij} \cdot p_j \cdot N_A}{T_j \cdot R} \Delta h \quad (4.13)$$

with  $\Delta h$  being the thickness of the layer  $j$ ,  $p_j$  and  $T_j$  being the pressure and temperature in this layer, respectively.  $R$  is the universal gas constant and  $N_A$  the Avogadro number. The  $dBAMF_{ij}$  is the differential block air mass factor relative to the reference measurement. In other words, the weighting function matrix describes a linear relationship between the measurement vector  $\vec{y} = (y_1, \dots, y_I)$  and the trace gas height profile  $\vec{x} = (x_1, \dots, x_J)$ :

$$\vec{y} = \mathbf{K}\vec{x} \quad (4.14)$$

To solve this linear system the well-known and in atmospheric science long-established method of *Optimal Estimation* by Rodgers (2000) is applied. Similar approaches to interpret remote-sensing data have been introduced in recent studies (e.g. Palmer et al., 2001; Martin et al., 2002; Eskes and Boersma, 2003; Bruns et al.,

2004; Nüß, 2005). Since the problem is ill-posed, an analytical solution for equation (4.14) can only be found when an a priori profile  $\bar{x}_a$  with its error covariance matrix  $S_a$  is assumed:

$$\bar{x} = \bar{x}_a + (\mathbf{K}^T \mathbf{S}_\varepsilon^{-1} \mathbf{K} + \mathbf{S}_a^{-1})^{-1} \mathbf{K}^T \mathbf{S}_\varepsilon (\bar{y} - \mathbf{K} \bar{x}_a) \quad (4.15)$$

The superscript T denotes the transposed matrix and the superscript (-1) the inverse of a matrix. The covariance matrix  $S_\varepsilon$  contains the errors of the measurements  $\bar{y}$ .

The averaging kernel matrix  $\mathbf{A}$  is a measure for the quality of the retrieval by assessing the change in the retrieved profile towards a change in the true, i.e. atmospheric profile  $\bar{x}_{\text{true}}$ :

$$\mathbf{A} = \frac{\partial \bar{x}}{\partial \bar{x}_{\text{true}}} = (\mathbf{K}^T \mathbf{S}_\varepsilon^{-1} \mathbf{K} + \mathbf{S}_a^{-1})^{-1} \mathbf{K}^T \mathbf{S}_\varepsilon \mathbf{K} \quad (4.16)$$

The trace of the averaging kernel matrix determines the number of pieces of independent information with respect to the height layers, i.e. the degrees of freedom of this measurement. Typical integration times (20 minutes to two hours) together with a moderate aerosol load yield a number of about two to three for about ten different viewing angles. The error characterisation of the retrieval is described in Wittrock (2006).

In the following, an example for the performance of the multi-axis measurements in combination with the profile retrieval is presented. Figure 4-18b shows the same ground-based DOAS measurements from the DANDELIONS campaign as in the previous paragraph and Figure 4-18a. But this time, the BREAM profile retrieval was applied to the calculated NO<sub>2</sub> SCDs. The concentrations in the lowest 50 m have been averaged to be able to compare the data to an *in-situ* monitor. The corresponding correlation plot is shown in Figure 4-19b. The situation is the other way round than the intercomparison with the satellite data: Here, the *in-situ* measurements are more local than the MAX-DOAS data hence the slope is expected to be smaller than unity:  $0.56 \pm 0.04$ . A large scatter is observed though and also, there is a significant offset of  $8.6 \pm 0.9 \mu\text{g}/\text{m}^3$  and the correlation is only fair: 0.58. However under clear sky conditions in a place like Cabauw, the visibility can be more than 10 km in the lowest layers. Consequently, the footprint of the MAX-DOAS measurements is very large in comparison to *in-situ* measurements.

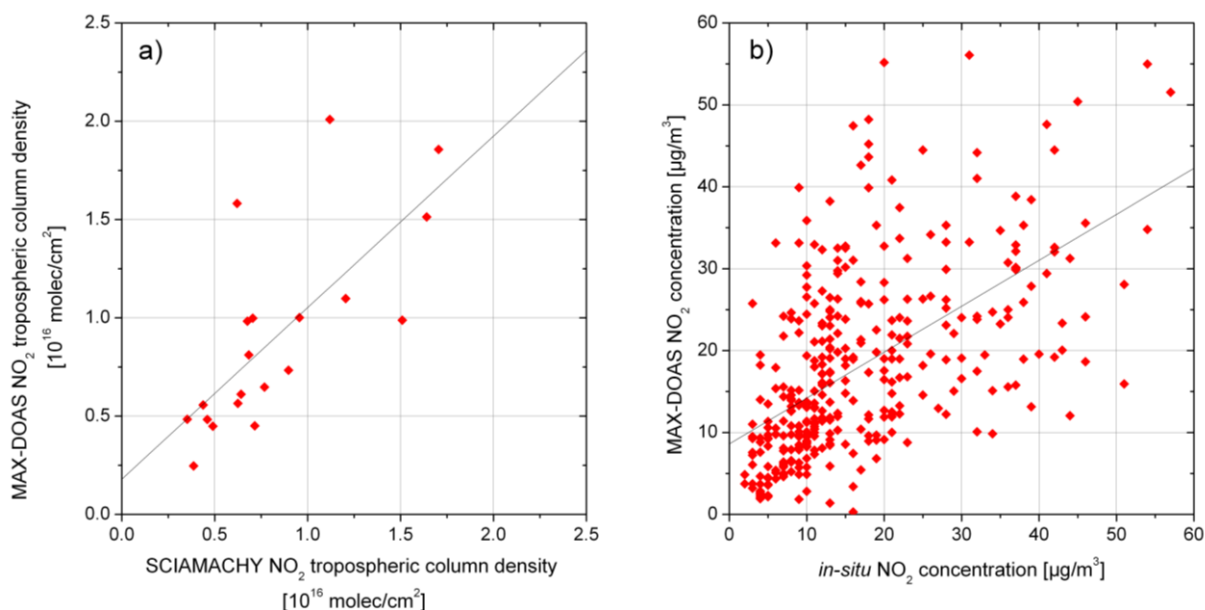


**Figure 4-19 Correlation plots for NO<sub>2</sub> data shown in figure Figure 4-18: a) The correlation of the MAX-DOAS tropospheric column density with the SCIAMACHY tropospheric column density is 0.72 with the linear fit giving a slope of  $0.87 \pm 0.20$  and an offset of  $(0.18 \pm 0.18) \times 10^{16}$  molecules/cm<sup>2</sup>. In general, a slope larger unity is expected since the satellite instrument is not as sensitive to the lowest layers as the MAX-DOAS, but also due to the ground size of the satellite pixel averaging over an area of 30×60 km<sup>2</sup>. However, only few SCIAMACHY data points are available for clear-sky conditions. b) The correlation of the MAX-DOAS NO<sub>2</sub> concentration in the lowest 50 m with the concentrations of an *in-situ* monitor is 0.58 and the linear fit has a slope of  $0.56 \pm 0.04$  and an offset of  $8.6 \pm 0.9$  μg/m<sup>3</sup>.**

To test the consistency of the two datasets, the NO<sub>2</sub> profiles retrieved with BREAM have been integrated over 3 km to obtain the tropospheric column density and this data has been compared to the geometrically retrieved tropospheric column density. For the data presented here, the correlation is 0.93 and the offset  $(0.07 \pm 0.03) \times 10^{16}$  molecules/cm<sup>2</sup>. As expected, BREAM retrieves larger tropospheric vertical column densities: The slope is  $0.78 \pm 0.02$ . This is due to the fact that the geometric AMF yields an upper limit to the actual AMF and a larger AMF gives a smaller vertical column density for the same slant column density (compare equation (4.1)).

**Table 8 Overview of correlation coefficients as well as offsets and slopes for the intercomparison of the different NO<sub>2</sub> data sets as described in this section (4.3) and Figure 4-18 to Figure 4-19.**

	correlation R	slope	offset
MAX-DOAS geometric tropospheric column density vs. MAX-DOAS integrated BREAM column density	0.93	$0.78 \pm 0.02$	$(0.07 \pm 0.03) \times 10^{16}$ molecules/cm <sup>2</sup>
MAX-DOAS geometric tropospheric column density vs. SCIAMACHY tropospheric column density	0.72	$0.87 \pm 0.20$	$(0.18 \pm 0.18) \times 10^{16}$ molecules/cm <sup>2</sup>
MAX-DOAS BREAM concentration within 50m-layer vs. <i>in-situ</i> monitor concentrations	0.58	$0.56 \pm 0.04$	$8.6 \pm 0.9 \mu\text{g}/\text{m}^3$

### **Summary**

In summary, the agreement in these three comparisons is good (see Table 8) and the observed differences are expected due to the different footprint areas that the different instruments are sampling. It has been shown that BREAM in combination with the radiative transfer model SCIATRAN is a powerful tool for the interpretation of MAX-DOAS data. In the following chapter, mainly the automated profile retrieval as well as the simple conversion into volume mixing ratios using off-axis AMFs are applied to iodine monoxide and to some extent to bromine monoxide SCDs retrieved from spectra measured in marine environments.



## 5 Measurements of tropospheric halogen oxides

The first measurements of IO were reported from a campaign at Mace Head, Ireland: Aliche et al. (1999) and Allan et al. (2000) observed concentrations of up to 6 ppt and 3 ppt, respectively, with an active longpath (LP) DOAS system. Several studies followed at sites where macroalgae were exposed at low tide: again at Mace Head, Ireland (Saiz-Lopez et al., 2006) and Brittany, France (Peters et al., 2005; Whalley et al., 2007; Wada et al., 2007), but also at Appledore Island in the Gulf of Maine, United States of America (Stutz et al., 2007). Since with MAX- as well as LP-DOAS only the average along a light path can be retrieved and IO concentrations are highly variable, the highest concentrations so far were measured using *in-situ* instruments: Whalley et al. (2007) using laser induced fluorescence spectroscopy report  $28 \pm 3$  ppt and Wada et al. (2007) using a cavity ring-down spectrometer report  $54 \pm 18$  ppt, both for Roscoff, France. Some night-time measurements of IO have been reported as well for Mace Head (Saiz-Lopez and Plane, 2004b) which can be linked to  $\text{NO}_3$  chemistry (compare reactions (2.48) and (2.49)).

The analysis of a strong decrease in ozone observed just after sunrise at several remote island sites and the open ocean suggested the presence of reactive halogen species as well in the marine background atmosphere (Dickerson et al., 1999; Nagao et al., 1999; Galbally et al., 2000; Watanabe et al., 2005). Although mainly bromine chemistry is discussed in these publications, a direct link to radical halogen chemistry could be recently established at Cape Verde with not only year-round  $\text{BrO}$ , but also IO detection: Read et al. (2008) report average daytime maxima of 2.5 ppt  $\text{BrO}$  and 1.4 ppt IO assigning about 1.8 ppb per day of the maximum observed ozone loss of overall about 5 ppb per day to the combined effect of iodine and bromine compounds. In further marine background studies, Allan et al. (2000) report up to 3.5 ppt IO from the island Tenerife (Spain). Sebastian (2004) measured up to 5.5 ppt IO at the Kerguelen Islands (France) in the Indian Ocean, but the concentrations stayed mostly below the detection limit. Hönninger (2002) report only upper limits of 0.8 ppt from Crete (Greece), and Schwärzle (2005) concentrations of up to 0.9 ppt from a mangrove forest on the shore of the Atlantic close to Alcantara (Brazil). In Dagebüll (Germany) in spring 2002, Peters et al. (2005) observed up to 1.9 ppt IO. They described the presence of some pools containing kelp, but those were not directly un-

derneath the light path. The location of these measurements is very close to the site List on the island Sylt where measurements have been performed in the frame of this study (see section 5.1). Cape Grim on Tasmania (Australia) is also rather a place to study oceanic background conditions. Although the brown seaweed *Durvillaea potatorum* is present in the intertidal zone at this site, this species does not seem to emit iodine compounds in large amounts when exposed to oxidative stress (Caine et al., 2007). Observed mixing ratios were about half a ppt (Caine et al., 2007; Allan et al., 2000).

**Table 9 Overview of observations of IO and the maximum observed mixing ratios.**

Location	Maximum mixing ratio [ppt]	Technique	Reference
Mace Head, Ireland	6	LP-DOAS	Alicke et al. (1999)
Mace Head	3	LP-DOAS	Allan et al. (2000)
Mace Head	7	LP-DOAS	Saiz-Lopez and Plane (2004b)
Brittany, France	8	LP-DOAS	Peters et al. (2005)
Brittany	10	LP-DOAS	A. S. Mahajan, pers. comm. (2008)
Brittany	28	laser induced fluorescence	Whalley et al. (2007)
Brittany	54	cavity ring-down spectroscopy	Wada et al. (2007)
Appledore Island, USA	4	LP-DOAS	Stutz et al. (2007)
Tenerife, Spain	3.5	LP-DOAS	Allan et al. (2000)
Dagebüll, Germany	1.9	LP-DOAS	Peters et al. (2005)
Cape Grim, Australia	0.3	LP-DOAS	Allan et al. (2000)
Cape Grim	0.5	LP-DOAS	Caine et al. (2007)
Kerguelen Islands, France	5.5	LP-DOAS	Sebastian (2004)
Sao Vicente, Cape Verde	1.4	LP-DOAS	Read et al. (2008)
Alcantara, Brasil	0.9	LP-DOAS	Schwärzle (2005)

**Table 10 Overview of observations of IO continued from Table 9.**

Location	Maximum mixing ratio [ppt]	Technique	Reference
Ny-Ålesund, Svalbard	na	zenith-sky DOAS	Wittrock et al. (2000)
Alert, Canada	0.8	MAX-DOAS	Hönninger (2002)
Kuujjuarapik, Canada	3	LP-DOAS	A. S. Mahajan, University of Leeds, pers. comm. (2008)
Neumayer Station, Antarctica	5-10	zenith-sky DOAS	Frieß et al. (2001)
Halley Station, Antarctica	20	LP-DOAS	Saiz-Lopez et al. (2007b)
Ross Island, Antarctica	1-2	MAX-DOAS	K. Kreher, NIWA, pers. comm. (2008)
global	na	satellite DOAS	Schönhardt et al. (2008)
southern hemisphere	na	satellite DOAS	Saiz-Lopez et al. (2007a)

Measurements of reactive iodine in polar regions are even less numerous: Tucker-mann et al. (1997) performed longpath DOAS measurements in Ny-Ålesund (Svalbard), but could not observe IO above the detection limit of a few ppt. First positive detection of IO in the polar boundary layer was reported by Wittrock et al. (2000) for Ny-Ålesund. Over four years, Wittrock et al. (2000) did measure tropospheric IO on individual days from spring to autumn (no data in wintertime) with a zenith-sky DOAS instrument. The enhanced dSCDs of IO did not correlate with observed BrO events. In the study presented here, the IO measurements from the same site, but with a MAX-telescope are continued and results are discussed in section 5.2. MAX-DOAS measurements at Alert (Canada) resulted in IO dSCDs of up to  $2 \times 10^{13}$  molecules/cm<sup>2</sup> for a 5° elevation angle on a few occasions. But, the IO was mostly below the detection limit during the 9 days of measurements (Hönninger, 2002). For Kuujjuarapik (Canada) located at the southern Hudson Bay, Hönninger et al. (2004) stated only detection limits averaging to 1.3 ppt for IO and Peters (2005) 2.1 ppt with a LP-DOAS. During a campaign at Kuujjuarapik in spring 2008, IO was measured in

concentrations of up to 3 ppt on two out of eleven days (A. S. Mahajan, University of Leeds, personal communication, 2008).

On the other hand in Antarctica, high concentrations of IO have been observed: Frieß et al. (2001) reported the first Antarctic observations of IO using zenith-sky passive DOAS. Model simulations of the radiative transfer indicated that the IO is situated in the boundary layer and maximum mixing ratios of 5 to 10 ppt could be inferred for the summertime. Year-round measurements of IO with longpath-DOAS showing a maximum in spring of up to 20 ppt and a secondary maximum in autumn of up to 6.5 ppt were performed by Saiz-Lopez et al. (2007b). Also global observations of IO by the SCIAMACHY instrument reveal these high concentrations in Antarctica (Schönhardt et al., 2008; Saiz-Lopez et al., 2007a). Schönhardt et al. (2008) confirmed the annual cycle of IO observed by Saiz-Lopez et al. (2007b) at Halley Bay, Antarctica. However, up to now, the existing satellite instruments lack the ability to detect small concentrations above oceanic surfaces. Global maps show some specks of enhanced IO in some regions over the oceans. But these concentrations are below the detection limit of the SCIAMACHY instrument (Schönhardt et al., 2008).

An overview of the IO measurements up to date is given in Table 9 and Table 10. An exception to the measurements described so far and only mentioned for completeness, is the observation of IO at the Dead Sea (Israel) most likely coming from inorganic sources (Zingler and Platt, 2005).

Observations of other reactive iodine species include OIO at Cape Grim (Allan et al., 2001) and Appledore Island (Stutz et al., 2007), OIO and I<sub>2</sub> at Mace Head (Saiz-Lopez and Plane, 2004b; Peters et al., 2005), I<sub>2</sub> in California (USA) (Finley and Saltzman, 2008), molecular and atomic iodine as well as the total photolabile iodine content using a resonance fluorescence technique again at Mace Head (Bale et al., 2008) as well as OIO and I<sub>2</sub> at Roscoff (A.S. Mahajan, personal communication, 2008).

Looking at bromine radical sources besides volcanoes (Bobrowski et al., 2003), salt lakes (Hebestreit et al., 1999), or the BrO explosion in polar regions (e.g. Hausmann and Platt, 1994; Kreher et al., 1997; Richter et al., 1998), models predict BrO background concentrations of 1 to 4 ppt from acid-catalysed activation of bromine from sea-salt aerosol (Vogt et al., 1996; von Glasow et al., 2002) (see also section 2.3.3). Only few positive detections of BrO in the marine boundary have been reported so

far though: Leser et al. (2003) observed BrO of about  $2.4 \pm 2.1$  ppt north of the Canary Islands but otherwise, the BrO stayed below the limit of detection of 1 to 3.6 ppt on a cruise from Germany to South Africa. Around the Cape Verde Islands, on average, similar daytime levels of  $2.5 \pm 1.1$  ppt could be observed year round (Read et al., 2008). Theys et al. (2007) report BrO in the free troposphere above the island La Réunion (France) in the Indian Ocean but only an upper limit of 0.5 ppt in the boundary layer using the MAX-DOAS technique. Up to 6.5 ppt BrO with average concentrations of 2 ppt during the day but below the detection limit during night-time have been observed at Mace Head (Saiz-Lopez et al., 2004). Hönninger (2002) states an upper limit of 1.5 ppt BrO for measurements carried out on Crete (Greece) and Müller-de Vries (2004) found the BrO mainly below the limit of detection of 1.4 ppt and only a few data points reached concentrations of up to 2 ppt on the Kerguelen Islands in the Indian Ocean. Peters (2005) stated 1.5 to 2 ppt as upper limit for BrO in Lilia, Brittany. However, some data points show larger concentrations of up to 4 ppt. Peters (2005) could not find any correlation with tidal height, solar radiation or brominated hydrocarbons. Similar results could be found at Roscoff and suggest a possible anthropogenic bromine source (A. S. Mahajan, pers. comm., 2008).

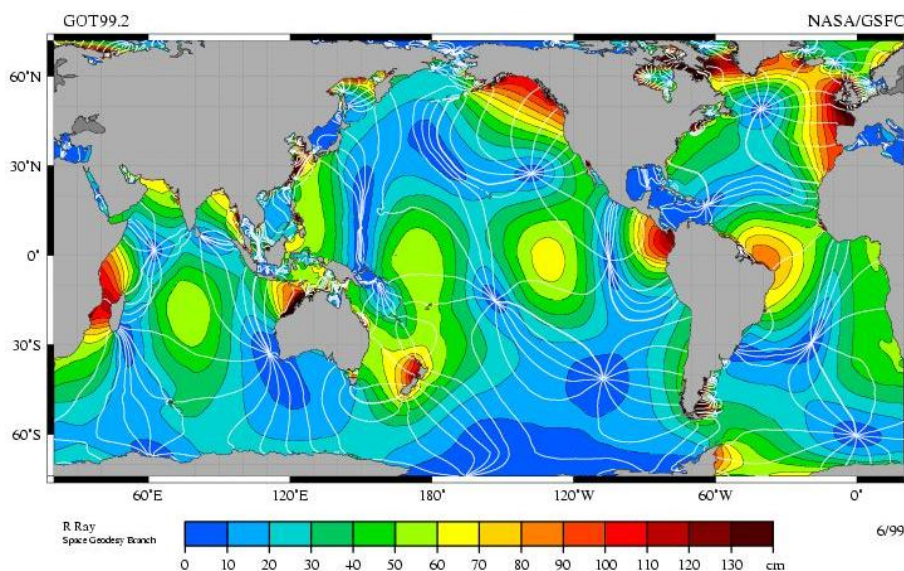


Figure 5-1 Amplitude of the modelled moon tide ([http://svs.gsfc.nasa.gov/stories/topex\\_tides.html](http://svs.gsfc.nasa.gov/stories/topex_tides.html)), Dr. Richard Ray, Space Geodesy branch, NASA, GSFC)

Iodine can have significant impact on the atmosphere through destroying ozone, oxidising DMS, and initialising particle bursts (see section 2.3.2). Especially, the west

coast of Ireland and Brittany are hotspots for iodine chemistry. This is caused by a combination of the right species of macroalgae, i.e. mainly *laminaria digitatis* and *laminaria saccharina*, with some of the largest variations in tidal height in the world (see Figure 5-1). These high concentrations can be explained by the direct emission of  $I_2$  from the macroalgae under stress with only some minor contributions of volatile organoiodines (Saiz-Lopez and Plane, 2004b). Basically, all studies at these locations are in agreement that IO peaks with low tide and depends during daytime more or less on the solar radiation, i.e. concentrations are highest when low tide coincides with noontime. During night-time the nitrate radical chemistry produces iodine monoxide again peaking with low tide.

Table 9 and Table 10 summarise the observations of IO carried out so far. However, rather than giving a comprehensive overview, the table states our scattered knowledge on the global distribution. Furthermore, mainly longpath-instruments have been used to study tropospheric halogen chemistry. But although the LP-DAOS has the advantage that it yields concentrations averaged over a certain distance directly and that it can also measure during night-time due to the artificial light source, this instrument is more difficult to handle than a stand-alone MAX-DOAS. Consequently, the MAX-DOAS is more suitable to study annual trends besides the obvious advantage of having the possibility to retrieve some information on the vertical distribution of a trace gas. Also, in polar regions where a visible range of up to 100 km is possible, the light path in the boundary layer of the MAX-DOAS exceeds the typical path length of about 8 km of a LP-system (e.g. Saiz-Lopez and Plane, 2004a) resulting in a better sensitivity.

The aim of the study presented in this chapter is to add some more measurements or upper limits at sites where rather background IO concentration are expected. Here, MAX-DOAS measurements of IO are presented from five different locations including long-term stations but also from campaigns. Furthermore, estimates for upper limits of BrO are given. The results are presented and discussed in the following sections: section 5.1 describes observations from Sylt (Germany), section 5.2 from Ny-Ålesund (Svalbard), section 5.3 from the Maldives, section 5.4 from Andøya (Norway), and section 5.5 from Crete (Greece). The results are summarised in section 5.6. But first, an overview for the settings for the retrieval of the slant column densities is given in the following.

All five measurement sites are equipped with similar instruments and in the following sections only the differences to the standard set-up as illustrated in section 3.3 are described. The basic settings for the retrievals of IO and BrO dSCDs are presented in Table 11. At some locations, this fitting procedure had to be adjusted to instrumental specifics or the chemical composition, e.g. some sites are more polluted than others and tropospheric NO<sub>2</sub> had to be considered in the fitting procedure. This will be discussed in the corresponding sections. In general, to retrieve the iodine monoxide, the spectral evaluation was performed between 417 and 439 nm with IO (Spietz et al., 2005), NO<sub>2</sub> (Vandaele et al., 1998), ozone (Burrows et al., 1999a), Ring (Vountas et al., 1998) and water (Rothman et al., 1992) cross sections as well as a polynomial of 3<sup>rd</sup> order and an additive linear polynomial, i.e. an additional cross section  $1/I$  is created from the current spectrum  $I$  (Noxon et al., 1979). This so-called stray light correction is not only useful to account for the instrumental stray light, but can also correct insufficiently compensated Ring structures. The spectra were analysed with the time-synchronous zenith spectra or the daily noon zenith spectrum. The water absorption cross section only features a few very minor lines in this region. Including this actually slightly decreases the retrieved IO although not significantly within the error bars, but also decreases the residual of the fit.

**Table 11 General settings for the retrieval of IO and BrO dSCDs**

	IO	BrO
wavelength	417-439 nm	346-359 nm
order of polynomial	3	2
absorbers	IO (Spietz et al., 2005) ozone at 221 K (Burrows et al., 1999a) NO <sub>2</sub> at 220 K (Vandaele et al., 1998) water (Rothman et al., 1992) Ring (Vountas et al., 1998)	BrO (Wilmouth et al., 1999) ozone at 221 K (Burrows et al., 1999a) NO <sub>2</sub> at 220 K (Vandaele et al., 1998) O <sub>4</sub> (Greenblatt et al., 1990) Ring (Vountas et al., 1998)

For the BrO fit, a 2<sup>nd</sup> order polynomial together with the BrO (Wilmouth et al., 1999), ozone (Burrows et al., 1999a), NO<sub>2</sub> (Vandaele et al., 1998), O<sub>4</sub>

(Greenblatt et al., 1990), and Ring (Vountas et al., 1998) cross sections plus the additive linear polynomial are simultaneously fitted to the measured optical density. Errors are usually given as  $2\sigma$ -errors, here the doubled fitting error unless stated otherwise. The limits of detection are calculated from the ratio of the RMS (see equation (3.7)) of the residual to the RMS of the differential cross section (see section 3.4) and then also doubled.

To put the results into context, a spectral fitting has also been performed to simultaneously retrieve  $O_4$  and  $NO_2$  in the same wavelength range from 425 to 485 nm including otherwise water, ozone, and Ring with the same reference cross sections as applied in the IO fit (compare Table 11).

## 5.1 Sylt: Mudflats at the German North Sea coast

Sylt is the northernmost island of the North-Friesian archipelago. It stretches along the coast of Germany and Denmark in the Wadden Sea of the German bight. Measurements were performed at the town List (55.0°N, 8.4°E) from March to August 2004. List is located in the north of the island. The MAX-DOAS instrument was installed in a building about 20 m away from the sea front and the telescope pointed into east-northeast direction towards the Danish coast. The distance to the continent in this direction is about 15 km (see Figure 5-2). At this location, the first half of the seaborne light path passes a deep waterway. Only the terrain under the second half of the path falls completely dry during low tide exposing the mudflats (indicated by grey-shaded areas in the left panel of Figure 5-2). These mudflats are wetlands where silt, clay and to some extent organic material have been deposited by the tides. This substrate does not provide a good anchoring material for seaweed which prefers rocks or other hard surfaces. The town Dagebüll, where Peters et al. (2005) carried out LP-DOAS measurements, is also marked on the map. In the following, the instrument specifics are described.

The wavelength interval of the spectrometer was set to cover 330 to 497 nm with a spectral resolution of 0.7 to 0.8 nm FWHM. For this set-up, continuous scanning with the MAX-telescope was not possible and the available five viewing directions were selected as 2°, 4°, 8° and 30° elevation as well as the zenith. Due to instrumental

problems on certain days, only a limited data set is available: overall about 68 days for the full measurement period. IO dSCDs have been retrieved according to the settings of Table 11. Additionally, an NO<sub>2</sub> cross section measured at 294 K has been included in the fitting procedure to account for pollution. The time-synchronous zenith spectra were applied as background measurement, i.e. the temporally closest zenith spectrum with respect to the time of the off-axis measurement.



**Figure 5-2 Map and satellite photo (from Google Earth) showing a detail of the German Bight. The grey-shaded area in the left panel represents the mudflats. The yellow arrow in the right hand panel indicates the pointing of the telescope for the location on Sylt.**

As the lowest telescope viewing direction is most sensitive to the absorption of tropospheric species, only the IO slant column densities for 2° elevation angle are presented in Figure 5-3. But also, since on many days a hazy layer persisted in the lowest kilometres of the troposphere, the dSCDs for the lowest three off-axis viewing angles often give the same numbers, whereas the 30° elevation angle results in dSCDs very similar to the zenith direction (compare the dSCDs in Figure 5-11 until about 10:00 AM). The data was filtered for IO column densities with errors smaller than  $8 \times 10^{12}$  molecules cm<sup>-2</sup> and a detection limit of  $2.7 \times 10^{12}$  molecules cm<sup>-2</sup> or less. Also, only measurements for SZA smaller than 70° are included. To increase the signal-to-noise ratio, the spectra were averaged for about 1 hour before applying the DOAS fit. This adds up to an accumulative exposure time of about 12 min due to the

cycling through the five different viewing directions. Examples for the quality of the spectral fit are given in Figure 5-4.

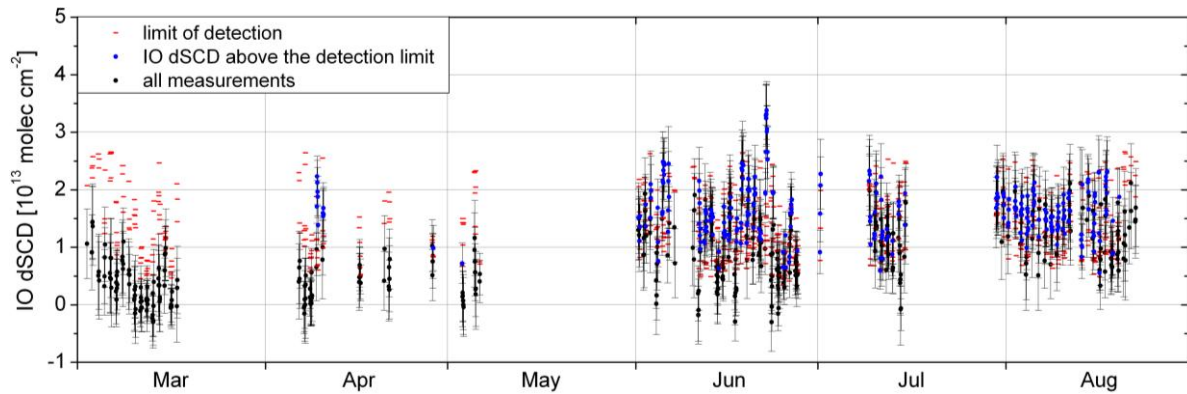


**Figure 5-3 Overview of IO dSCDs from the 6-month-long campaign in List, Sylt. Only results from the 2° elevation angle and SZA < 70° are presented. The data was averaged for 1 hr adding up to a cumulative exposure time of about 12 min for each data point. The data was filtered for errors smaller than  $8 \times 10^{12}$  molecules  $\text{cm}^{-2}$  and a detection limit of  $2.7 \times 10^{12}$  molecules  $\text{cm}^{-2}$ .**

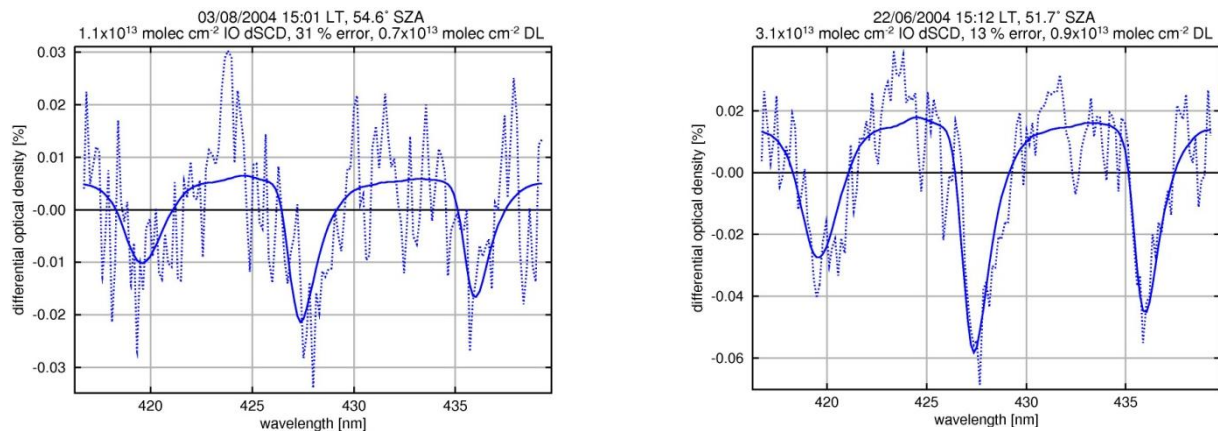


**Figure 5-4 Examples for the quality of the IO fit for List, Sylt: The corresponding differential slant column densities (SC),  $2\sigma$ -errors, and the  $2\sigma$ -detection limits (DL) are stated in the header.**

Maximum slant column densities of  $3.4 \times 10^{13}$  molecules  $\text{cm}^{-2}$  could be detected on 22<sup>nd</sup> June 2004. Most values over the limit of detection were observed during June to August. However, the quality of the data seems to have improved towards the summer in general. There is an indication for a possible seasonal cycle with minimum in spring and maximum in summer. This will be further investigated below.

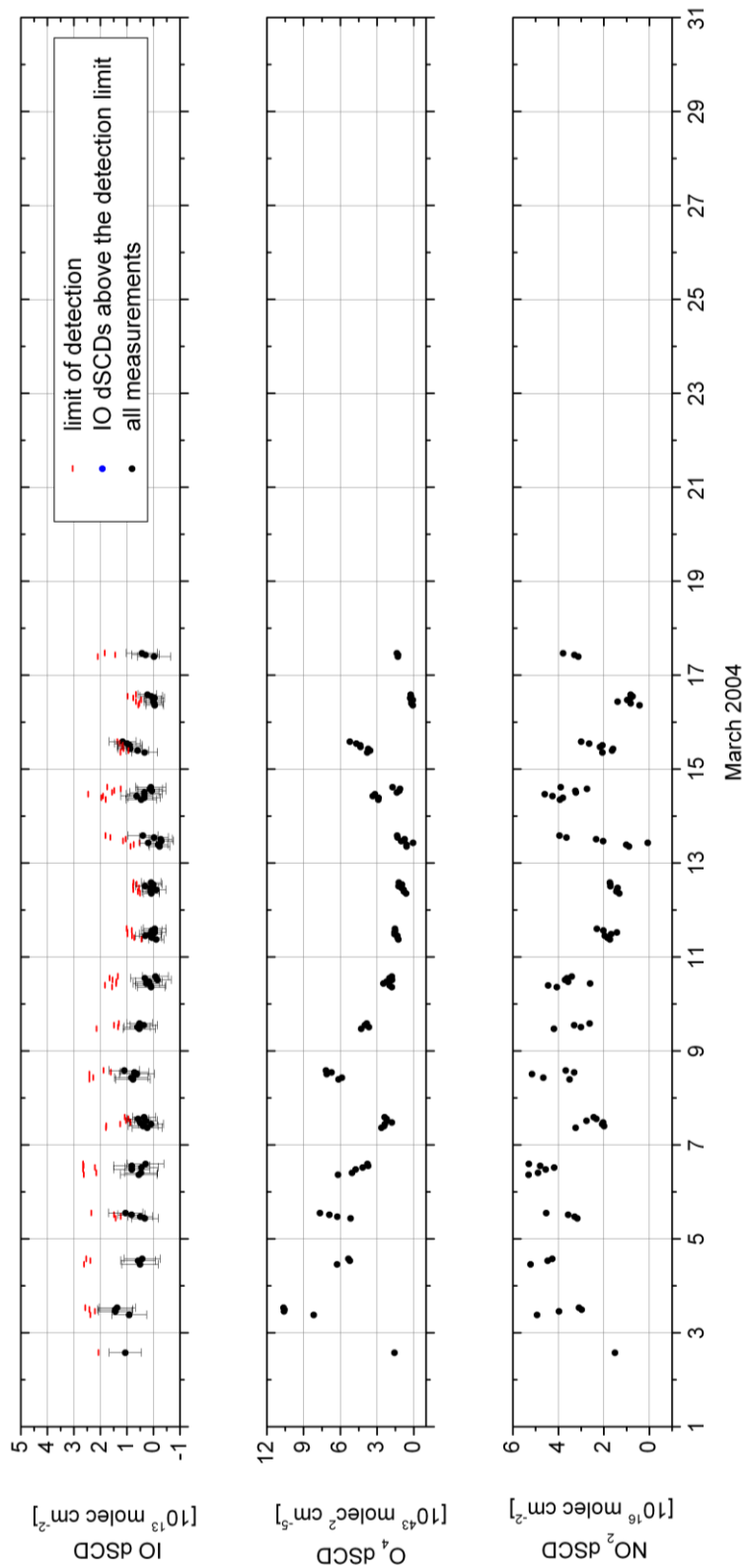


Figure 5-5 March IO, O<sub>4</sub>, and NO<sub>2</sub> off-axis dSCDs for List for the 2° elevation angle analysed with the time-synchronous zenith measurements. Only data for SZA < 70° are shown. Compare also caption of Figure 5-3.

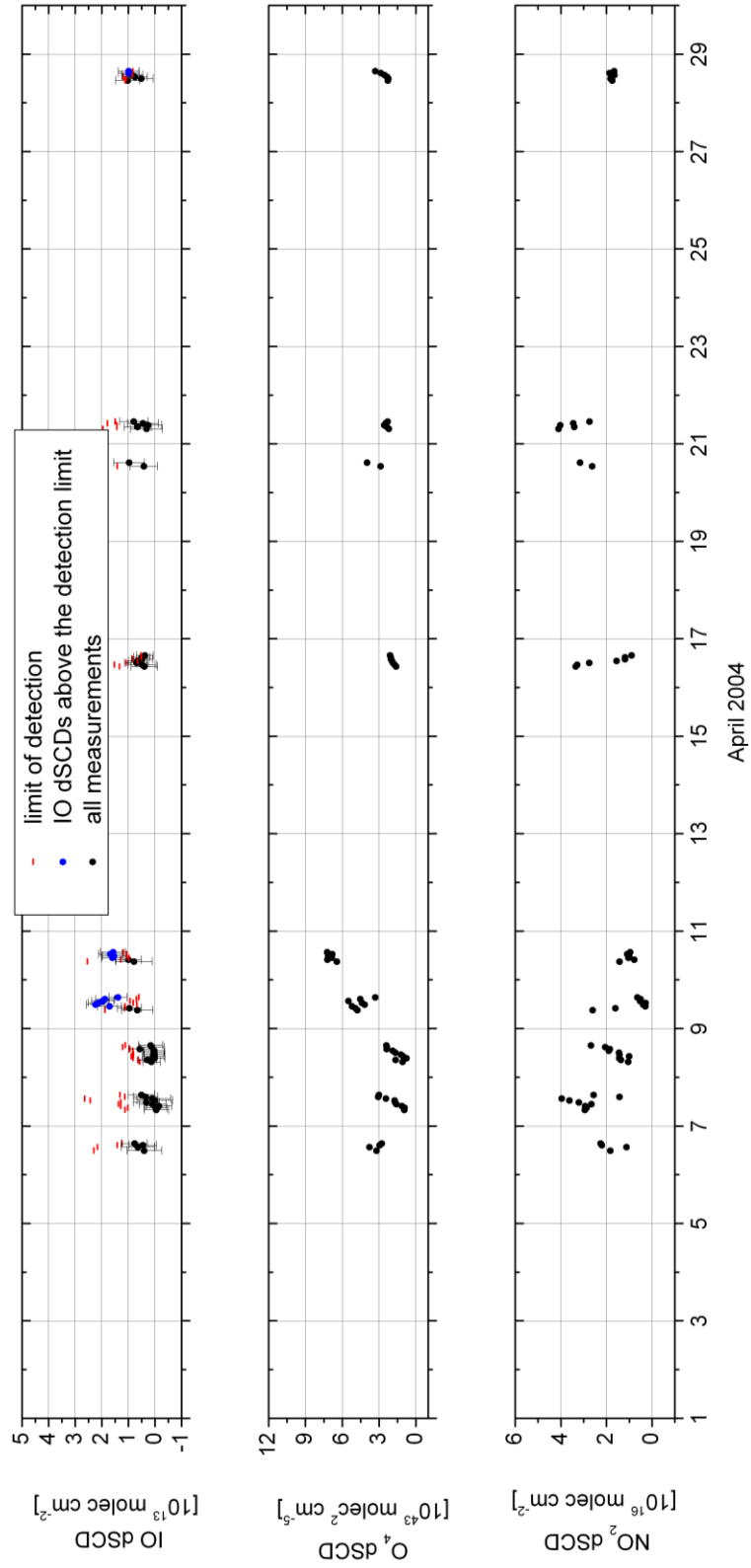


Figure 5-6 Same as Figure 5-5 but for April.

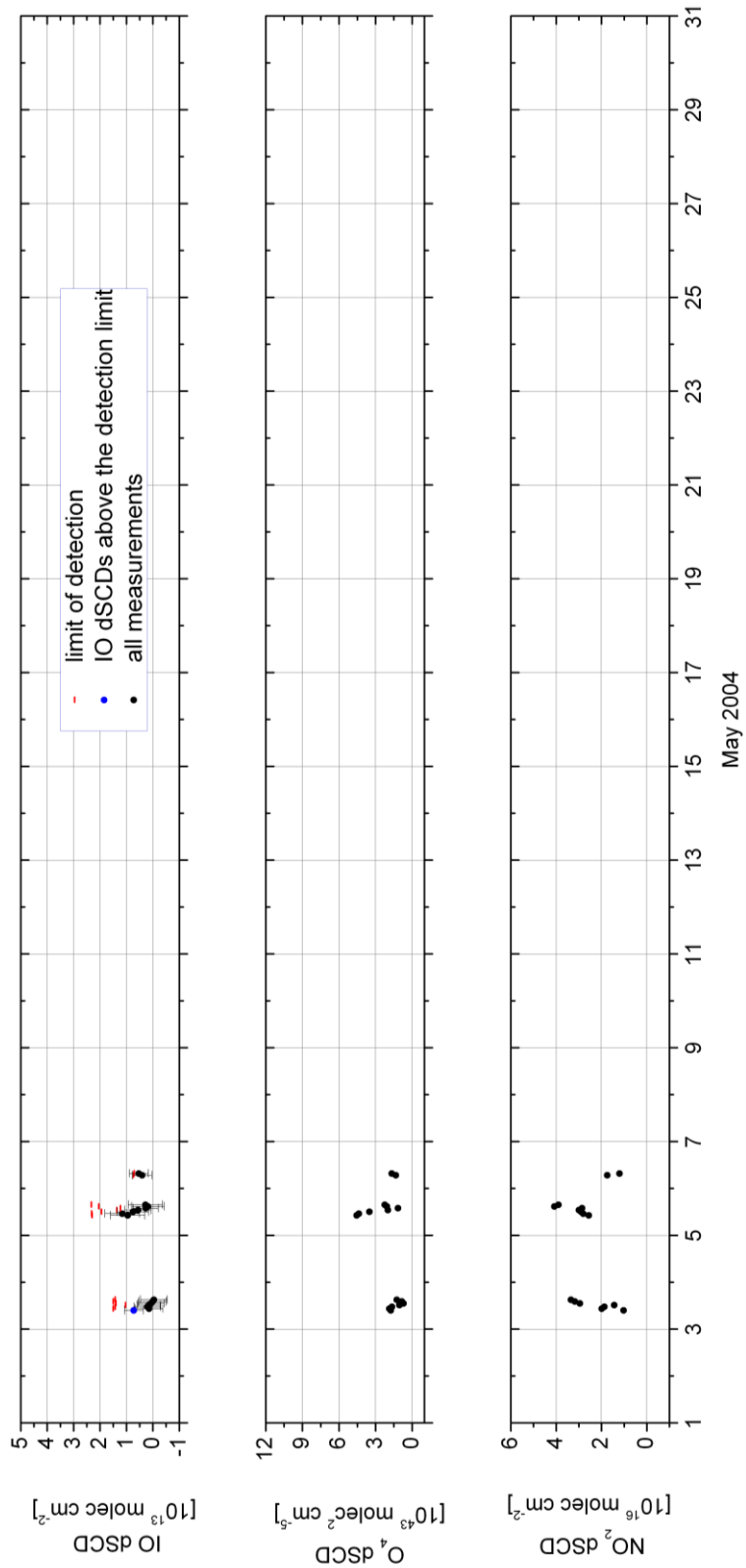


Figure 5-7 Same as Figure 5-5 but for May.

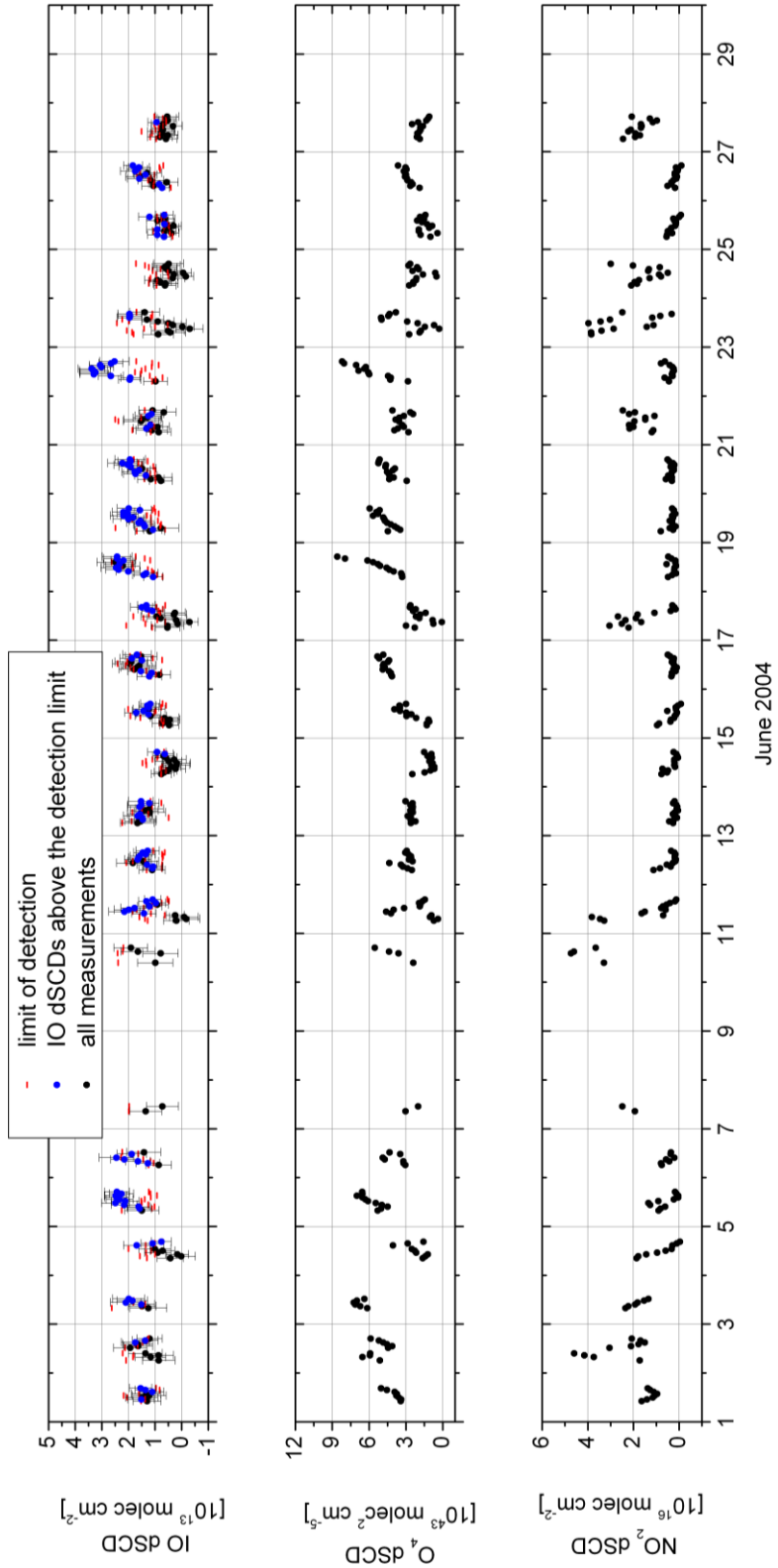


Figure 5-8 Same as Figure 5-5 but for June.

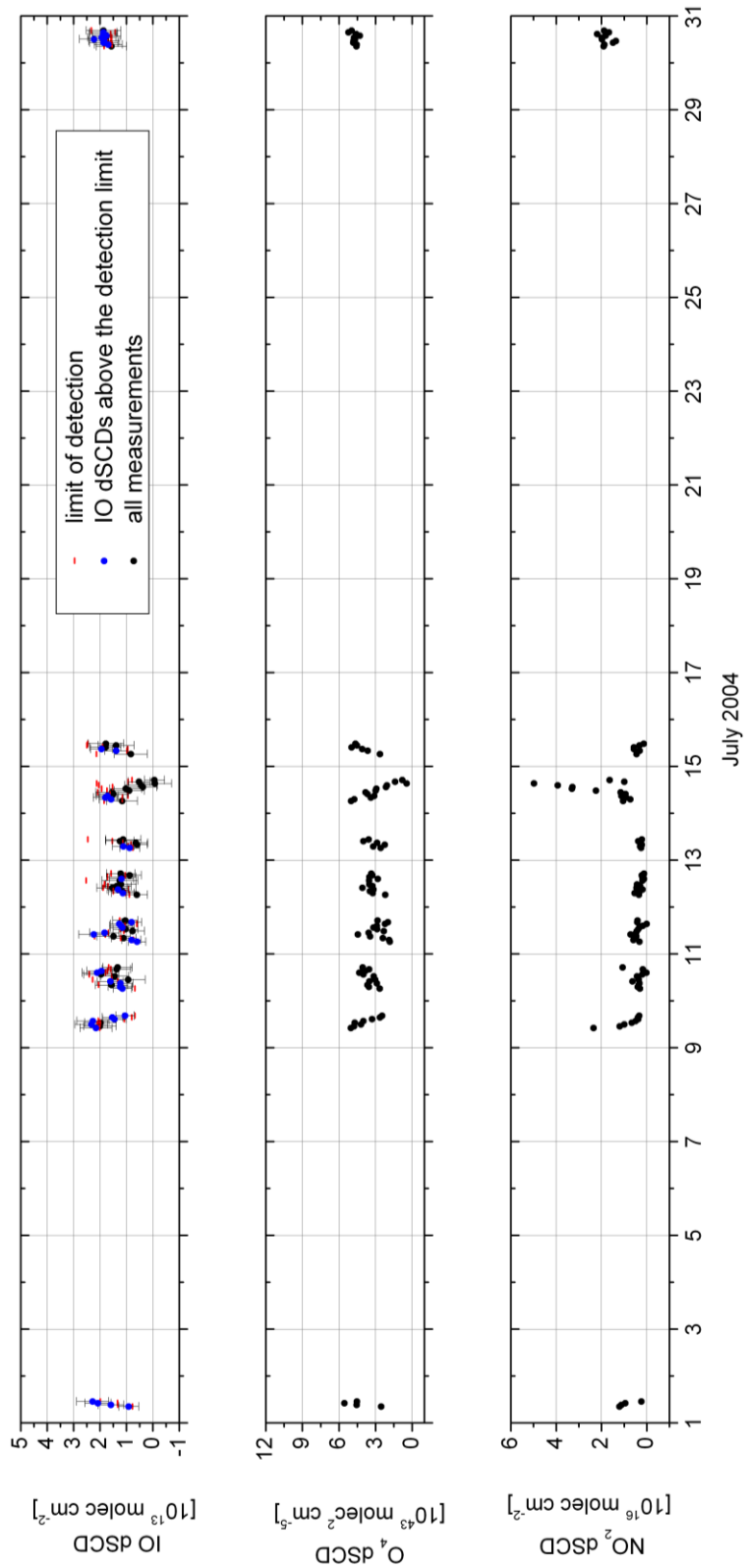


Figure 5-9 Same as Figure 5-5 but for July.

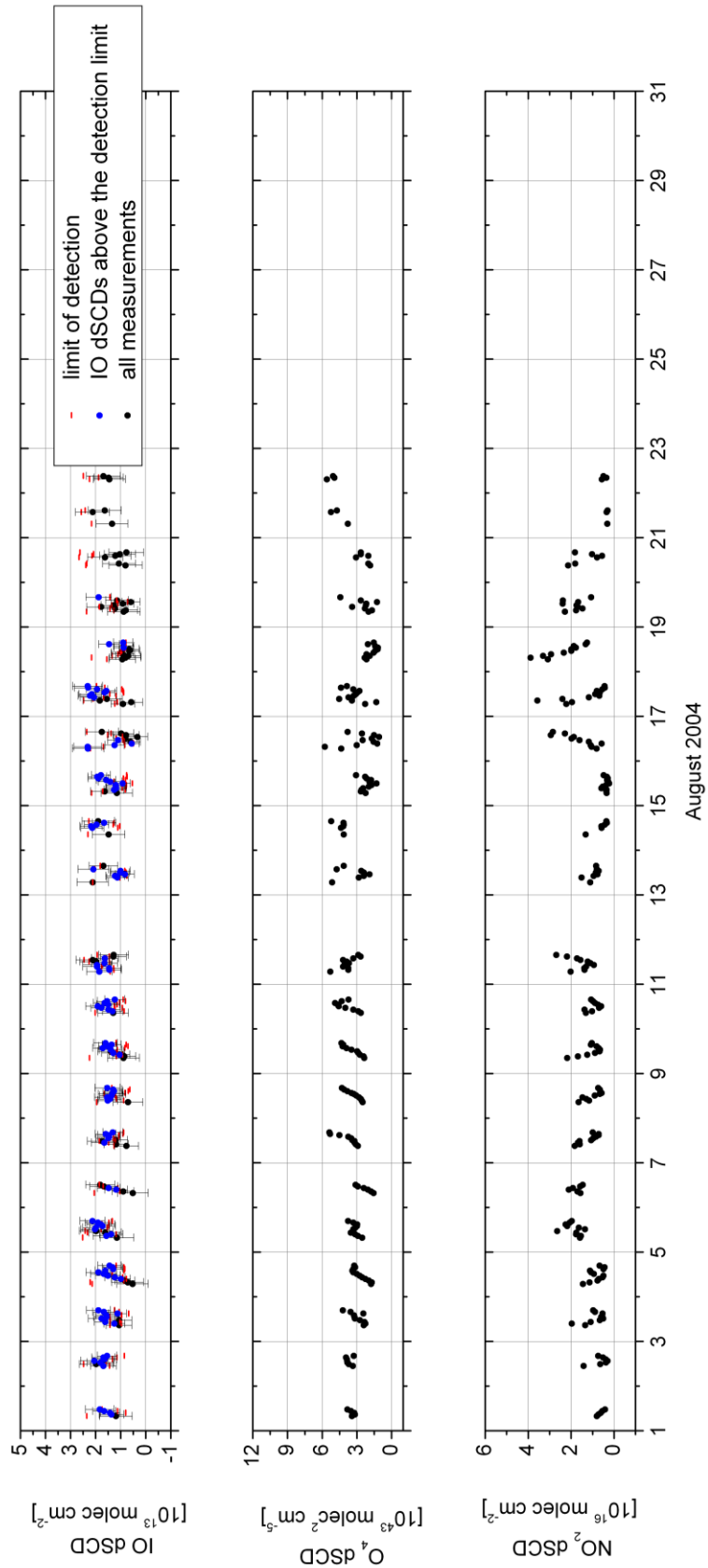
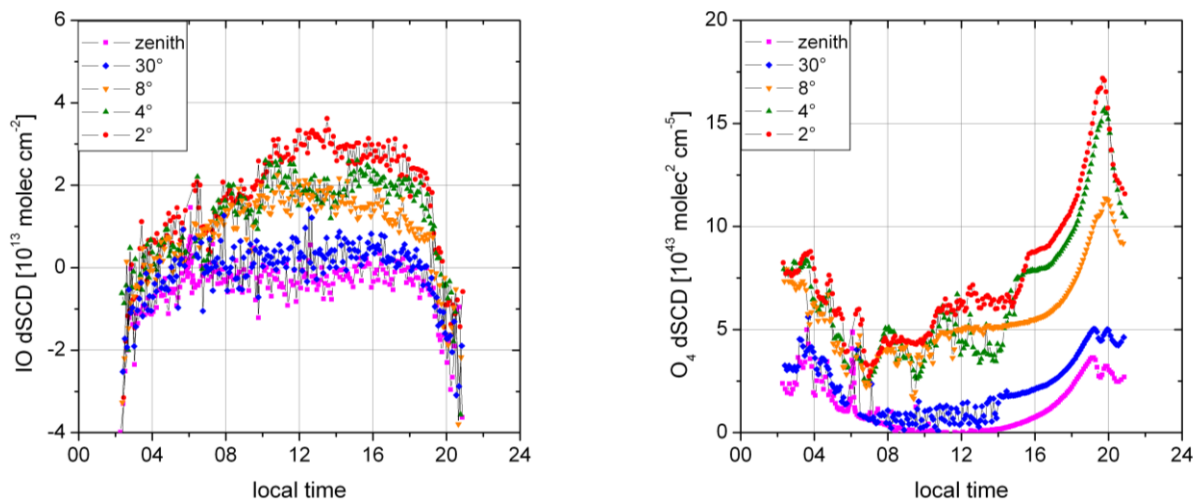


Figure 5-10 Same as Figure 5-5 but for August.

To test whether the variations in the dSCDs are caused by a change in the concentration or in the radiative transfer, also the  $O_4$  slant column densities have been retrieved and the data is presented together with the IO dSCDs in more detail in Figure 5-5 to Figure 5-10.  $NO_2$  is included as well. Here, the  $NO_2$  and  $O_4$   $2^\circ$  dSCDs are also analysed with the synchronised zenith reference. This should result in the removal of the stratospheric absorption for  $NO_2$ .



**Figure 5-11 IO and  $O_4$  dSCDs for List on 22<sup>nd</sup> June. This day shows maximum IO dSCDs during the 6-month campaign. Applying the BREAM profile retrieval to this data yields maximum concentrations of 1.4 ppt IO (compare Figure 5-12).**

On many clear days, the  $O_4$  as well as the IO column densities increase during the course of the day (e.g. 18<sup>th</sup> June). This diurnal profile is caused by the changing solar geometry. In the morning, the relative azimuth is smallest for the eastward-pointing telescope. Since the sun is positioned in the back of the telescope in the afternoon, the angular distribution of the Mie phase function becomes important. Compare also Figure 4-12. On the other hand on other days, e.g. 9<sup>th</sup> July, there is a steep decrease in the morning which is related to a change in aerosol content: The morning hours were extremely clear, but the visibility significantly reduced over the day. The correlation of IO with  $O_4$  and  $NO_2$  is investigated in more detail further below.

As a case study, the profile retrieval BREAM was applied to the data of 22<sup>nd</sup> June, the day with the largest IO column densities. The un-averaged IO and  $O_4$  dSCDs of this day are shown in Figure 5-11. Due to the limited number of viewing directions, the trace of the averaging kernel matrix yields a value of about 1. Consequently, only

the concentrations in the bottom layer, here averaged between 0 and 200 m can be obtained from the retrieval (Figure 5-12). Maximum concentrations of 1.4 ppt IO were found and on average during daytime about 1.2 ppt. However, the error is rather large between 2 and 3 ppt and averaging over a larger height would result in smaller concentrations. The correlation between the measured and modelled  $O_4$  dSCDs varies between 0.85 and 0.95. A diurnal cycle of the IO, as expected from the photochemically driven reaction mechanisms (see section 2.3.2) and from other studies (e.g. Read et al., 2008), can be observed on this day: A rise in the morning, maximum concentrations at noon, and a decrease with the setting sun. However, this pattern cannot be inferred from the diurnal of the IO dSCDs. These seem to be mainly determined by the diurnal pattern of the  $O_4$  dSCDs, i.e. the aerosol optical depth (Figure 5-12, right panel). In the following, correlations studies are presented to test the dependence of the IO dSCDs on several parameters.

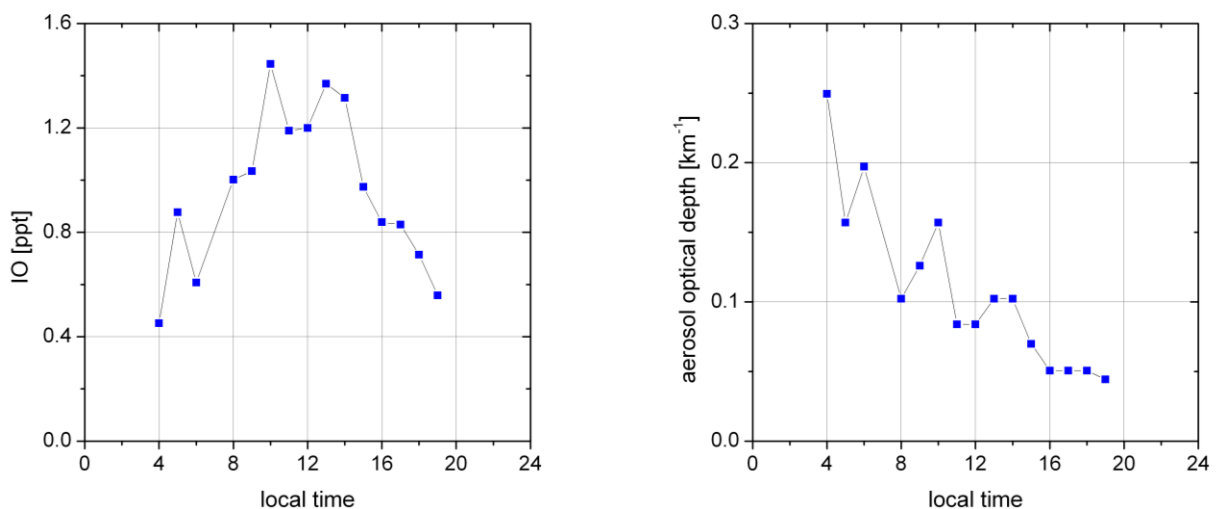


**Figure 5-12 IO volume mixing ratios and aerosol optical depths (AOD) retrieved with BREAM for List on 22<sup>nd</sup> June averaged over 200 m. The corresponding dSCDs of IO and  $O_4$  are presented in Figure 5-11.**

The correlation between the slant column densities of IO and  $O_4$  is obvious (see Figure 5-13a) and the correlation coefficients for 2° and 4° elevation angle are 0.68 and 0.59, respectively. This confirms that these two absorbers have similar profiles as well as little temporal variations since the concentration is mainly determined by the visibility in the boundary layer. Here, the raw data is used with integration times of 1 min only.

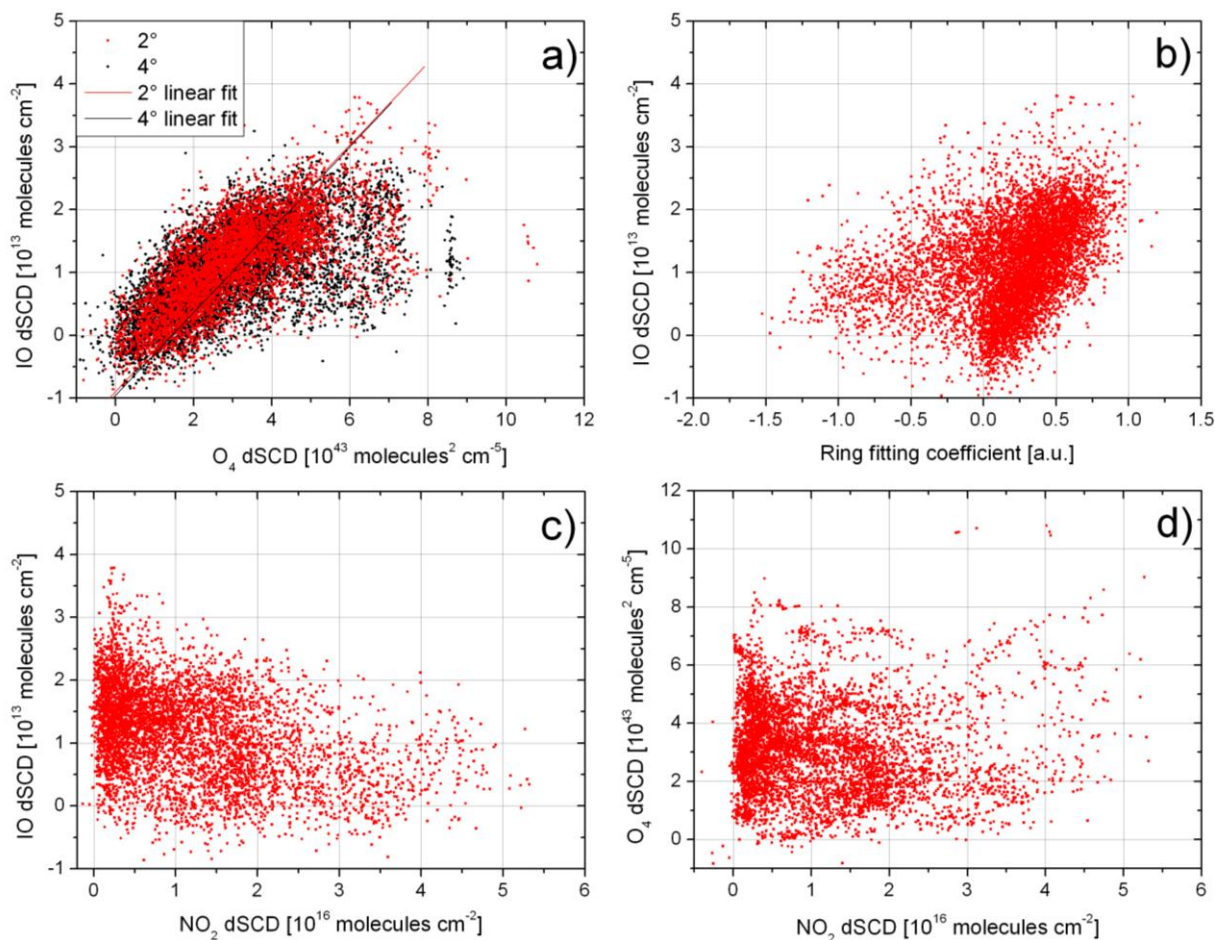


**Figure 5-13 a) – c) Correlation plots for IO with Ring, O<sub>4</sub> as well as NO<sub>2</sub>; d) Correlation plot for O<sub>4</sub> and NO<sub>2</sub> for List.**

In contrast to the IO dSCDs, tropospheric NO<sub>2</sub> does not correlate with the visibility, i.e. O<sub>4</sub> (correlation coefficient:  $-0.04$ , see Figure 5-13d). This is expected for a trace gas with highly variable concentrations in the troposphere. There is only a weak relation between the concentrations of NO<sub>2</sub> and IO although very high IO is associated with low NO<sub>2</sub> and high NO<sub>2</sub> with IO below the detection limit whereas the reverse statements are not true (Correlation coefficient:  $-0.37$ , Figure 5-13c).

It is always a risk for IO retrievals that some of the Ring spectral features are assigned to IO (e.g. Schönhardt et al., 2008). This effect is difficult to quantify since similarities in the diurnal pattern are expected. However here, the Ring correlation plot shows two regimes (Figure 5-13b): When it is very clear, the fitting coefficient can become negative for small azimuth angles in the morning resulting in a highly asymmetric diurnal pattern. This could not be observed for the IO dSCDs. Otherwise, the diurnal profile of IO and Ring look quite similar. Though with a correlation coeffi-

cient of 0.35 and considering the quality of the spectral fit for all three considered absorption lines in the selected wavelength window (see Figure 5-4), an influence of the Ring cross section seems to be highly unlikely.

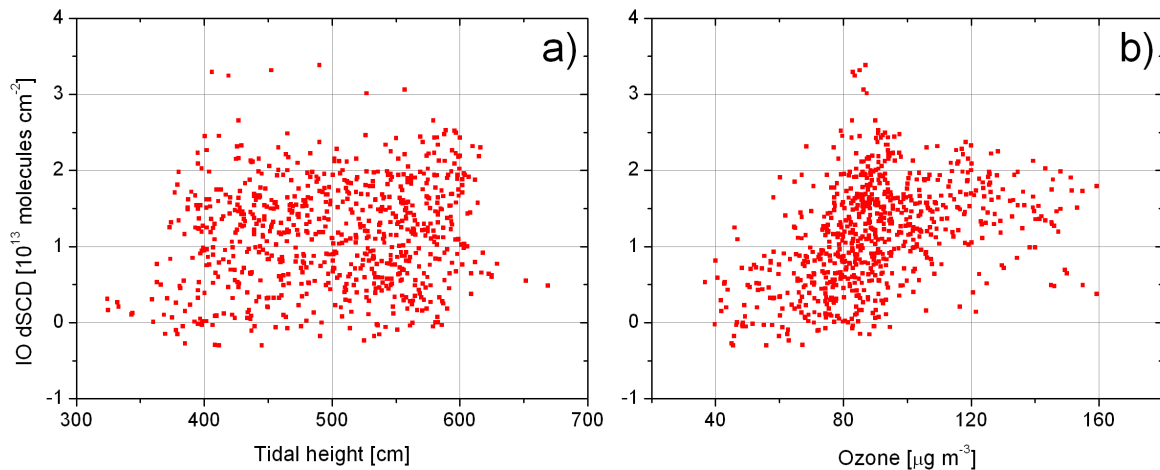


**Figure 5-14 Correlation plot for IO dSCDs with the tidal height (a) as well as ozone (b) for List.**

For the following comparisons (Figure 5-14, Figure 5-15, Table 12), the hourly averaged IO data as in Figure 5-3 was applied. The radiation, tidal height, as well as the ozone data was interpolated to the IO time axis. Ozone and radiation were measured in Westerland and Tinnum, respectively. Both towns are located about 12 km to the south of List. The radiation is a measure for the UV radiation harmful for living organism. Here, it is assumed to be linearly correlated to the overall radiation in the atmosphere. The tidal height was recorded in List itself.

There is no negative correlation of the IO dSCDs with low tide (see Figure 5-14a). This finding backs up the argument that List indeed can be treated as a site representing marine background conditions and is not influenced by direct emissions of  $I_2$  from macroalgae. Contrary, there is a very weak positive correlation of IO with the tidal height of 0.15. This seems to be not quite significant. However, the correlation coefficients of factors which are without doubt unrelated to the tides like ozone, radiation, or  $O_4$  are all about a factor two smaller or even less than that (see Table 12). This slightly positive correlation suggests that the sea close to the light path acts as a weak source of the observed enhanced IO.

**Table 12 Correlation coefficients for the data from List. All data sets have been interpolated to the time axis of the hourly averaged IO as in Figure 5-3. The radiation and ozone concentrations were measured about 12 km to the south of the MAX-DOAS site. The tidal height was recorded in List itself. Note that the correlation coefficient for IO with O<sub>4</sub> is slightly different from the number stated above, i.e. 0.68, since this number here is valid for the averaged data.**

	IO dSCD	Radiation	Tidal height	O <sub>4</sub> dSCD	O <sub>3</sub> concentration
IO dSCD	1	0.61 Figure 5-15a	0.15 Figure 5-14a	0.66	0.41 Figure 5-14b
Radiation	0.61	1	0.08	0.31 Figure 5-15b	0.47 Figure 5-15c
Tidal height	0.15	0.08	1	0.06	0.05
O <sub>4</sub> dSCD	0.66	0.31	0.06	1	0.23
O <sub>3</sub> concentration	0.41	0.47	0.05	0.23	1

Comparing the IO dSCDs with the ozone concentrations yields a positive correlation (Figure 5-14c). At first, this seems to be rather surprising. However, ozone has a similar annual variation as observed for the IO: Maximum in summer and minimum in winter. Although the IO might be a rather wide-spread phenomenon in the horizontal, it might be confined to a very shallow layer close to the surface and it is not necessarily expected to observe a drop in the ozone concentrations for high IO as ozone is rapidly replenished from above. However for the interpretation of this result, it has to be kept in mind that ozone is actually measured about 12 km away from the site of the MAX-DOAS.

Figure 5-15a and b show the correlations of IO and O<sub>4</sub> dSCDs with the radiation. The correlation coefficients of 0.61 for IO but only 0.31 for O<sub>4</sub> show that the enhanced IO slant column densities are not only related to a ‘good weather’ effect, i.e. whenever the visibility is good, there is a positive signal in IO. Also the ozone shows a much weaker correlation of 0.47. Figure 5-15d illustrates the seasonal cycle of the radiation

during the six month of measurements from March to August which resembles the seasonal cycle of the observed IO dSCDs (Figure 5-3).

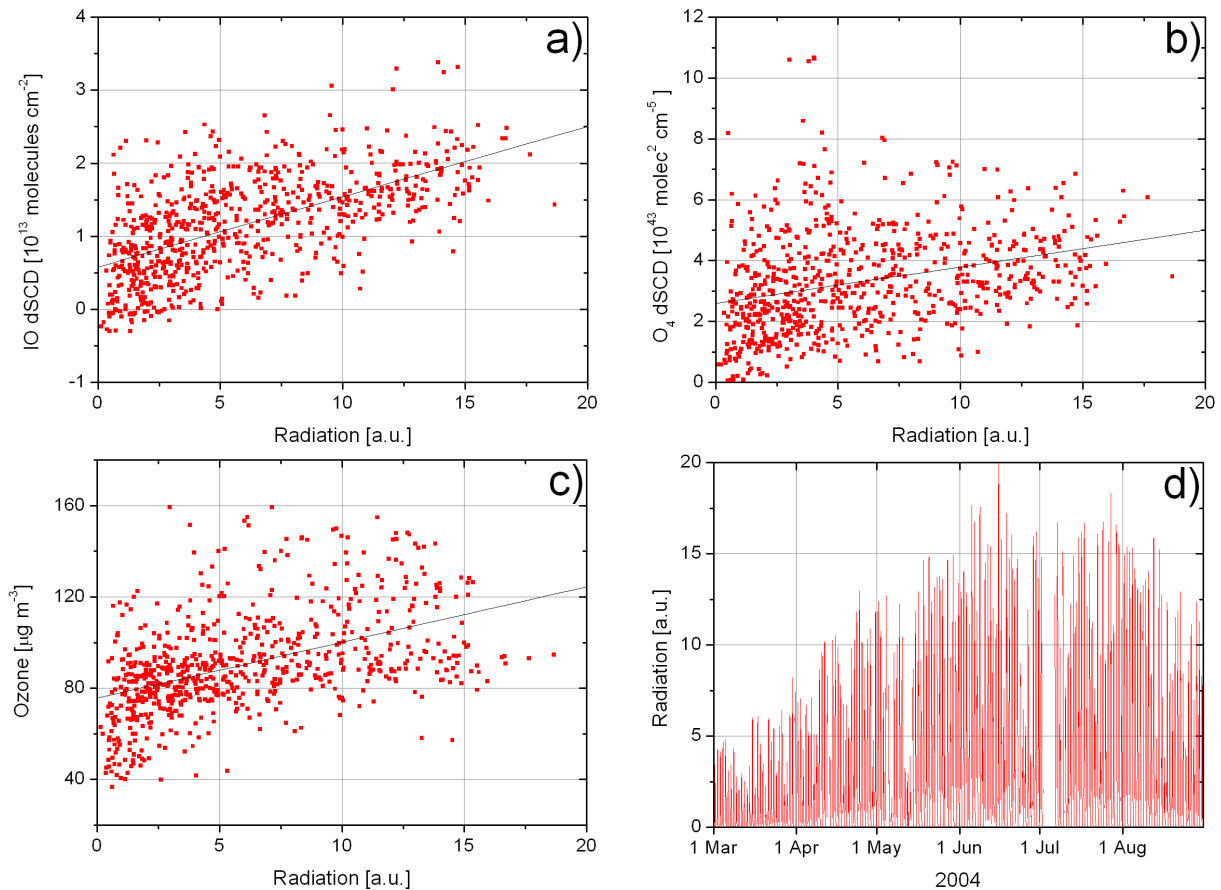


**Figure 5-15 a)-c) Correlation plots for the  $2^\circ$  IO dSCDs,  $2^\circ$   $\text{O}_4$  dSCDs, as well as ozone concentrations with radiation; d) time series for the radiation.**

Furthermore, a wind sector analysis has been performed. Although only daily measurements are available from the meteorological station in List, large diurnal variations could not be observed in the IO data on many days anyways. Hence it is acceptable to perform a binning of a full day for the IO data, here again for SZAs less than  $70^\circ$ . Overall, 82 data points from different days could be compared (see Figure 5-16). The concentrations seem to be lowest when the wind is blowing towards the telescope (wind direction of  $45^\circ$ , see Figure 5-16a). This is also the direction pointing towards the land (see Figure 5-2), but there are only three data points (see also Figure 5-16b) and also air masses coming from the east (wind direction  $90^\circ$ ) have travelled a comparatively short distance over the water. Largest values are observed for north-westerly winds. This is the only direction in the wind rose which is pointing towards

the open ocean and being least obstructed by the island's topography itself. However overall, there is no clear correlation for IO with wind direction or wind speed.

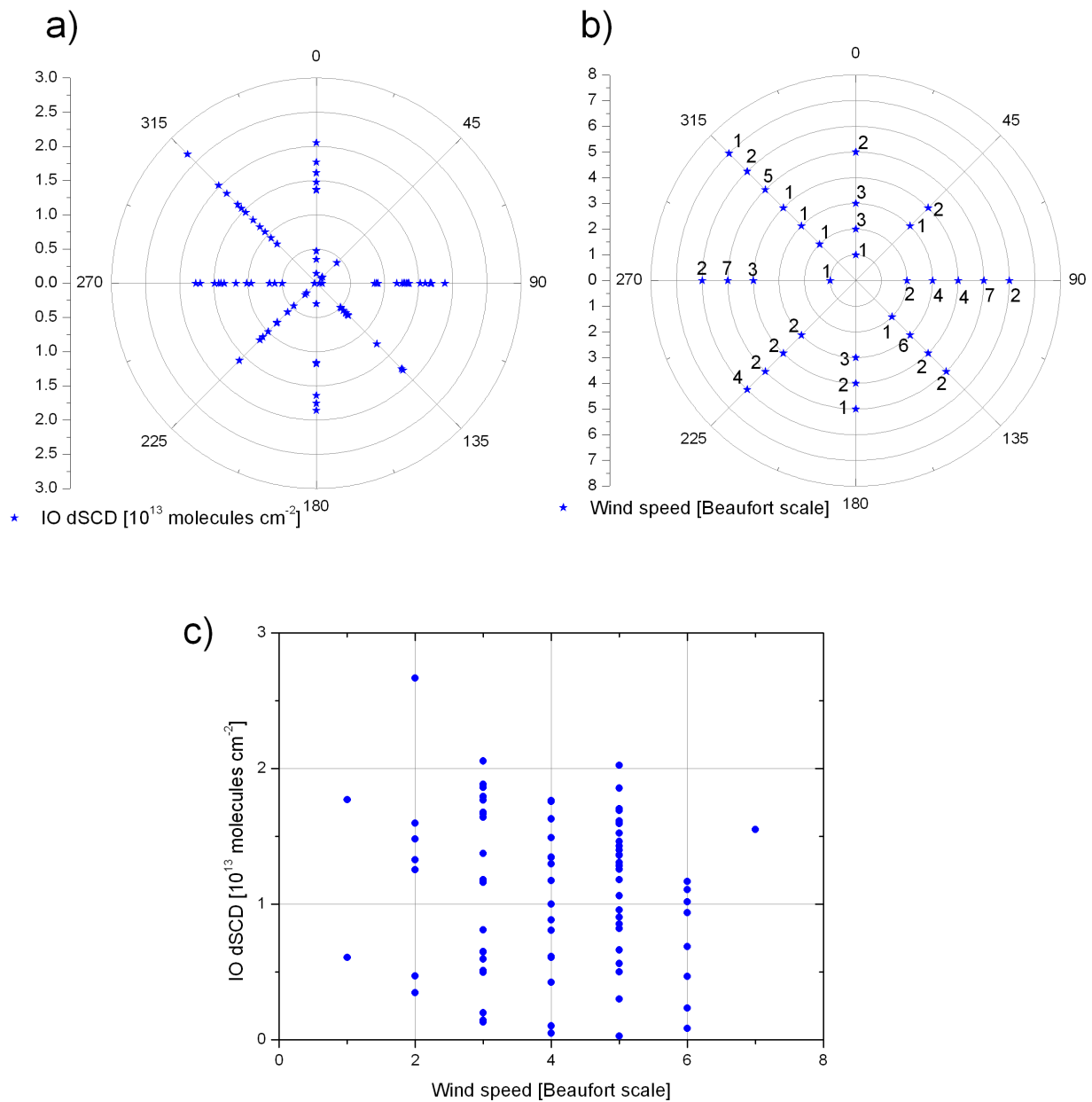


**Figure 5-16** a) Wind sector analysis for the IO slant column densities; b) wind rose with numbers indicating the number of days per data point; c) correlation plot for IO with wind speed.

In summary, the 2° IO dSCDs are predominantly determined by the visibility and a scaling of the column densities to volume mixing ratios can be performed after a normalisation by the O<sub>4</sub> dSCDs. In practice, the hourly averaged IO dSCDs for the six months of data have been divided by the corresponding O<sub>4</sub> dSCDs to remove the trend caused by the change in the radiative transfer. After that, the obtained diurnal

profile for 22<sup>nd</sup> June was plotted against the concentrations calculated by BREAM for that day (see Figure 5-12). A correlation coefficient of 0.89 could be obtained. The retrieved slope and offset were then applied to convert the full data set into mixing ratios. The data is presented in Figure 5-17. The dynamic range of only 0.6 ppt on 22<sup>nd</sup> June (for SZA < 70°) introduces large uncertainties though and the errors in the offset as well as the slope have been used to perform an error propagation for the VMRs. The errors of the mixing ratios retrieved with BREAM as well as the errors of the dSCDs for IO and O<sub>4</sub> have not been considered. On average during the summer months, about 1 ppt IO could be retrieved and the seasonality, as already observed in the dSCDs, is more emphasised. However this result should be interpreted with caution since a systematic error in the slope of the interpolation would cause an enhanced seasonal cycle. Individual outliers are produced when a small IO dSCD is divided by a small O<sub>4</sub> dSCD introducing large uncertainties.

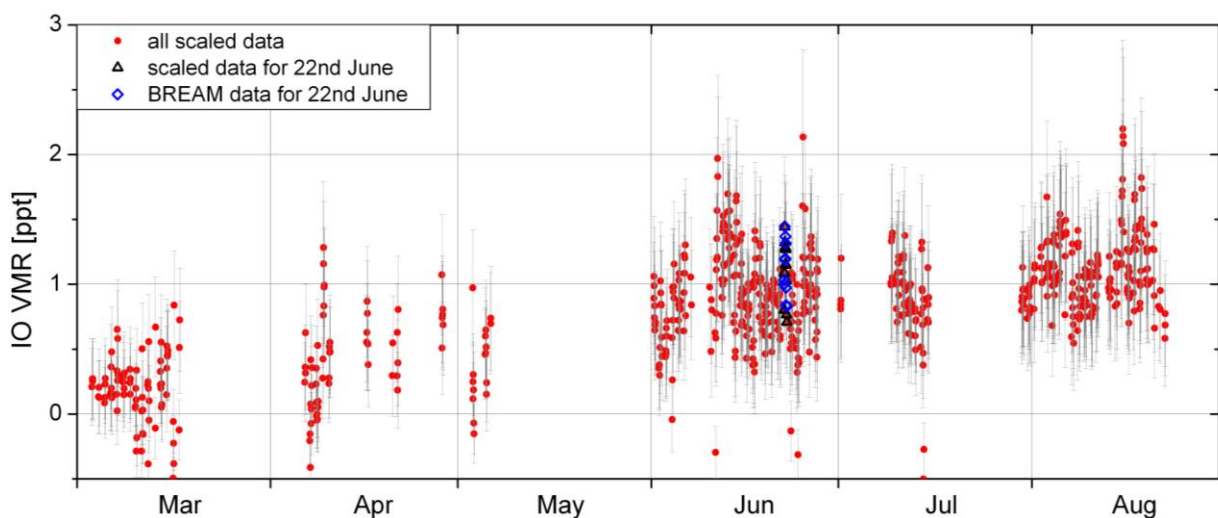


**Figure 5-17 Time series of IO mixing ratios for List. This data was obtained by normalising the IO dSCDs to the O<sub>4</sub> dSCDs and then correlating the result to the BREAM IO VMRs for 22<sup>nd</sup> June (see Figure 5-12). A correlation coefficient of 0.89 was retrieved and the calculated slope and offset are used to scale the full data set of IO as in Figure 5-3. The error bars are calculated from the error of the slope and offset only and do not consider the errors of the dSCDs or the profile retrieval. The normalisation can introduce large errors when for a low visibility two small numbers are divided by each other hence some outliers. The scaled IO data for 22<sup>nd</sup> June is highlighted in black and the VMRs retrieved with BREAM (for SZAs < 70° only) are included as well. The limit of detection will only be scaled as well and ranges between 0.5 and 2.5 ppt.**

The instrument was optimised for measuring IO. But, also BrO possesses spectral features in the set wavelength range. For BrO, only upper limits could be retrieved. The  $2\sigma$  detection limit for the zenith direction for SZA smaller than  $60^\circ$  is about  $5 \times 10^{13}$  molecules  $\text{cm}^{-2}$  and about twice as much for the  $2^\circ$  viewing geometry. Simulating the  $\text{O}_4$  dSCDs for  $2^\circ$  elevation of  $6 \times 10^{43}$  molecules<sup>2</sup>  $\text{cm}^{-5}$  first and applying the retrieved aerosol extinction profile to calculate BrO AMF for the given geometry (compare section 4.3), this number translates to a volume mixing ratio of 2.8 ppt for a 500 m thick well-mixed layer on a clear day or twice as much for the  $2^\circ$  DL. It should be noted that normally the zenith dSCDs have smaller detection limits due to smaller Ring structures in comparison to off-axis directions.

## 5.2 Svalbard: Fjord in the Arctic at Ny-Ålesund

In Ny-Ålesund ( $78.9^\circ\text{N}$ ,  $11.9^\circ\text{E}$ ), the DOAS instrument is installed in the German Koldewey Station about 100 m away from the coastline of the Kongsfjord and the telescope points towards the open ocean, i.e. the Barents Sea (Figure 5-18). Continuous measurements, although with some updates to the set-up over the years, have been performed at this location since 1995. Due to the West Spitzbergen Current, which is part of the Gulf Stream system, on the west coast of Svalbard, the climate is rather mild in comparison to other locations that far north on the globe and the Barents Sea is one of the world's most productive oceans. A register for Svalbard includes 1122 species of cyanobacteria and algae (including ice algae) (Elvebakk and Prestrud, 1996). A prominent feature which can be observed around Svalbard is the so-called ice-edge effect: The algal bloom follows the retreating ice edge in spring. Since the surface layer of the water is full of nutrition-rich salts, the algal bloom is much stronger here than in other areas of the open oceans (Sakshaug et al., 1994). However, in the years presented in this study here, the ice edge did not reach as far south as Ny-Ålesund on the west coast of Svalbard (maps of sea ice concentrations can be found at: <ftp://ftp.ifremer.fr/ifremer/cersat/products/gridded/psi-concentration/quicklooks/arctic>). Also, the macroalgae species *laminaria digitata* and *laminaria saccharina* grow along the shallow shelves around Svalbard and also in the Kongsfjord itself (Wiencke et al., 2004).

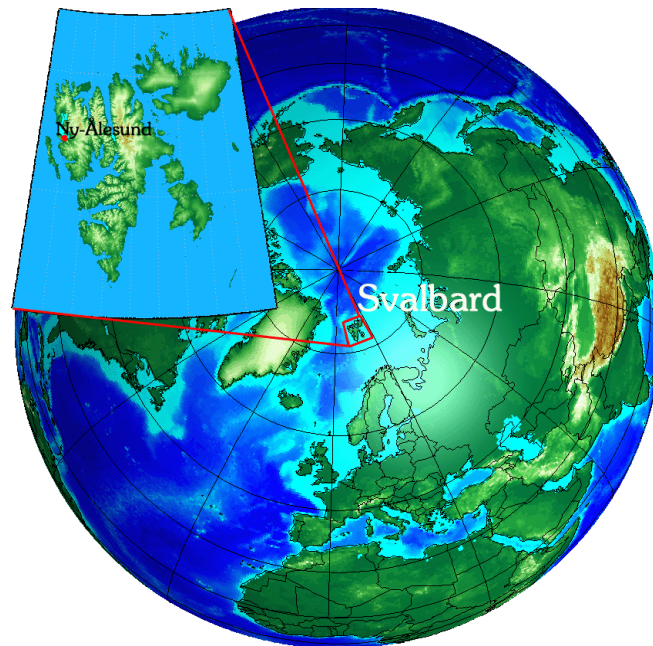


**Figure 5-18** Location of measurement site Ny-Ålesund at Svalbard situated in the Barents Sea. The MAX-DOAS telescope points towards northwest and the instrument is set-up about 100 m away from the coastline.

Since 1995, zenith-sky DOAS measurements have been performed by the Institute of Environmental Physics, University of Bremen at this Arctic site. After a successful test in April 1998, the instrument was equipped with initially a dual-axis telescope in spring 1999 and then upgraded to the full multi-axis telescope in spring 2002 which was set to the scanning mode with  $2^\circ$  to  $18^\circ$  elevation in  $2^\circ$ -steps plus  $30^\circ$  and zenith from July 2006. Before that measurements were performed at  $3^\circ$ ,  $6^\circ$ ,  $10^\circ$ ,  $18^\circ$ , and zenith.

The telescope is connected to two spectrometers one for the UV (325 - 413 nm) with a resolution of 0.5 nm FWHM and the second one for the visible wavelength (397 - 566 nm) with 0.7 nm FWHM. Due to the northern location, measurements of scattered sunlight are only possible from about March to September.

Iodine monoxide was analysed with retrieval parameters similar to the ones described in Table 11 but with a few exceptions due to instrumental problems which will be discussed in the following:

- Using the zenith noon spectrum as background spectrum in the DOAS fit leads to a stable negative offset between the retrieved zenith dSCDs and the off-axis ones. This feature occurs for minor absorbers and for both spectrome-

ter systems indicating that the source of the problem is likely polarisation of light in the telescope itself, possibly by the off-axis mirror. To overcome this problem, the spectra are analysed with the noon spectrum of the 30° off-axis direction as the background. However the resulting dSCDs will lose the information content for the free troposphere.

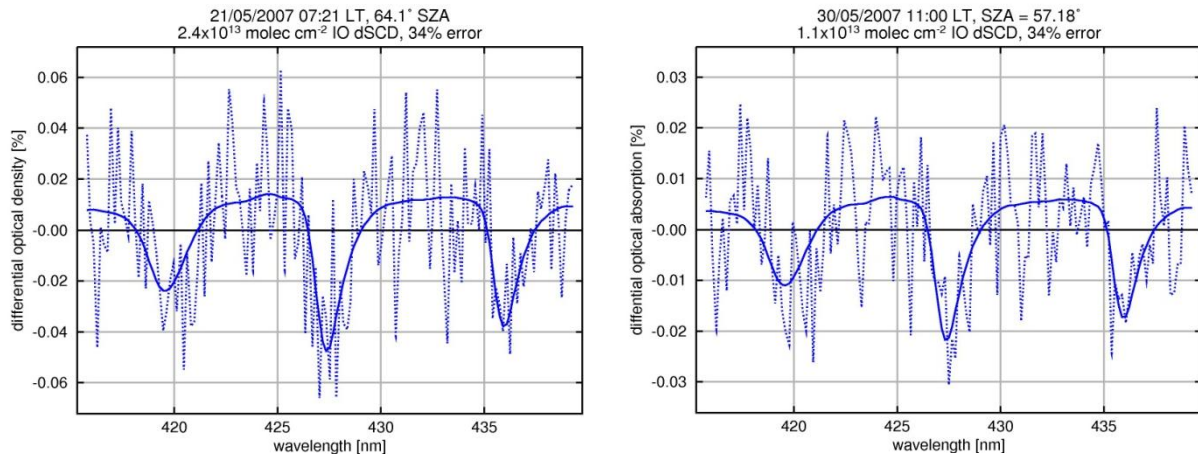


**Figure 5-19 Examples for the quality of the IO fit for Ny-Ålesund: The corresponding dSCDs and  $2\sigma$ -errors are stated in the header.**

- Especially in the IO wavelength window, emission lines from the town lighting can be observed. The closest residential building is about 10 m away from the Koldewey Station. The emission lines change over the years when different light bulbs are used but also during the day when lamps are turned on and off. Tests have shown that these lines do not affect the retrieved concentrations of IO since their lines do not coincide with the wavelengths of the absorption lines of the IO. However, the RMS cannot be used as a measure for the quality of the fit. Also, including a spectrum of a line with the instrumental line shape at the specific wavelength in the DOAS fitting procedure does not fully compensate the spectral structures of the line lamps as the actual line shape is unknown; it could be non-Gaussian or asymmetric. Here, a diurnally averaged residual from 30<sup>th</sup> May 2007 is included in the DOAS fit for the years 2004 to 2008 to account for one of the most prominent lines at about 423 nm. However, a limit of detection calculated from the RMS rather yields an upper limit.

- Correlation with Ring in the DOAS fitting is a known problem for the IO retrievals (Schönhardt et al., 2008): The largest differential structures between 416 and 439 nm are caused by the Raman scattering. Even small uncertainties in the cross section can result in highly structured and also stable spectral features that dominate the residual of the DOAS fit. These features are sometimes assigned to the iodine monoxide absorption leading to a large apparent column density. Here, all individual fits have been visually inspected and disregarded if Ring interference seemed to be likely.

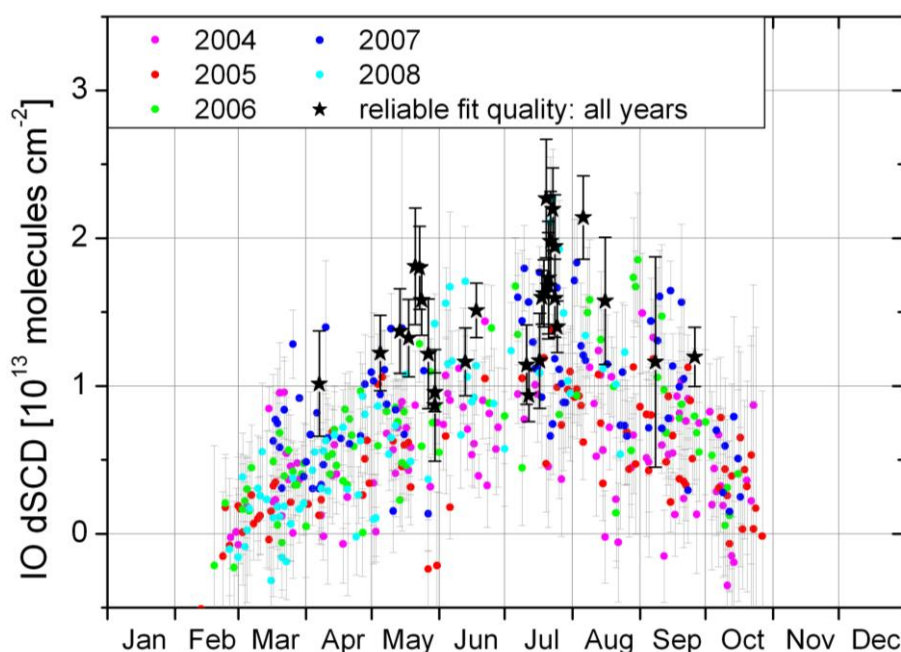


**Figure 5-20 Annual overview for off-axis IO dSCDs for Ny-Ålesund from 2004 until June 2006 with 3° elevation angle and afterwards 2°. Included are daily averages of IO, regardless of the DL, if the off-axis O<sub>4</sub> dSCDs are larger than  $4.5 \times 10^{43}$  molecules<sup>2</sup> cm<sup>-5</sup>. It should be noted that the O<sub>4</sub> levels can be up to a factor 3 larger than the threshold and consequently, the actual path length is highly variable. The error bars are the standard deviation for the averaging only. The black stars indicate days where the IO absorption features could be positively detected in the fit. From this data, the IO DL can be estimated to range between  $0.8 - 1.9 \times 10^{13}$  molecules cm<sup>-2</sup>.**

In summary, only data of 29 days out of five years were remaining after the selection according to the spectral fitting quality (see Figure 5-19 for examples of good fitting quality). From this data a detection limit of  $0.8 - 1.9 \times 10^{13}$  molecules cm<sup>-2</sup> could be estimated. IO could be detected with maximum slant column densities of  $3 \times 10^{13}$  molecules cm<sup>-2</sup> in an individual spectrum for the lowest elevation angle.

On almost all clear days in summer the off-axis IO column densities were enhanced. However, the spectral fits on many of these days could be identified as being corrupted by Ring structures. It is not clear whether a possible IO signal was modulated by the Ring features and hence IO was omnipresent in summer or whether there was no IO at all on these days. However in general in March but also in October, some of the clearest days could be experienced in Ny-Ålesund, but IO was not detected. The earliest positive detection occurred in April and the latest in September. An overview of the five years of data is presented in Figure 5-20. For this plot, the IO dSCDs for the lowest elevation angle have been averaged over a certain SZA range (which is changing during the course of the year) for a day when the corresponding  $O_4$  dSCDs exceed  $4.5 \times 10^{43} \text{ molecules}^2 \text{ cm}^{-5}$ . A similar annual cycle and similar column densities can be observed in all years. However, considering the error bars (here, only the standard deviation of the daily averages) and the limit of detection, this seasonality cannot be considered to be significant. Although such an annual pattern would be in agreement with the observations from Sylt, a possible seasonal cycle of the rotational Raman scattering due to the changing solar geometry during the year cannot be excluded. Midnight sun prevails from 17<sup>th</sup> April to 27<sup>th</sup> August which coincides with the nearly plateau-like pattern in summertime.

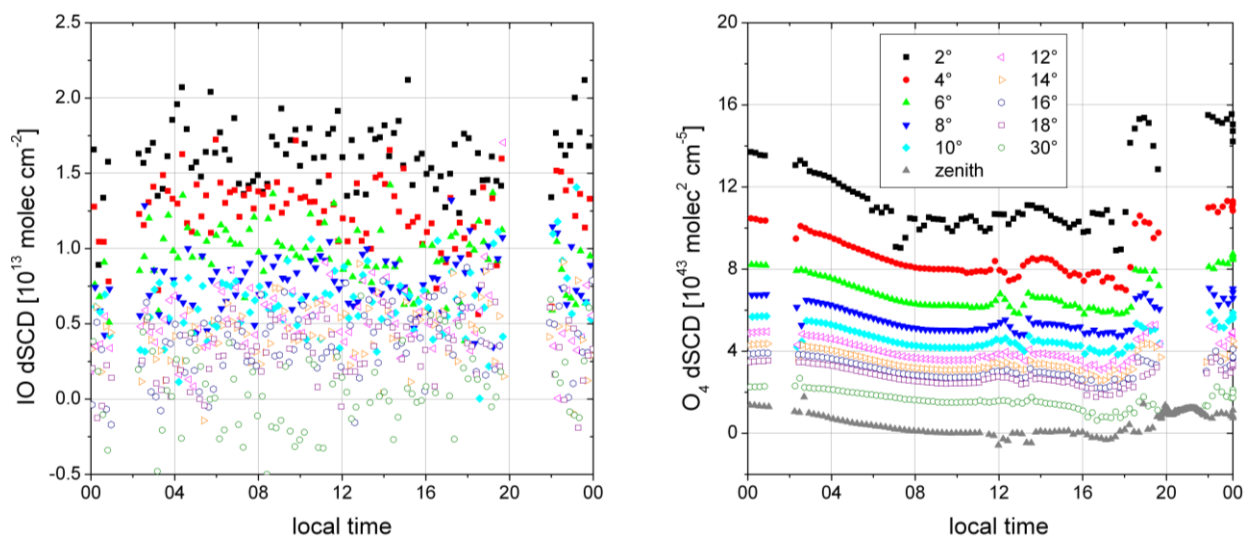


**Figure 5-21** IO and  $O_4$  dSCDs for Ny-Ålesund on 18<sup>th</sup> July, 2006. The IO data was analysed with the noon spectrum at 30° elevation whereas the  $O_4$  data with the zenith noon spectrum. The data gap in the morning is due to a break in the automated measurements to record calibration spectra and in the evening, the off-axis telescope points towards the sun hence only zenith spectra are recorded.

The BREAM profile retrieval was applied to one day of measurements with a rather smooth diurnal of the IO dSCDs with maximum densities of  $2.1 \times 10^{13}$  molecules  $\text{cm}^{-2}$ . The column densities for IO and  $\text{O}_4$  for 18<sup>th</sup> July, 2006 are presented in Figure 5-21. Since this is a very clear day with very high  $\text{O}_4$  column densities, the radiative transfer calculations were performed without aerosols. On average, a mixing ratio of 0.27 ppt in a 200 m thick surface layer could be retrieved. A simple scaling, without considering changes in the radiative transfer, transforms the SCD DL into a limit of detection for the mixing ratio of 0.13-0.30 ppt. However, these calculations assume that the IO is homogeneously distributed along the light path which is rather unlikely if the macroalgae are the emitters of the precursors for the observed IO.

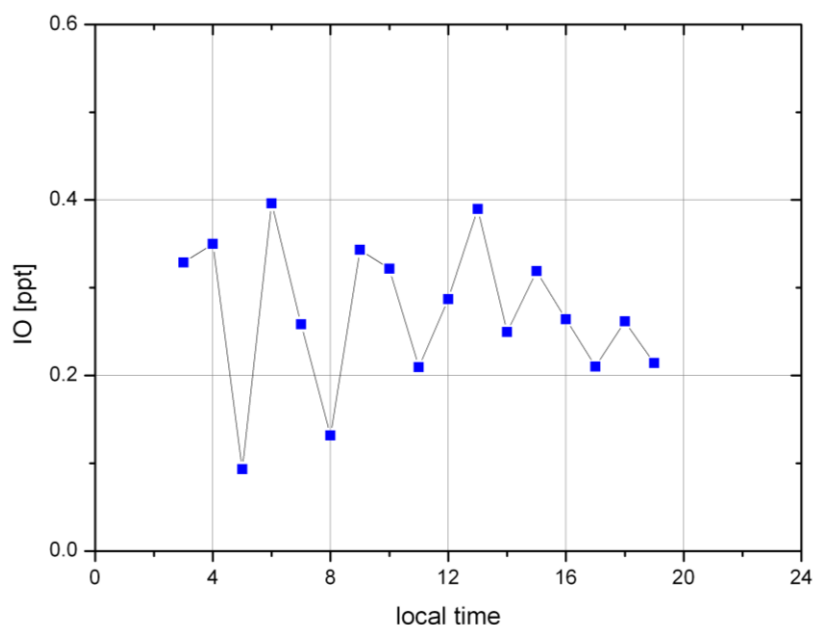


**Figure 5-22** IO mixing ratios averaged over 200 m and retrieved with BREAM for Ny-Ålesund on 18<sup>th</sup> July 2006. The corresponding dSCDs of IO and  $\text{O}_4$  are presented in Figure 5-21.

### 5.3 Maldives: Open ocean site in the Indian Ocean

In the framework of the Indian Ocean Experiment (INDOEX, Ramanathan et al., 2001) DOAS measurements were performed at the Kaashidhoo Climate Observatory (5.0°N, 73.5°E, Republic of Maldives) from 13<sup>th</sup> February to 16<sup>th</sup> March 1999. The instrument was equipped with a dual-axis telescope switching between the zenith and 2° elevation angle. The wavelength range covered 327 to 492 nm with a spectral

resolution of about 0.5 nm FWHM. The stability of the instrument suffered from several power failures hence for BrO, only upper limits of  $3 \times 10^{14}$  molecules  $\text{cm}^{-2}$  could be retrieved (Ladstätter-Weißmayer et al., 2007). This is six times larger than the limit of detection for BrO for List.

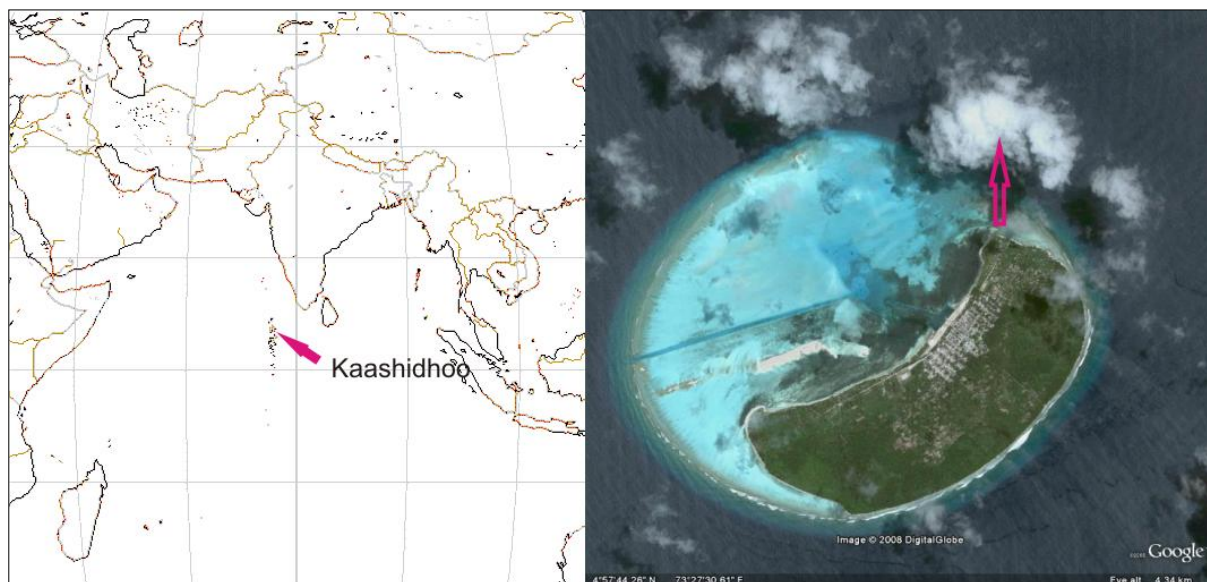


**Figure 5-23** Left: Map of Maldives archipelago in the Indian Ocean. Right: Photo of the Island Kaashidhoo with arrow indicating the pointing of the telescope (picture from Google Earth).

Kaashidhoo is the only Island on its atoll (Figure 5-23) with a reef that quickly drops off to about 500 to 600 m ocean depth. Several studies discussed the importance of halogen chemistry in the Indian Ocean before. They found in general that observations could not be explained with chlorine chemistry or combined chlorine-bromine chemistry alone and suggest a possible influence of iodine species (Dickerson et al., 1999; Burkert et al., 2003). Also, SCIAMACHY measurements show enhanced IO column densities around the Maldives archipelago (see Figure 5-28) albeit with large uncertainties.

For the IO analysis, the same fitting parameters as in Table 11 are applied and the noon zenith spectrum is included as background measurement. Figure 5-25 shows a typical diurnal cycle retrieved for the campaign. The strong U-shape of the IO dSCDs is characteristic for hazy conditions and is confirmed by the  $\text{O}_4$  observations having a similar pattern and rather low maximum dSCDs of  $2.3 \times 10^{43}$  molecules<sup>2</sup>  $\text{cm}^{-5}$  for the off-axis direction (not shown). However, this shape makes it difficult to exclude a

possible correlation with the ozone absorption cross section in the IO fitting procedure since a similar diurnal pattern is expected for ozone column densities. Hence interpretations of the measurements have to be treated with care. Also especially, the installed detector, an IKS photodiode array is known to have problems, for instance nonlinearities, and possible instrumental artefacts cannot be completely ruled out despite the quite low theoretical limit of detection, since this is only calculated for the random errors (see also section 3.4). The quality of the fit is illustrated in Figure 5-24.

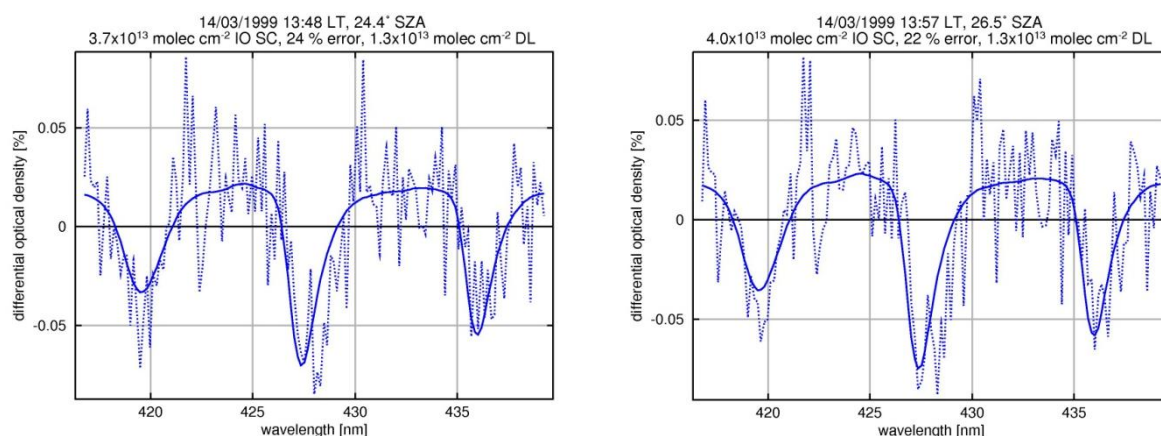


**Figure 5-24** Two examples for the quality of the IO fit for Kaashidhoo, Maldives: The corresponding differential slant column densities (SC),  $2\sigma$ -errors, and the  $2\sigma$ -detection limits (DL) are stated in the header.

As described in section 4.3, applying the technique similar to a simplified profile retrieval by simulating the off-axis  $O_4$  slant column densities to retrieve the aerosol load first, yields an extinction of  $0.22 \text{ km}^{-1}$  in the lowest layer. This is in good agreement with measurements of Welton et al. (2002) for the same campaign. With this information, off-axis dAMFs of 6, 10, and 13 can be calculated for a layer thickness of 1 km, 500 m, and 350 m, respectively. For an IO dSCD of  $3.5 \times 10^{13}$  molecules  $\text{cm}^{-2}$ , this is consistent with concentrations of 2.4 ppt, 2.8 ppt and 3.1 ppt when distributing the resulting vertical column uniformly over the corresponding layer depth. Here, only the noon data is used. Applying the same settings in the radiative transfer modelling but for the satellite geometry, results in an AMF of 1 at a SZA of about  $38^\circ$  for the time of over-flight at 10:00 AM. A 500 m layer and an albedo of 0.03 were selected for the simulations. The SCIAMACHY SCD of  $0.5 \times 10^{13}$  molecules  $\text{cm}^{-2}$  (see Figure 5-28) then corresponds to 4 ppt. For the ground-based BrO measurements, an off-axis

dAMF of 9 was simulated for a 500 m layer for the noon geometry. That translates to the rather large detection limit of 27 ppt.

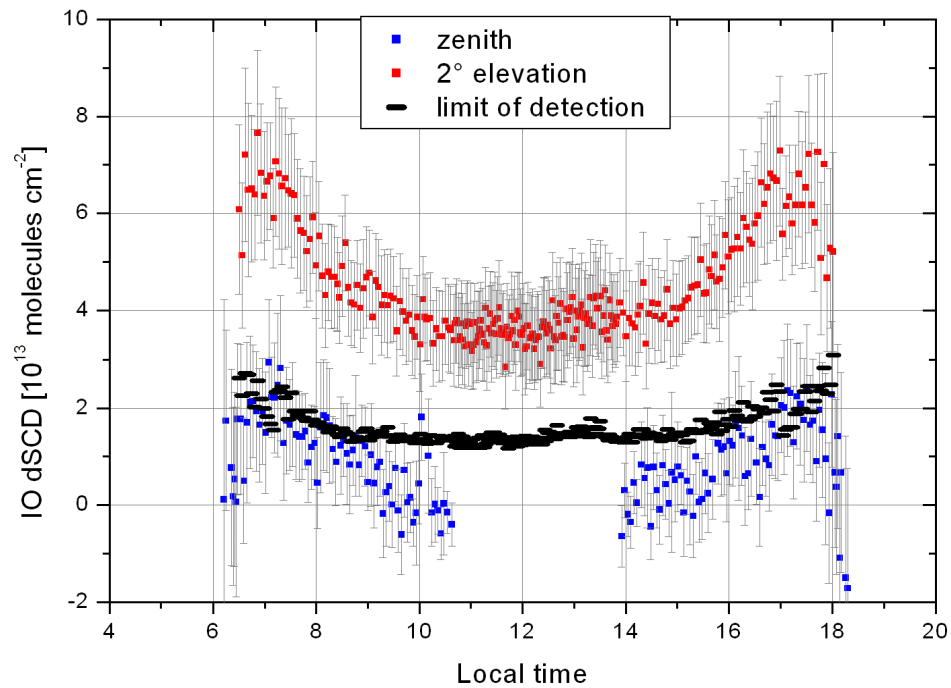


Figure 5-25 IO dSCDs for Kaashidhoo on 14<sup>th</sup> March 1999 with  $2\sigma$  errors and detection limits. A similar diurnal pattern and similar concentrations have been observed on all 29 days of measurements.

## 5.4 Andøya: Coastal zone at the Norwegian Sea



Figure 5-26 Location of the instrument at the Andøya Rocket Range, Norway. The arrows indicate the direction of the telescope towards the Atlantic.

An intercomparison campaign for zenith-sky scattered-sunlight instruments was held at the Andøya Rocket Range in Andenes, northern Norway (69.3°N, 1.2°E) in spring

2003 (Vandaele et al., 2005). Seven groups from Europe and a group from New Zealand participated. In the framework of the NDSC/NDACC, the aim of this study was to quantify the quality of the measurements and test the consistency of retrieval results for the stratospheric column densities of the absorbers  $\text{NO}_2$ , BrO and OCIO. Hence only a limited time of the day was spent on off-axis measurements. Also only three off-axis directions were chosen during measurements from 19<sup>th</sup> February to 6<sup>th</sup> March: 3°, 7.5°, and 12.5° elevation. The telescope was connected to two spectrometers: In the UV, the wavelength range was set to 324–408 nm with a spectral resolution of 0.4 nm FWHM and in the visible to 336–504 nm with 0.7 nm FWHM. The instrument was installed about 100 m away from the Atlantic coast. The dark areas in the sea in the photo on the left of Figure 5-26 are rocks covered with seaweed. Also on the beach some beds with macroalgae can be seen. However, those species are not members of the *laminaria* family but the brown algae *ascophyllum nodosum*.

The IO fit, performed with the settings given in Table 11, did not result in any positive detection although the instrument performed quite well with a typical limit of detection of  $1.1 \times 10^{13}$  molecules  $\text{cm}^{-2}$ . Overall during this campaign the detection limit ranged from  $0.7 - 2.2 \times 10^{13}$  molecules  $\text{cm}^{-2}$ . This leads to a detection limit on average of 0.6 ppt with a dAMF of 15.4 for a 500 m thick layer and  $\text{O}_4$  dSCDs of  $6 \times 10^{43}$  molecules<sup>2</sup>  $\text{cm}^{-5}$ . But in combination with an amazing visibility of over 100 km on a few days when the  $\text{O}_4$  dSCDs for 3° elevation reached values of more than  $10 \times 10^{43}$  molecules<sup>2</sup>  $\text{cm}^{-5}$ , the DL was as low as 0.4 ppt. Due to a memory effect of the CCD camera of the UV-instrument, the detection limit for BrO off-axis dSCDs is in the same range as for Kaashidhoo of  $3 \times 10^{14}$  molecules  $\text{cm}^{-2}$ . However here with the clear skies, this corresponds to the still too high limit of 18 ppt or 11 ppt on very clear days.

## 5.5 Crete: Island in the Mediterranean

Since August 2007, Heraklion on Crete, Greece (35.3°N, 25.1°E) is one of the permanent MAX-DOAS measurement sites of the University of Bremen. Crete is situated in the eastern part of the Mediterranean Sea and the instrument is set-up at the Heraklion University approximately 3.5 km away from the coastline (see Figure 5-27). Here, two spectrometers are deployed: one covering a wavelength region from 324 to 408 nm with a resolution of about 0.3 nm FWHM and the second 389 to 558 nm

with 0.6–0.8 nm FWHM. The MAX-DOAS telescope points towards the north scanning the horizon in 2°-steps from -1° to 15°, followed by a measurement at 30° elevation and then zenith. The standard fitting retrievals (see Table 11) are supplemented by the inclusion of the NO<sub>2</sub> absorption cross section at tropospheric temperatures since this is a rather polluted location with the path partly passing over the city Heraklion itself. Spectra from October 2007 to July 2008 have been analysed.



**Figure 5-27** Measurement site at Heraklion University on Crete, Greece. The MAX-DOAS telescope points towards the north (orange arrow) and the distance to the coast is about 3.5 km (map from Wikipedia).

Only upper limits of IO can be reported from this site. The detection limit for the slant column densities ranges from  $1.5$  to  $3.5 \times 10^{13}$  molecules  $\text{cm}^{-2}$ . On average, the upper limit is about  $2.5 \times 10^{13}$  molecules  $\text{cm}^{-2}$ . The BrO dSCD limit of detection is quite variable from day to day:  $3.6 \times 10^{13}$  to  $2.6 \times 10^{14}$  molecules  $\text{cm}^{-2}$ . Also, BrO could not be identified in the spectra.

Due to a hazy layer in the lowest regions of the troposphere, usually the 3 or 5° off-axis dSCDs show the largest column densities for O<sub>4</sub>. Here, the 3° direction was simulated for a noon O<sub>4</sub> dSCD of about  $6 \times 10^{43}$  molecules<sup>2</sup>  $\text{cm}^{-5}$  although on some days values of more than  $8 \times 10^{43}$  molecules<sup>2</sup>  $\text{cm}^{-5}$  could be observed. For a 500 m thick absorber layer, this yields dAMFs of 15.3 and 13.2 for IO and BrO, respectively. Hence upper limits for IO are 0.8–1.9 ppt and on average 1.3 ppt. BrO upper limits range from 2.2 to 16.0 ppt.

## 5.6 Summary and discussion

Measurements of the halogen oxides BrO and IO have been performed at five islands ranging from polar regions (Svalbard), over mid-latitudes (Andøya<sup>1</sup>, Sylt, and Crete) to the tropics (Maldives). First, the results for iodine monoxide are summarised (see also Table 13).

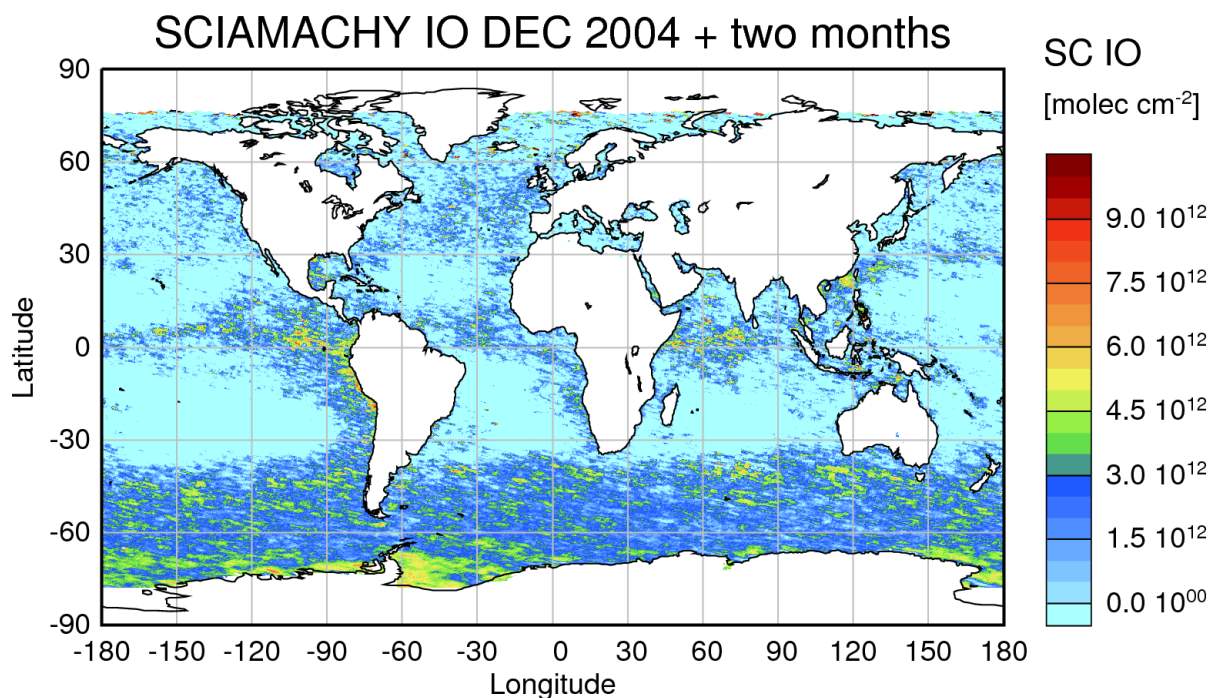


**Figure 5-28** IO SCDs retrieved from SCIAMACHY spectra for winter 2004/2005 (data from A. Schönhardt, University of Bremen (Schönhardt et al., 2008)). Data has been averaged from December 2004 to February 2005.

During a six month-long campaign in List on Sylt, IO has been observed almost every day above the detection limit during summer but not in spring. The differential slant column densities have been correlated to NO<sub>2</sub> and O<sub>4</sub> dSCDs, to the Ring fitting coefficient, the tidal height, ozone concentrations, solar radiation, and wind direction as well as wind speed. These studies did show that the measured IO dSCDs mainly depend on the solar radiation and the length of the slant path through the lower atmosphere determined by the visible range. Noteworthy is also a weak positive dependence on the tidal height. The lack of a negative correlation of IO with the tides excludes a local macroalgal source. Contrary, the small day-to-day changes in combination with a negligible dependence on wind speed and direction indicate the rather

<sup>1</sup> Although Andøya is situated within the Arctic Circle, the climate is considered to be temperate.

wide-spread nature of the observed IO most likely coming from the open water. The annual variability of the IO which is also reflected in a strong positive correlation with radiance shows that this source must have a seasonal cycle governed by the solar radiation in the atmosphere. Figure 5-29 shows the *chlorophyll a* concentrations from the MODIS instrument as a seasonal composite for winter 2003/2004 and summer 2004. Only small differences can be observed for the North Sea between these two seasons. However, the whole area is biologically highly active suggesting iodocarbons being the precursors for the observed inorganic iodine.

The profile retrieval Bream has been applied to one day of data from Sylt and maximum mixing ratios of 1.4 ppt IO were obtained. This data has been used to scale the entire data set and the maximum concentrations of 2.2 ppt are in good agreement with maximum values of 1.9 ppt measured at the near-by location Dagebüll during April to May 2002 by Peters et al. (2005). However, the overall error is about 3 ppt.

In Ny-Ålesund due to some instrumental problems, IO was positively detected only on 29 days out of five years with column densities of up to  $3 \times 10^{13}$  molecules  $\text{cm}^{-2}$ . Albeit large uncertainties, an overview of the dSCDs for all 5 years suggests a seasonal cycle with a maximum in summer and concentrations below the DL in spring and autumn. For one individual day with IO dSCDs of up to  $2.2 \times 10^{13}$  molecules  $\text{cm}^{-2}$ , an average mixing ratio of  $\sim 0.3$  ppt could be retrieved with BREAM. However, the coast of Svalbard is populated with kelp: Schall et al. (1994) investigated three species of macroalgae collected directly east of Ny-Ålesund and found in an incubation study that the highest amounts of  $\text{CH}_2\text{I}_2$  were released from *laminaria saccharina*. *Laminaria digitata* was not included in this study which was initiated by observations of Schall and Heumann (1993) having measured halocarbons in the air above the Kongsfjord as well as in the sea water and detected up to 1.02 ppt of  $\text{CH}_2\text{I}_2$  in air in September 1992. Consequently, besides the fact that the observed IO could mainly originate from direct  $\text{I}_2$  emissions and hence disqualifies Ny-Ålesund as a site to study marine background conditions, it is highly unlikely that the observed IO is homogeneously distributed along the light path in the boundary layer hence concentrations are expected to be locally much higher than the observed maximum mixing ratio of 0.4 ppt.

**Table 13 Overview for the IO results: When only upper limits could be determined from the data, the numbers are given in brackets, i.e. for Andøya and Heraklion. These values state typical concentrations and smaller upper limits could be retrieved on days with very good visibility. For Ny-Ålesund and List, the results from the BREAM profile retrieval case studies are presented. Here, the IO concentrations are given as the average of the lowest 200 m otherwise a well-mixed layer of 500 m thickness is assumed in the calculations.**

	Coordinates	IO dSCD [ $10^{13}$ molecules $\text{cm}^{-2}$ ]	IO dAMF	IO VMR for a 500 m layer [ppt]	O <sub>4</sub> dSCD used in radiative transfer calculations [ $10^{40}$ molecules <sup>2</sup> $\text{cm}^{-5}$ ]	viewing angle used to retrieve IO VMR	season
Ny-Ålesund Svalbard	79°N	1.9	BREAM	maximal 0.4 in ground layer	11000	all (dSCDs for 2°)	spring, summer, autumn
Andøya Norway	69°N	(average: 1.1) (range: 0.7-2.2)	15.3	(average: 0.6) (range: 0.4-1.2)	6000	3°	late winter, early spring
List Germany	55°N	3.7	BREAM	maximal 1.4 in ground layer	8000	all (dSCDs for 2°)	spring, summer
Heraklion Greece	35°N	(average: 2.5) (range 1.5-3.5)	15.3	(average: 1.3) (range: 0.8-1.9)	6000	3°	spring, summer, autumn, winter
Kaashidhoo Maldives	5°N	3.5	10.4	2.8	2300	2°	spring

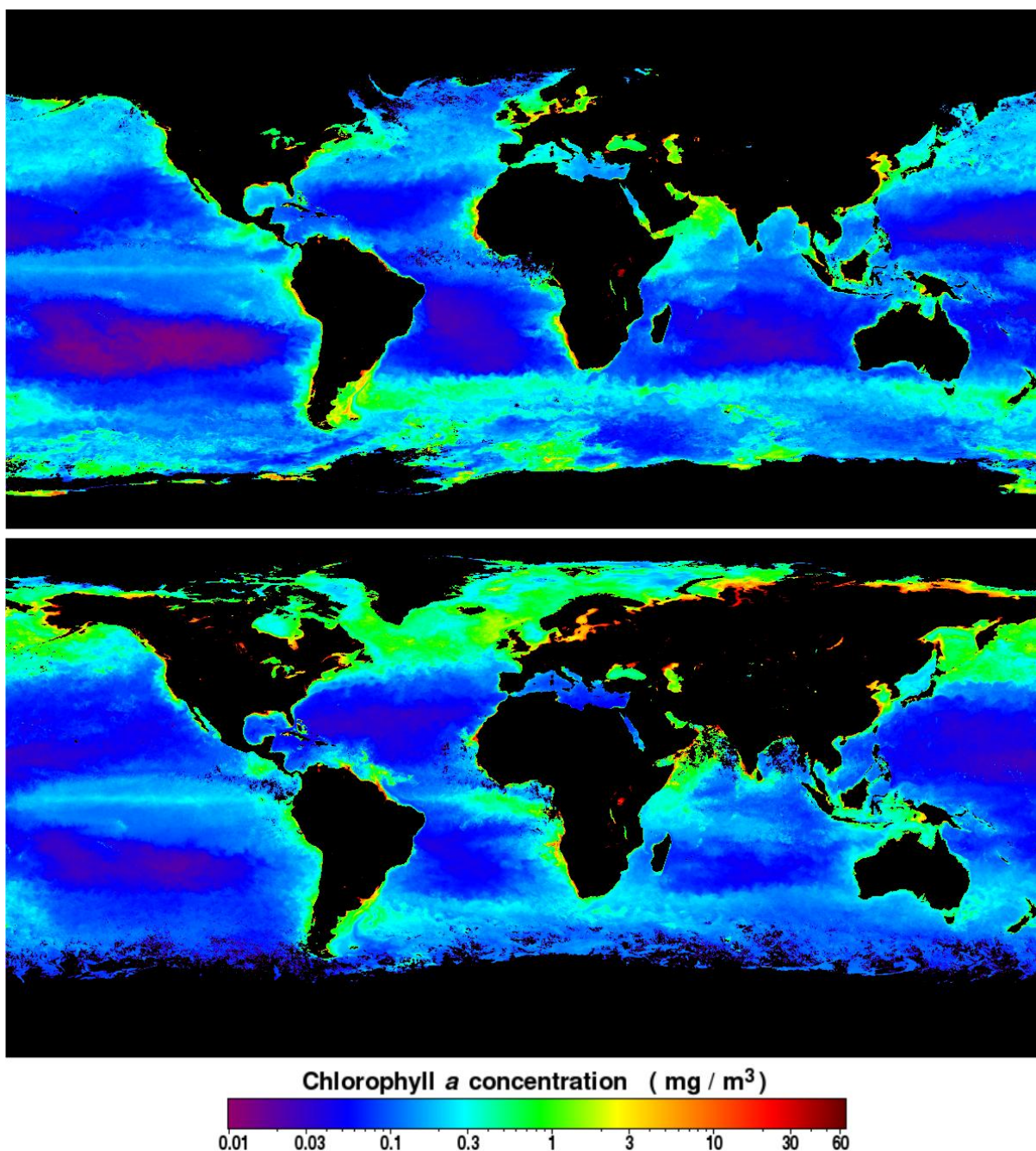


Figure 5-29 Aqua MODIS seasonal composite of *chlorophyll a* concentrations for winter 2003/2004 (top) and summer 2004 (bottom) (<http://oceancolor.gsfc.nasa.gov/cgi/l3?per=DAY>).

There are two other studies about IO in Ny-Ålesund (Tuckermann et al., 1997; Witrock et al., 2000). Whether these observations are consistent with the measurements of the study presented here, is difficult to assess though due to rather different conditions: LP-DOAS measurements performed over three different path lengths ranging from 3.5-11.6 km in April to May 1995 as well as March to May 1996 yielded only upper limits of 1-2 ppt IO (Tuckermann et al., 1997). The seasonal variation de-

scribed in the study here, disagrees with Wittrock et al. (2000) who did not report absolute concentrations but could detect tropospheric IO in spring to autumn for the years 1995 to 1998 with a scattered-sunlight zenith-viewing DOAS. However, some of these differences might be explained by a different extent of the sea ice cover in the area over the different years.

At Kaashidhoo, IO has been measured with concentrations of about 2.4 to 3.1 ppt depending on the assumed layer depth of 1 km to 350 m. The retrieved dSCDs are quite similar for all days during the campaign from February to March in 1999. Spectral features due to instrumental artefacts cannot be excluded for this set-up though. However, the observed levels of IO in Kaashidhoo are consistent with concentrations retrieved from SCIAMACHY data (Schönhardt et al., 2008) of ~4 ppt. Also the *chlorophyll a* maps show locally enhanced values along the Maldives Archipelago (see Figure 5-29).

At Andøya and Crete, IO could not be observed above the average detection limits of 0.6 ppt and 1.3 ppt, respectively. However, the data from Sylt as well as the *chlorophyll a* charts (Figure 5-29) suggest that the measurements from Andøya in early spring are outside the expected biologically active season anyways: Andøya is situated just north of the Arctic Circle and in February the dark period around the polar night has just ended.

The results for Crete are in agreement with a study by Hönninger (2002) stating 0.8 ppt as upper limit for IO and also the *chlorophyll a* map indicates that the Mediterranean Sea, especially where it is very deep in the east, is not very biologically active (see Figure 5-29).

There are mainly two open questions concerning the observations of IO in the troposphere. First, why is there a difference between polar regions in the northern and the southern hemisphere (e.g. Schönhardt et al., 2008) and can the relatively high IO concentrations retrieved by SCIAMACHY for central Antarctica be confirmed by ground-based measurements? It is speculated that the precursors of the IO are produced from algae living underneath or within the sea ice (Saiz-Lopez and Boxe, 2008). Unfortunately, the ice edge was usually located at least 100 km further to the north from Ny-Ålesund hence the possibility to contribute to an answer is rather limited. Although a visible range of more than 100 km is possible in Arctic regions, the observed seasonal cycle seems to be rather determined by length of day than by the

sea ice edge which will be closest in winter and spring. Independent of the Arctic pack ice, locally the fjord, but also the Barents Sea close to the coastline of Svalbard can be covered by sea ice from spring onwards for a few months. Although the extent and thickness can be highly variable from day-to-day, in general, the area under the light path was more or less ice-free in the years 2006-2008 whereas some sea ice was present in the years 2004-2005. However, the scatter in the data (see Figure 5-20) does not allow drawing any conclusions about year-to-year variability.

The second question is whether the open ocean, which covers 70% of the Earth's surface, is a significant global source of iodine and consequently for aerosols at all or whether the locations where IO has been detected so far under so-called background conditions are in fact limited to oceanic upwelling regions or are in general influenced by coastal flora. Furthermore are the concentrations large enough to have an influence on the global tropospheric ozone budget? From the study presented in this chapter, the answer is maybe: The enhanced IO concentrations seem to be rather localised, i.e. three locations out of five, but also temporally variable. Furthermore, the DLs are basically still too high, e.g. at Crete. To quantify these effects, which is certainly only achievable on a longer timescale, ship-borne campaigns would be ideal, but also improved satellite retrievals and instrumentation are needed. However the study presented here offers a small contribution in quantifying iodine monoxide at selected coastal locations and hence closing some gaps on the map as well as helping to identify locations for more detailed studies.

The estimates of the overall atmospheric bromine load show large uncertainties as well: Is there a global background signal of BrO in the free troposphere and how large is it? Are volcanoes important sources of bromine? But also, the presence of BrO in the marine boundary layer is poorly studied with positive detection reported from only a handful of location so far. This raises the question whether sea-salt is in fact an important source of reactive bromine or whether there might be the possibility of a biogenic contribution after all (von Glasow, 2008).

Here, bromine monoxide (exclusive during bromine explosions in Ny-Ålesund) could not be detected at any of the five locations although the detection limits for Kaashidhoo and Andøya are rather large. Upper limits are given with 18 ppt for Andøya, 2.8 ppt for List, 2.2 to 16 ppt for Heraklion, and 27 ppt for Kaashidhoo. The conclusion for these observations is that BrO needs a highly focused and well-maintained instru-

ment and cannot be simply measured as a by-product with an existing set-up at low concentrations.

## 6 Stratospheric OCIO in the 2005 north polar spring

In this chapter results are presented from a study of the chlorine chemistry in the Arctic stratosphere by means of ground-based and satellite observations of OCIO in comparison with model simulations for spring 2005. The Arctic winter 2004/2005 was characterised by extremely cold temperatures in the stratosphere and a large and also persistent vortex developed in the northern hemisphere leading to chlorine activation and large OCIO signals (see Figure 6-1 for a monthly average of the SCIAMACHY OCIO slant column densities). Although OCIO does not participate directly in the destruction of ozone, its accurate measurement as well as modelling is crucial to understand the highly perturbed chlorine chemistry in the polar vortices. In contrast to ClO, which cannot be measured by scattered-light UV-visible absorption spectroscopy, OCIO is accessible to the DOAS technique.

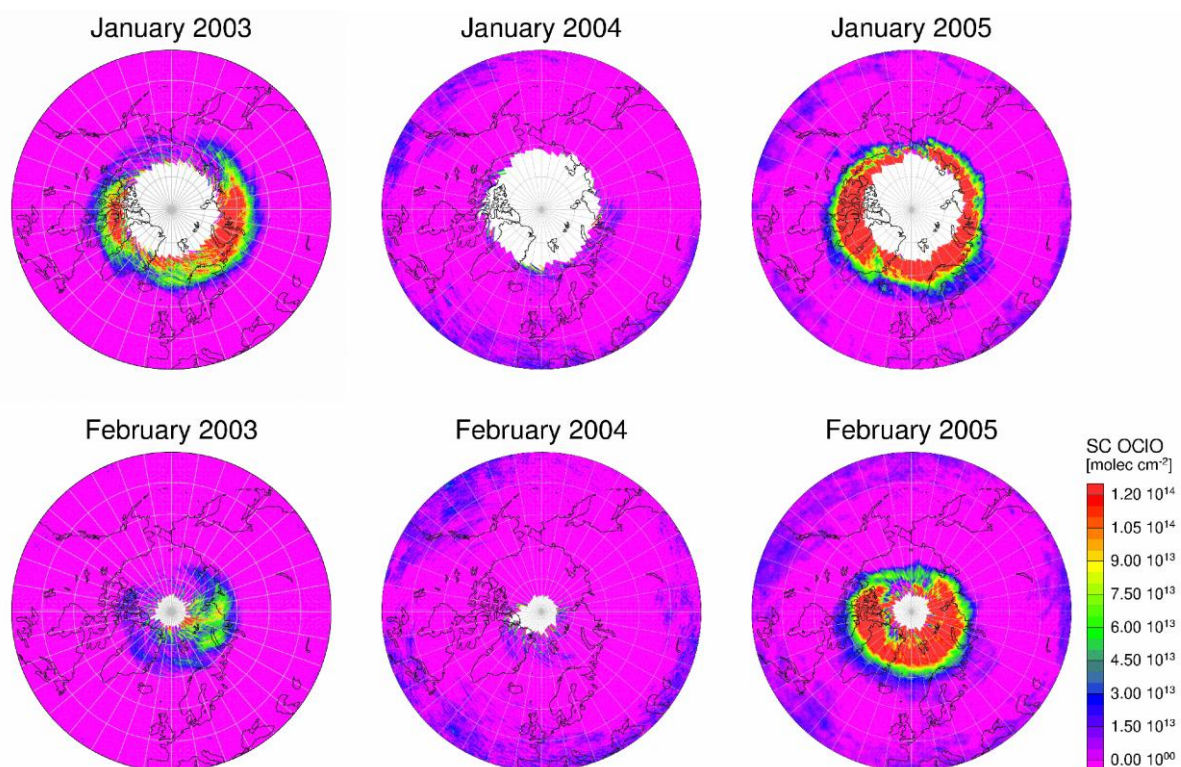
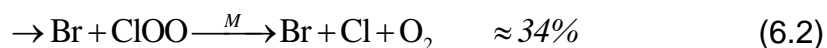


**Figure 6-1** Monthly averages of OCIO slant column densities retrieved from SCIAMACHY observations over the Arctic for the winters 2003 to 2005. Data provided by A. Richter (University of Bremen, Germany).

As stated in section 2.4.1, the combined BrO-ClO cycle is one of the two main ozone destruction cycles in the polar vortex and it accounts for more than 40% of the ozone loss over the Arctic at the 475 K isentropic surface but depending on the coldness of the winter (Chipperfield and Pyle, 1998). In a side channel of the BrO+ClO reaction, chlorine dioxide OCIO is produced:



The branching ratios of reactions (6.1) to (6.3) are given for a temperature of 195 K and are taken from the photochemical recommendation data of the Jet Propulsion Laboratory (JPL) by Sander et al. (2003b) in future referred to as JPL 2002. The second (6.2) and the third channels (6.3) of the BrO+ClO reaction initiate a catalytic cycle converting two ozone molecules into three oxygen molecules. The first reaction channel (6.1) is thought to be the predominant production mechanism for atmospheric OCIO during daytime (Friedl and Sander, 1989; Tung et al., 1986) and leads to a null cycle in ozone destruction. Another possibility for the formation of OCIO is the self-reaction of ClO initialising the ClO-dimer-cycle for ozone destruction (see reaction (2.114)). This reaction is one of the minor channels and can compete with reaction (6.1) only at extremely low temperatures in the highly perturbed polar springtime stratosphere (Nickolaisen et al., 1994).

The destruction of OCIO mainly takes place via photolysis:



This results in a pronounced diurnal cycle of the chlorine dioxide with high concentrations at night and hardly any during daytime. Reaction (6.4) is the main photolysis channel of OCIO in the atmosphere (Lawrence et al., 1990) and also constitutes a null cycle in the ozone budget when the atomic oxygen recombines with molecular oxygen. The chlorine monoxide, produced in reaction (6.4) reacts with BrO and can yield again OCIO. Consequently, when assuming a steady-state between OCIO and ClO, the chlorine dioxide concentration [OCIO] is proportional to both concentrations [BrO] and [ClO]:

$$[\text{OCIO}] \approx \frac{k_{1a} [\text{ClO}][\text{BrO}]}{J_{\text{OCIO}}} \quad (6.5)$$

with the rate constant  $k_{1a}$  for reaction (6.1) and the photolysis frequency  $J_{\text{OCIO}}$  for OCIO (Solomon et al., 1990).

Equation (6.5) allows inferring changes in the ClO concentration from the OCIO concentration since the BrO is almost not affected by the presence of PSCs and consequently, an increase in OCIO is mainly associated with an increase in ClO due to activation of chlorine through heterogeneous reactions on PSC surfaces. However, the steady-state assumption is only valid for solar zenith angles less than  $90^\circ$ . For SZAs beyond about  $92^\circ$ , the photolysis of BrCl in the reaction sequence (6.3) ceases and less bromine is available for reaction (6.1) whereas the photolysis of OCIO discontinues at about  $94^\circ$  SZA depending on the height in the atmosphere (Schiller and Wahner, 1996). Sessler et al. (1995), Schiller and Wahner (1996), and Sessler et al. (1996) discussed whether OCIO may be used as a quantitative measure for active chlorine or not. However, all studies agree that for SZAs smaller than  $90^\circ$ , the concentration of OCIO can be considered as linearly related to the ClO concentration. Beyond  $90^\circ$  and up to  $92^\circ$  SZA, the concentrations are still approximately proportional to each other.

First measurements of atmospheric OCIO were performed by means of ground-based UV-visible spectroscopy by Solomon et al. (1987a) over Antarctica followed by several other studies for the southern hemisphere (e.g. Sanders et al., 1993; Kreher et al., 1996; Frieß et al., 2005) but also for the Arctic (e.g. Solomon et al., 1988; Perner et al., 1994; Gil et al., 1996; Otten et al., 1998; Tørnkqvist et al., 2002) and at mid-latitudes (Richter et al., 1999; Aliwell et al., 1997). The same spectroscopic technique has been applied for balloon and air-borne measurements in order to retrieve profile information (e.g. Wahner et al., 1989; Schiller et al., 1990; Pommereau and Piquard, 1994; Renard et al., 1997; Riviere et al., 2002).

The first satellite-based remote sensing of OCIO became available with the launch of the Global Ozone Monitoring Experiment (GOME) in April 1995. These data have been used extensively for OCIO studies (Burrows et al., 1999b; Wagner et al., 2001a; Wagner et al., 2002; Köhl et al., 2004b; Köhl et al., 2004a; Richter et al., 2005). GOME-1 OCIO measurements were followed by observations from the Scanning Imaging Spectrometer for Atmospheric Cartography (SCIAMACHY) on ENVISAT (Envi-

ronmental Satellite) (Kühl, 2005) and also by OSIRIS (Odin Spectrometer and Infra-red Imager System) on the Odin satellite (Krecl et al., 2006). Recently, the global presence of night-time OCIO could be detected in stellar occultation measurements performed by the GOMOS (Global Ozone Monitoring by Occultation of Stars) instrument which also operates on ENVISAT (Fussen et al., 2006).

Other species of the active chlorine family measured in the stratosphere are chlorine monoxide ClO through remote sensing (Solomon et al., 2000), and *in-situ* measurements (e.g. Brune and Anderson, 1986; Pierson et al., 1999; Avallone and Toohey, 2001; Vogel et al., 2003) and recently its dimer Cl<sub>2</sub>O<sub>2</sub> (Stimpfle et al., 2004; von Hobe et al., 2005). Extensive measurements of ClO from space have been provided by the Microwave Limb Sounder (MLS) instruments on the Upper Atmosphere Research Satellite (UARS) and Aura satellite as well as the Sub-millimeter Microwave Radiometer (SMR) instrument on Odin (e.g. Barret et al., 2006; Berthet et al., 2005; Santee et al., 2008).

Here, SCIAMACHY OCIO slant column densities for the spring 2005 have been quantitatively validated by comparison with slant column densities retrieved from measurements made in Ny-Ålesund (79°N, 12°E), Summit (73°N, 38°W) and Bremen (53°N, 9°E). OCIO slant column densities modelled with a set of stacked box models and considering the light path through the atmosphere are also included in this comparison. The model predictions differ significantly from the measured quantities. OCIO amounts are underestimated for conditions of strong chlorine activation and at large solar zenith angles. Sensitivity studies for several parameters in the box model have been performed and possible explanations for the discrepancies discussed.

This chapter is organised as follows: Section 6.1 describes the details for retrieving the OCIO column densities for the three different data sets. Sections 6.2 and 6.3 are dedicated to the validation of the SCIAMACHY OCIO column densities. The solar zenith angle dependence of the OCIO column densities is investigated in section 6.4. In section 6.5, the sensitivity of the chemistry model to various parameters is tested and discussed. The results are then summarised in section 6.6

## 6.1 Data sets

Comparisons of different measurements of OCIO with each other or with model predictions require the following issues to be taken adequately into account:

- the photolysis of OCIO, which in daylight is rapid,
- a changing column and profile during twilight,
- the change of solar zenith angle (SZA) along the line of sight,
- low signal to noise of the remote sensing of solar scattered radiation at large SZAs.

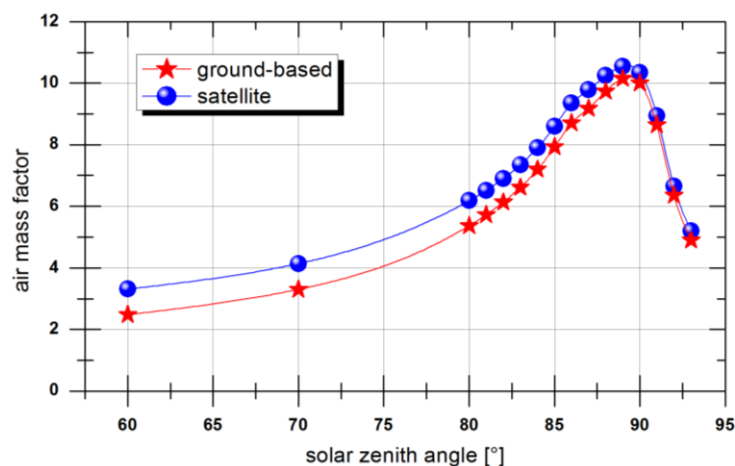


**Figure 6-2 Air mass factors for the satellite and the ground-based observational geometries for a model OCIO profile for Ny-Ålesund on 4<sup>th</sup> March.**

The comparison is best performed directly for the slant column densities. Although the viewing geometries of the satellite- and ground-based measurements are very different, the air mass factors yield similar values at large solar zenith angles. The AMF modelled for the same vertical profile (model OCIO profile for Ny-Ålesund on 4<sup>th</sup> March, see section 6.1.3) for the two observation geometries agree within 4% in the SZA range between 89° and 91° (Figure 6-2). Consequently, the slant column densities of OCIO from the different platforms can be compared directly. The modelled OCIO profiles are also converted to slant column densities for the given observational geometry assuming Arctic background conditions for the aerosol in the radiative

transfer calculations. In the following, the three data sets used in this study are described.

### 6.1.1 SCIAMACHY

The SCIAMACHY (SCanning Imaging Absorption spectroMeter for Atmospheric CartograpHY) instrument is a spectrometer designed to measure sunlight, transmitted, reflected and scattered by the Earth's atmosphere or surface in the ultraviolet, visible and near infrared wavelength region (240 – 2380 nm) at a moderate spectral resolution (0.2 – 1.5 nm FWHM) (Bovensmann et al., 1999; Burrows et al., 1995). SCIAMACHY was launched on ENVISAT into a sun-synchronous orbit on 1<sup>st</sup> March 2002 having an equator crossing time of 10:00 AM local time. Global coverage is obtained within six days at the equator and within one day at 70° latitude in spring. The spatial resolution varies between 30 km × 30 km and 240 km × 30 km depending on location and season.

Interpretation of the satellite measurements is complicated by the rapid photochemistry of OCIO combined with the sun-synchronous orbit of the satellite. Along the satellite orbit, the solar zenith angle varies with latitude leading to a latitude dependent change in photolysis rates and thus OCIO amounts. In order to facilitate systematic validation with ground-based measurements, the OCIO amounts retrieved from the satellite over the stations are therefore compared with the OCIO column density measured from the ground at the time of satellite-overpass.

The measured spectra are analysed with the DOAS method. The fitting procedure, in a window from 365 to 389 nm, includes in addition to the OCIO cross section (Kromminga et al., 2003) and a polynomial for the compensation of broad-band features, NO<sub>2</sub> (Vandaele et al., 2003), and O<sub>4</sub> (Hermans et al., 1999) absorption cross sections as well as a rotational Raman scattering cross section (Vountas et al., 1998). A solar irradiance measurement is chosen as the background spectrum. Additional corrections have to be included to account for under-sampling and the polarisation sensitivity of the instrument. As an individual measurement of SCIAMACHY has only a very short exposure time and therefore limited signal-to-noise at low sun, all measurements within 200 km of a station are averaged over a day. The resulting fitting quality for OCIO is illustrated in Figure 6-3. The overall accuracy of the averaged slant col-

umn densities is estimated to be about 30% or higher. The SCIAMACHY OCIO slant column densities have been provided by A. Richter (University of Bremen, Germany).

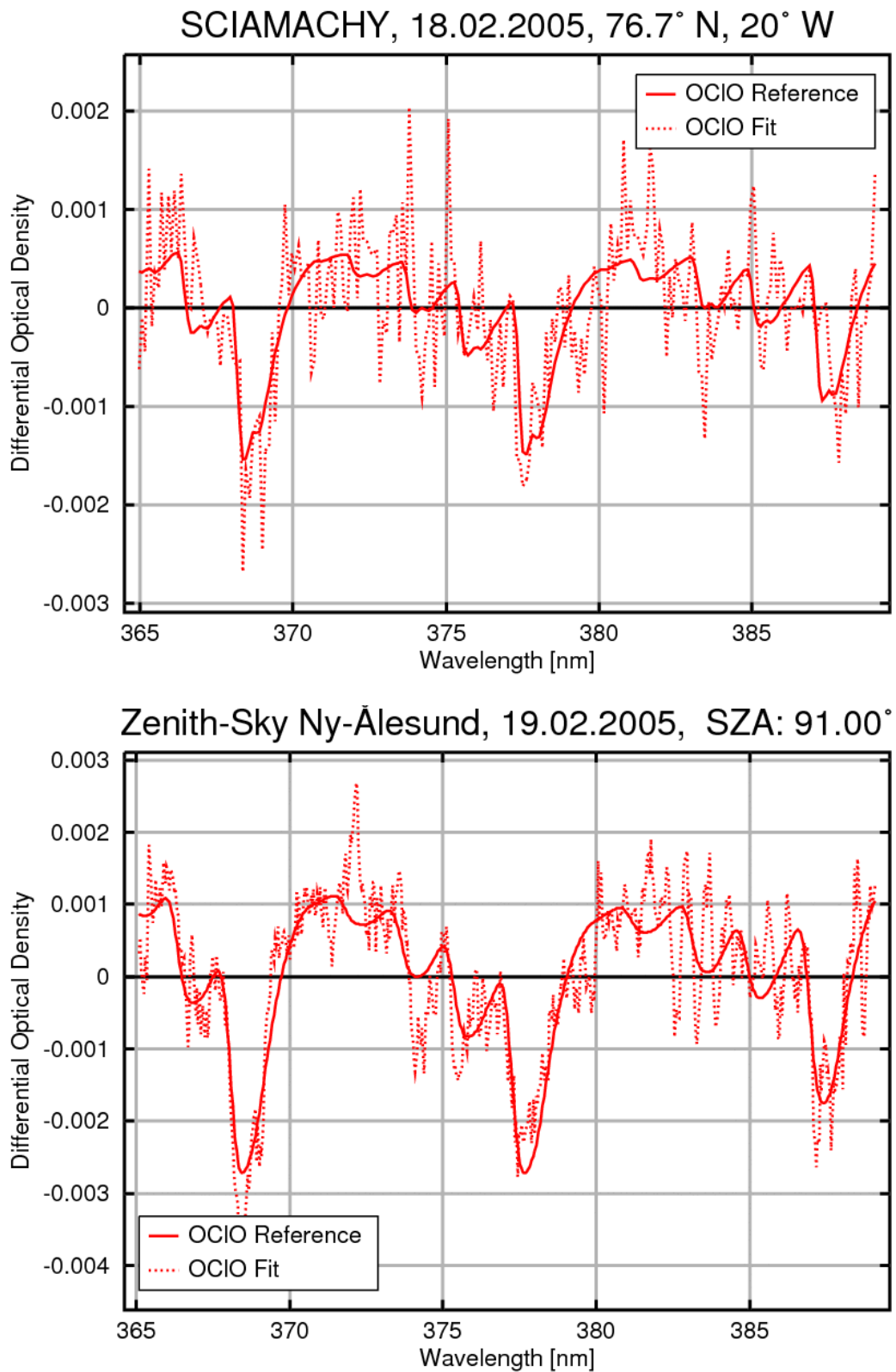


**Figure 6-3** Example of the OCIO retrieval fit for SCIAMACHY (top) and for ground-based measurement for Ny-Ålesund (bottom).

### 6.1.2 Ground-based measurement sites

Only measurements of light scattered in the zenith are used. The measurement sites include Ny-Ålesund (Svalbard, 79°N, 12°E), Summit (Greenland, 73°N, 38°) and Bremen (Germany, 53°N, 9°E) (see also chapter 5).

Similar settings for the retrieval and the same algorithm as for the SCIAMACHY data are applied to the ground-based spectra to retrieve the OCIO slant column densities. A measurement recorded at a small solar zenith angle is used as the reference or background spectrum for the whole time series. It is assumed that there is no OCIO present in the background spectrum. Hence retrieved SCDs are absolute and not differential. A fit example for an OCIO slant column density of approximately  $4 \times 10^{14}$  molecules  $\text{cm}^{-2}$  measured in Ny-Ålesund on 18<sup>th</sup> February is presented in Figure 6-3.

The spectral fit error is usually below 10% at 90° SZA ( $1\sigma$  error). This includes uncertainties introduced by spectral interferences of the different absorption cross sections, by the Ring effect, which results in in-filling of Fraunhofer lines and is produced by the inelastic rotational Raman scattering on air molecules, and by the wavelength calibration of the cross sections. The fit error increases towards smaller SZAs. Not included are systematic errors e.g. uncertainties in the absorption cross section of OCIO. The overall accuracy is about 20% at 90° SZA. The precision is much better. For most spectra, used in this study, the detection limit is smaller than  $5 \times 10^{13}$  molecules  $\text{cm}^{-2}$  at 90° SZA.

### 6.1.3 Modelling

The ground-based measurements and SCIAMACHY OCIO are compared to modelled slant column densities. These are calculated in three steps: First of all, the results of the three-dimensional (3D) chemical transport model SLIMCAT (Chipperfield, 1999) are extracted on a daily basis at 12:00 UT over the stations and thereafter, in a second step, used to initialise a set of one-dimensional (1D) photochemical stacked box models to obtain absorber profiles for the individual species at high temporal resolution. More details can be found in Sinnhuber et al. (2002; 2005) where an almost identical model is used to simulate stratospheric bromine chemistry.

The OCIO profiles as a function of solar zenith angle are then used to derive slant column densities for the ground-based observation geometry. This third step is accomplished with the radiative transfer model SCIATRAN (see section 4.1). SCIATRAN can include the correct treatment of the photochemistry along the line of sight, i.e. the change of concentration of the absorber with local SZA is taken into account when the light path is simulated. This so-called photochemical enhancement is necessary for photo-labile substances with a short lifetime such as OCIO.

## 6.2 Validation

In the following comparison, for SCIAMACHY data, all pixels with their centre within a radius of 200 km around the station are used and then the average SZA is given. The ground-based measurements are averaged over  $2^\circ$  SZA, i.e.  $\pm 1^\circ$  SZA around the SCIAMACHY SZA. The modelled column densities on the other hand are calculated at the exact angle.

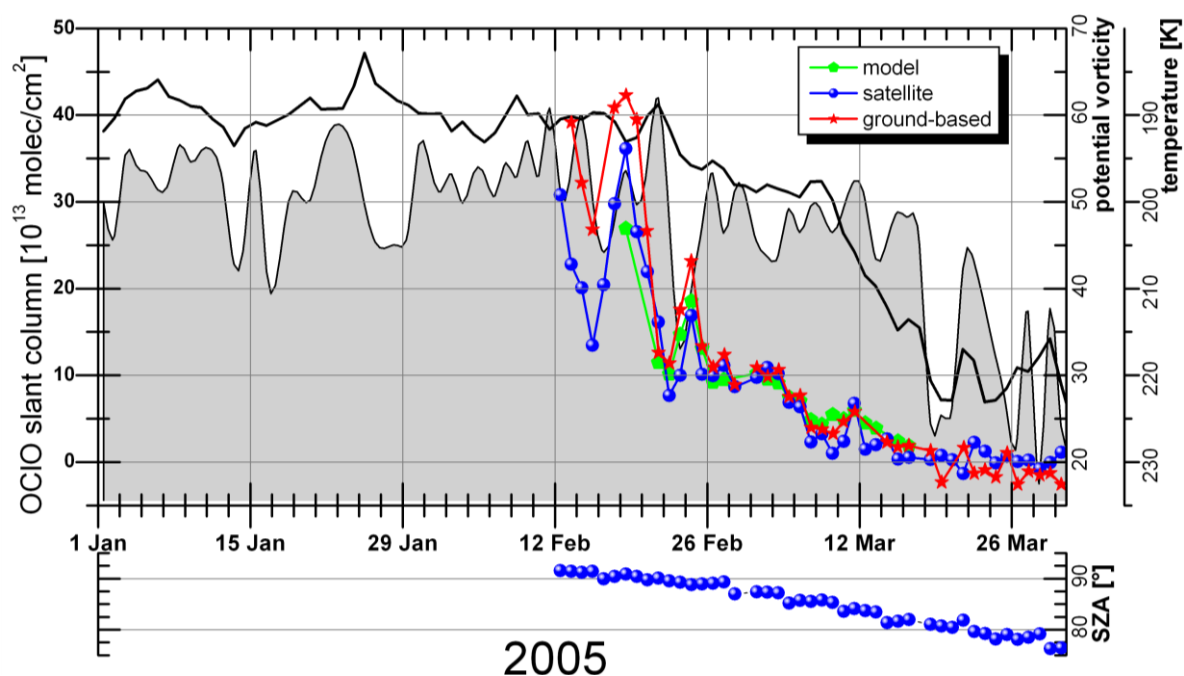


Figure 6-4 OCIO column densities over Ny-Ålesund in spring 2005. The ground-based data was sampled at the time of ENVISAT overpass. Also shown are potential vorticity (shaded area) and temperature (black line) at the 475 K isentropic surface.

Figure 6-4 and Figure 6-5 show the OCIO slant column densities for spring 2005 over Ny-Ålesund and Summit. Note that the SZA of SCIAMACHY measurement is changing over the time series since the overpass takes place at a fixed time close to the local noon. Therefore, the variation during this time period is mainly caused by the decreasing SZA and the associated increased photolysis rate of OCIO.

In Ny-Ålesund, apart from the first few days, the agreement between ground-based and satellite-measured OCIO column densities is excellent. As SZAs are rather large this early in year and in addition due to the rapid changes in photochemistry, only few photons are available reducing the signal-to-noise and introducing large scatter in the individual data of the ground-based measurements.

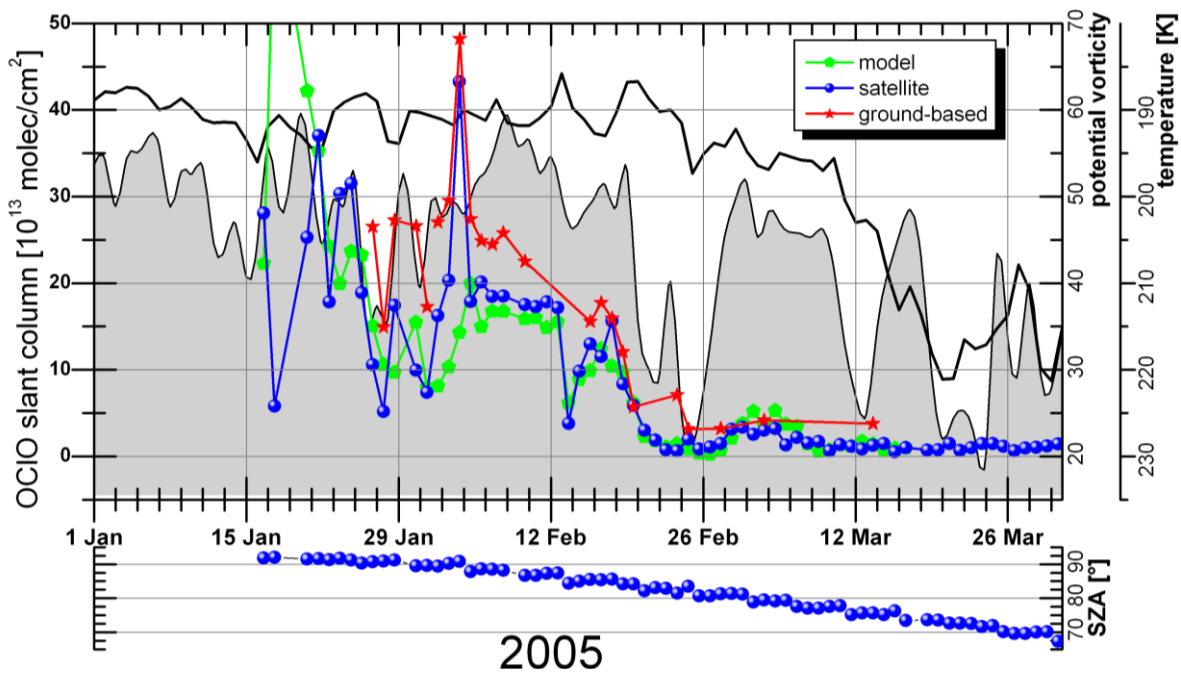


Figure 6-5 As Figure 6-4 but for Summit, Greenland.

It should be noted that although the radiative transfer model simulations consider the photochemical enhancement, the 1D model cannot reproduce possible horizontal gradients along the light path which can result from varying chlorine activation or different air mass origins. On the other hand, the ground-based and satellite-based measurements in fact probe the atmosphere several hundred kilometres away from the ground station. The exact location of the probed air in turn depends on the position of the sun but is approximately the same for SCIAMACHY and the ground-based instrument: In polar spring, the sun is always located towards the south resulting in a

shift of the measurement volume into this direction. In addition, as the SCIAMACHY data is averaged within a radius around the ground station and as there is a lack of measurements towards the polar night, i.e. the north, the majority of the measurements within this circle is shifted southward to smaller SZAs for days early in the year increasing the effect of the solar azimuth. A similar effect can be observed for the ground-based data: The averaging over a  $2^\circ$  range of SZAs results in a bias of the presented data to lower SZAs. In Ny-Ålesund, the SZA of  $90^\circ$  is only reached from February 18<sup>th</sup> onwards, but the time series already starts on 13<sup>th</sup> February indicating that the SZA for these days is rather at the lower limit of the accepted range given by the SCIAMACHY measurement.

Over Summit, the agreement is only fair and variable. The ground-based measurements are up to 50% larger than the SCIAMACHY data whereas SCIAMACHY column densities agree rather well with the modelled OCIO densities although the large peak on January 3<sup>rd</sup> is missed. On the other hand, to the end of the chlorine activation the qualitative agreement between model and satellite is excellent despite the fact that measurements are already close to the detection limit: Note the slight enhancement in OCIO in the beginning of March. Also the decrease of OCIO on February 13<sup>th</sup> is captured by the model but unfortunately missed by the ground-based measurement due to some equipment problems on these days.

### **6.3 OCIO over Bremen**

When the polar vortex becomes deformed and elongated, it is possible that chlorine-activated air masses are transported to mid-latitudes. This provides an opportunity for OCIO to also be detected above Bremen. In Figure 6-6, the ground-based and modelled data at  $90^\circ$  SZA are compared, including the SCIAMACHY data which was taken at much smaller SZAs and the corresponding modelled data at the time of over-flight. As the OCIO signal is small under these conditions, the SCIAMACHY data had to be normalised by subtraction of measurements over the Pacific to remove small instrumental drifts. Several episodes with enhanced OCIO are apparent in the data sets and excellent agreement is found between measurements and model results.

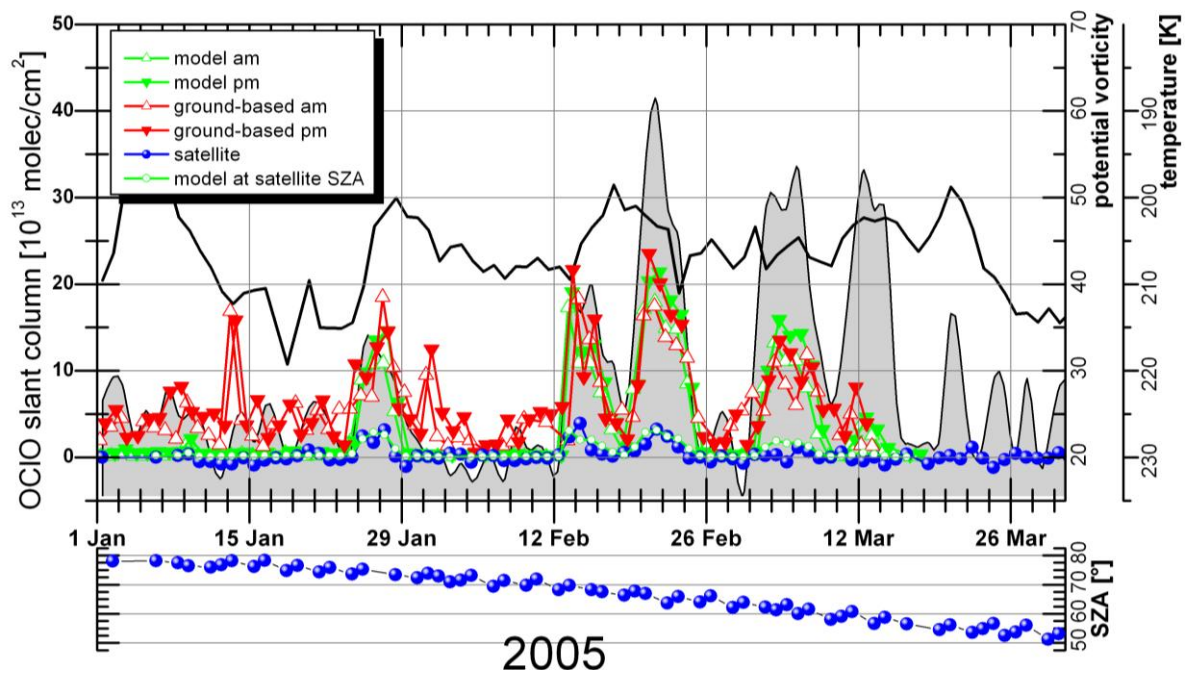
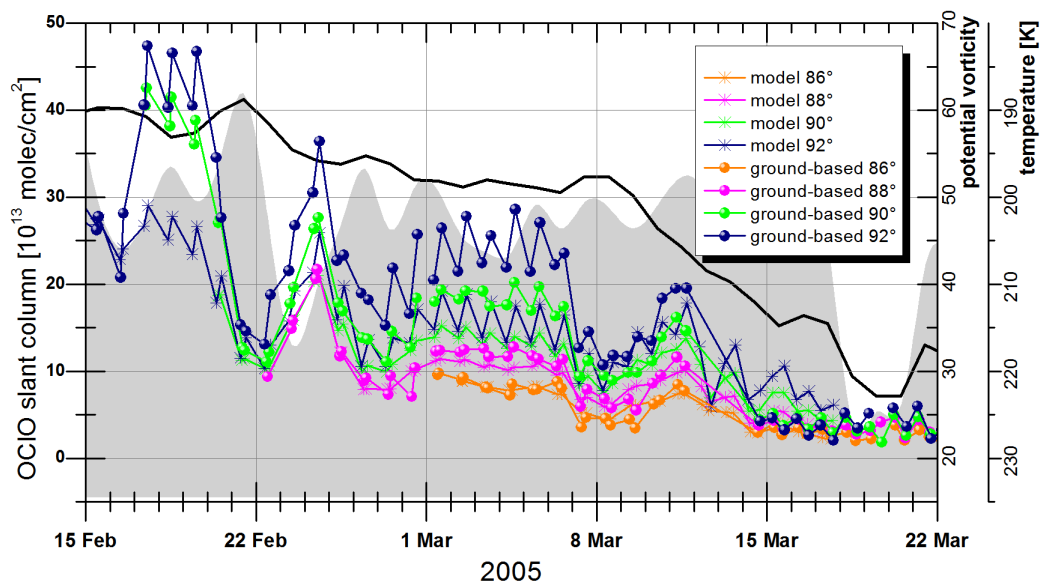


Figure 6-6 OCIO over Bremen: Model and ground-based data at 90° SZA and satellite at the SZA given below as well as model at the SCIAMACHY SZA, potential vorticity (shaded area) and temperature (black line) at the 475 K isentropic surface.

It is interesting to note that despite the relatively high sun, SCIAMACHY detects enhanced OCIO over Bremen during vortex excursions at SZAs as small as 65°. This illustrates the low detection limit of the measurements in spite of the offset problems which necessitate normalisation of the data. Unfortunately, the ground-based instrument in Bremen is not sensitive enough to detect these low amounts of OCIO present at these small SZAs, but modelled OCIO column densities reproduce the observations from satellite. This is confirmation for the ability of the model to accurately reproduce OCIO column densities at high sun.

## 6.4 SZA dependence of OCIO

For the SCIAMACHY validation, only the OCIO data at the time of the satellite overpass was used and very good agreement between model and measurements was found. However it is also interesting and conventional to investigate the agreement between model and ground-based measurements at different SZAs.



**Figure 6-7 Model and measurements at Ny-Ålesund at several SZAs. Potential vorticity (shaded area) and temperature (black line) at the 475 K isentropic surface are also shown. Note that the zigzag pattern in the curves for high SZAs is caused by the diurnal cycle of OCIO with higher concentrations in the afternoon.**

In 2005, Ny-Ålesund was positioned well inside the vortex until March 18<sup>th</sup>. Figure 6-7 shows the ground-based and modelled OCIO slant column densities for different SZAs. The general evolution of the chlorine activation as well as the AM/PM-variation is captured correctly by the model. In both data sets, individual events like the peak on February 24<sup>th</sup> are also picked up. However, the model generally underestimates the OCIO column densities. This effect increases towards larger SZA but also with increasing chlorine activation. On average, over the time period of strong chlorine activation until March 8<sup>th</sup>, the modelled column densities are too low by about 10% at 88° SZA, about 20% at 90° and about 30% at 92° SZA. This is interpreted as indicating missing chemistry in the model, either related to photochemistry at low sun or to the formation of OCIO, which seems to be underestimated. The next section will investigate these model and measurement differences by examining the sensitivity of the results towards changes in certain model parameters.

## 6.5 Model studies

The box model simulations as well as the initialisation of it, presented in the previous sections 6.2 to 6.4, were performed using the JPL 2002 (Sander et al., 2003b) recommendations for the kinetic and photochemical parameters including the reaction of BrONO<sub>2</sub> with O(<sup>3</sup>P) (Soller et al., 2001).

Uncertainties in chemistry models originate from the limited accuracy of our knowledge of:

- the involved rate and equilibrium constants
- the absorption cross sections and quantum yields
- the photolysis frequencies of molecules
- the initialisation amount of trace species in the model
- the meteorology

Recently, several sensitivity studies of stratospheric chlorine chemistry suggested the need for adjusting some of the reaction rates as well as the absorption cross sections and consequently the photolysis rates of certain gases. These will be discussed in the following sections. The JPL recommendations have partly been updated (Sander et al., 2006, in future referred to as JPL 2006). Here, sensitivity tests are performed for the box model simulations only and not for the simulation of the radiative transfer. Several scenarios will be investigated. The focus is on two days in Ny-Ålesund, i.e. 24<sup>th</sup> February with very high OCIO column densities and 4<sup>th</sup> March with moderate chlorine activation. At 90° SZA, the measurements exceed the modelled column densities by 30% on February 24<sup>th</sup> and by about 40% on March 4<sup>th</sup>, respectively.

### 6.5.1 ClO-dimer cycle chemistry

Comparisons of OCIO measurements with model results are rather sparse (e.g. Butz et al., 2007; Fussen et al., 2006). Studies mainly concentrate on the simulation of measured ClO (e.g. Schofield et al., 2008), sometimes in combination with Cl<sub>2</sub>O<sub>2</sub> measurements (e.g. von Hobe et al., 2005) testing the ClO-dimer cycle chemistry. In general, it has been found that modelled chlorine monoxide is too low (Pierson et al.,

1999; Solomon et al., 2000). Alongside the ClO-BrO catalytic cycle, the ClO-dimer cycle is a very efficient ozone depleting mechanism which is initiated by the ClO-self-reaction. The main product has been shown to be chlorine peroxide ClOOCl, which is the most stable one of the three possible isomers. The ClO-dimer is thermally decomposed in the presence of a third body M:



or removed by photolysis:



To increase the ClO and hence the ClOO concentrations, the partitioning within the active chlorine family ClO<sub>x</sub> (= ClO + 2 × ClOOCl) has to be shifted in favour of the ClO. This can be achieved in three ways: Either by increasing the photolysis rate or by speeding up the thermal decomposition of Cl<sub>2</sub>O<sub>2</sub> or by decreasing the forward rate constant of reaction (6.6).

### ***ClOOCl absorption cross section***

The absorption of radiation by the ClOOCl molecule leads to a preferred breaking of one of the two Cl-O bonds. There is disagreement whether or not another reaction channel forming two chlorine monoxide molecules is possible (see the discussion in JPL 2006):



Most studies agree that the quantum yield is very small since the weakest bond is between the chlorine atom and the oxygen atom (see Plenge et al. (2004) and JPL 2002 and references therein). Here, the only products for the photolysis of ClOOCl implemented in the box model are two chlorine atoms and O<sub>2</sub>.



The JPL 2002/06 recommendations for the ClOOCl absorption cross section are an average of several values (Cox and Hayman, 1988; Burkholder et al., 1990; Permien et al., 1988; DeMore and Tschuikow-Roux, 1990). More recent studies (Huder and DeMore, 1995; Pope et al., 2007) obtained significantly lower values in the tail region (see Figure 6-8) and overall, the spectra disagree by a factor of up to 20.

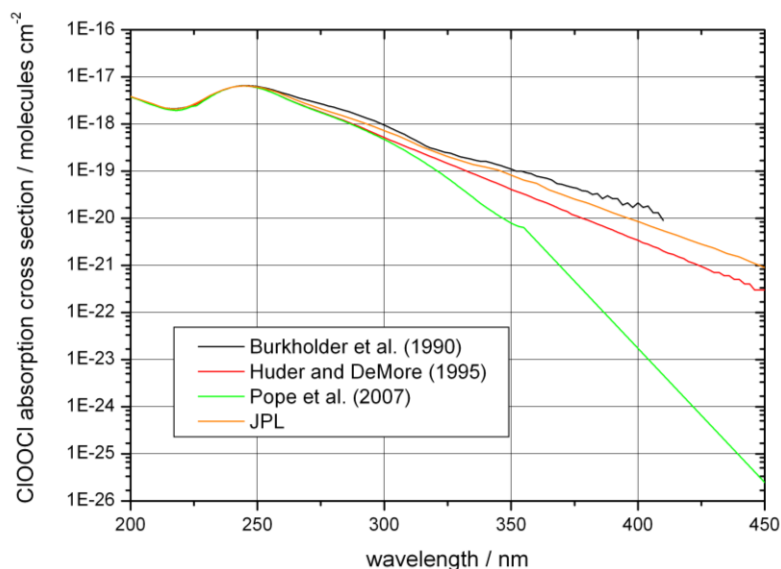


**Figure 6-8 ClOOCl absorption cross sections from selected studies.**

Avallone and Toohey (2001) studied the photolysis rate of ClOOCl with an airborne chemical conversion/resonance fluorescence instrument. By measuring BrO and ClO and assuming complete chlorine activation, they derived a photolysis rate which is rather at the lower limit of the individual cross sections applied for the JPL 2002 average, but on the other hand they consider the Huder and DeMore (1995) cross section as too small. These results are consistent with observations by Pierson et al. (1999). Measurements of ClO and Cl<sub>2</sub>O<sub>2</sub> of Stimpfle et al. (2004) are more in line with the absorption cross section by Burkholder et al. (1990). The Burkholder et al. cross section is recommended in model studies about ozone loss (e.g. Hoppel et al., 2005; Frieler et al., 2006).

Here, the extremes are tested: The Pope et al. (2007) cross section is the smallest available and the Burkholder et al. (1990) absorption cross section represents the upper limit of the set. Both have been extended to longer wavelengths by a log-linear extrapolation. The impact of using the different absorption cross sections for Cl<sub>2</sub>O<sub>2</sub> in modelled OCIO slant column densities is large (see Figure 6-9): up to 12% at 90° SZA for the Burkholder et al. cross section and up to -36% for the Pope et al. values (see Table 15). However, the change in absorption cross section causes simply an offset relative to the original model run and does not explain the diurnal behaviour of the OCIO.

### **Equilibrium constant between ClO and Cl<sub>2</sub>O<sub>2</sub>**

During the daytime, at smaller SZA, photolysis dominates over the thermal decomposition of Cl<sub>2</sub>O<sub>2</sub>. However, with increasing SZAs, the thermal decomposition becomes more important. Several laboratory studies determining the equilibrium constant between ClO and Cl<sub>2</sub>O<sub>2</sub> exist (Basco and Hunt, 1979; Cox and Hayman, 1988; Horowitz et al., 1994; Nickolaisen et al., 1994; Plenge et al., 2005; Bröske and Zabel, 2006). The JPL 2002/2006 recommendations are an average of Cox and Hayman (1988) and Nickolaisen et al. (1994), which were then extrapolated to the temperatures prevailing in the atmosphere. The recent photo-ionisation mass spectroscopy study by Plenge et al. (2005) suggests that the ClOOCl is less stable than previously assumed by a factor of 0.3. This observation is confirmed at atmospheric temperatures by several studies based on air-borne *in-situ* measurements (Brune et al., 1991; Pierson et al., 1999; Avallone and Toohey, 2001; Stimpfle et al., 2004; von Hobe et al., 2005) and night-time OSIRIS measurements (Berthet et al., 2005). An overview of the available constants is given in Table 14. By changing the equilibrium constant to the most recent value obtained by Bröske and Zabel (2006), a maximum increase in OCIO of 3% at 90° SZA is achieved. As expected, the difference increases towards larger SZAs (Figure 6-9).

**Table 14 Equilibrium constants from selected studies at a temperature of 195K**

	Equilibrium constant at 195 K [cm <sup>3</sup> /molecule]
Nickolaisen et al. (1994)	5.46 x 10 <sup>-8</sup>
JPL 2006	4.42 x 10 <sup>-8</sup>
JPL 2002	3.78 x 10 <sup>-8</sup>
Cox and Hayman (1988)	2.11 x 10 <sup>-8</sup>
Avallone and Toohey (2001)	2.03 x 10 <sup>-8</sup>
Bröske and Zabel (2006)	1.81 x 10 <sup>-8</sup>
Plenge et al. (2005)	1.14 x 10 <sup>-8</sup>
von Hobe et al. (2005)	0.49 x 10 <sup>-8</sup>

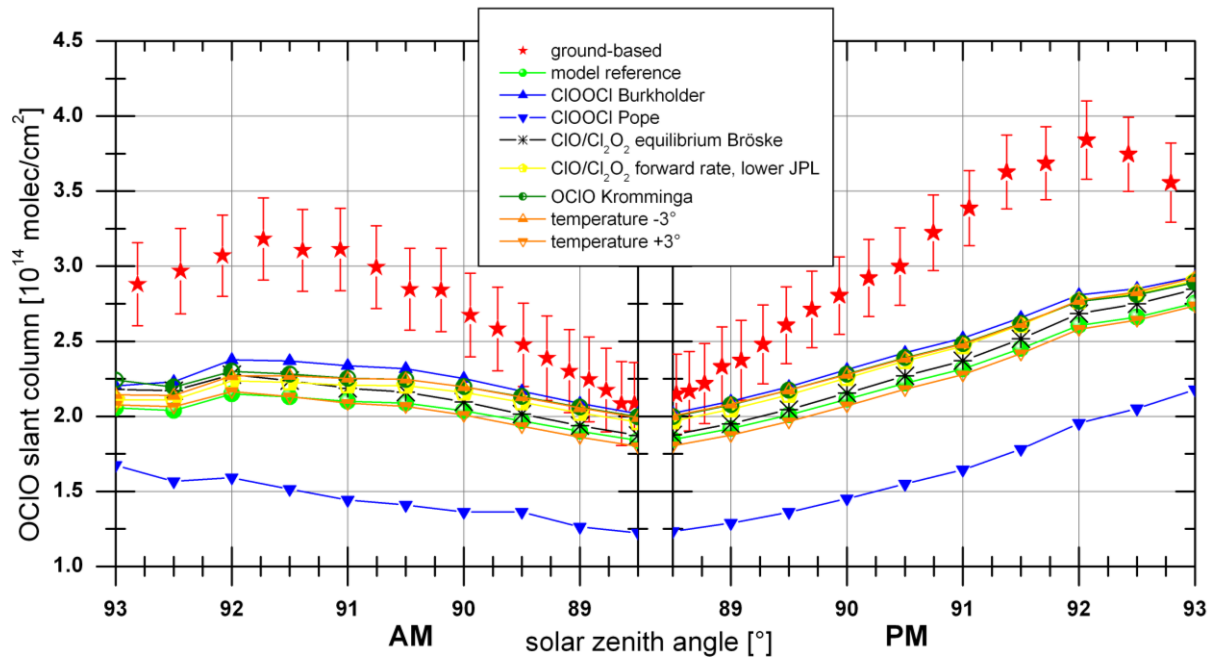


Figure 6-9 Sensitivity Studies (1<sup>st</sup> part): measurements and model calculations of OCIO slant column densities at Ny-Ålesund for February 24<sup>th</sup>. The error bars represent the  $2\sigma$  error of the measurements. Sensitivity studies have been undertaken by changing the mechanism. The different scenarios are explained in section 6.5.

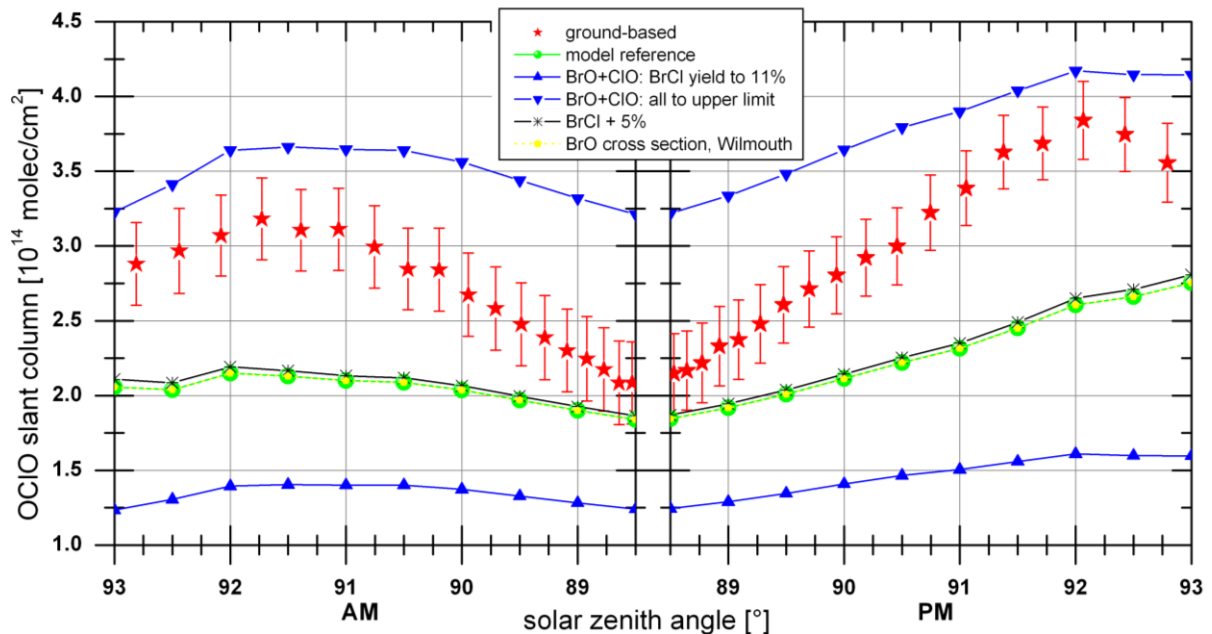


Figure 6-10 Sensitivity Studies (2<sup>nd</sup> part): As Figure 6-9.

### ***Forward rate constant for reaction (6.6)***

Another way to shift the partitioning within the Cl<sub>y</sub> family in favour of ClO in the model simulations is achieved by decreasing the forward rate constant for the three-body formation of Cl<sub>2</sub>O<sub>2</sub>. JPL 2006 is an average of the values by Bloss et al. (2001), Nikolaisen et al. (1994), and Trolier et al. (1990). The more recent study by Boakes et al. (2005) rather increased the rate for this reaction. However, adjusting the rate constant to the lower limit of the JPL recommendations increases the OCIO column density by 5% at 90° SZA (Figure 6-9) and yields similar values to using Nikolaisen et al. alone.

### ***Combined parameters***

Schofield et al. (2008) retrieved a possible range for the combinations of the three model parameters from airborne measurements of ClO and they are in favour of a decreased forward rate constant for the Cl<sub>2</sub>O<sub>2</sub> formation in combination with a smaller equilibrium constant in comparison to the JPL recommendations. The Pope et al. cross section cannot explain their observations.

Von Hobe et al. (2007) also reviewed the available laboratory references as well as rate theory calculations for the equilibrium constant between ClO and Cl<sub>2</sub>O<sub>2</sub>. They concluded that the best overall consistency with atmospheric observations as well as rate theory calculations can be found for the combination of the photolysis rates based on the Cl<sub>2</sub>O<sub>2</sub> absorption cross section in the range of Burkholder et al. (1990) and JPL 2006, the equilibrium constant by Plenge et al. (2005), and the Cl<sub>2</sub>O<sub>2</sub> formation rate constant by Nikolaisen et al. (1994). Although column densities are enhanced by up to 20%, this is still not sufficient to explain the ground observations of OCIO reported here.

### **6.5.2 BrO-ClO cycle chemistry**

Important for the modelling of the OCIO is of course the reaction of BrO with ClO as well as the photochemistry that influences the abundance of BrO. The following scenarios will investigate the sensitivity of the model on these parameters:

### ***Br<sub>y</sub> initialisation***

As the amount of BrO determines how much OCIO is produced (Schiller and Wahner, 1996), the implementation of the correct bromine load of the atmosphere is a crucial parameter for accurate modelling of the chlorine chemistry. In general, the inorganic bromine loading is assumed to originate from a combination of long-lived bromine species with contribution of ~16 ppt and very short-lived bromine source gases of 3 to 8 ppt (WMO, 2007).

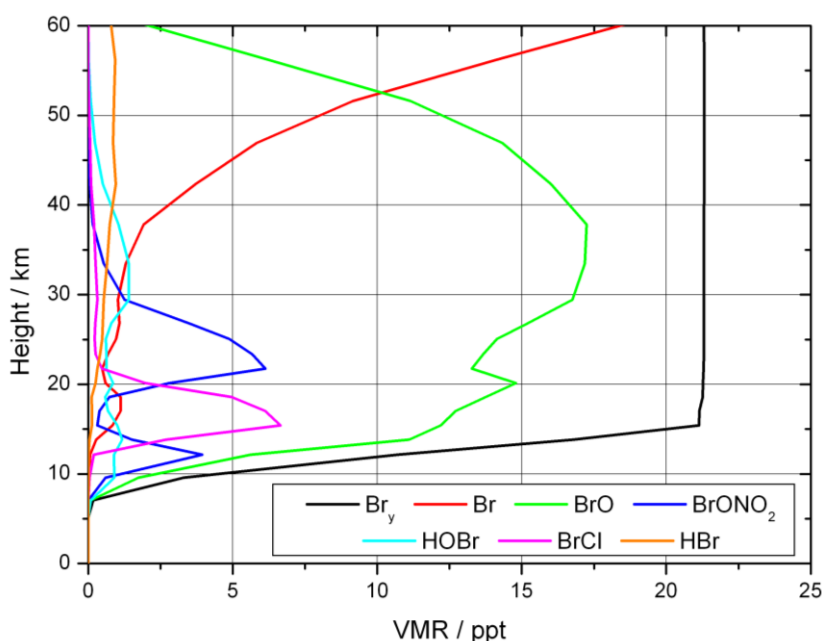


**Figure 6-11 Volume mixing ratios of inorganic bromine species and the total inorganic bromine load Br<sub>y</sub> for 4<sup>th</sup> March 2005 in the initialisation of the box model, i.e. at noon.**

BrO<sub>x</sub> (= BrO + BrCl) profiles derived from balloon-borne UV-visible absorption spectroscopy measurements of BrO suggest mixing ratios of up to 21 ppt (Fitzenberger et al., 2000; Dorf et al., 2006). Adopting these profiles did yield excellent agreement for the comparison of measured and modelled polar ozone loss (Frieler et al., 2006). Canty et al. (2005) estimated the BrO<sub>x</sub> to be 24 ppt and Hoppel et al. (2005) 22 to 24 ppt.

Recently, global satellite-based BrO profile measurements became possible with the SCIAMACHY instrument (Rozanov et al., 2004). A maximum BrO mixing ratio of  $12 \pm 4$  ppt at 89° SZA could be retrieved for both chosen days by averaging six profiles from February 24 to March 5. This is a much lower number than in the model initiali-

sation: The maximum mixing ratios of BrO are about 18 and 17 ppt and the total inorganic bromine Br<sub>y</sub> (= Br + BrO + BrONO<sub>2</sub> + HOBr + BrCl + HBr) about 21 ppt on the two days at a SZA of 90° (see Figure 6-11). This profile is achieved by scaling methyl bromide CH<sub>3</sub>Br to represent all bromine sources. This can underestimate the bromine load in the lower stratosphere when the other BrO precursors have a shorter lifetime than CH<sub>3</sub>Br (Hendrick et al., 2007; Theys et al., 2007; Schofield et al., 2006; Feng et al., 2007).

In order to test the effects towards the Br<sub>y</sub> initialisation, the profiles of the individual active bromine species are scaled to yield a maximum Br<sub>y</sub> load of 24 ppt and 18 ppt. The observed difference in the SCDs is symmetrical around the reference simulation with 14% at 90° and it shows only a slight SZA dependence.

### ***BrO absorption cross section***

The JPL 2006 recommendations for the BrO cross section were updated from that reported by Wahner et al. (1988) to the high-resolution data set by Wilmouth et al. (1999) resulting in negligible effects of less than 1% in the OCIO concentration (Figure 6-10).

### ***BrCl yield***

Bromine chloride BrCl is the product in one of the three channels of the BrO+ClO reaction. It is the main inorganic bromine species during the night in periods of chlorine activation (Sinnhuber et al., 2002). On the basis of a night-time OCIO profile measurement, Canty et al. (2005) suggest an increase in the BrCl yield from 7 to 11% , which is consistent within the error bars of the rate constants given by JPL 2002/2006. However, this gain will be on the expense of the two other reaction channels and therefore will decrease the OCIO concentration. Atkinson et al. (2000) found a constant partitioning of 8% for this yield over a wide temperature range motivating Sinnhuber et al. (2002) to increase the rate constants of all three branches. As expected, changes in the rates of the directly involved reactions lead to the most dramatic effects on the SCDs of up to 84% and -33% for increasing all or just one rate constant, respectively. However the increase and decrease stay constant over a SZA

range of up to about 91° resulting in much poorer agreement between model simulation and the measurements at local noon (Figure 6-10).

### ***BrCl absorption cross section***

Increasing the photolysis rate of BrCl will shift the partitioning of bromine to active forms such as BrO during daytime but would also cause a faster increase of BrO in the morning. The model takes into account the temperature dependence of the BrCl absorption cross section as suggested by Maric et al. (1994). Tellinghuisen (2003) reports the largest of the available cross sections with a peak height exceeding Maric et al. (1994) by about 2.5% around 375 nm whereas the cross section by Hubinger and Nee (1995) is about 3.5% smaller in this wavelength region. Since the absorption cross sections exhibit a rather smooth distribution with wavelength, a simple scaling by 5% seems to be appropriate in order to simulate larger cross section. However, this increase changes the OCIO column densities by only 1% (Figure 6-10).

### **6.5.3 Further sensitivity tests**

Before testing some physical properties in the model, the sensitivity towards changes in the OCIO cross section will be investigated:

### ***OCIO absorption cross section***

For the DOAS method, the absolute cross sections are not of interest. However, for the calculation of the photolysis rate of a trace gas, absolutely calibrated spectra are required. The absorption cross sections for OCIO at a temperature of 204 K, recommended by JPL 2002/06, are taken from Wahner et al. (1987). The DOAS fits of the measurements presented here are performed applying the cross sections by Kromminga et al. (2003) at 213 K. Kromminga et al. report band peaks ~8% smaller than Wahner et al. leading to a constant offset in the slant column densities for OCIO (Figure 6-9).

## Stratospheric temperatures

An accurate knowledge of the temperature in the model simulations is crucial since it determines whether chlorine will be activated or not. Figure 6-12 shows the temperature profiles for the two selected days. Gorbunov and Kornblüh (2003) have investigated the differences of the ECMWF temperature fields with data derived from Challenging Minisatellite Payload (CHAMP) and they find differences that do not exceed 1 K for polar regions. It is possible that the temperature of an air mass at a higher spatial resolution might locally drop below the threshold for the formation of PSCs. Such effects are missed by the coarser vertical resolution of the model profile. In order to test the sensitivity of the simulations towards the temperature, a constant offset of 3 K has been subtracted. Decreasing the temperature, increases the vertical extent of the layer where chlorine activation is possible leading to higher concentrations of OCIO of up to 9% at 90° SZA (Figure 6-9).

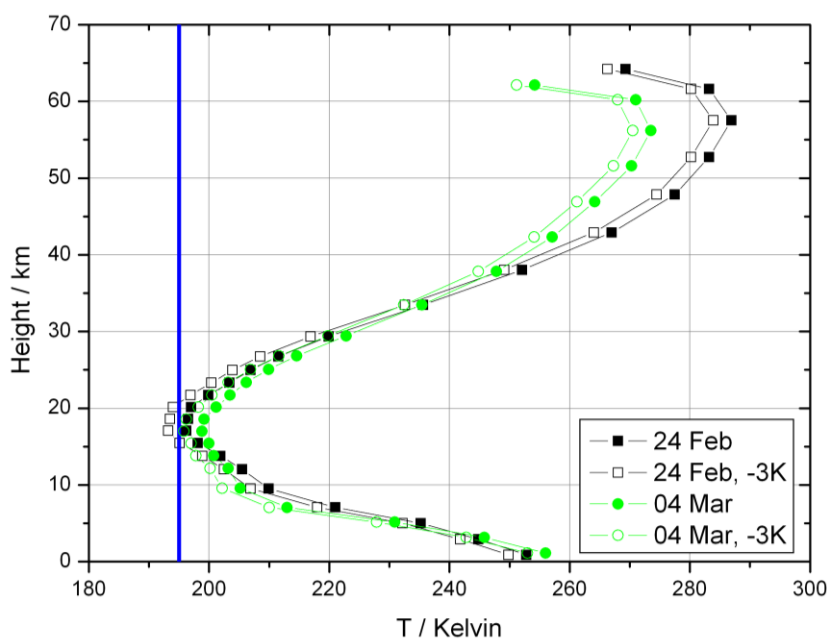


Figure 6-12 Temperature profiles in the model. The blue line represents the threshold for the formation of PSCs.

## Model albedo, photolysis rate calculations, and NO<sub>2</sub> initialisation

Changes in the albedo in the model also have minor impacts of about 2%. As expected, the photolysis of OCIO and consequently the concentration decreases to-

wards larger albedo. However, this does not influence the SZA dependence of the OCIO column densities up to 91° SZA.

Furthermore, the photolysis rates of the box model calculated for OCIO have been checked for consistency with SCIATRAN. The rates of the two models agree within a few percent. Also, reducing NO<sub>2</sub> by 5% to impede the formation of the reservoir species chlorine nitrate yields a negligible effect.

## 6.6 Discussion and summary

Table 15 summarises the contributions from the different scenarios to the OCIO slant column densities at 90° SZA for the two chosen days. The SZA dependence is presented for February 24<sup>th</sup> only in Figure 6-9 and Figure 6-10.

One of the largest uncertainties of the parameters considered here is the BrO load in the stratosphere. Here, the total bromine load was increased by 3 ppt. But measurements of the BrO profiles are sparse and a thorough study of the SZA dependence has not been performed so far. Also adjusting the rate constant of the BrO+ClO reaction has a large influence on the OCIO SCD but introduces only an offset in the data. However, to reproduce the measurements a scaling is needed since the column densities agree for low SZAs. In summary, none of the selected scenarios can fully explain the diurnal variation of the OCIO observations or the absolute values at high SZAs. In the following, some possible additional mechanisms are discussed although implementations in the model are beyond the scope of this study.

Laboratory measurements have shown that OCIO evaporates from ice surfaces via heterogeneous reactions after being exposed to ClO radicals (McKeachie et al., 2004). It is suggested that this release is initiated by the formation of the ClO•H<sub>2</sub>O radical complex (Francisco and Sander, 1995; Galvez and Gomez, 2007). This could potentially increase the OCIO column densities.

Thornton et al. (2003; 2005) report measurements of ClO in the lowermost stratosphere at high latitude regions. They suggest heterogeneous chlorine activation on cold particulate surfaces as water-rich background aerosols containing sulphate and nitrate.

**Table 15 Summary of the sensitivity studies of the box model in comparison to the JPL 2002 simulation at a SZA of 90°. Texts in bold characters represent scenarios shown in Figure 6-9 and Figure 6-10. More details can be found in the section 6.5.**

Parameter	Study	Differences in OCIO to the reference scenario at 90° SZA			
		2005-02-24		2005-03-04	
		AM	PM	AM	PM
ClOOCl absorption cross section	<b>Burkholder et al.</b>	+ 11%	+ 9%	+ 12%	+ 9%
	<b>Pope et al.</b>	-33%	-31%	-36%	-31%
ClO/Cl <sub>2</sub> O <sub>2</sub> equilibrium constant	<b>Bröske and Zabel</b>	+ 3%	+ 2%	+ 3%	+ 1%
ClO/Cl <sub>2</sub> O <sub>2</sub> forward rate constant	<b>lower JPL limit/ Nickolaisen et al.</b>	+ 5%	+ 5%	+ 5%	+ 5%
Combination according to von Hobe et al.	Burkholder et al. + Plenge et al. + Nickolaisen et al.	+ 19%	+ 17%	+ 20%	+ 15%
Br <sub>y</sub> initialisation	+ 3 ppt	+ 14%	+ 14%	+ 14%	+ 14%
	- 3 ppt	-14%	-14%	-14%	-14%
BrO cross section	<b>Wilmouth et al.</b>	<<1%	<<1%	<<1%	<<1%
BrO+ClO rate constants	<b>BrCl yield to 11%</b>	-33%	-33%	-29%	-30%
	<b>all react. to upper limit</b>	+ 75%	+ 72%	+ 84%	+ 79%
BrCl absorption cross section	<b>+ 5%</b>	+ 1%	+ 1%	+ 1%	+ 1%
OCIO absorption cross section	<b>Kromminga et al.</b>	+ 8%	+ 8%	+ 8%	+ 8%
Temperature initialisation	<b>-3 K</b>	+ 8%	+ 8%	+ 9%	+ 9%

A chlorine species neglected in the model is Cl<sub>2</sub>. If significant amounts of active chlorine are stored in the form of this molecule, then this would give rise to an additional source of a SZA dependent formation of ClO and consequently OCIO in the model. However, the explicit treatment of Cl<sub>2</sub> would mainly increase the morning concentrations of OCIO but leave the afternoon concentrations unchanged.

Possible roles of the two other  $\text{Cl}_2\text{O}_2$  isomers chloryl chloride  $\text{ClClO}_2$  and chlorine chlorite  $\text{ClOClO}$  have been discussed in the literature before (Plenge et al., 2004; Bloss et al., 2001). Although these two species are much less stable than  $\text{ClOOCl}$ , an additional source for  $\text{OCIO}$  could arise from their photolysis.

To summarise, the measurements described in this study, are the first validation attempt of the  $\text{OCIO}$  retrieved from  $\text{SCIAMACHY}$  observations made by comparison with ground-based remote sensing  $\text{DOAS}$  measurements. The agreement is excellent and  $\text{OCIO}$  could even be detected over the mid-latitude station Bremen during vortex excursions. It can be concluded that  $\text{SCIAMACHY}$  is delivering  $\text{OCIO}$  slant column densities with high accuracy and can thus be used to study the long-term evolution of stratospheric chlorine loading.

The  $\text{SLIMCAT}$ -initialised stacked box model simulations of  $\text{OCIO}$  show very good qualitative agreement with the measurements but somewhat underestimate the measured amount of  $\text{OCIO}$ , in particular at low sun and large chlorine activation. In addition to the overall underestimation, the model does not capture the magnitude of the  $\text{OCIO}$  variation as a function of  $\text{SZA}$ . The modelled amount of  $\text{OCIO}$  can be varied by changing the chemistry in the model within the uncertainties of absorption cross-sections and rate coefficients. None of the sensitivity studies performed lead to a result which was in good agreement with the measurements with respect to the  $\text{SZA}$  dependence of the  $\text{OCIO}$  column density. From the model simulations of the  $\text{OCIO}$  behaviour, it can be concluded that our knowledge of the physical and chemical processing within the vortex is not sufficient to explain the  $\text{OCIO}$  behaviour adequately. This implies that the chlorine chemistry and its relevant mechanisms for the formation of  $\text{OCIO}$  taking into account the range of the accuracies of the laboratory kinetics are not completely understood. Further research especially for the key rate constants of the chemical and photochemical reactions involving the chlorine oxides is needed.

Further validation of  $\text{SCIAMACHY}$   $\text{OCIO}$  in the Southern Hemisphere using ground based measurements and comparisons with models will provide more information with respect to our understanding of the  $\text{OCIO}$  sources and sinks and related halogen chemistry. A comparison of  $\text{OCIO}$  retrieved with  $\text{GOME}$  and the new  $\text{GOME-2}$  data in the period of overlapping measurements would be valuable to produce consolidated data sets.

## 7 Summary

In this work, MAX-DOAS instruments have been installed and maintained at the permanent measurement site Ny-Ålesund since 2002 as well as for campaigns in List and Andøya for six months and four weeks, respectively. Spectra measured at List, Ny-Ålesund, Kaashidhoo, Andøya, and Heraklion have been evaluated for tropospheric halogen oxides with the method of the differential optical absorption spectroscopy for overall more than 1600 days of data. Iodine monoxide and bromine monoxide concentrations or upper limits of these species have been quantified with the help of a radiative transfer model and interpreted when available with independent data sets. In summary, IO was detected in Ny-Ålesund, List, and Kaashidhoo with concentrations of up to 0.4 ppt, 2.2 ppt, and 2.8 ppt, respectively, but was below the detection limit in Andøya and Heraklion. The stated concentrations assume a homogeneous distribution in the surface layer. For Ny-Ålesund as well as List, a possibly seasonal cycle with maximum in summer can be inferred from the data. Tropospheric BrO could not be identified in any of the spectra.

Model studies for the radiative transfer have been carried out with SCIATRAN to assess the information content of MAX-DOAS measurements towards tropospheric species. The influences of the telescope elevation angle, the azimuth angle between sun and telescope, aerosols, the wavelength, and the surface reflectivity have been studied. It was found that mostly the aerosol extinction determines the sensitivity of MAX-DOAS observation and is a crucial parameter when estimating concentrations of absorbers in the boundary layer.

Furthermore, stratospheric OClO has been retrieved by zenith-sky DOAS observations for Ny-Ålesund, Summit, and Bremen for spring 2005. A chemical stacked box model initialised with SLIMCAT data was used to simulate profiles and these were converted into slant column densities considering the changing solar geometry along the light path with the help of SCIATRAN. These column densities have been compared to the ground-based measurements directly as well as to observations by the satellite instrument SCIAMACHY. For the time of the overpass of SCIAMACHY just before local noon, all three datasets show excellent agreement. But large discrepancies were found between model and measurements for large solar zenith angles. Sensitivity studies have been performed for the photochemical processes determin-

ing the OCIO concentrations and the BrO+ClO reaction in combination with the uncertainties of the stratospheric BrO concentrations have been identified as the main unknown factors.

## Danksagung / Acknowledgements

An dieser Stelle möchte ich den Menschen danken, die mich während dieser Arbeit unterstützt haben und zum Gelingen dieser Studie beigetragen haben.

My supervisor, Prof. John Burrows deserves my gratitude for his guidance and support over many years.

Vielen Dank auch an Prof. Otto Schrems für die Übernahme des Zweitgutachtens.

Speziell bei Folkard Wittrock und Andreas Richter möchte ich mich für die gute Zusammenarbeit, für die unterhaltsame Zeit auf gemeinsamen Meßkampagnen und für die interessanten Diskussionen bedanken, aber auch bei Alexei Rozanov, der immer wieder meine Fragen zum Strahlungstransport beantwortet hat und SCIATRAN meinen Wünschen entsprechend angepaßt hat. An dieser Stelle ist auch Thomas Wagner vom MPI Mainz zu erwähnen, der sehr viel Zeit in die Block AMF Studie investiert hat. Vielen Dank auch an Ninad Sheode und Björn-Martin Sinnhuber, die mich in die chemische Modellierung eingeführt haben.

Ferner möchte ich mich bei allen Kollegen bedanken, die mich über die Jahre begleitet haben; I am also very grateful to all colleagues over many years: Annette, Andreas, Sixten, Thomas, Marco, Hendrick, Ping, Bernd, Anne-Marie, Astrid, Silvia, Anja, Henning, Mihalis, Yemi, Tibi, Juan-Carlos, Nicole, Mareile, Tine, Peter, Lola, Bilgehan, Deniz, Lars, Jörn, Tilman, Sandip, Vladimir, Miriam, Sabine, Birgit, Petra, Susanne, Heidemarie, Anoop, Deborah, Tomas, Russell, Sarah, Charlotte, Kate, Lisa, Roisin, Pete, Trevor, Stewart, Ben, Maite and Andy.

Also, I would like to acknowledge Prof. John Plane's patience.

Diese Arbeit wäre so nicht möglich gewesen ohne die Hilfe all der Stationsleiter, Ingenieure und Institute, welche die diversen Stationen betreut und auch finanziert haben: Das sind vor allem das Alfred-Wegener-Institut und die zahlreichen Stationsbetreuer für die Koldewey-Station auf Spitzbergen, die Wattenmeerstation und speziell Werner Armonies und Nils Volkenborn auf Sylt, Michael Gausa und Reidar Lyngra für die Kampagne in Andøya, KNMI und Ellen Brinksma für die Kampagne in Cabauw, die National Science Foundation für das Greenland Summit camp, die Universität

Kreta für das MAX-DOAS in Heraklion und das Kaashidhoo Climate Observatory für die Messungen auf den Malediven.

Ein großes Dankeschön gilt auch meiner Familie, die mich über all die Jahre unterstützt hat.

## List of acronyms

1D	one-dimensional
AM	ante meridiem
AMF	air mass factor
AOD	aerosol optical depth
BL	boundary layer
BREAM	Bremen Advanced MAX-DOAS Retrieval Algorithm
CCD	charge-coupled device
CCN	cloud condensation nuclei
CFC	chlorofluorocarbons
CHAMP	Challenging Minisatellite Payload
dAMF	differential air mass factor
DANDELIONS	Dutch Aerosol and Nitrogen Dioxide Experiments for Validation of OMI and SCIAMACHY
DL	detection limit
DMS	dimethyl sulphide
DNA	deoxyribonucleic acid
DOAS	differential optical absorption spectroscopy
dSCD	differential slant column density
ECMWF	European Centre for Medium-Range Weather Forecasts
ENVISAT	Environmental Satellite
FWHM	full width half maximum
GOME	Global Monitoring Experiment
GOMOS	Global Ozone Monitoring by Occultation of Stars
ID	integro-differential

INDOEX	Indian Ocean Experiment
LOS	line of sight
MAX	multi-axis
MBL	marine boundary layer
MLS	Microwave Limb Sounder
NDACC	Network for the Detection of Atmospheric Change and Climate
NDSC	Network for the Detection of Stratospheric Change
OMI	Ozone Monitoring Instrument
OSIRIS	Odin Spectrometer and Infrared Imager System
PBL	planetary boundary layer
PM	post meridiem
PSC	polar stratospheric clouds
PVC	polyvinyl chloride
RMS	root mean square
RTE	radiative transfer equation
RTM	radiative transfer model
SAA	solar azimuth angle
SCD	slant column density
SCIAMACHY	Scanning Imaging Spectrometer for Atmospheric Cartography
SCIATRAN	Bremen radiative transfer model
SLIMCAT	Three-dimensional atmospheric chemical transport model
SMR	Sub-millimeter Microwave Radiometer
SZA	solar zenith angle
TOA	top of the atmosphere
UARS	Upper Atmosphere Research Satellite
UT	universal time

UV	ultra-violet
VCD	vertical column density
VMR	volume mixing ratio
VOD	vertical optical depth



# Bibliography

Alicke, B., Hebestreit, K., Stutz, J., and Platt, U.: Iodine oxide in the marine boundary layer, *Nature*, 397, 572-573, 1999.

Aliwell, S. R., Jones, R. L., and Fish, D. J.: Mid-latitude observations of the seasonal variation of BrO .1. Zenith-sky measurements, *Geophysical Research Letters*, 24, 1195-1198, 1997.

Aliwell, S. R., Van Roozendaal, M., Johnston, P. V., Richter, A., Wagner, T., Arlander, D. W., Burrows, J. P., Fish, D. J., Jones, R. L., Tørnkvist, K. K., Lambert, J. C., Pfeilsticker, K., and Pundt, I.: Analysis for BrO in zenith-sky spectra: An intercomparison exercise for analysis improvement, *Journal of Geophysical Research-Atmospheres*, 107, 20, 4199, doi:10.1029/2001jd000329, 2002.

Allan, B. J., McFiggans, G., Plane, J. M. C., and Coe, H.: Observations of iodine monoxide in the remote marine boundary layer, *Journal of Geophysical Research-Atmospheres*, 105, 14363-14369, 2000.

Allan, B. J., Plane, J. M. C., and McFiggans, G.: Observations of OIO in the remote marine boundary layer, *Geophysical Research Letters*, 28, 1945-1948, 2001.

Andrews, D. G., Holton, J. R., and Leovy, C. B.: *Middle Atmosphere Dynamics*, Academic Press, 1987.

Atkinson, R., Baulch, D. L., Cox, R. A., Hampson, R. F., Kerr, J. A., Rossi, M. J., and Troe, J.: Evaluated kinetic and photochemical data for atmospheric chemistry: Supplement VIII, halogen species - IUPAC Subcommittee on Gas Kinetic Data Evaluation for Atmospheric Chemistry, *J. Phys. Chem. Ref. Data*, 29, 167-266, 2000.

Avallone, L. M., and Toohey, D. W.: Tests of halogen photochemistry using in situ measurements of ClO and BrO in the lower polar stratosphere, *Journal of Geophysical Research-Atmospheres*, 106, 10411-10421, 2001.

Bale, C. S. E., Ingham, T., Commane, R., Heard, D. E., and Bloss, W. J.: Novel measurements of atmospheric iodine species by resonance fluorescence, *Journal of Atmospheric Chemistry*, DOI 10.1007/s10874-008-9108-z, 2008.

Ball, S. M., and Jones, R. L.: Broad-band cavity ring-down spectroscopy, *Chem. Rev.*, 103, 5239-5262, 10.1021/cr020523k, 2003.

Barret, B., Ricaud, P., Santee, M. L., Attie, J. L., Urban, J., Le Flochmoen, E., Berthet, G., Murtagh, D., Eriksson, P., Jones, A., de la Noe, J., Dupuy, E., Froidevaux, L., Livesey, N. J., Waters, J. W., and Filipiak, M. J.: Intercomparisons of trace gases profiles from the Odin/SMR and Aura/MLS limb sounders, *Journal of Geophysical Research-Atmospheres*, 111, 11, D21302, doi:10.1029/2006jd007305, 2006.

Barrie, L. A., Bottenheim, J. W., Schnell, R. C., Crutzen, P. J., and Rasmussen, R. A.: Ozone destruction and photochemical reactions at polar sunrise in the lower Arctic atmosphere, *Nature*, 334, 138-141, 1988.

Basco, N., and Hunt, J. E.: Mutual Combination of ClO Radicals, *International Journal of Chemical Kinetics*, 11, 649-664, 1979.

Bates, D. R., and Nicolet, M.: The Photochemistry of Atmospheric Water Vapor, *Journal of Geophysical Research*, 55, 301-327, 1950.

Berthet, G., Ricaud, P., Lefevre, F., Le Flochmoen, E., Urban, J., Barret, B., Lautie, N., Dupuy, E., De la Noe, J., and Murtagh, D.: Nighttime chlorine monoxide observations by the Odin satellite and implications for the ClO/Cl<sub>2</sub>O<sub>2</sub> equilibrium, *Geophysical Research Letters*, 32, 5, L11812, doi:10.1029/2005gl022649, 2005.

Bloss, W. J., Nickolaisen, S. L., Salawitch, R. J., Friedl, R. R., and Sander, S. P.: Kinetics of the ClO self-reaction and 210 nm absorption cross section of the ClO dimer, *Journal of Physical Chemistry A*, 105, 11226-11239, 2001.

Bloss, W. J., Lee, J. D., Johnson, G. P., Sommariva, R., Heard, D. E., Saiz-Lopez, A., Plane, J. M. C., McFiggans, G., Coe, H., Flynn, M., Williams, P., Rickard, A. R., and Fleming, Z. L.: Impact of halogen monoxide chemistry upon boundary layer OH and HO<sub>2</sub> concentrations at a coastal site, *Geophysical Research Letters*, 32, 4, L06814, 10.1029/2004gl022084, 2005.

Boakes, G., Mok, W. H. H., and Rowley, D. M.: Kinetic studies of the ClO plus ClO association reaction as a function of temperature and pressure, *Physical Chemistry Chemical Physics*, 7, 4102-4113, 2005.

Bobrowski, N., Hönninger, G., Galle, B., and Platt, U.: Detection of bromine monoxide in a volcanic plume, *Nature*, 423, 273-276, 2003.

Bobrowski, N., von Glasow, R., Aiuppa, A., Inguaggiato, S., Louban, I., Ibrahim, O. W., and Platt, U.: Reactive halogen chemistry in volcanic plumes, *Journal of Geophysical Research-Atmospheres*, 112, Artn D06311, Doi 10.1029/2006jd007206, 2007.

Bogumil, K., Orphal, J., Homann, T., Voigt, S., Spietz, P., Fleischmann, O. C., Vogel, A., Hartmann, M., Kromminga, H., Bovensmann, H., Frerick, J., and Burrows, J. P.: Measurements of molecular absorption spectra with the SCIAMACHY pre-flight model: instrument characterization and reference data for atmospheric remote-sensing in the 230-2380 nm region, *Journal of Photochemistry and Photobiology a-Chemistry*, 157, 167-184, 2003.

Bösch, H., Camy-Peyret, C., Chipperfield, M. P., Fitzenberger, R., Harder, H., Platt, U., and Pfeilsticker, K.: Upper limits of stratospheric IO and OIO inferred from center-to-limb-darkening-corrected balloon-borne solar occultation visible spectra: Implications for total gaseous iodine and stratospheric ozone, *Journal of Geophysical Research-Atmospheres*, 108, doi: 10.1029/2002JD003078, 2003.

Bottenheim, J. W., Gallant, A. G., and Brice, K. A.: Measurements of NO<sub>y</sub> Species and O<sub>3</sub> at 82°N Latitude, *Geophysical Research Letters*, 13, 113-116, 1986.

Bovensmann, H., Burrows, J. P., Buchwitz, M., Frerick, J., Noel, S., Rozanov, V. V., Chance, K. V., and Goede, A. P. H.: SCIAMACHY: Mission objectives and measurement modes, *Journal of the Atmospheric Sciences*, 56, 127-150, 1999.

Brasseur, G. P., Orlando, J. J., Tyndall, G. S., and National Center for Atmospheric Research (U.S.): Atmospheric chemistry and global change, *Topics in environmental chemistry*, Oxford University Press, New York, 654 pp., 1999.

Brewer, A. W., McElroy, C. T., and Kerr, J. B.: Nitrogen dioxide concentrations in the atmosphere, *Nature*, 246, 129-133, 1973.

Brinksma, E. J., Pinardi, G., Volten, H., Braak, R., Richter, A., Schönhardt, A., van Roozendaal, M., Fayt, C., Hermans, C., Dirksen, R. J., Vlemmix, T., Berkhout, A. J. C., Swart, D. P. J., Oetjen, H., Wittrock, F., Wagner, T., Ibrahim, O. W., de Leeuw, G., Moerman, M., Curier,

R. L., Celarier, E. A., Cede, A., Knap, W. H., Veeffkind, J. P., Eskes, H. J., Allaart, M., Rothe, R., Piters, A. J. M., and Levelt, P. F.: The 2005 and 2006 DANDELIONS NO<sub>2</sub> and aerosol intercomparison campaigns, *Journal of Geophysical Research-Atmospheres*, 113, 18, D16s46, doi:10.1029/2007jd008808, 2008.

Bröske, R., and Zabel, F.: Thermal decomposition of ClOOCl, *Journal of Physical Chemistry A*, 110, 3280-3288, 2006.

Brune, W. H., and Anderson, J. G.: In situ observations of midlatitude stratospheric ClO and BrO, *Geophysical Research Letters*, 13, 1391-1394, 1986.

Brune, W. H., Anderson, J. G., Toohey, D. W., Fahey, D. W., Kawa, S. R., Jones, R. L., McKenna, D. S., and Poole, L. R.: The potential for ozone depletion in the Arctic polar stratosphere, *Science*, 252, 1260-1266, 1991.

Bruns, M., Bühler, S. A., Burrows, J. P., Heue, K. P., Platt, U., Pundt, I., Richter, A., Rozanov, A., Wagner, T., and Wang, P.: Retrieval of profile information from airborne multi-axis UV-visible skylight absorption measurements, *Applied Optics*, 43, 4415-4426, 2004.

Burkert, J., Andres-Hernandez, M. D., Reichert, L., Meyer-Arnek, J., Doddridge, B., Dickerson, R. R., Mühle, J., Zahn, A., Carsey, T., and Burrows, J. P.: Trace gas and radical diurnal behaviour in the marine boundary layer during INDOEX 1999, *Journal of Geophysical Research-Atmospheres*, 108, 25, 8000, doi:10.1029/2002jd002790, 2003.

Burkholder, J. B., Orlando, J. J., and Howard, C. J.: Ultraviolet-Absorption Cross-Section of Cl<sub>2</sub>O<sub>2</sub> between 210 and 410 nm, *Journal of Physical Chemistry*, 94, 687-695, 1990.

Burrows, J. P., and Chance, K. V.: SCIAMACHY and GOME: The scientific objectives, *Journal of Atmospheric Chemistry*, 1715, 502-511, 1992.

Burrows, J. P., Holzle, E., Goede, A. P. H., Visser, H., and Fricke, W.: SCIAMACHY - Scanning Imaging Absorption Spectrometer for Atmospheric Cartography, *Acta Astronautica*, 35, 445-451, 1995.

Burrows, J. P., Richter, A., Dehn, A., Deters, B., Himmelmann, S., and Orphal, J.: Atmospheric remote-sensing reference data from GOME - 2. Temperature-dependent absorption cross sections of O<sub>3</sub> in the 231-794 nm range, *Journal of Quantitative Spectroscopy & Radiative Transfer*, 61, 509-517, 1999a.

Burrows, J. P., Weber, M., Buchwitz, M., Rozanov, V., Ladstätter-Weissenmayer, A., Richter, A., DeBeek, R., Hoogen, R., Bramstedt, K., Eichmann, K. U., and Eisinger, M.: The global ozone monitoring experiment (GOME): Mission concept and first scientific results, *Journal of the Atmospheric Sciences*, 56, 151-175, 1999b.

Butz, A., Bösch, H., Camy-Peyret, C., Dorf, M., Engel, A., Payan, S., and Pfeilsticker, K.: Observational constraints on the kinetics of the ClO-BrO and ClO-ClO ozone loss cycles in the Arctic winter stratosphere, *Geophysical Research Letters*, 34, 5, L05801, doi:10.1029/2006gl028718, 2007.

Cainey, J. M., Keywood, M., Grose, M. R., Krummel, P., Galbally, I. E., Johnston, P., Gillett, R. W., Meyer, M., Fraser, P., Steele, P., Harvey, M., Kreher, K., Stein, T., Ibrahim, O., Ristovski, Z. D., Johnson, G., Fletcher, C. A., Bigg, E. K., and Gras, J. L.: Precursors to Particles (P2P) at Cape Grim 2006: campaign overview, *Environ Chem*, 4, 143-150, 10.1071/en07041, 2007.

Canty, T., Riviere, E. D., Salawitch, R. J., Berthet, G., Renard, J. B., Pfeilsticker, K., Dorf, M., Butz, A., Bosch, H., Stimpfle, R. M., Wilmouth, D. M., Richard, E. C., Fahey, D. W., Popp, P.

- J., Schoeberl, M. R., Lait, L. R., and Bui, T. P.: Nighttime OCIO in the winter Arctic vortex, *Journal of Geophysical Research D: Atmospheres*, 110, 1-13, 2005.
- Carpenter, L. J., Malin, G., Liss, P. S., and Küpper, F. C.: Novel biogenic iodine-containing trihalomethanes and other short-lived halocarbons in the coastal East Atlantic, *Global Biogeochemical Cycles*, 14, 1191-1204, 2000.
- Carpenter, L. J.: Iodine in the marine boundary layer, *Chem. Rev.*, 103, 4953-4962, 10.1021/cr0206465, 2003.
- Carlsaw, K. S., Peter, T., and Clegg, S. L.: Modeling the composition of liquid stratospheric aerosols, *Reviews of Geophysics*, 35, 125-154, 1997.
- Chameides, W. L., and Davis, D. D.: Iodine - Its possible Role in Tropospheric Photochemistry, *Journal of Geophysical Research-Oceans and Atmospheres*, 85, 7383-7398, 1980.
- Chapman, S.: On ozone and atomic oxygen in the upper atmosphere, *Philos. Mag.*, 10, 369-383, 1930.
- Chipperfield, M. P., and Pyle, J. A.: Model sensitivity studies of Arctic ozone depletion, *Journal of Geophysical Research-Atmospheres*, 103, 28389-28403, 1998.
- Chipperfield, M. P.: Multiannual simulations with a three-dimensional chemical transport model, *Journal of Geophysical Research-Atmospheres*, 104, 1781-1805, 1999.
- Chubachi, S.: Preliminary result of ozone observations at Syowa station from February 1982 to January 1983, *Mem. Natl. Inst. Polar Res.*, 13-19, 1984.
- Cox, R. A., and Hayman, G. D.: The Stability and Photochemistry of Dimers of the ClO Radical and Implications for Antarctic Ozone Depletion, *Nature*, 332, 796-800, 1988.
- Crespo-Hernández, C. E., Cohen, B., and Kohler, B.: Base stacking controls excited-state dynamics in A-T DNA, *Nature*, 436, 1141-1144, 10.1038/nature03933, 2005.
- Crutzen, P.: Estimates of Possible Future Ozone Reductions from Continued use of Fluoro-Chloro-Methanes (CF<sub>2</sub>Cl<sub>2</sub>, CFCl<sub>3</sub>), *Geophysical Research Letters*, 1, 205-208, 1974.
- Crutzen, P. J.: Influence of Nitrogen Oxides on Atmospheric Ozone Content, *Quarterly Journal of the Royal Meteorological Society*, 96, 320ff, 1970.
- Crutzen, P. J.: Possible Importance of CSO for Sulfate Layer of Stratosphere, *Geophysical Research Letters*, 3, 73-76, 1976.
- DeMore, W. B., and Tschuikow-Roux, E.: Ultraviolet-Spectrum and Chemical-Reactivity of the ClO Dimer, *Journal of Physical Chemistry*, 94, 5856-5860, 1990.
- Dickerson, R. R., Rhoads, K. P., Carsey, T. P., Oltmans, S. J., Burrows, J. P., and Crutzen, P. J.: Ozone in the Remote Marine Boundary Layer: A Possible Role for Halogens, *Journal of Geophysical Research*, 104, 21385-21395, 1999.
- Dobson, G. M. B., and Harrison, D. N.: Measurements of the amount of ozone in the earth's atmosphere and its relation to other geophysical conditions, *Proc. R. soc. Lond. Ser. A-Contain. Pap. Math. Phys. Character*, 110, 660-693, 1926.
- Dorf, M., Bösch, H., Butz, A., Camy-Peyret, C., Chipperfield, M. P., Engel, A., Goutail, F., Grunow, K., Hendrick, F., Hrechanyy, S., Naujokat, B., Pommereau, J. P., van Roozendaal, M., Sioris, C., Stroh, F., Weidner, F., and Pfeilsticker, K.: Balloon-borne stratospheric BrO

measurements: comparison with Envisat/SCIAMACHY BrO limb profiles, *Atmospheric Chemistry and Physics*, 6, 2483-2501, 2006.

Douglass, A. R., Schoeberl, M. R., Stolarski, R. S., Waters, J. W., Russell, J. M., Roche, A. E., and Massie, S. T.: Interhemispheric Differences in Springtime Production of HCl and ClONO<sub>2</sub> in the Polar Vortices, *Journal of Geophysical Research-Atmospheres*, 100, 13967-13978, 1995.

Drdla, K., and Schoeberl, M. R.: Microphysical modeling of the 1999-2000 Arctic winter 2. Chlorine activation and ozone depletion, *Journal of Geophysical Research-Atmospheres*, 108, 8319, doi:10.1029/2001JD001159, 2002.

Duce, R. A., Wason, J. T., Winchester, J. W., and Burns, E.: Atmospheric iodine, bromine, and chlorine, *Journal of Geophysical Research*, 68, 3943-3947, 1963.

Elkins, J. W., Thompson, T. M., Swanson, T. H., Butler, J. H., Hall, B. D., Cummings, S. O., Fisher, D. A., and Raffo, A. G.: Decrease in the Growth-Rates of Atmospheric Chlorofluorocarbon-11 and Chlorofluorocarbon-12, *Nature*, 364, 780-783, 1993.

Elvebakk, A., and Prestrud, P.: A catalogue of Svalbard plants, fungi algae and cyanobacteria, Norsk Polarinstitutt, Oslo, 395 p., 1996.

Eskes, H. J., and Boersma, K. F.: Averaging kernels for DOAS total-column satellite retrievals, *Atmospheric Chemistry and Physics*, 3, 1285-1291, 2003.

Fan, S. M., and Jacob, D. J.: Surface Ozone Depletion in Arctic Spring sustained by Bromine Reactions on Aerosols, *Nature*, 359, 522-524, 1992.

Farman, J. C., Gardiner, B. G., and Shanklin, J. D.: Large losses of total ozone in Antarctica reveal seasonal ClO<sub>x</sub>/NO<sub>x</sub> interaction, *Nature*, 315, 207-210, 1985.

Feng, W., Chipperfield, M. P., Dorf, M., Pfeilsticker, K., and Ricaud, P.: Mid-latitude ozone changes: studies with a 3-D CTM forced by ERA-40 analyses, *Atmos. Chem. Phys.*, 7, 2357-2369, 2007.

Fickert, S., Adams, J. W., and Crowley, J. N.: Activation of Br<sub>2</sub> and BrCl via uptake of HOBr onto aqueous salt solutions, *Journal of Geophysical Research-Atmospheres*, 104, 23719-23727, 1999.

Finlayson-Pitts, B. J., and Pitts, J. N.: *Atmospheric Chemistry: Fundamentals and Experimental Techniques*, John Wiley, New York, 1986.

Finlayson-Pitts, B. J., Ezell, M. J., and Pitts, J. N.: Formation of chemically active chlorine compounds by reactions of atmospheric NaCl particles with gaseous N<sub>2</sub>O<sub>5</sub> and ClONO<sub>2</sub>, *Nature*, 337, 241-244, 1989.

Finley, B. D., and Saltzman, E. S.: Observations of Cl<sub>2</sub>, Br<sub>2</sub>, and I<sub>2</sub> in coastal marine air, *Journal of Geophysical Research-Atmospheres*, 113, 14, D21301, 10.1029/2008jd010269, 2008.

Fitzenberger, R., Bösch, H., Camy-Peyret, C., Chipperfield, M. P., Harder, H., Platt, U., Sinnhuber, B. M., Wagner, T., and Pfeilsticker, K.: First profile measurements of tropospheric BrO, *Geophysical Research Letters*, 27, 2921-2924, 2000.

Francisco, J. S., and Sander, S. P.: Existence of a Chlorine Oxide and Water (ClO•H<sub>2</sub>O) Radical Complex, *Journal of the American Chemical Society*, 117, 9917-9918, 1995.

- Friedl, R. R., and Sander, S. P.: Kinetics and Product Studies of the Reaction ClO + BrO Using Discharge-Flow Mass-Spectrometry, *Journal of Physical Chemistry*, 93, 4756-4764, 1989.
- Frieler, K., Rex, M., Salawitch, R. J., Canty, T., Streibel, M., Stimpfle, R. M., Pfeilsticker, K., Dorf, M., Weisenstein, D. K., and Godin-Beekmann, S.: Toward a better quantitative understanding of polar stratospheric ozone loss, *Geophysical Research Letters*, 33, 4, L10812, doi:10.1029/2005gl025466, 2006.
- Frieß, U., Wagner, T., Pundt, I., Pfeilsticker, K., and Platt, U.: Spectroscopic measurements of tropospheric iodine oxide at Neumayer Station, Antarctica, *Geophysical Research Letters*, 28, 1941-1944, 2001.
- Frieß, U., Kreher, K., Johnston, P. V., and Platt, U.: Ground-based DOAS measurements of stratospheric trace gases at two Antarctic stations during the 2002 ozone hole period, *Journal of the Atmospheric Sciences*, 62, 765-777, 2005.
- Frieß, U., Monks, P. S., Remedios, J. J., Rozanov, A., Sinreich, R., Wagner, T., and Platt, U.: MAX-DOAS O<sub>4</sub> measurements: A new technique to derive information on atmospheric aerosols: 2. Modeling studies, *Journal of Geophysical Research-Atmospheres*, 111, 20, D14203, doi:10.1029/2005jd006618, 2006.
- Fuse, H., Inoue, H., Murakami, K., Takimura, O., and Yamaoka, Y.: Production of free and organic iodine by *Roseovarius* spp, *Fems Microbiol Lett*, 229, 189-194, 10.1016/s0378-1097(03)00839-5, 2003.
- Fussen, D., Vanhellemont, F., Dodion, J., Bingen, C., Matshvili, N., Daerden, F., Fonteyn, D., Errera, Q., Chabrilat, S., Kyrola, E., Tamminen, J., Sofieva, V., Hauchecorne, A., Dalaudier, F., Bertaux, J. L., Renard, J. B., Fraisse, R., d'Andon, O. F., Barrot, G., Guirlet, M., Mangin, A., Fehr, T., Snoeij, P., and Saavedra, L.: A global OCIO stratospheric layer discovered in GOMOS stellar occultation measurements, *Geophysical Research Letters*, 33, L13815, doi:10.1029/2006GL026406, 2006.
- Galbally, I. E., Bentley, S. T., and Meyer, C. P.: Mid-latitude marine boundary-layer ozone destruction at visible sunrise observed at Cape Grim, Tasmania, 41°S, *Geophysical Research Letters*, 27, 3841-3844, 2000.
- Galvez, O., and Gomez, P. C.: An ab initio study on the structure and energetics of the ClO hydrates, *Chemical Physics Letters*, 448, 16-23, 10.1016/j.cplett.2007.09.072, 2007.
- Giese, B., Laturnus, F., Adams, F. C., and Wiencke, C.: Release of volatile iodinated C<sub>1</sub>-C<sub>4</sub> hydrocarbons by marine macroalgae from various climate zones, *Environmental Science & Technology*, 33, 2432-2439, 1999.
- Gil, M., Puentedura, O., Yela, M., Parrondo, C., Jadhav, D. B., and Thorkelsson, B.: OCIO, NO<sub>2</sub> and O<sub>3</sub> total column observations over Iceland during the winter 1993/94., *Geophysical Research Letters*, 23, 3337-3340, 1996.
- Gomez Martin, J. C., Spietz, P., and Burrows, J. P.: Kinetic and mechanistic studies of the I<sub>2</sub>/O<sub>3</sub> photochemistry, *Journal of Physical Chemistry A*, 111, 306-320, 10.1021/jp061186c, 2007.
- Gorbunov, M. E., and Kornblüh, L.: Analysis and validation of challenging minisatellite payload (CHAMP) radio occultation data, *Journal of Geophysical Research-Atmospheres*, 108, 10, 4584, doi:10.1029/2002jd003175, 2003.
- Grainger, J. F., and Ring, J.: Anomalous Fraunhofer Line Profiles, *Nature*, 193, 762, 1962.

Greenblatt, G. D., Orlando, J. J., Burkholder, J., and Ravishankara, A. R.: Absorption Measurements of Oxygen between 330 and 1140 nm, *Journal of Geophysical Research*, 95, 18577-18582, 1990.

Harsch, D. E., and Rasmussen, R. A.: Identification of Methyl-Bromide in Urban Air, *Anal. Lett.*, 10, 1041-1047, 1977.

Hausmann, M., and Platt, U.: Spectroscopic Measurement of Bromine Oxide and Ozone in the High Arctic during Polar Sunrise Experiment 1992, *Journal of Geophysical Research-Atmospheres*, 99, 25399-25413, 1994.

Hebestreit, K., Stutz, J., Rosen, D., Matveiv, V., Peleg, M., Luria, M., and Platt, U.: DOAS measurements of tropospheric bromine oxide in mid-latitudes, *Science*, 283, 55-57, 1999.

Heckel, A., Richter, A., Tarsu, T., Wittrock, F., Hak, C., Pundt, I., Junkermann, W., and Burrows, J. P.: MAX-DOAS measurements of formaldehyde in the Po-Valley, *Atmospheric Chemistry and Physics*, 5, 909-918, 2005.

Hendrick, F., Van Roozendaal, M., Kylling, A., Petritoli, A., Rozanov, A., Sanghavi, S., Schofield, R., von Friedeburg, C., Wagner, T., Wittrock, F., Fonteyn, D., and De Maziere, M.: Intercomparison exercise between different radiative transfer models used for the interpretation of ground-based zenith-sky and multi-axis DOAS observations, *Atmospheric Chemistry and Physics*, 6, 93-108, 2006.

Hendrick, F., Van Roozendaal, M., Chipperfield, M. P., Dorf, M., Goutail, F., Yang, X., Fayt, C., Hermans, C., Pfeilsticker, K., Pommereau, J. P., Pyle, J. A., Theys, N., and De Maziere, M.: Retrieval of stratospheric and tropospheric BrO profiles and columns using ground-based zenith-sky DOAS observations at Harestua, 60°N, *Atmospheric Chemistry and Physics*, 7, 4869-4885, 2007.

Heney, L. G., and Greenstein, J. L.: Diffuse radiation in the galaxy, *Astrophysical Journal*, 93, 70-83, 1941.

Hermans, C., Vandaele, A. C., Carleer, M., Fally, S., Colin, R., Jenouvrier, A., Coquart, B., and Merienne, M. F.: Absorption cross-sections of atmospheric constituents: NO<sub>2</sub>, O<sub>2</sub>, and H<sub>2</sub>O, *Environmental Science and Pollution Research*, 6, 151-158, 1999.

Holton, J. R.: *An introduction to dynamic meteorology*, Academic Press, 1992.

Holton, J. R., Haynes, P. H., McIntyre, M. E., Douglass, A. R., Rood, R. B., and Pfister, L.: Stratosphere-Troposphere Exchange, *Review Geophysicae*, 33, 403-439, 1995.

Hönninger, G.: *Halogen Oxide Studies in the Boundary Layer by Multi Axis Differential Optical Absorption Spectroscopy and Active Longpath-DOAS*, Ph.D. Thesis, Institute of Environmental Physics, University of Heidelberg, Heidelberg, 2002.

Hönninger, G., Leser, H., Sebastian, O., and Platt, U.: Ground-based measurements of halogen oxides at the Hudson Bay by active longpath DOAS and passive MAX-DOAS, *Geophysical Research Letters*, 31, L04111, doi: 10.1029/2003GL018982, 2004.

Hoppel, K., Bevilacqua, R., Canty, T., Salawitch, R., and Santee, M.: A measurement/model comparison of ozone photochemical loss in the Antarctic ozone hole using Polar Ozone and Aerosol Measurement observations and the Match technique, *Journal of Geophysical Research-Atmospheres*, 110, 12, D1930410.1029/2004jd005651, 2005.

- Horowitz, A., Crowley, J. N., and Moortgat, G. K.: Temperature-Dependence of the Product Branching Ratios of the ClO Self-Reaction in Oxygen, *Journal of Physical Chemistry*, 98, 11924-11930, 1994.
- Hubinger, S., and Nee, J. B.: Absorption-Spectra of Cl<sub>2</sub>, Br<sub>2</sub> and BrCl between 190nm and 600nm, *Journal of Photochemistry and Photobiology a-Chemistry*, 86, 1-7, 1995.
- Huder, K. J., and DeMore, W. B.: Absorption Cross-Sections of the ClO Dimer, *Journal of Physical Chemistry*, 99, 3905-3908, 1995.
- Huntrieser, H., Schlager, H., Feigl, C., and Holler, H.: Transport and production of NO<sub>x</sub> in electrified thunderstorms: Survey of previous studies and new observations at midlatitudes, *Journal of Geophysical Research-Atmospheres*, 103, 28247-28264, 1998.
- Irie, H., Kanaya, Y., Akimoto, H., Iwabuchi, H., Shimizu, A., and Aoki, K.: First retrieval of tropospheric aerosol profiles using MAX-DOAS and comparison with lidar and sky radiometer measurements, *Atmospheric Chemistry and Physics*, 8, 341-350, 2008.
- Itoh, N., Tsujita, M., Ando, T., Hisatomi, G., and Higashi, T.: Formation and emission of monohalomethanes from marine algae, *Phytochemistry*, 45, 67-73, 1997.
- Jimenez, J. L., Bahreini, R., Cocker, D. R., Zhuang, H., Varutbangkul, V., Flagan, R. C., Seinfeld, J. H., O'Dowd, C. D., and Hoffmann, T.: New particle formation from photooxidation of diiodomethane (CH<sub>2</sub>I<sub>2</sub>), *Journal of Geophysical Research-Atmospheres*, 108, 1, 4733, 10.1029/2003jd004249, 2003.
- Johnston, H.: Reduction of Stratospheric Ozone by Nitrogen Oxide Catalysts from Supersonic Transport Exhaust, *Science*, 173, 517-522, 1971.
- Junge, C. E., Manson, J. E., and Chagnon, C. W.: A World-wide Stratospheric Aerosol Layer, *Science*, 133, 1478-1479, 1961.
- Kaleschke, L., Richter, A., Burrows, J., Afe, O., Heygster, G., Notholt, J., Rankin, A. M., Roscoe, H. K., Hollwedel, J., Wagner, T., and Jacobi, H. W.: Frost flowers on sea ice as a source of sea salt and their influence on tropospheric halogen chemistry, *Geophysical Research Letters*, 31, 10.1029/2004GL020655, 2004.
- Kaltsayannis, N., and Plane, J. M. C.: Quantum chemical calculations on a selection of iodine-containing species (IO, OIO, INO<sub>3</sub>, (IO)<sub>2</sub>, I<sub>2</sub>O<sub>3</sub>, I<sub>2</sub>O<sub>4</sub> and I<sub>2</sub>O<sub>5</sub>) of importance in the atmosphere, *Physical Chemistry Chemical Physics*, 10, 1723-1733, 10.1039/b715687c, 2008.
- Karlsson, A., Auer, N., Schulz-Bull, D., and Abrahamsson, K.: Cyanobacterial blooms in the Baltic - A source of halocarbons, *Marine Chemistry*, 110, 129-139, 10.1016/j.marchem.2008.04.010, 2008.
- Koop, T., Carslaw, K. S., and Peter, T.: Thermodynamic stability and phase transitions of PSC particles, *Geophysical Research Letters*, 24, 2199-2202, 1997.
- Koop, T., Kapilashrami, A., Molina, L. T., and Molina, M. J.: Phase transitions of sea-salt/water mixtures at low temperatures: Implications for ozone chemistry in the polar marine boundary layer, *Journal of Geophysical Research-Atmospheres*, 105, 26393-26402, 2000.
- Krecl, P., Haley, C. S., Stegman, J., Brohede, S. M., and Berthet, G.: Retrieving the vertical distribution of stratospheric OCIO from Odin/OSIRIS limb-scattered sunlight measurements, *Atmospheric Chemistry and Physics*, 6, 1879-1894, 2006.

Kreher, K., Keys, J. G., Johnston, P. V., Platt, U., and Liu, X.: Ground-based measurements of OCIO and HCl in austral spring 1993 at Arrival Heights, Antarctica, *Geophysical Research Letters*, 23, 1545-1548, 1996.

Kreher, K., Johnston, P. V., Wood, S. W., Nardi, B., and Platt, U.: Ground-based measurements of tropospheric and stratospheric BrO at Arrival Heights, Antarctica, *Geophysical Research Letters*, 24, 3021-3024, 1997.

Kromminga, H., Orphal, J., Spietz, P., Voigt, S., and Burrows, J. P.: New measurements of OCIO absorption cross-sections in the 325-435 nm region and their temperature dependence between 213 and 293 K, *Journal of Photochemistry and Photobiology a-Chemistry*, 157, 149-160, 2003.

Kühl, S., Dornbrack, A., Wilms Grabe, W., Sinnhuber, B. M., Platt, U., and Wagner, T.: Observational evidence of rapid chlorine activation by mountain waves above northern Scandinavia, *Journal of Geophysical Research D: Atmospheres*, 109, 1-18, 2004a.

Kühl, S., Wilms-Grabe, W., Beirle, S., Frankenberg, C., Grzegorski, M., Hollwedel, J., Khokhar, F., Kraus, S., Platt, U., Sanghavi, S., von Friedeburg, C., and Wagner, T.: Stratospheric chlorine activation in the Arctic winters 1995/96-2001/02 derived from GOME OCIO measurements, *Trace Constituents in the Troposphere and Lower Stratosphere*, 34, 798-803, 2004b.

Kühl, S.: Quantifying Stratospheric Chlorine Chemistry by the Satellite Spectrometers GOME and SCIAMACHY, Dr. rer nat, Institute of Environmental Physics, University of Heidelberg, Heidelberg, 2005.

Küpper, F. C., Carpenter, L. J., McFiggans, G. B., Palmer, C. J., Waite, T. J., Boneberg, E. M., Woitsch, S., Weiller, M., Abela, R., Grolimund, D., Potin, P., Butler, A., Luther, G. W., Kroneck, P. M. H., Meyer-Klaucke, W., and Feiters, M. C.: Iodide accumulation provides kelp with an inorganic antioxidant impacting atmospheric chemistry, *Proceedings of the National Academy of Sciences of the United States of America*, 105, 6954-6958, 10.1073/pnas.0709959105, 2008.

Ladstätter-Weißmayer, A., Altmeyer, H., Bruns, M., Richter, A., Rozanov, A., Rozanov, V., Wittrock, F., and Burrows, J. P.: Measurements of O<sub>3</sub>, NO<sub>2</sub> and BrO during the INDOEX campaign using ground based DOAS and GOME satellite data, *Atmospheric Chemistry and Physics*, 7, 283-291, 2007.

Lary, D. J.: Catalytic Destruction of Stratospheric Ozone, *Journal of Geophysical Research*, 102, 21515-21526, 1997.

Lawrence, W. G., Clemitshaw, K. C., and Apkarian, V. A.: On the relevance of OCIO photodissociation to the destruction of stratospheric ozone, *Journal of Geophysical Research*, 95, 18591-18595, 1990.

LeBras, G., and Platt, U.: A possible mechanism for combined chlorine and bromine catalyzed destruction of tropospheric ozone in the arctic, *Geophysical Research Letters*, 22, 599-602, 1995.

Lee, C., Kim, Y. J., Tanimoto, H., Bobrowski, N., Platt, U., Mori, T., Yamamoto, K., and Hong, C. S.: High ClO and ozone depletion observed in the plume of Sakurajima volcano, Japan, *Geophysical Research Letters*, 32, 4, L21809, doi: 10.1029/2005gl023785, 2005.

Leser, H., Hönninger, G., and Platt, U.: MAX-DOAS measurements of BrO and NO<sub>2</sub> in the marine boundary layer, *Geophysical Research Letters*, 30, doi: 10.1029/2002GL015811, 2003.

- Liou, K.-N.: Radiation and Cloud Processes in the Atmosphere, Oxford Monographs on Geology and Geophysics, No. 20, Oxford University Press, Oxford, 1992.
- Manley, S. L., and de la Cuesta, J. L.: Methyl iodide production from marine phytoplankton cultures, *Limnology and Oceanography*, 42, 142-147, 1997.
- Maric, D., Burrows, J. P., and Moortgat, G. K.: A Study of the UV-Visible Absorption-Spectra of Br<sub>2</sub> and BrCl, *J. Photochem. Photobiol. A-Chem.*, 83, 179-192, 1994.
- Martin, R. V., Chance, K., Jacob, D. J., Kurosu, T. P., Spurr, R. J. D., Bucsela, E., Gleason, J. F., Palmer, P. I., Bey, I., Fiore, A. M., Li, Q. B., Yantosca, R. M., and Koelemeijer, R. B. A.: An improved retrieval of tropospheric nitrogen dioxide from GOME, *Journal of Geophysical Research-Atmospheres*, 107, doi: 10.1029/2001JD001027, 2002.
- Martino, M., Mills, G. P., Woeltjen, J., and Liss, P. S.: A new source of volatile organoiodine compounds in surface seawater, *Geophys. Res. Lett.*, 36, 2009.
- McFiggans, G., Coe, H., Burgess, R., Allan, J., Cubison, M., Alfarra, M. R., Saunders, R., Saiz-Lopez, A., Plane, J. M. C., Wevill, D. J., Carpenter, L. J., Rickard, A. R., and Monks, P. S.: Direct evidence for coastal iodine particles from *Laminaria* macroalgae - linkage to emissions of molecular iodine, *Atmospheric Chemistry and Physics*, 4, 701-713, 2004.
- McKeachie, J. R., Appel, M. F., Kirchner, U., Schindler, R. N., and Benter, T.: Observation of a heterogeneous source of OCIO from the reaction of ClO radicals on ice, *Journal of Physical Chemistry B*, 108, 16786-16797, 2004.
- Midgley, T., and Henne, A. L.: Organic fluorides as refrigerants, *Industrial and Engineering Chemistry*, 22, 542-545, 1930.
- Molina, J. M., and Rowland, F. S.: Stratospheric sink for chlorofluoromethanes: chlorine atom-catalysed destruction of ozone, *Nature*, 249, 810-812, 1974.
- Moore, R. M., Webb, M., Tokarczyk, R., and Wever, R.: Bromoperoxidase and iodoperoxidase enzymes and production of halogenated methanes in marine diatom cultures, *Journal of Geophysical Research-Oceans*, 101, 20899-20908, 1996.
- Mössinger, J. C., Shallcross, D. E., and Cox, R. A.: UV-VIS absorption cross-sections and atmospheric lifetimes of CH<sub>2</sub>Br<sub>2</sub>, CH<sub>2</sub>I<sub>2</sub> and CH<sub>2</sub>Brl, *Journal of the Chemical Society-Faraday Transactions*, 94, 1391-1396, 1998.
- Müller-de Vries, O. S.: The relative contribution of free radicals to the oxidation chain of Dimethylsulphide in the marine boundary layer, Ph.D. Thesis, Institute of Environmental Physics, University of Heidelberg, Heidelberg, 2004.
- Nagao, I., Matsumoto, K., and Tanaka, H.: Sunrise ozone destruction found in the subtropical marine boundary layer, *Geophysical Research Letters*, 26, 3377-3380, 1999.
- Nakano, Y., Enami, S., Nakamichi, S., Aloisio, S., Hashimoto, S., and Kawasaki, M.: Temperature and pressure dependence study of the reaction of IO radicals with dimethyl sulfide by cavity ring-down laser spectroscopy, *Journal of Physical Chemistry A*, 107, 6381-6387, 10.1021/jp0345147, 2003.
- Nickolaisen, S. L., Friedl, R. R., and Sander, S. P.: Kinetics and Mechanism of the ClO+ClO Reaction - Pressure and Temperature Dependences of the Bimolecular and Termolecular Channels and Thermal-Decomposition of Chlorine Peroxide, *Journal of Physical Chemistry*, 98, 155-169, 1994.

Noxon, J. F.: Nitrogen dioxide in the stratosphere and troposphere measured by ground-based absorption spectroscopy, *Science*, 189, 547-549, 1975.

Noxon, J. F., Whipple Jr, E. C., and Hyde, R. S.: Stratospheric NO<sub>2</sub>. 1. Observational method and behaviour at mid-latitude, *Journal of Geophysical Research*, 84, 5047-5065, 1979.

Nüß, H.: Verbesserung des troposphärischen NO<sub>2</sub>-Retrievals aus GOME und SCIAMACHY-Daten, Dr. rer. nat., Institut für Umweltphysik, Universität Bremen, Bremen, 2005.

O'Dowd, C. D., Jimenez, J. L., Bahreini, R., Flagan, R. C., Seinfeld, J. H., Hameri, K., Pirjola, L., Kulmala, M., Jennings, S. G., and Hoffmann, T.: Marine aerosol formation from biogenic iodine emissions, *Nature*, 417, 632-636, 2002.

Oltmans, S. J., and Komhyr, W. D.: Surface Ozone Distributions and Variations from 1793-1984 Measurements at the NOAA Geophysical Monitoring for Climate-Change Base-Line Observatories, *Journal of Geophysical Research-Atmospheres*, 91, 5229-5236, 1986.

Oppenheimer, C., Bani, P., Calkins, J. A., Burton, M. R., and Sawyer, G. M.: Rapid FTIR sensing of volcanic gases released by Strombolian explosions at Yasur volcano, Vanuatu, *Applied Physics B-Lasers and Optics*, 85, 453-460, 10.1007/s00340-006-2353-4, 2006.

Otten, C., Ferlemann, F., Platt, U., Wagner, T., and Pfeilsticker, K.: Groundbased DOAS UV/visible measurements at Kiruna (Sweden) during the SESAME winters 1993/94 and 1994/95., *Journal of Atmospheric Chemistry*, 30, 141-162, 1998.

Palmer, P. I., Jacob, D. J., Chance, K., Martin, R. V., Spurr, R. J. D., Kurosu, T. P., Bey, I., Yantosca, R., Fiore, A., and Li, Q. B.: Air mass factor formulation for spectroscopic measurements from satellites: Application to formaldehyde retrievals from the Global Ozone Monitoring Experiment, *Journal of Geophysical Research-Atmospheres*, 106, 14539-14550, 2001.

Perliski, L. M., and Solomon, S.: On the evaluation of air mass factors for atmospheric near-ultraviolet and visible absorption spectroscopy, *Journal of Geophysical Research*, 98, 10363-10374, 1993.

Permien, T., Vogt, R., and Schindler, R. N.: Mechanisms of Gas Phase-Liquid Phase Chemical Transformations, in: *Air Pollution Report #17*, edited by: Cox, R. A., Environmental Research Program of the CEC, Brussels, 1988.

Perner, D., and Platt, U.: Detection of Nitrous-Acid in the Atmosphere by Differential Optical-Absorption, *Geophysical Research Letters*, 6, 917-920, 1979.

Perner, D., and Platt, U.: Absorption of light in the atmosphere by collision pairs of oxygen (O<sub>2</sub>)<sub>2</sub>, *Geophysical Research Letters*, 7, 1053-1056, 1980.

Perner, D., Roth, A., and Klüpfel, T.: Groundbased measurements of stratospheric OClO, NO<sub>2</sub>, and O<sub>3</sub> at Søndre Strømfjord in winter 1991/92, *Geophysical Research Letters*, 21, 1367-1370, 1994.

Peters, C.: Studies of Reactive Halogen Species (RHS) in the Marine and mid-latitude Boundary Layer by Active Longpath Differential Optical Absorption Spectroscopy, Ph.D. Thesis, Institute of Environmental Physics, University of Heidelberg, Heidelberg, 2005.

Peters, C., Pechtl, S., Stutz, J., Hebestreit, K., Hönninger, G., Heumann, K. G., Schwarz, A., Winterlik, J., and Platt, U.: Reactive and organic halogen species in three different European coastal environments, *Atmospheric Chemistry and Physics*, 5, 3357-3375, 2005.

- Pfeilsticker, K., and Platt, U.: Airborne Measurements during the Arctic Stratospheric Experiment - Observation of O<sub>3</sub> and NO<sub>2</sub>, *Geophysical Research Letters*, 21, 1375-1378, 1994.
- Pierson, J. M., McKinney, K. A., Toohey, D. W., Margitan, J., Schmidt, U., Engel, A., and Newman, P. A.: An investigation of ClO photochemistry in the chemically perturbed arctic vortex, *Journal of Atmospheric Chemistry*, 32, 61-81, 1999.
- Planck, M.: Über die Natur des weissen Lichtes, *Annalen der Physik*, 312, 390-400, 1902.
- Platt, U., Perner, D., and Patz, H. W.: Simultaneous Measurements of Atmospheric CH<sub>2</sub>O, O<sub>3</sub>, and NO<sub>2</sub> by Differential Optical-Absorption, *Journal of Geophysical Research-Oceans and Atmospheres*, 84, 6329-6335, 1979.
- Plenge, J., Flesch, R., Kühl, S., Vogel, B., Muller, R., Stroh, F., and Ruhl, E.: Ultraviolet photolysis of the ClO dimer, *Journal of Physical Chemistry A*, 108, 4859-4863, 10.1021/jp049690, 2004.
- Plenge, J., Kühl, S., Vogel, B., Muller, R., Stroh, F., von Hobe, M., Flesch, R., and Ruhl, E.: Bond strength of chlorine peroxide, *Journal of Physical Chemistry A*, 109, 6730-6734, 10.1021/jp044142h, 2005.
- Pommereau, J. P., and Piquard, J.: Ozone and nitrogen dioxide vertical distributions by UV-visible solar occultation from balloons, *Geophysical Research Letters*, 21, 1227-1230, 1994.
- Pope, F. D., Hansen, J. C., Bayes, K. D., Friedl, R. R., and Sander, S. P.: Ultraviolet absorption spectrum of chlorine peroxide, ClOOCl, *Journal of Physical Chemistry A*, 111, 4322-4332, 10.1021/jp067660w, 2007.
- Prather, M., and Jaffe, A. H.: Global impact of the Antarctic ozone hole: chemical propagation, *Journal of Geophysical Research*, 95, 3473-3492, 1990.
- Pundt, I., Pommereau, J. P., Phillips, C., and Lateltin, E.: Upper limit of iodine oxide in the lower stratosphere, *Journal of Atmospheric Chemistry*, 30, 173-185, 1998.
- Ramanathan, V., Crutzen, P. J., Lelieveld, J., Mitra, A. P., Althausen, D., Anderson, J., Andreae, M. O., Cantrell, W., Cass, G. R., Chung, C. E., Clarke, A. D., Coakley, J. A., Collins, W. D., Conant, W. C., Dulac, F., Heintzenberg, J., Heymsfield, A. J., Holben, B., Howell, S., Hudson, J., Jayaraman, A., Kiehl, J. T., Krishnamurti, T. N., Lubin, D., McFarquhar, G., Novakov, T., Ogren, J. A., Podgorny, I. A., Prather, K., Priestley, K., Prospero, J. M., Quinn, P. K., Rajeev, K., Rasch, P., Rupert, S., Sadourny, R., Satheesh, S. K., Shaw, G. E., Sheridan, P., and Valero, F. P. J.: Indian Ocean Experiment: An integrated analysis of the climate forcing and effects of the great Indo-Asian haze, *Journal of Geophysical Research-Atmospheres*, 106, 28371-28398, 2001.
- Rattigan, O. V., Shallcross, D. E., and Cox, R. A.: UV absorption cross-sections and atmospheric photolysis rates of CF<sub>3</sub>I, CH<sub>3</sub>I, C<sub>2</sub>H<sub>5</sub>I and CH<sub>2</sub>ICl, *Journal of the Chemical Society-Faraday Transactions*, 93, 2839-2846, 1997.
- Read, K. A., Mahajan, A. S., Carpenter, L. J., Evans, M. J., Faria, B. V. E., Heard, D. E., Hopkins, J. R., Lee, J. D., Moller, S. J., Lewis, A. C., Mendes, L., McQuaid, J. B., Oetjen, H., Saiz-Lopez, A., Pilling, M. J., and Plane, J. M. C.: Extensive halogen-mediated ozone destruction over the tropical Atlantic Ocean, *Nature*, 453, 1232-1235, 10.1038/nature07035, 2008.
- Renard, J. B., Lefevre, F., Pirre, M., Robert, C., and Huguenin, D.: Vertical profile of nighttime stratospheric OClO, *Journal of Atmospheric Chemistry*, 26, 65-76, 1997.

Richter, A.: Absorptionsspektroskopische Messungen stratosphärischer Spurengase über Bremen, 53° N, Dr. rer nat, Institute of Environmental Physics, University of Bremen, Bremen, 1997.

Richter, A., Wittrock, F., Eisinger, M., and Burrows, J. P.: GOME observations of tropospheric BrO in northern hemispheric spring and summer 1997, *Geophysical Research Letters*, 25, 2683-2686, 1998.

Richter, A., Eisinger, M., Ladstätter-Weißenmayer, A., and Burrows, J. P.: DOAS Zenith sky observations: 2. Seasonal variation of BrO over Bremen (53° N) 1994-1995, *Journal of Atmospheric Chemistry*, 32, 83-99, 1999.

Richter, A., Wittrock, F., Weber, M., Beirle, S., Kühl, S., Platt, U., Wagner, T., Wilms-Grabe, W., and Burrows, J. P.: GOME observations of stratospheric trace gas distributions during the splitting vortex event in the Antarctic winter of 2002. Part I: Measurements, *Journal of the Atmospheric Sciences*, 62, 778-785, 2005.

Riviere, E. D., Pirre, M., Berthet, G., Renard, J. B., Taupin, F. G., Huret, N., Chartier, M., Knudsen, B., and Lefevre, F.: On the interaction between nitrogen and halogen species in the Arctic polar vortex during THESEO and THESEO 2000, *Journal of Geophysical Research D: Atmospheres*, 108, doi: 10.1029/2002JD002087, 2002.

Rodgers, C. D.: *Inverse Methods for Atmospheric Sounding, Theory and Practise*, World Scientific Publishing, London, 2000.

Roscoe, H. K., Freshwater, R. A., Wolfenden, R., Jones, R. L., Fish, D. J., Harries, J. E., South, A. M., and Oldham, D. J.: Using Stars for Remote-Sensing of the Earth's Stratosphere, *Applied Optics*, 33, 7126-7131, 1994.

Rothman, L. S., Gamache, R. R., Tipping, R. H., Rinsland, C. P., Smith, M. A. H., Benner, C. D., Devi, V. M., Flaud, J. M., Camy-Peyret, C., Perrin, A., Goldman, A., Massie, S. T., and Brown, L. R.: The HITRAN molecular database editions 1991 and 1992, *J. Quant. Spectrosc. Radiat. Transfer*, 48, 469-507, 1992.

Rozanov, A.: A numerical Radiative Transfer Model for a Spherical Planetary Atmosphere: Combined Differential-Integral Approach involving the Picard Iterative Approximation, Dr. rer nat, Institute of Environmental Physics, University of Bremen, Bremen, 2001.

Rozanov, A., Rozanov, V., and Burrows, J. P.: A numerical radiative transfer model for a spherical planetary atmosphere: combined differential-integral approach involving the Picard iterative approximation, *Journal of Quantitative Spectroscopy & Radiative Transfer*, 69, 491-512, 2001.

Rozanov, A., Bovensmann, H., Bracher, A., Hrechanyy, S., Rozanov, V., Sinnhuber, M., Strohm, F., and Burrows, J. P.: NO<sub>2</sub> and BrO vertical profile retrieval from SCIAMACHY limb measurements: Sensitivity studies, 35th COSPAR Scientific Assembly, Paris, FRANCE, 2004, 846-854

Rozanov, A., Rozanov, V., Buchwitz, M., Kokhanovsky, A., and Burrows, J. P.: SCIATRAN 2.0 - A new radiative transfer model for geophysical applications in the 175-2400 nm spectral region, *Advanced Space Research*, 36, 1015-1019, DOI 10.1016/j.asr.2005.03.012, 2005.

Rozanov, V. V., and Rozanov, A. V.: Relationship between different approaches to derive weighting functions related to atmospheric remote sensing problems, *Journal of Quantitative Spectroscopy & Radiative Transfer*, 105, 217-242, DOI 10.1016/j.jqsrt.2006.12.006, 2007a.

Rozanov, V. V., and Rozanov, A. V.: Generalized form of the direct and adjoint radiative transfer equations, *Journal of Quantitative Spectroscopy & Radiative Transfer*, 104, 155-170, DOI 10.1016/j.jqsrt.2006.08.017, 2007b.

Saiz-Lopez, A., and Plane, J. M. C.: Recent applications of differential optical absorption spectroscopy: Halogen chemistry in the lower troposphere, *Journal De Physique Iv*, 121, 223-238, 2004a.

Saiz-Lopez, A., and Plane, J. M. C.: Novel iodine chemistry in the marine boundary layer, *Geophysical Research Letters*, 31, L04112, doi:10.1029/2003GL019215, 2004b.

Saiz-Lopez, A., Plane, J. M. C., and Shillito, J. A.: Bromine oxide in the mid-latitude marine boundary layer, *Geophysical Research Letters*, 31, L03111, doi: 10.1029/2003gl018956, 2004.

Saiz-Lopez, A., Shillito, J. A., Coe, H., and Plane, J. M. C.: Measurements and modelling of I<sub>2</sub>, IO, OIO, BrO and NO<sub>3</sub> in the mid-latitude marine boundary layer, *Atmospheric Chemistry and Physics*, 6, 1513-1528, 2006.

Saiz-Lopez, A., Chance, K., Liu, X., Kurosu, T. P., and Sander, S. P.: First observations of iodine oxide from space, *Geophysical Research Letters*, 34, 5, L12812, 10.1029/2007gl030111, 2007a.

Saiz-Lopez, A., Mahajan, A. S., Salmon, R. A., Bauguitte, S. J. B., Jones, A. E., Roscoe, H. K., and Plane, J. M. C.: Boundary layer halogens in coastal Antarctica, *Science*, 317, 348-351, 10.1126/science.1141408, 2007b.

Saiz-Lopez, A., and Boxe, C. S.: A mechanism for biologically-induced iodine emissions from sea-ice, *Atmos. Chem. Phys. Discuss.*, 8, 2953-2976, 2008.

Sakshaug, E., Björge, A., Gulliksen, B., Loeng, H., and Mehlum, F.: Økosystem Barentshavet, Norges Forskningsråd, Universitetsforlaget, Oslo, 304 pp., 1994.

Salawitch, R. J.: Atmospheric chemistry - Biogenic bromine, *Nature*, 439, 275-277, 10.1038/439275a, 2006.

Sander, R., Keene, W. C., Pszenny, A. A. P., Arimoto, R., Ayers, G. P., Baboukas, E., Cainey, J. M., Crutzen, P. J., Duce, R. A., Hönninger, G., Huebert, B. J., Maenhaut, W., Mihalopoulos, N., Turekian, V. C., and Van Dingenen, R.: Inorganic bromine in the marine boundary layer: a critical review, *Atmospheric Chemistry and Physics*, 3, 1301-1336, 2003a.

Sander, S. P., Friedel, R. R., Golden, D. M., Kurylo, M. J., Huie, R. E., Orkin, V. L., Moortgat, G. K., Ravishankara, A. R., Kolb, C. E., Molina, M. J., and Finlayson-Pitts, B. J.: Chemical Kinetics and Photochemical Data for Use in Atmospheric Studies - Evaluation Number 14, Jet Propulsion Laboratory, California Institute of Technology, Pasadena, California, 2003b.

Sander, S. P., Friedel, R. R., Golden, D. M., Kurylo, M. J., Moortgat, G. K., Keller-Rudek, H., Wine, P. H., Ravishankara, A. R., Kolb, C. E., Molina, M. J., Finlayson-Pitts, B. J., Huie, R. E., and Orkin, V. L.: Chemical Kinetics and Photochemical Data for Use in Atmospheric Studies - Evaluation Number 15, Jet Propulsion Laboratory, California Institute of Technology, Pasadena, California, 2006.

Sanders, R. W., Solomon, S., Smith, J. P., Perliski, L., Miller, H. L., Mount, G. H., Keys, J. G., and Schmeltekopf, A. L.: Visible and near-ultraviolet spectroscopy at McMurdo Station, Antarctica 9. Observations of OCIO from April to October 1991, *Journal of Geophysical Research*, 98, 7219-7228, 1993.

- Santee, M. L., MacKenzie, I. A., Manney, G. L., Chipperfield, M. P., Bernath, P. F., Walker, K. A., Boone, C. D., Froidevaux, L., Livesey, N. J., and Waters, J. W.: A study of stratospheric chlorine partitioning based on new satellite measurements and modeling, *Journal of Geophysical Research-Atmospheres*, 113, 25, D12307, 10.1029/2007jd009057, 2008.
- Saunders, R. W., and Plane, J. M. C.: Formation pathways and composition of iodine oxide ultra-fine particles, *Environ Chem*, 2, 299-303, 10.1071/en05079, 2005.
- Schall, C., and Heumann, K. G.: GC determination of volatile organoiodine and organobromine compounds in arctic seawater and air samples, *Fresenius Journal of Analytical Chemistry*, 346, 717-722, 1993.
- Schall, C., Laturnus, F., and Heumann, K. G.: Biogenic volatile organoiodine and organobromine compounds released from polar macroalgae, *Chemosphere*, 28, 1315-1324, 1994.
- Schiller, C., Wahner, A., Platt, U., Dorn, H. P., Callies, J., and Ehhalt, D. H.: Near UV atmospheric absorption measurements of column abundances during Airborne Arctic Stratospheric Expedition, January-February 1989: 2. OCIO observations, *Geophysical Research Letters*, 17, 501-504, 1990.
- Schiller, C., and Wahner, A.: Comment on "Stratospheric OCIO measurements as a poor quantitative indicator of chlorine activation", *Geophysical Research Letters*, 23, 1053-1054, 1996.
- Schlieter, S.: Spurengasmessungen während der Nacht mittels Mondlichtspektroskopie im Vergleich mit Modellrechnungen, *Dr. rer nat, Institut für Umweltphysik, Universität Bremen, Bremen*, 2001.
- Schnaiter, M., Horvath, H., Mohler, O., Naumann, K. H., Saathoff, H., and Schock, O. W.: UV-VIS-NIR spectral optical properties of soot and soot-containing aerosols, *Journal of Aerosol Science*, 34, 1421-1444, 10.1016/s0021-8502(03)00361-6, 2003.
- Schneising, O., Buchwitz, M., Burrows, J. P., Bovensmann, H., Bergamaschi, P., and Peters, W.: Three years of greenhouse gas column-averaged dry air mole fractions retrieved from satellite - Part 2: Methane, *Atmos. Chem. Phys. Discuss.*, 8, 8273-8326, 2008.
- Schoeberl, M. R., and Hartmann, D. L.: The dynamics of the stratospheric polar vortex and its relation to springtime ozone depletions, *Science*, 251, 46-52, 1991.
- Schofield, R., Johnston, P. V., Thomas, A., Kreher, K., Connor, B. J., Wood, S., Shooter, D., Chipperfield, M. P., Richter, A., von Glasow, R., and Rodgers, C. D.: Tropospheric and stratospheric BrO columns over Arrival Heights, Antarctica, 2002, *Journal of Geophysical Research-Atmospheres*, 111, 14, D22310, doi: 10.1029/2005jd007022, 2006.
- Schofield, R., Frieler, K., Wohltmann, I., Rex, M., von Hobe, M., Stroh, F., Koch, G., Peter, T., Canty, T., Salawitch, R., and Volk, C. M.: Polar stratospheric chlorine kinetics from a self-match flight during SOLVE-II/EUPLEX, *Geophysical Research Letters*, 35, 6, L01807, 10.1029/2007gl031740, 2008.
- Schönhardt, A., Richter, A., Wittrock, F., Kirk, H., Oetjen, H., Roscoe, H. K., and Burrows, J. P.: Observations of iodine monoxide columns from satellite, *Atmospheric Chemistry and Physics*, 8, 637-653, 2008.
- Schwärzle, J.: Spektroskopische Messung von Halogenoxiden in der marinen Grenzschicht in Alcantara/Brasilien, Staatsexamensarbeit, Institute of Environmental Physics, University of Heidelberg, Heidelberg, Germany, 2005.

Schweitzer, F., Mirabel, P., and George, C.: Heterogeneous chemistry of nitril halides in relation to tropospheric halogen activation, XXIII General Assembly of the European-Geophysical-Society, Nice, France, 1998, ISI:000082797800008, 101-117

Sebastian, O.: The relative contribution of free radicals to the oxidation chain of Dimethylsulphide in the marine boundary layer, Ph.D. Thesis, Institute of Environmental Physics, University of Heidelberg, Heidelberg, Germany, 2004.

Sessler, J., Chipperfield, M. P., Pyle, J. A., and Toumi, R.: Stratospheric OClO Measurements as a Poor Quantitative Indicator of Chlorine Activation, *Geophysical Research Letters*, 22, 687-690, 1995.

Sessler, J., Chipperfield, M. P., Pyle, J. A., and Toumi, R.: Stratospheric OClO measurements as a poor quantitative indicator of chlorine activation - Reply, *Geophysical Research Letters*, 23, 1055-1055, 1996.

Simpson, W. R., Carlson, D., Hönninger, G., Douglas, T. A., Sturm, M., Perovich, D., and Platt, U.: First-year sea-ice contact predicts bromine monoxide (BrO) levels at Barrow, Alaska better than potential frost flower contact, *Atmospheric Chemistry and Physics*, 7, 621-627, 2007a.

Simpson, W. R., von Glasow, R., Riedel, K., Anderson, P., Ariya, P., Bottenheim, J., Burrows, J., Carpenter, L. J., Frieß, U., Goodsite, M. E., Heard, D., Hutterli, M., Jacobi, H. W., Kaleschke, L., Neff, B., Plane, J., Platt, U., Richter, A., Roscoe, H., Sander, R., Shepson, P., Sodeau, J., Steffen, A., Wagner, T., and Wolff, E.: Halogens and their role in polar boundary-layer ozone depletion, *Atmospheric Chemistry and Physics*, 7, 4375-4418, 2007b.

Singh, H. B., Salas, L. J., and Stiles, R. E.: Methyl Halides in and over the Eastern Pacific (40°N - 32°S), *Journal of Geophysical Research-Oceans and Atmospheres*, 88, 3684-3690, 1983.

Sinnhuber, B. M., Arlander, D. W., Bovensmann, H., Burrows, J. P., Chipperfield, M. P., Enell, C. F., Frieß, U., Hendrick, F., Johnston, P. V., Jones, R. L., Kreher, K., Mohamed-Tahrin, N., Muller, R., Pfeilsticker, K., Platt, U., Pommereau, J. P., Pundt, I., Richter, A., South, A. M., Tørnkvist, K. K., Van Roozendaal, M., Wagner, T., and Wittrock, F.: Comparison of measurements and model calculations of stratospheric bromine monoxide, *Journal of Geophysical Research-Atmospheres*, 107, 10.1029/2001JD000940, 2002.

Sinnhuber, B. M., Rozanov, A., Sheode, N., Afe, O. T., Richter, A., Sinnhuber, M., Wittrock, F., Burrows, J. P., Stiller, G. P., von Clarmann, T., and Linden, A.: Global observations of stratospheric bromine monoxide from SCIAMACHY, *Geophysical Research Letters*, 32, L20810, doi:10.1029/2005GL023839, 2005.

Soller, R., Nicovich, J. M., and Wine, P. H.: Temperature-dependent rate coefficients for the reactions of Br( $^2P_{3/2}$ ), Cl( $^2P_{3/2}$ ), and O( $^3P_J$ ) with BrONO<sub>2</sub>, *Journal of Physical Chemistry A*, 105, 1416-1422, 2001.

Solomon, P., Barrett, J., Connor, B., Zoonematkermani, S., Parrish, A., Lee, A., Pyle, J., and Chipperfield, M.: Seasonal observations of chlorine monoxide in the stratosphere over Antarctica during the 1996-1998 ozone holes and comparison with the SLIMCAT three-dimensional model, *Journal of Geophysical Research-Atmospheres*, 105, 28979-29001, 2000.

Solomon, S., Mount, G. H., Sanders, R. W., and Schmeltekopf, A. L.: Visible Spectroscopy at McMurdo Station, Antarctica - 2. Observations of OClO, *Journal of Geophysical Research*, 92, 8329-8338, 1987a.

- Solomon, S., Schmeltekopf, A. L., and Sanders, R. W.: On the Interpretation of Zenith Sky Absorption Measurements, *Journal of Geophysical Research*, 92, 8311-8319, 1987b.
- Solomon, S., Mount, G. H., Sanders, R. W., Jakoubek, R. O., and Schmeltekopf, A. L.: Observations of the nighttime abundance of OCIO in the winter stratosphere above Thule, Greenland, *Science*, 242, 550-555, 1988.
- Solomon, S., Sanders, R. W., and Miller, H. L.: Visible and near-Ultraviolet spectroscopy at McMurdo Station, Antarctica. 7. OCIO diurnal photochemistry and implications for ozone destruction, *Journal of Geophysical Research*, 95, 13807-13817, 1990.
- Solomon, S., Garcia, R. R., and Ravishankara, A. R.: On the role of iodine in ozone depletion, *Journal of Geophysical Research*, 99, 20491-20499, 1994.
- Spietz, P., Gomez Martin, J. C., and Burrows, J. P.: Spectroscopic studies of the I-2/O-3 photochemistry - Part 2. Improved spectra of iodine oxides and analysis of the IO absorption spectrum, *Journal of Photochemistry and Photobiology a-Chemistry*, 176, 50-67, 10.1016/j.jphotochem.2005.08.023, 2005.
- Stimpfle, R. M., Wilmouth, D. M., Salawitch, R. J., and Anderson, J. G.: First measurements of ClOOCl in the stratosphere: The coupling of ClOOCl and ClO in the Arctic polar vortex, *Journal of Geophysical Research-Atmospheres*, 109, 16, D03301, 10.1029/2003jd003811, 2004.
- Stolarski, R. S., and Cicerone, R. J.: Stratospheric Chlorine - Possible Sink for Ozone, *Canadian Journal of Chemistry-Revue Canadienne De Chimie*, 52, 1610-1615, 1974.
- Stutz, J., Ackermann, R., Fast, J. D., and Barrie, L.: Atmospheric reactive chlorine and bromine at the Great Salt Lake, Utah, *Geophysical Research Letters*, 29, 4, 138010.1029/2002gl014812, 2002.
- Stutz, J., Pikelnaya, O., Hurlock, S. C., Trick, S., Pechtl, S., and von Glasow, R.: Daytime OIO in the gulf of Maine, *Geophysical Research Letters*, 34, 5, L22816, doi: 10.1029/2007gl031332, 2007.
- Tanimoto, H., Sawa, Y., Yonemura, S., Yumimoto, K., Matsueda, H., Uno, I., Hayasaka, T., Mukai, H., Tohjima, Y., Tsuboi, K., and Zhang, L.: Diagnosing recent CO emissions and ozone evolution in East Asia using coordinated surface observations, adjoint inverse modeling, and MOPITT satellite data, *Atmos. Chem. Phys.*, 8, 3867-3880, 2008.
- Tellinghuisen, J.: Precise equilibrium constants from spectrophotometric data: BrCl in Br<sub>2</sub>/Cl<sub>2</sub> gas mixtures, *Journal of Physical Chemistry A*, 107, 753-757, 10.1021/jp027227w, 2003.
- Theiler, R., Cook, J. C., and Hager, L. P.: Halohydrocarbon Synthesis by Bromoperoxidase, *Science*, 202, 1094-1096, 1978.
- Theys, N., Van Roozendaal, M., Hendrick, F., Fayt, C., Hermans, C., Baray, J. L., Goutail, F., Pommereau, J. P., and De Maziere, M.: Retrieval of stratospheric and tropospheric BrO columns from multi-axis DOAS measurements at Reunion Island (21° S, 56° E), *Atmospheric Chemistry and Physics*, 7, 4733-4749, 2007.
- Thornton, B. F., Toohey, D. W., Avallone, L. M., Harder, H., Martinez, M., Simpas, J. B., Brune, W. H., and Avery, M. A.: In situ observations of ClO near the winter polar tropopause, *Journal of Geophysical Research-Atmospheres*, 108, 8, 8333, 10.1029/2002jd002839, 2003.
- Thornton, B. F., Toohey, D. W., Avallone, L. M., Hallar, A. G., Harder, H., Martinez, M., Simpas, J. B., Brune, W. H., Koike, M., Kondo, Y., Takegawa, N., Anderson, B. E., and Avery, M.

A.: Variability of active chlorine in the lowermost Arctic stratosphere, *Journal of Geophysical Research-Atmospheres*, 110, 11, D22304, 10.1029/2004jd005580, 2005.

Tørnkvist, K. K., Arlander, D. W., and Sinnhuber, B. M.: Ground-based UV measurements of BrO and OClO over Ny-Ålesund during winter 1996 and 1997 and Andøya during winter 1998/99, *Journal of Atmospheric Chemistry*, 43, 75-106, 2002.

Toumi, R.: BrO as a sink for dimethylsulfide in the marine atmosphere, *Geophysical Research Letters*, 21, 117-120, 1994.

Trolier, M., Mauldin, R. L., and Ravishankara, A. R.: Rate Coefficient for the Termolecular Channel of the Self-Reaction of ClO, *Journal of Physical Chemistry*, 94, 4896-4907, 1990.

Tuckermann, M., Ackermann, R., Götz, C., Lorenzen-Schmidt, H., Senne, T., Stutz, J., Trost, B., Unold, W., and Platt, U.: DOAS-observation of halogen radical-catalysed arctic boundary layer ozone destruction during the ARCTOC-campaigns 1995 and 1996 in Ny-Ålesund, Spitsbergen, *Tellus Series B-Chemical and Physical Meteorology*, 49, 533-555, 1997.

Tung, K. K., Ko, M. K. W., Rodriguez, J. M., and Sze, N. D.: Are Antarctic ozone variations a manifestation of dynamics or chemistry?, *Nature*, 322, 811-814, 1986.

Vandaele, A. C., Hermans, C., Simon, P. C., Carleer, M., Colin, R., Fally, S., Merienne, M. F., Jenouvrier, A., and Coquart, B.: Measurements of the NO<sub>2</sub> absorption cross-section from 42 000 cm<sup>-1</sup> to 10 000 cm<sup>-1</sup> (238-1000 nm) at 220 K and 294 K, *Journal of Quantitative Spectroscopy & Radiative Transfer*, 59, 171-184, 1998.

Vandaele, A. C., Hermans, C., Fally, S., Carleer, M., Merienne, M. F., Jenouvrier, A., Coquart, B., and Colin, R.: Absorption cross-sections of NO<sub>2</sub>: simulation of temperature and pressure effects, *Journal of Quantitative Spectroscopy & Radiative Transfer*, 76, 373-391, 2003.

Vandaele, A. C., Fayt, C., Hendrick, F., Hermans, C., Humbled, F., Van Roozendaal, M., Gil, M., Navarro, M., Puentedura, O., Yela, M., Braathen, G., Stebel, K., Tornkvist, K., Johnston, P., Kreher, K., Goutail, F., Mieville, A., Pommereau, J. P., Khaikine, S., Richter, A., Oetjen, H., Wittrock, F., Bugarski, S., Frieß, U., Pfeilsticker, K., Sinreich, R., Wagner, T., Corlett, G., and Leigh, R.: An intercomparison campaign of ground-based UV-visible measurements of NO<sub>2</sub>, BrO, and OClO slant columns: Methods of analysis and results for NO<sub>2</sub>, *Journal of Geophysical Research-Atmospheres*, 110, 26, D08305, doi:10.1029/2004jd005423, 2005.

Verhaeghe, E. F., Fraysse, A., Guerquin-Kern, J. L., Wu, T. D., Deves, G., Mioskowski, C., Leblanc, C., Ortega, R., Ambroise, Y., and Potin, P.: Microchemical imaging of iodine distribution in the brown alga *Laminaria digitata* suggests a new mechanism for its accumulation, *J. Biol. Inorg. Chem.*, 13, 257-269, 10.1007/s00775-007-0319-6, 2008.

Vogel, B., Muller, R., Deshler, T., Grooss, J. U., Karhu, J., McKenna, D. S., Muller, M., Toohy, D., Toon, G. C., and Strohm, F.: Vertical profiles of activated ClO and ozone loss in the Arctic vortex in January and March 2000: In situ observations and model simulations, *Journal of Geophysical Research-Atmospheres*, 108, 19, 8334, 10.1029/2002jd002564, 2003.

Vogt, R., Crutzen, P. J., and Sander, R.: A mechanism for halogen release from sea-salt aerosol in the remote marine boundary layer, *Nature*, 383, 327-330, 1996.

von Glasow, R., Sander, R., Bott, A., and Crutzen, P. J.: Modeling halogen chemistry in the marine boundary layer - 1. Cloud-free MBL, *Journal of Geophysical Research-Atmospheres*, 107, 4341, doi:10.1029/2001JD000942, 2002.

von Glasow, R., and Crutzen, P. J.: Tropospheric Halogen Chemistry, in: *The Atmosphere*, edited by: Keeling, R. F., Treatise on Geochemistry, Elsevier-Pergamon, Oxford, 2007.

von Glasow, R.: Atmospheric chemistry - Sun, sea and ozone destruction, *Nature*, 453, 1195-1196, 10.1038/4531195a, 2008.

von Hobe, M., Grooss, J. U., Muller, R., Hrechanyy, S., Winkler, U., and Stroh, F.: A re-evaluation of the ClO/Cl<sub>2</sub>O<sub>2</sub> equilibrium constant based on stratospheric in-situ observations, *Atmospheric Chemistry and Physics*, 5, 693-702, 2005.

von Hobe, M., Salawitch, R. J., Canty, T., Keller-Rudek, H., Moortgat, G. K., Grooss, J. U., Muller, R., and Stroh, F.: Understanding the kinetics of the ClO dimer cycle, *Atmospheric Chemistry and Physics*, 7, 3055-3069, 2007.

Vountas, M., Rozanov, V. V., and Burrows, J. P.: Ring effect: Impact of rotational Raman scattering on radiative transfer in earth's atmosphere, *Journal of Quantitative Spectroscopy & Radiative Transfer*, 60, 943-961, 1998.

Wada, R., Beames, J. M., and Orr-Ewing, A. J.: Measurement of IO radical concentrations in the marine boundary layer using a cavity ring-down spectrometer, *Journal of Atmospheric Chemistry*, 58, 69-87, 10.1007/s10874-007-9080-z, 2007.

Wagner, T., and Platt, U.: Satellite Mapping of Enhanced BrO Concentrations in the Troposphere, *Nature*, 1998.

Wagner, T., Otten, C., Pfeilsticker, K., Pundt, I., and Platt, U.: DOAS moonlight observation of atmospheric NO<sub>3</sub> in the Arctic winter, *Geophysical Research Letters*, 27, 3441-3444, 2000.

Wagner, T., Leue, C., Pfeilsticker, K., and Platt, U.: Monitoring of the stratospheric chlorine activation by Global Ozone Monitoring Experiment (GOME) OCIO measurements in the austral and boreal winters 1995 through 1999, *Journal of Geophysical Research-Atmospheres*, 106, 4971-4986, 2001a.

Wagner, T., Leue, C., Wenig, M., Pfeilsticker, K., and Platt, U.: Spatial and temporal distribution of enhanced boundary layer BrO concentrations measured by the GOME instrument aboard ERS-2, *Journal of Geophysical Research-Atmospheres*, 106, 24225-24235, 2001b.

Wagner, T., Wittrock, F., Richter, A., Wenig, M., Burrows, J. P., and Platt, U.: Continuous monitoring of the high and persistent chlorine activation during the Arctic winter 1999/2000 by the GOME instrument on ERS-2, *Journal of Geophysical Research-Atmospheres*, 107, 10.1029/2001JD000466, 2002.

Wagner, T., Dix, B., von Friedeburg, C., Frieß, U., Sanghavi, S., Sinreich, R., and Platt, U.: MAX-DOAS O<sub>4</sub> measurements: A new technique to derive information on atmospheric aerosols - Principles and information content, *Journal of Geophysical Research-Atmospheres*, 109, 21, D22205, doi:10.1029/2004jd004904, 2004.

Wagner, T., Burrows, J. P., Deutschmann, T., Dix, B., von Friedeburg, C., Frieß, U., Hendrick, F., Heue, K. P., Irie, H., Iwabuchi, H., Kanaya, Y., Keller, J., McLinden, C. A., Oetjen, H., Palazzi, E., Petritoli, A., Platt, U., Postlyakov, O., Pukite, J., Richter, A., van Roozendaal, M., Rozanov, A., Rozanov, V., Sinreich, R., Sanghavi, S., and Wittrock, F.: Comparison of box-air-mass-factors and radiances for Multiple-Axis Differential Optical Absorption Spectroscopy (MAX-DOAS) geometries calculated from different UV/visible radiative transfer models, *Atmospheric Chemistry and Physics*, 7, 1809-1833, 2007.

Wahner, A., Tyndall, G. S., and Ravishankara, A. R.: Absorption cross sections for OClO as a function of temperature in the wavelength range 240-480 nm, *Journal of Physical Chemistry*, 91, 2734-2738, 1987.

Wahner, A., Ravishankara, A. R., Sander, S. P., and Friedl, R. R.: Absorption Cross-Section of BrO between 312 and 385 nm at 298 and 223 K, *Chemical Physics Letters*, 152, 507-512, 1988.

Wahner, A., Jakoubek, R. O., Mount, G. H., Ravishankara, A. R., and Schmeltekopf, A. L.: Remote sensing observations of nighttime OClO column during the Airborne Antarctic Ozone Experiment, September 8, 1987, *Journal of Geophysical Research*, 94, 11405-11411, 1989.

Wallace, J. M., and Hobbs, P. V.: *Atmospheric Science: An Introductory Survey*, Academic Press, 2006.

Wang, P., Richter, A., Bruns, M., Rozanov, V. V., Burrows, J. P., Heue, K. P., Wagner, T., Pundt, I., and Platt, U.: Measurements of tropospheric NO<sub>2</sub> with an airborne multi-axis DOAS instrument, *Atmospheric Chemistry and Physics*, 5, 337-343, 2005.

Watanabe, K., Nojiri, Y., and Kariya, S.: Measurements of ozone concentrations on a commercial vessel in the marine boundary layer over the northern North Pacific Ocean, *Journal of Geophysical Research-Atmospheres*, 110, 8, D11310, doi: 10.1029/2004jd005514, 2005.

Wayne, R. P.: *Chemistry of Atmospheres*, 3rd ed., Oxford Science Publications, 2000.

Welton, E. J., Voss, K. J., Quinn, P. K., Flatau, P. J., Markowicz, K., Campbell, J. R., Spinhirne, J. D., Gordon, H. R., and Johnson, J. E.: Measurements of aerosol vertical profiles and optical properties during INDOEX 1999 using micropulse lidars, *Journal of Geophysical Research-Atmospheres*, 107, 22, 8019, doi:10.1029/2000jd000038, 2002.

Wennberg, P. O., Brault, J. W., Hanisco, T. F., Salawitch, R. J., and Mount, G. H.: The atmospheric column abundance of IO: implications for stratospheric ozone, *Journal of Geophysical Research*, 102, 8887-8898, 1997.

Whalley, L. K., Furneaux, K. L., Gravestock, T., Atkinson, H. M., Bale, C. S. E., Ingham, T., Bloss, W. J., and Heard, D. E.: Detection of iodine monoxide radicals in the marine boundary layer using laser induced fluorescence spectroscopy, *Journal of Atmospheric Chemistry*, 58, 19-39, 10.1007/s10874-007-9075-9, 2007.

Wiencke, C., Vögele, B., Kovaltchouk, N. A., and Hop, H.: Species composition and zonation of marine benthic macroalgae at Hansneset in Kongsfjorden, Svalbard, in: *The coastal ecosystem of Kongsfjorden, Svalbard. Synopsis of biological research performed at the Koldewey Station in the years 1991 - 2003*, 492 p., *Berichte zur Polar- und Meeresforschung* 244, Bremen, Germany, 2004.

Wilmouth, D. M., Hanisco, T. F., Donahue, N. M., and Anderson, J. G.: Fourier Transform Ultraviolet Spectroscopy of the  $A^2\Pi_{3/2} \leftarrow X^2\Pi_{3/2}$  Transition of BrO, *J. Phys. Chem. A*, 103, 8935-8945, 1999.

Wittrock, F., Müller, R., Richter, A., Bovensmann, H., and Burrows, J. P.: Measurements of iodine monoxide (IO) above Spitsbergen, *Geophysical Research Letters*, 27, 1471-1474, 2000.

Wittrock, F., Oetjen, H., Richter, A., Fietkau, S., Medeke, T., Rozanov, A., and Burrows, J. P.: MAX-DOAS measurements of atmospheric trace gases in Ny-Ålesund - Radiative transfer studies and their application, *Atmospheric Chemistry and Physics*, 4, 955-966, 2004.

Wittrock, F.: The retrieval of oxygenated volatile organic compounds by remote sensing techniques, Dr. rer. nat., Institute of Environmental Physics, University of Bremen, Bremen, Germany, 192 pp., 2006.

WMO: Scientific Assessment of Ozone Depletion: 2006, World Meteorological Organization, Geneva, 2007.

Wofsy, S. C., McElroy, M. B., and Yung, Y. L.: The chemistry of atmospheric bromine, *Geophysical Research Letters*, 2, 215-218, 1975.

Yang, X., Cox, R. A., Warwick, N. J., Pyle, J. A., Carver, G. D., O'Connor, F. M., and Savage, N. H.: Tropospheric bromine chemistry and its impacts on ozone: A model study, *Journal of Geophysical Research-Atmospheres*, 110, Artn D23311, Doi 10.1029/2005jd006244, 2005.

Yang, X., Pyle, J. A., and Cox, R. A.: Sea salt aerosol production and bromine release: Role of snow on sea ice, *Geophys Res Lett*, 35, doi:10.1029/2008GL034536, 2008.

Yokouchi, Y., Machida, T., Barrie, L. A., Toom-Sauntry, D., Nojiri, Y., Fujinuma, Y., Inuzuka, Y., Li, H. J., Akimoto, H., and Aoki, S.: Latitudinal distribution of atmospheric methyl bromide: Measurements and modeling, *Geophysical Research Letters*, 27, 697-700, 2000.

Yokouchi, Y., Hasebe, F., Fujiwara, M., Takashima, H., Shiotani, M., Nishi, N., Kanaya, Y., Hashimoto, S., Fraser, P., Toom-Sauntry, D., Mukai, H., and Nojiri, Y.: Correlations and emission ratios among bromoform, dibromochloromethane, and dibromomethane in the atmosphere, *Journal of Geophysical Research-Atmospheres*, 110, 9, D23309, doi:10.1029/2005jd006303, 2005.

Yokouchi, Y., Osada, K., Wada, M., Hasebe, F., Agama, M., Murakami, R., Mukai, H., Nojiri, Y., Inuzuka, Y., Toom-Sauntry, D., and Fraser, P.: Global distribution and seasonal concentration change of methyl iodide in the atmosphere, *Journal of Geophysical Research-Atmospheres*, 113, 9, D18311, doi:10.1029/2008jd009861, 2008.

Yung, Y. L., Pinto, J. P., Watson, R. Z., and Sander, S. P.: Atmospheric Bromine and Ozone Perturbations in the Lower Stratosphere, *Journal of the Atmospheric Sciences*, 37, 339-353, 1980.

Zingler, J., and Platt, U.: Iodine oxide in the Dead Sea Valley: Evidence for inorganic sources of boundary layer IO, *Journal of Geophysical Research-Atmospheres*, 110, 10, D0730710.1029/2004jd004993, 2005.